(4)

AFAL-TR-88-008

AD:

Final Report
for the period
May 1984 to
May 1988

Combustion Mechanisms of Wide Distribution Propellants

AD-A199 761

June 1988

Author:
R. A. Fredrick, Jr.

Purdue University
Research Foundation
Hove Hall of Administration
West Lafayette, IN 47907

F04611-84-K-0019

prepared for the: **Air Force Astronautics Laboratory**

Air Force Space Technology Center
Space Division, Air Force Systems Command
Edwards Air Force Base,
California 93523-5000

88 10 03 048

SECURITY CLASSIFICATION OF THIS PAGE

REPORT DOCUMENTATION PAGE

Form Approved
OMB No 0704-0188

1a REPORT SECURITY CLASSIFICATION UNCLASSIFIED	1b RESTRICTIVE MARKINGS
2a SECURITY CLASSIFICATION AUTHORITY	3 DISTRIBUTION/AVAILABILITY OF REPORT Approved for public release, distribution is unlimited.
2b DECLASSIFICATION/DOWNGRADING SCHEDULE	
4 PERFORMING ORGANIZATION REPORT NUMBER(S)	5 MONITORING ORGANIZATION REPORT NUMBER(S) AFAL-TR-88-008
6a NAME OF PERFORMING ORGANIZATION Purdue University 6b OFFICE SYMBOL (If applicable)	7a NAME OF MONITORING ORGANIZATION Air Force Astronautics Laboratory
6c ADDRESS (City, State, and ZIP Code) Research Foundation Hove Hall of Administration West Lafayette, IN 47907	7b ADDRESS (City, State, and ZIP Code) LSCF Edwards Air Force Base, CA 93523-5000
8a NAME OF FUNDING/SPONSORING ORGANIZATION 8b OFFICE SYMBOL (If applicable)	9 PROCUREMENT INSTRUMENT IDENTIFICATION NUMBER F04611-84-K-0019
8c ADDRESS (City, State, and ZIP Code)	10 SOURCE OF FUNDING NUMBERS PROGRAM ELEMENT NO: 62302F; PROJECT NO: 2308; TASK NO: M1; WORK UNIT ACCESSION NO: AV

11 TITLE (Include Security Classification)

Combustion Mechanisms of Wide Distribution Propellants (U)

12 PERSONAL AUTHOR(S)
Fredrick, Robert A. Jr.

13a TYPE OF REPORT	13b TIME COVERED	14 DATE OF REPORT (Year, Month, Day)	15 PAGE COUNT
Final	FROM 84/5 TO 88/5	88/6	283

16 SUPPLEMENTARY NOTATION

17 COSATI CODES		
FIELD	GROUP	SUB-GROUP
21	09	2

18 SUBJECT TERMS (Continue on reverse if necessary and identify by block number)
Particle Size Distribution, Burning Rate, Solid Propellants, Rocket Motors, Combustion Mechanisms, AP/HTPB Propellants, Laser Diagnostics, Acoustic Emissions, Scanning Electron

19 ABSTRACT (Continue on reverse if necessary and identify by block number)

The objective of this research is to describe the effects of oxidizer particle size distribution on the burning rate of solid propellants used in rocket motors. Current models over predict the burning rate of wide distribution (wide distribution denotes two oxidizer modes that have extreme differences in mean diameter) formulations by 40 to 200 percent indicating combustion mechanisms unique to this type of propellant. Four sets of AP/HTPB propellants were formulated to control the physical and chemical

20 DISTRIBUTION/AVAILABILITY OF ABSTRACT	21 ABSTRACT SECURITY CLASSIFICATION
☒ UNCLASSIFIED/UNLIMITED ☐ SAME AS RPT ☐ DTIC USERS	UNCLASSIFIED
22a NAME OF RESPONSIBLE INDIVIDUAL Philip A. Kessel	22b TELEPHONE (Include Area Code) (805) 275-5591
	22c OFFICE SYMBOL LSCF

DD Form 1473, JUN 86 Previous editions are obsolete SECURITY CLASSIFICATION OF THIS PAGE

Block 19 (continued):

heterogenities characteristic of the propellant surface using 400 and 200 micron oxidizer particles. The propellants were tested at pressure levels from 0 to 2000psig.

An optical, distance measurement technique was developed and used to measure the local, non-steady surface deflagration of the propellant burning surface. The method uses a laser beam, synchronous detection, and closed-loop tracking to locate the surface in the hostile combustion environment. An acoustic emission technique determined average burning rates. Combustion phenomena were also accessed using high-speed photography and scanning electron microscopy.

The results indicate that the burning rate of wide distribution propellants is suppressed by the formation of a layer of liquid binder on the burning surface. High-speed motion pictures showed molten binder flowing off the burning surface during the propellant combustion. The flow increased as the oxidizer-to-fuel ratio of the pocket propellant is decreased. Examination propellant surfaces, extinguished by depressurization, showed that the oxidizer surface was partially covered with a thin binder layer during the burning. This establishes a condensation reaction over the covered portion of the oxidizer which reduces its burning rate. This phenomenon accounts for the difference in model predictions and experimental resuls

Because of the fuel-rich nature of the fine particle combustion, the propellants also exhibited extreme sensitivity to changes in binder composition. This indicated a shift from the dominace of the oxidizer deflagration to the dominance of the binder pyrolysis.

Block 18 (continued):

Microscopy.

Accession For	
NTIS GRA&I	☒
DTIC TAB	☐
Unannounced	☐
Justification	
By	
Distribution/	
Availability Codes	
Dist	Avail and/or Special
A-1	

TABLE OF CONTENTS

Page

LIST OF TABLES

Table | Page

LIST OF FIGURES

Figure Page

Figure Page

Figure Page

LIST OF SYMBOLS

Symbol	*Definition*
A	reference point for linearizing equations
AP	ammonium perchlorate
A_{OX}	oxidizer kinetics prefactor
A_b	binder kinetics prefactor
A_s	strand burning surface area
b	characteristic diffusion flame dimension
c	constant in St. Robert's burning rate expression
c_p	propellant and gas specific heat
C(s)	transfer function of controller
$C_{ss}(s)$	compensation to meet steady state requirements
$CLTF_A$	transfer function of the actual closed loop system
$CLTF_I$	transfer function of the ideal closed loop system
D(s)	detector transfer function
$D_c(s)$	denominator of controller transfer function
D_o	oxidizer particle diameter
$\bar{D}_o$	mean oxidizer particle diameter
d	distance from top of oxidizer particle

E	activation energy
f_s	space dependent distribution function
f_t	time dependent distribution function
F_{LN}	log-normal distribution function
K_1	geometric transfer function
K_2	geometric transfer function
K_{FDI}	gain representing the propellant, detector, and laser
K_{PLA}	gain of the lock-in amplifier
K_s	gain of the scanner
$\bar{\bar{K}}$	open-loop gain
$L(s)$	lock-in amplifier transfer function
$\dot{m}_{ox}$	mass flux of the oxidizer
$\dot{m}_b$	mass flux of the binder
$\dot{m}_f$	mass flux of propellant
n	burning rate exponent
$N_c(s)$	numerator of the controller transfer function
O/F	oxidizer-to-fuel ratio
OF_p	oxidizer-to-fuel ratio of pocket propellant
OLTF	open-loop transfer function
P	pressure
Q	heat release
Q_f	heat of fuel pyrolysis
Q_L	heat of binder pyrolysis
$\dot{r}$	propellant burning rate
$\dot{r}_a$	average propellant burning rate

$\dot{r}_i$	instantaneous propellant burning rate
$\bar{r}$	integrated/average propellant burning rate
R	gas constant
s	LaPlace transform variable
S_o	total surface area
S_{ox}	oxidizer burning surface area
S(s)	scanner transfer function
t	time
T	temperature
T_o	initial propellant temperature
T_s	propellant burning surface temperature
V_c	controller output voltage
V_d	detector output voltage
V_e	lock-in output voltage; error voltage
V_{AO}	acousto-optic amplifier input voltage
x_a	$x_s - x_e$
x_e	local, lateral error of beam spot from optic axis
x_s	local, lateral distance from reference line to optic axis
y_a	local beam crossing distance
y_s	local propellant surface height
Y_s	global propellant surface height

GREEK SYMBOL	*DEFINITION*
α	weight fraction of ingredient in propellant
γ	fraction of AP surface covered with molten binder
ε	position error
$\bar{\varepsilon}$	velocity error
γ_o	normalized weight percentage of oxidizer
ϕ	local beam angle
ρ	density
ρ_p	density of entire propellant
σ	modal standard deviation for distribution function
τ	integration time
τ_{AO}	time constant of acousto-optic deflector
τ_b	time constant of the scanner damping
τ_c	time constant of the controller
τ_{L1}	time constant of the lock-in output filter
τ_{L2}	time constant of the lock-in internal amplifiers
θ	beam angle
θ_o	reference beam angle
ω_n	undamper natural frequency
ζ	damping ratio

SUMMARY

Recent requirements for minimum smoke propellants has resulted in the development of non-aluminized, wide distribution propellants. Wide distribution denotes a multimodal oxidizer blend containing both very large (200 to 400μ) and very small (1 to 25μ) AP particles. The size difference allows higher levels of oxidizer-to fuel ratio for the propellant to be achieved. The general need is to describe the burning rate of these propellants in terms of oxidizer particle size distribution and binder composition. The objective of this research is to describe the combustion mechanisms unique to these propellants and provide a systematic data base of propellant burning rates for future modeling studies. This report is divided into three parts.

Part I presents the background of the research program. Combustion models, based on the multiple flame concept, have been unable to predict the burning rate of wide distribution propellants. Previous work has suggested that the combustion is controlled by the fine-AP particles and binder react preferentially so that combustion controlling mechanisms are not primarily related to the coarse particles. This fine AP/binder matrix, called a pocket propellant, is thought to burn at fuel-rich conditions. Local surface extinction and long ignition delays of the coarse oxidizer particles -often referred to as intermittent burning- have also been observed for these propellants.

Part II presents an optical technique that was developed to continuously measure the local deflagration of the propellant surface. The optical technique, called a Laser Position Detector, was designed, developed and tested in an effort to produce an new tool for solid propellant research. The Laser Position Detector uses a laser beam, synchronous detection, and a closed-loop tracking system to geometrically locate the position of the propellant surface. The control system was developed to have a frequency response that is adequate to measure the local, intermittent burning of 400 micron oxidizer particles. Results show that the device can continuously detect the position of the burning surface at pressures from 0 to 250 psig. Smoke and perturbations of the combustion gases lower the performance at the higher pressure levels.

Part III describes an experimental research program concerned with the ballistic properties of wide distribution propellants. In this program, one set of monomodal, three sets of bimodal, and one set of trimodal propellants were formulated. Each set contains an HTPB binder and duplicate formulations were made with either a IPDI or a DDI curative. The monomodal propellants simulate the composition of the pocket propellants, using 20μAP at oxidizer-to-fuel ratios of 2.0 to 4.0. The bimodal propellants were formulated with controlled pocket propellant chemistry and controlled volume packing of the coarse particles or constant constant total solids level. Bimodal and trimodal 87% solids propellants were formulated to extend the data base for the two type binders into propellants more typical of actual applications. Propellant strands were burned at pressure levels from 0 to 2000 psig. Burning rates were measured using an acoustic emission technique. High-speed photography of combustion scanning electron microscopy of extinguished surfaces were used to access the surface combustion mechanisms.

The propellant studies indicate a strong influence of the pocket propellant composition on the total propellant combustion. The fuel-rich nature of the pocket propellant causes the formation of a liquid layer of molten binder to form and flow on the burning surface. This is a major combustion mechanism that accounts for the difference in the predicted and measured burning rates of wide distribution propellants

The propellants all have greatly reduced burning rates because the binder preferentially reacts with the fine particles. This local fuel rich combustion greatly lowers the fine particle burning rate. The fuel-rich nature of the local combustion did increase the sensitivity of the burning rate to change in binder chemistry. The DDI curative, in all cases, reduced the burning rate of the propellants when compared to identical IPDI cured formulations. The addition of plasticizer is believed to enhance the suppressing effects of both curatives. Measurements with high-speed photography and the Laser Position Detector did not reveal significant ignition delays of the coarse oxidizer particles for these formulations at the conditions tested, however, it is postulated that the intermittent combustion when observed would be related to the excess binder on the propellant surface (solid or liquid).

PART I

RESEARCH PROGRAM

1.0 SOLID PROPELLANTS

When designing a solid propellant rocket motor, there are four classic areas that place constraints on the selection of the propellant. They are:

1. Performance - What is the specific impulse?
2. Ballistics - How fast does it burn?
3. Structures - Will it maintain its shape?
4. Viscometrics - Can it be cast?

The research presented in this report is concerned with predicting the ballistic properties of solid propellants as a function of oxidizer particle size distribution. This chapter provides a general background to introduce the basic concepts involved in describing oxidizer particle size effects on propellant ballistic properties.

1.1. Introduction

Much research has been performed to describe the ballistic properties of solid propellants. Both experimental and theoretical studies have been used to describe the effects of formulation changes on the propellant burning rate. Experiments have varied from burning small samples in pressurized vessels to propellants grains in an actual motor. Combustion models have been developed that predict the burning rate of a limited scope of propellant formulations using one-dimensional, steady, linear approximations [1].

Describing the effect of pressure on the propellant burning rate is a primary concern. The effect of pressure on propellant burning rate is shown in Figure 1. The burning rate is classically described with an empirical St. Robert's law expression

$$\dot{r} = cP^n \qquad (1)$$

where the power "n" is referred to as the burning rate exponent or simply as the exponent. The results are shown plotted on log scales making the exponent proportional to the slope of the curve.

Achieving a particular burning rate and exponent at a given pressure and composition is a major goal of propellant formulation tailoring. Several parameters can be used to change the propellant burning rate. For a fixed chemical composition, changing the size or size distribution of the oxidizer particles can be used to influence the burning rate and the exponent. Also, certain catalysts can be added to the formulation to augment the combustion.

1.2. Propellants

Composite propellants are a heterogeneous grain with oxidizer crystals held together in a matrix of synthetic rubber (or plastic) binder such as polybutadiene as sketched in Figure 2.

1.2.1. Binder The binder fills the interstitial space between the oxidizer particles, provides its mechanical properties, and acts as a fuel in the combustion. The binder can be used to control the burning rate mainly through the addition of catalysts or ingredients such as various curing agents.

1.2.2. Oxidizer The oxidizer provides oxidizing species to produce the hot gases. Ammonium perchlorate (AP), NH_4ClO_4, is the most widely used crystalline oxidizer in solid propellants. Ammonium perchlorate is available as small white crystals that are

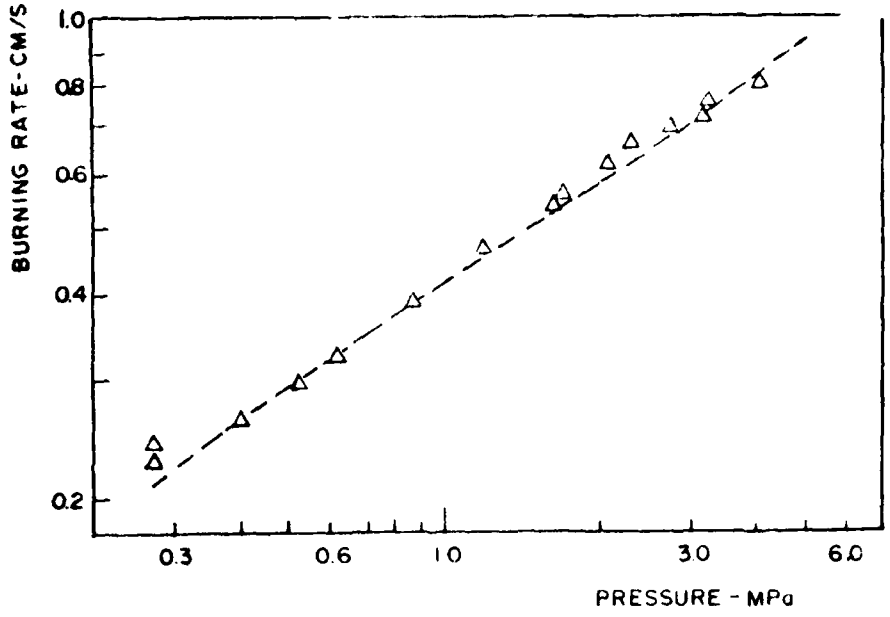

Figure 1. Typical Burning Rate-Pressure Curve

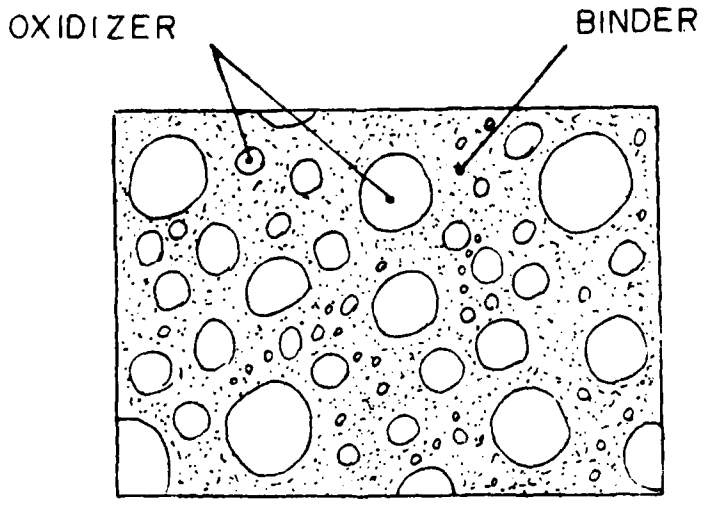

Figure 2. Composite Propellant

ground into the desired sizes before the propellant is mixed.

Since the particle size of the oxidizer influences the propellant burning rate, the AP particle size distribution must be formally described. The relationship of particle size and mass distribution for a single mode is accurately described [2,3] with an average diameter and a mode width by a log-normal distribution

$$F_{ox}(\bar{D},\sigma) = \frac{1}{\sqrt{2\pi}\ln\sigma} \exp\left\{ \frac{-1}{2}\left[\frac{\ln D_o - \ln \bar{D}_o}{\ln\sigma} \right]^2 \right\} \qquad (2)$$

and results for two example mode widths are illustrated in Figure 3. For a multimodal propellant, the mass distribution is described with additional log-normal distribution functions

$$F_{ox}[(\bar{D}_1,\sigma_1),(\bar{D}_2,\sigma_2),\ldots,(\bar{D}_n,\sigma_n)] = \gamma_1 F_{ox,1} + \gamma_2 F_{ox,2} + \ldots + \gamma_n F_{ox,n} \qquad (3)$$

and an example plot for a trimodal distribution is shown in Figure 4. Multimodal oxidizer blends are used to increase the mass fraction of oxidizer in the propellant and control the the burning rate exponent.

1.2.3. Other Ingredients Other ingredients are often included in solid propellants and are generally classified according to their function e.g. fuel, oxidizer, curing agent, burn rate catalyst. The other prominent fuel of note is aluminum powder. One or two high explosives such as HMX (cyclotetramethylene) or RDX (cyclotrimethylene) are sometimes included to achieve specific performance characteristics.

1.3. Observed Burning Characteristics

The burning surface of a composite propellant is a random, chemically discrete structure. At any instant, individual oxidizer particles are emerging through the surface at various stages of exposure. On the scale of the oxidizer particles, the surface deflagration is a three-dimensional, unsteady process with a complex sequence of

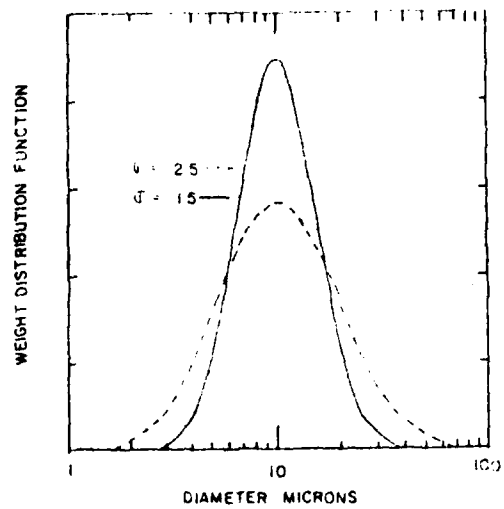

Figure 3. Log-Normal Distribution Function

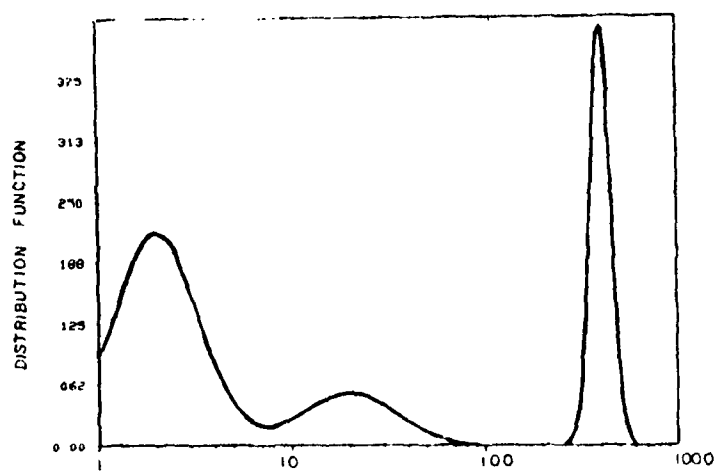

Figure 4. Multi-Modal Distribution Function

interactions. Yet the overall surface, over distances larger than an individual oxidizer particle, burns at a measurable "steady-state" rate. The observed and implied processes that occur during combustion can be described by following a single oxidizer particle from below the burning surface to its consumption above the surface by the various flames.

An oxidizer particle lying a few millimeters below the burning surface is unaffected by the high temperature combustion gases since the propellant itself is a good insulator [4]. As the particle nears the burning surface, however, a thermal wave affects an energy transfer into the particle raising its temperature. A crystalline phase change from orthorhombic to cubic occurs when the local temperature reaches about 513 K [5]. As the particle emerges through the burning surface, its temperature quickly approaches the auto-ignition temperature and after some finite ignition delay, the particle then decomposes into gaseous products (an intermediate liquid phase is possible). Simultaneously, the adjacent binder is undergoing an endothermic pyrolysis. The decomposition products of the oxidizer and binder burn in exothermic reactions above the propellant surface producing a flame structure above the particle that is controlled both by kinetic and diffusion processes due to the heterogeneous surface structure. Some of this energy released by the flames is transferred back to the propellant surface and the rest is carried away by the product gases. The heat fed back to the surface directly controls the surface deflagration rate.

1.4. Combustion Models

Statistical combustion models [6-13] provide a framework for describing the complex sequence of events involved in the burning of a composite propellant. A model must describe the structure of the propellant surface, the combustion and heat transfer of the gas phase, and the deflagration of the surface. Models typically analyze

a single oxidizer particle and an associated amount of binder then use this result as the basis of predicting the propellant burning rate. The following sections describe the general approach followed.

1.4.1. Surface Structure The complex structure of the surface is simplified by using a mean state concept [6]. The many stages of exposure of an individual oxidized particle are modeled using only one state. This state is chosen as the statistically averaged surface diameter exposed when a random plane is passed through a particle bed. The entire emergence process is then equated to this statistically representative state as illustrated in Figure 5. Figure 6 shows additional detail that is included to describe the instantaneous surface of the AP crystal protruding above (or below) the binder. So the complexity of the particle evolution is simplified by using a statistically mean state to represent the entire emergence process.

1.4.2. Flame Structure The flame structure used in modern combustion models was developed by Beckstead, Derr, and Price [7]. The drawing in Figure 7 shows the proposed flame structure above the statistically mean state. Three flames are considered in the model: a primary flame that is controlled by kinetic and diffusion processes; an AP flame that is a kinetic controlled monopropellant flame; and a final flame that is a diffusion controlled flame. These three flames compete for the decomposition products based on kinetic and diffusion mechanisms causing the proportion of energy released in each flame to be a function of both pressure and particle size.

The position of each flame above the propellant surface influences the heat conducted back to the surface. For the AP flame, a one-dimensional heat transfer from a flame sheet is a reasonable approximation. For the diffusion flames, that are columnar

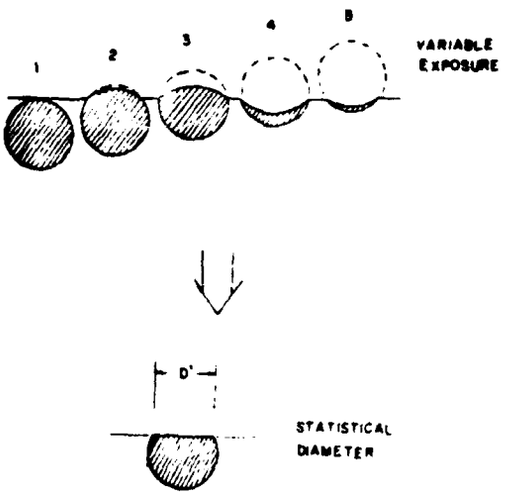

Figure 5. Statistically Averaged State

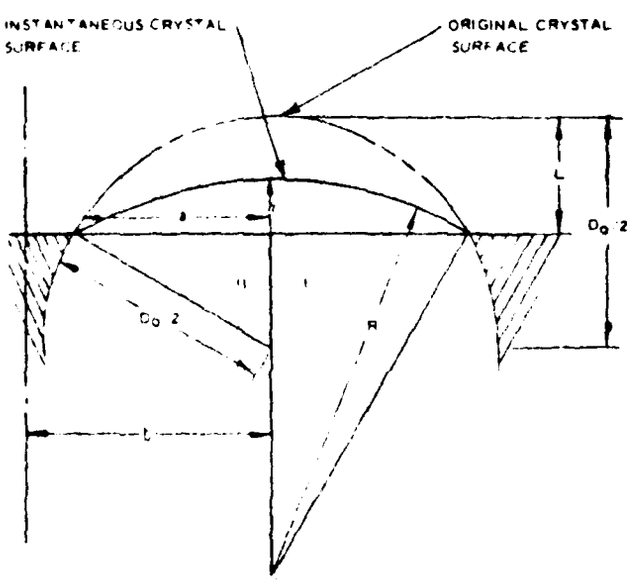

Figure 6. Detailed Surface Geometry

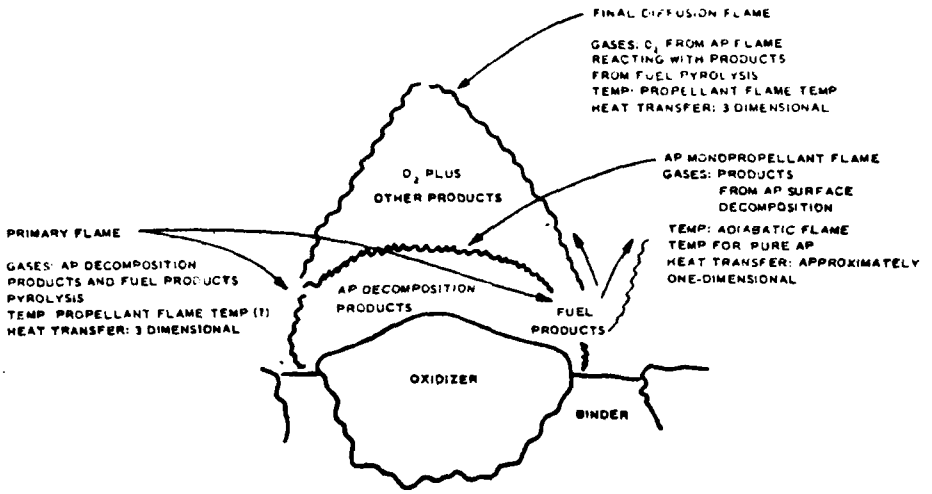

Figure 7. Multiple Flame Structure

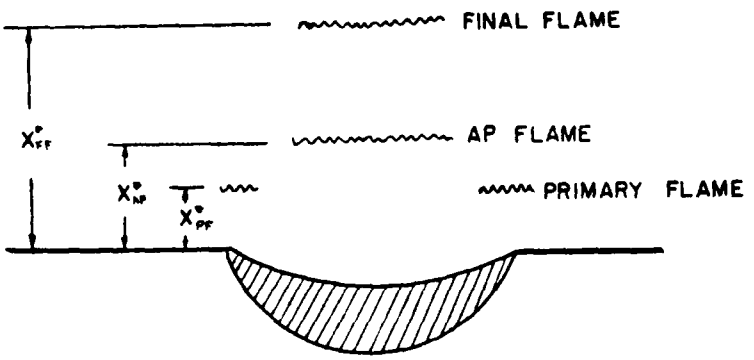

Figure 8. Simplified Flame Structure

in nature, the heat transfer would be three-dimensional but results are converted into a one-dimensional flame sheet. The resulting flame sheets and their standoff distances as represented by an analysis are sketched in Figure 8.

The flame structure then accounts for the partitioning of the decomposition products into three flames predicting a flame temperature and a position for each flame above the surface.

1.4.3. Surface Deflagration The oxidizer and binder of the statistically mean state are assumed to deflagrate with a mass flux that is an Arrhenius function of surface temperature

$$\dot{m}_{ox} = A_{ox} \exp\left\{\frac{-E_{ox}}{RT_s}\right\} \tag{4}$$

$$\dot{m}_{b} = A_{b} \exp\left\{\frac{-E_{b}}{RT_s}\right\} \tag{5}$$

The surface temperature is computed by performing an energy balance at the propellant surface. Sources that influence a control volume that moves with the burning propellant surface are shown in Figure 9. Energy is conducted to the surface by the three propellant flames. Energy is also supplied by two additional mechanisms. First, the heat of decomposition of the binder (endothermic) and the heat of decomposition of the AP (net exothermic) is released at the burning surface. Second, energy is also convected into the control volume by the propellant and out by the hot gases. The deflagration rate of the surface is then determined by using conservation of energy to determine the surface temperature.

1.4.4. Predicting Rate For a monomodal oxidizer propellant, the total burning rate can be derived from the analysis of one representative state. If the oxidizer deflagration is

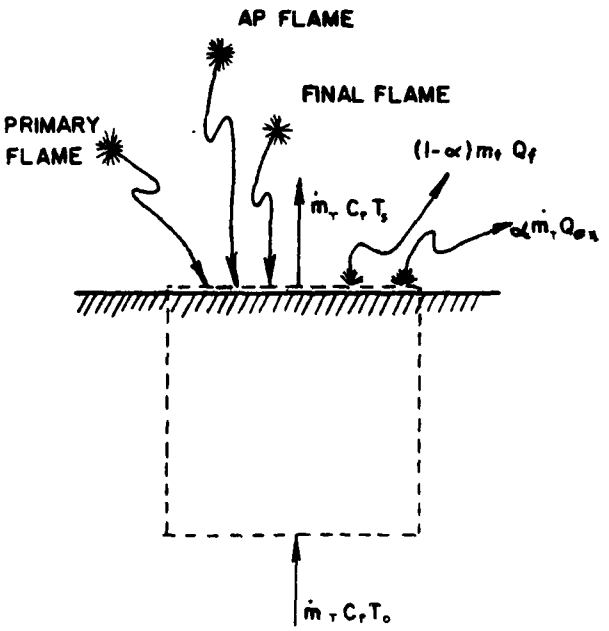

Figure 9. Surface Energy Balance

assumed to dominate the surface reaction, then the binder is consumed at a rate proportional to its mass fraction. The mass flux of the propellant is then

$$\dot{m}_t = \left\{ \frac{\dot{m}_{ox}}{\alpha} \right\} \left\{ \frac{S_{ox}}{S_o} \right\} \tag{6}$$

The surface area ratio is computed using the surface structure description. The linear burning rate of the propellant is then the total mass flux divided by the propellant density.

$$\dot{r} = \frac{\dot{m}_t}{\rho_p} \tag{7}$$

For polydisperse or multimodal oxidizer distributions this approach must be extended. Several oxidizer diameters are partitioned into pseudopropellants that each describe a mean state based on the oxidizer particle size distribution. Each pseudopropellant is assumed to burn with an oxidizer-to-fuel ratio identical to the overall formulation. The propellant burning rate is then computed by integrating together the contributions of each pseudopropellant.

The average rate can be determined from the pseudopropellant rates using two approaches. An average is generally computed by integrating a local value of a dependent variable about an independent variable. For the propellant either time or space could be considered as an independent variable with burning rate as the dependent variable. This leads to two possible approaches for integrating the pseudopropellant burning. The area-averaged approach

$$\bar{r} = \frac{\int_S r_L f_s dS}{\int_S f_s dS} \tag{8}$$

and the time-averaged approach

$$\bar{r} = \frac{\int_t r_L f_t dt}{\int_t f_t dt} \tag{9}$$

where f_s and f_t are space and time dependent distribution functions respectively. Equation 8 has been used with the multiple flame model to describe particle size distribution effects with the Petite Ensemble Model.

Results of burning rates, predicted with the Petite Ensemble Model, are sketched in Figures 10 and 11. Figure 10 shows the effect of the various flame mechanisms on the burning rate as a function of pressure for a monomodal oxidizer propellant. At low pressures, the primary flame kinetics control the combustion resulting in an exponent of nearly unity. As the pressure increases, the combustion transitions to an intermediate stage where diffusion processes compete for the reacting species. Diffusion control lowers the pressure exponent. Then, at high pressures, the exponent again approaches unity as the mechanism return to a kinetics reaction. This time, however, it is the AP monopropellant flame that controls the combustion.

The onset of the diffusion control is a function of AP particle size. Figure 11 shows the burning rate-pressure curve for three monomodal propellants. The results show that larger particles introduce the diffusion processes into the combustion at lower pressures.

1.5. Summary

Ballistic properties of solid propellants must be controlled to attain the desired performance of a rocket motor. The ballistic properties can be controlled by selection of the AP particle sizes included in the formulation. Both the burning rate and the exponent are influenced by AP particle size distribution.

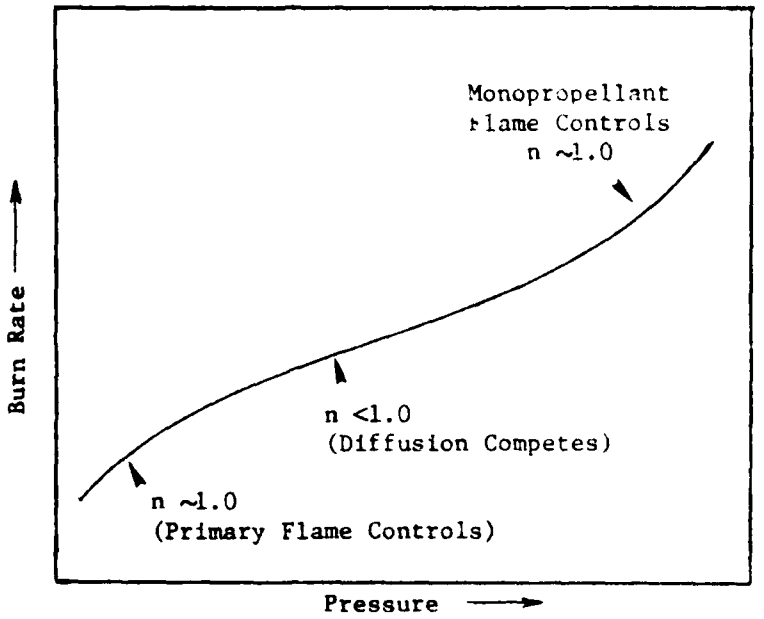

Figure 10. Effect of Flame Mechanisms on Pressure-Rate Curve

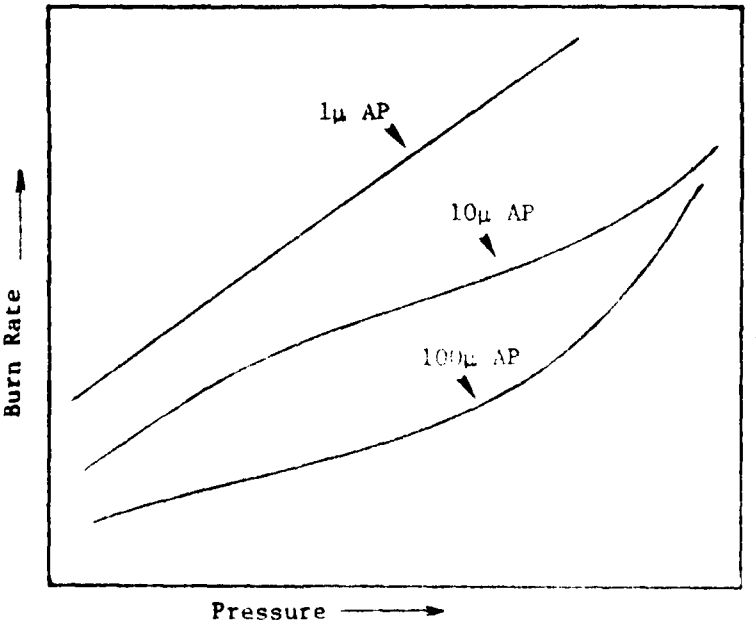

Figure 11. Effect of Monomodal AP Size on Pressure Rate Curves

2.0 OVERVIEW OF RESEARCH

2.1. Wide Distribution Propellants

The recent requirements for minimum smoke propellants has forced the removal of aluminum powder from certain propellant compositions. Aluminum products in the rocket plume can contaminate spacecraft or can leave a visible trail between the rocket motor and the launching platform that is a problem in air combat. To make up for the impulse lost from removing the aluminum, more oxidizer must be packed into the propellant matrix. Since there is a finite interstitial space between unimodal oxidizer particles, the overall oxidizer to fuel (O/F) ratio is increased by packing smaller diameter modes between larger particles. This has resulted in the development of non-aluminized, wide oxidizer distribution* AP propellants. A typical oxidizer blend for a wide distribution propellant was shown previously in Figure 4. The coarse mode usually has mean diameters ranging from 120-400 microns.

Combustion models based on the multiple flame concept (previously discussed in section 1.4), such as the BDP [5] and the PEM [9] have been able to predict the ballistic properties (burning rate and exponent) of previous polydisperse propellants to within about 10 percent. The influence of the size distribution on average rate is predicted by integrating together the results of independent analyses of each particle size. These models, however, are not able to predict the burn rate-pressure behavior of the wide

* Wide Distribution will be defined as a polydisperse, multimodal oxidizer blend having a factor of 10 difference between the mean diameters of the largest two modes.

distribution propellants, especially over large variations in coarse particle concentration.

2.2. Distinctive Mechanisms

Previous studies [12,13] have shown that HTPB** propellants with wide AP distributions burn at rates much different than predictions based on theoretical or even extrapolated experimental values. Comparison of measured [19] and predicted burning rates are shown in Figure 12 as a function of coarse oxidizer fraction. Incrementally replacing the fine oxidizer with coarse particles in this trimodal propellant, results in an decrease in measured burning rate. Results of PEM calculations are close to the measured rate at lower concentrations of coarse particles but miss the decrease in rate as the coarse fraction is increased. Two phenomena could possibly cause these differences.

2.2.1. Heterogeneous Surface Chemistry The first is a change in the local allocation of the oxidizer and fuel. Scanning electron microscopic pictures of the propellant surface [19] have shown the heterogeneous nature of the coarse and fine AP exposed on the propellant surface. The heterogeneity is illustrated in Figure 13 for a typical, trimodal propellant formulation. For every 400μ AP particle, there are over two-thousand, 20μ particles and over two-million, 3μ particles. The fine AP and binder make up a matrix that appears homogeneous when compared to a coarse particle. This fine-AP/binder matrix is often called a pocket propellant because it lies in a pocket between the large particles. Figure 14 shows the pocket propellant concept. The pocket propellant consists only of the fine AP particles and all of the binder. It is equivalent to casting the propellant without the coarse particles. The pocket propellant

** hydroxy-terminated polybutadiene binder

concept is used because significant amounts of the fine AP/binder matrix are then reacting away from the influence of the coarse particles. The model, however, allocates binder in equal proportions to all particle sizes. The difference is that fine AP/binder matrix could be burning at a significantly different stiochiometry that controls the ballistics of the overall propellant and the coarse particles having only a secondary effect. Variations in the coarse fraction would change this local chemistry.

2.2.2. Intermittent Combustion. The second phenomena that could cause unpredictable burning rates is intermittent combustion. Initial measurements of the local burning rates of wide distribution propellants [20,21] have revealed a local starting and stopping of the surface caused by long ignition delays of the coarse particles. Figure 15 shows this phenomenon. Traditional models have constrained the propellant to burn with a certain order based on either area-averaged or time-averaged integration schemes that combine the burning rates of each particle size to produce an average burning rate. Long ignition delays can invalidate the assumption that all particles are burning simultaneously on the surface implicit in the area-averaged approach. They can also invalidate the assumption that particles burn sequentially (slow particles could be bypassed) inherent in the time-averaged approach. The sequence that the particles burn could be augmented by the long ignition delays.

Thus, two factors force departure from the conventional models of combustion; the reallocation of fuel and intermittent combustion.

2.3. Statement of the Problem

The results of past investigations suggest that two questions must be answered to predict the burning rate of wide distribution propellants.

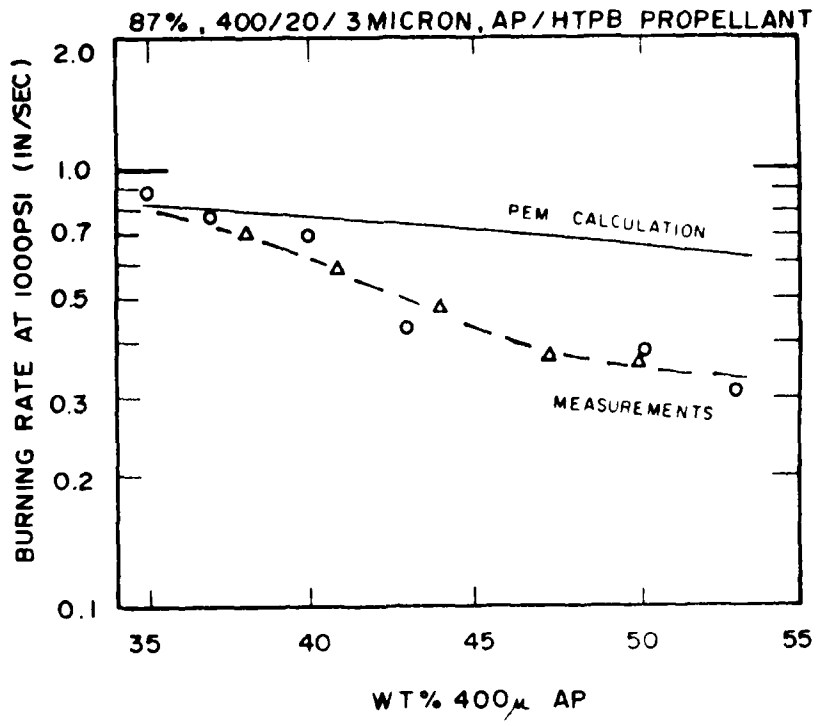

Figure 12. Comparison of Measured and Predicted Propellant Burning Rates of Wide Distribution Propellants

1. *How does the oxidizer particle size distribution effect the local combustion chemistry?*

Current multiple flame models allocate constant proportions of the oxidizer and binder to each size oxidizer without regard for the local chemical heterogeneity caused by the propellant matrix. A mechanism that describes the reallocation of the binder with changes in oxidizer particle size distribution is needed

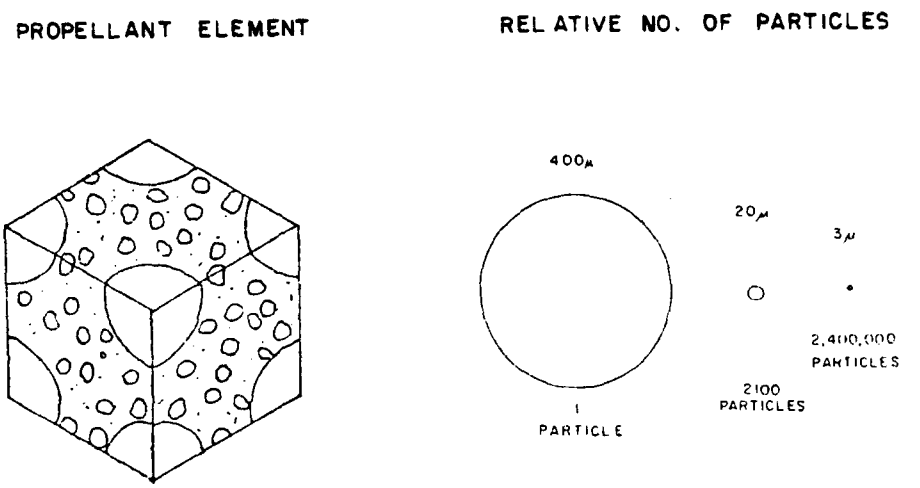

Figure 13. Wide Distribution Propellant

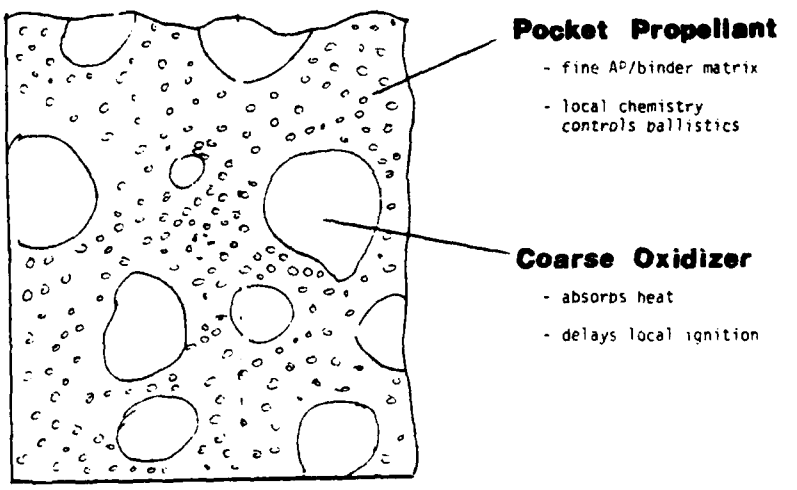

Figure 14. Pocket Propellant Concept

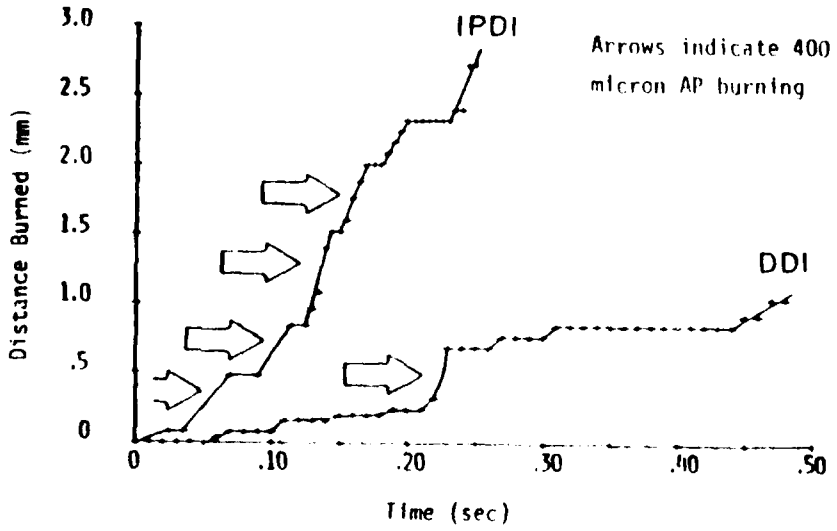

Figure 15. Local, Intermittent Combustion

2. *What conditions produce unusually long oxidizer ignition delay periods?*

Current models for combining the burning rates of different sized particles are invalid if the ignition delay of the coarse oxidizer particles becomes too long. The conditions that produce intermittent combustion must be described to identify formulations outside the scope of current theories.

The problem then is that the local combustion processes of wide distribution propellants must be measured or inferred to understand how to they control the average burning rate.

2.4. Scope of Research

The major emphasis of the research is in the experimental area. The scope is divided into two major sections; development of an instrument to measure the local burning, and combustion studies.

1. DEVELOP INSTRUMENT

   - Develop technique to continuously detect the *local* movements of the propellant surface.
   - Evaluate the instrument performance on controlled inputs and on propellant strands at pressure level from 1.0 to 34.0 ATM.

2. COMBUSTION STUDIES

   Propellants

   - Formulate 6 series of wide distribution propellants that control fine-AP/binder chemistry, coarse oxidizer volume fraction, and binder curative.
   - Formulate 2 series of trimodal wide distribution propellants that represent formulations used in actual applications.

   Ballistics

   - Measure average burning rates as a function of pressure of all propellant formulations at pressure levels from 8.5 to 68.0 ATM.
   - Measure local burning of propellant strands with the device developed above for selected formulations quantifying the ignition delay of the coarse particles, and the average burning rate of the propellant.
   - Examine the extinguished surface of two formulations having different binder curatives and an identical oxidizer distribution at pressure levels from 8.5 to 68.9 ATM.
   - Interpret results in light of current theories and propose mechanisms that account for observed behavior.

PART II

INSTRUMENT DEVELOPMENT

3.0 SURVEY OF BURNING RATE MEASUREMENT TECHNIQUES

Propellant burning rate is a locally unsteady process that fluctuates about a long term mean rate as illustrated in Figure 16. The instantaneous burning rate fluctuates by a small amount about the mean value as the local heterogeneities of the propellant are encountered. This low frequency, intermittent combustion is not the instability associated with pressure or velocity coupled burning rate responses. The instantaneous burning rate of a propellant is defined by

$$\dot{r}_i = \lim_{\Delta t \to 0} \left\{ \frac{\Delta X}{\Delta t} \right\} = \frac{dX}{dt} \tag{10}$$

If the instantaneous rate were known, the mean value theorem could be applied to determine the average rate

$$\bar{r} = \frac{1}{t_1} \int_0^{t_1} \dot{r}_t dt \tag{11}$$

In practice however, continuous or infinitesimal distance measurements cannot always be obtained. The burning surface is rough, and the exhaust gases are hot (3000K), corrosive (HCl), and luminous making conventional precision measurement techniques inappropriate. To further complicate the matter, the propellant must be burn at elevated pressures (100-10,000 psig) to simulate operating conditions. Equation 6 then can be approximated by

$$\dot{r}_a = \frac{X_2 - X_1}{t_2 - t_1} \tag{13}$$

and if the time is sufficiently long this value will be the average value also. What

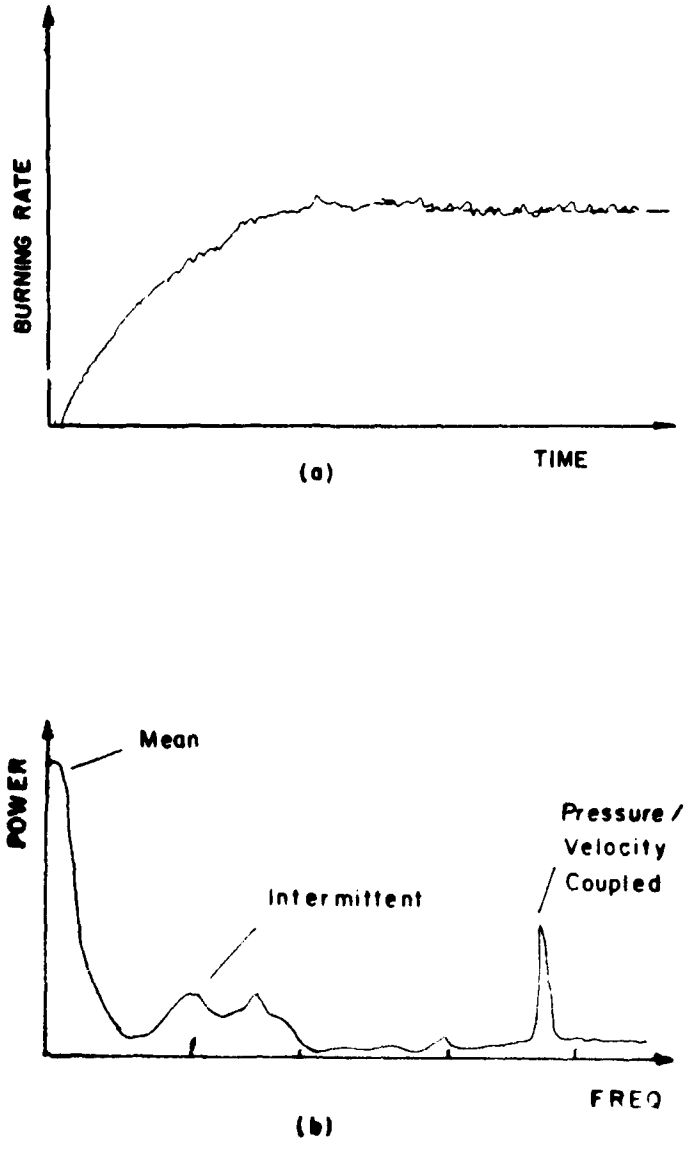

Figure 16. Frequency Spectra of Burning Rate

follows is a description of the various techniques and detection principles that have been used for measuring the burning rate of a solid propellant strand in a strand burner. A brief description of the strand burner is given. Surface detection techniques are then reviewed that have been applied with combustion bombs to find a suitable technique for measuring local surface movements. A summary is presented at the end of the chapter.

3.1. Strand Bombs

In testing new propellant formulations to determine the burning rate, two categories of devices are used: subscale test motors and strand bombs. Test motors provide reliable and accurate burning rate information [20], however, test motors are more costly to operate and provide limited access for direct measurements of the propellant burning rate. Combustion bombs, on the other hand, provide a pressure controlled environment where a variety of surface detection schemes can be applied. While combustion bombs do not produce burning rates that correlate consistently to results from test motors, they do allow investigations of combustion phenomena that cannot be measured using subscale test motors. Further, for research purposes where many ambient condition and formulation changes are desired, the strand bomb allows many tests to be run with minimal cost.

The hardware for a typical combustion bomb is shown in Figure 17. The shell of this vessel is designed to withstand high pressures (up to 3000 psig) and hold windows for optical access. Small sized strands, typically 0.25 x .25 inches in cross-section are burned under a steady pressure. Gaseous nitrogen enters the bomb at the base and is flushed through the interior and out exhaust ports at the top. This provides a constant pressure, constant flow rate condition around the sample during a given experiment. Optical access is provided by quartz windows and electrical leads come through pressure-sealed bulkheads. Several detection schemes have been used to sense the

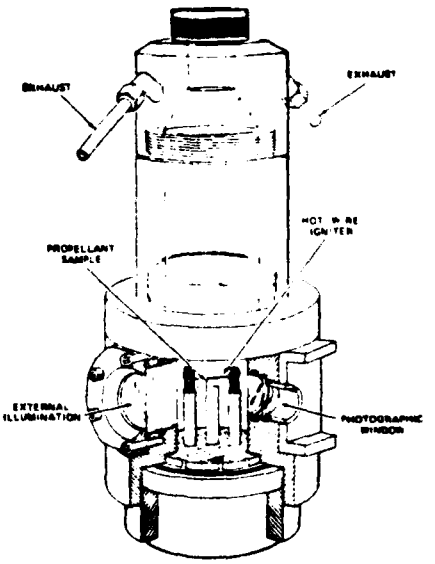

Figure 17. NWC Strand Bomb

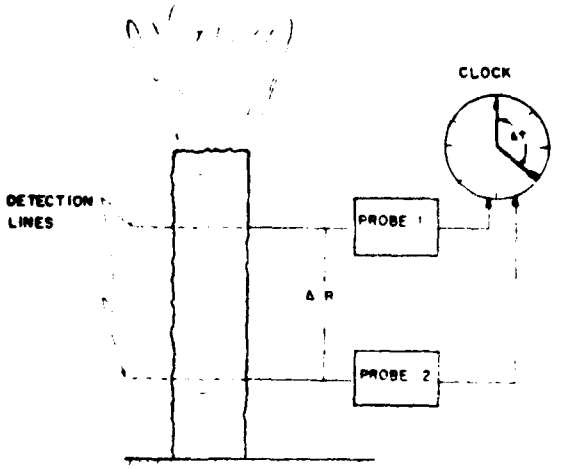

Figure 18. Principle of Discrete Measurement

position of the burning front with the combustion bomb.

3.2. Discrete Techniques

Several methods have been used to detect the propellant surface position at discrete time or distance intervals. The approximate expression for average burning rate is

$$\dot{r}_a = \frac{\Delta X}{\Delta t} \tag{13}$$

The measurement can be made either by measuring the action time, Δt over a controlled distance, ΔX or conversely by measuring the distance burned over a specified time period. The principle is illustrated in Figure 18.

3.2.1. Timing Wires [23,24] Fine wires are fed through small holes drilled in the propellant strand. The holes are spaced at known intervals and connected to electronic circuits. When the burning front reaches the wire, the wire is quickly melted and the resulting continuity loss in the circuit triggers a timer. Several wires my be inserted along a single strand. Placing the wires is time consuming, and the wire increases the burning rate momentarily by enhancing the heat transferred to the propellant surface. Inaccuracies are also inherent in the positioning of the wire.

3.2.2. Thermocouples [25] Thermocouples are placed in small holes drilled in the side of the propellant strand at measured intervals. The surface is detected by the rapid rise in temperature as the burning front passes the thermocouple bead. The same difficulties associated with timing wires are present however, less of the burning front is disturbed.

3.2.3. Ionization and Conductivity Probes [26,27] Ionization or conductivity probes are inserted in small holes that are drilled at predetermined depths in the propellant. The ionization probes are charged to a high potential. As the burning front passes, the

gases allows the voltage to discharge. Conductivity probes similarly sense exposure to the gases except the gas is used as a conductor to complete an electrical circuit.

3.2.4. Laser Beams [28,29] When optical access is possible, a laser beam can be used to measure the burn time. Two beams are directed through the combustion bomb and into two photodetectors stationed outside the opposite window. Optical filters admit only the light wavelength near the laser light's color. The beams are then blocked by positioning the strand in their path. When the burning front passes the beam, the laser light passes through the combustion bomb and enters the photodetectors. The output of the photodetectors triggers a clock. Inaccuracies are introduced by the beam being bent as is passes through the changing refractive index of the gases above the propellant.

A variation of this technique has been attempted [30] in which the laser beam is expanded and directed toward a linear array of photodiodes. Each photodiode is triggered as the laser light shining over the moving surface enters successive detectors. The array can have a close measurement interval (ΔX) however the problems with beam bending are still present.

3.2.5. Pressure Sensor [32] In a stand bomb, a slight pressure rise will occur while the propellant is burning. By timing the duration of this pressure rise over the duration of the entire burn, the burn time is determined.

3.2.6. Acoustic Emissions Sensor [33,37] When a propellant burns, it gives a off high frequency sound when the oxidizer particles crack. By attaching an acoustic emission sensor to the combustion bomb, the RMS sound level triggers a clock. Sometimes, small notches are cut in the side of the strand that produce spikes in the sound level. This is a fast, reliable technique for determining the burn time of a strand.

3.2.7. Strand Measurement [38] A discrete technique that controls the time variable and measures the distance burned is called extinguishment. By suddenly rupturing a diaphragm in the bomb wall, the pressure inside the strand bomb drops and most propellants extinguish. The length of the remaining sample can be directly measured. This technique is time consuming for burning rate determination and is more often used to study the details of the propellant surface or to study other phenomena.

3.2.8. Motion Picture Camera [18,21,39-43] High speed cameras, with framing rates from 4-44,000 frames per second, are used in propellant burn rate studies. Pin-registered cameras record the profile of the burning surface at rates of from 4 to 500 frames per second, while rotating prism cameras have framing rates ranging from 20 to 44,000 frames per second. With the surface position recorded at known intervals, the burning rate can be determined at many locations depending on the camera framing rate, the film resolution, and the propellant burning rate. Motion analyzers are used to project the film and measure the time-motion phenomena. This setup requires additional light sources and sequencers to do the photography. Cinephotomicrography begins to approximate the time intervals necessary to see the fluctuating component of the burning rate although distance resolution is somewhat prohibitive.

One new approach [39], uses a pulsed copper vapor laser to illuminate the propellant and eliminate flame glare.

3.3. Continuous Techniques

A few techniques for continuously measuring the surface position of a burning propellant strand have been used with the strand bomb. The techniques generally involve an energy source and a sensor as illustrated in Figure 19. The movement of the burning surface continuously changes the amount of energy transmitted to the detector

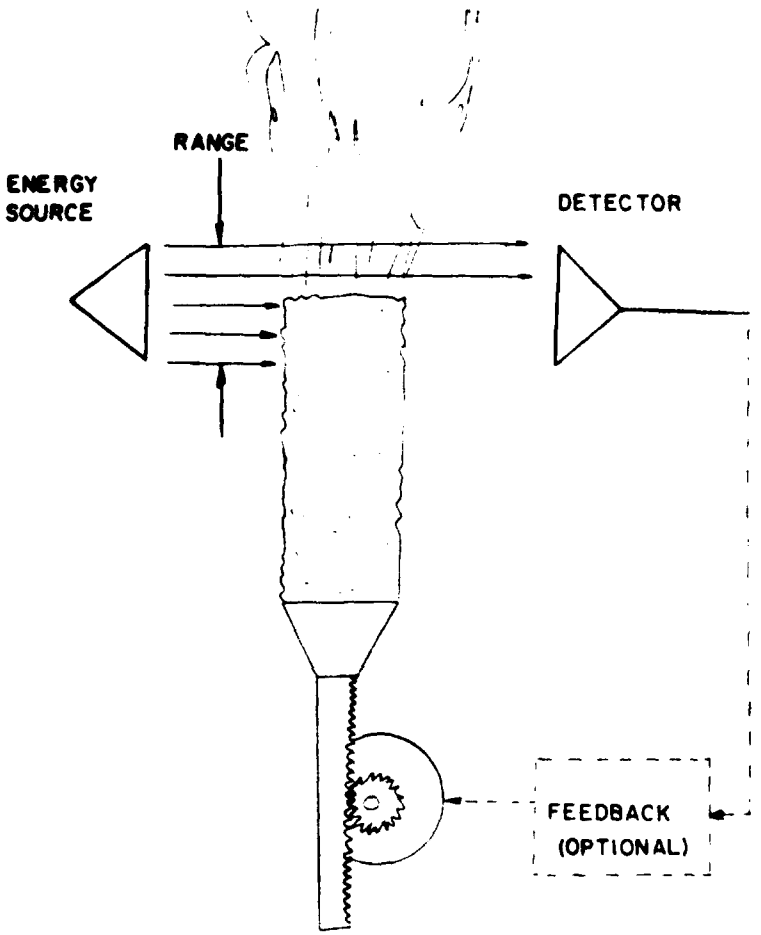

Figure 19. Principle of Continuous Measurement

so that an intensity-surface height correlation may be drawn. The following discussion of continuous measurement techniques is ordered by the energy source used to detect the burning rate.

3.3.1. Electromagnetic Radiation Electromagnetic radiation has mainly been used with detectors positioned on the opposite side of the propellant strand. The output is an analogue signal measured by a detector that has a continuous distance sensitivity over a limitied range. The radiation is blocked to varying degrees by the position of the burning surface as illustrated in Figure 19. Light sources, such as a tungsten lamp [44-46] and a He-Ne laser [47-51] directed across the propellant have been used. Light from the tungsten lamp has problems with sample heating and emitting light in the same spectrum as the propellant introducing bias in the detection. For the laser, a band pass light filter is positioned in front of the detector to screen most combustion light. Problems are possible however from the laser beam being deflected from a straight path by the refractive index differences of the combustion products and the purge gas. Laser beam measurements have been successful although they are also susceptible to attenuation by the propellant smoke and irregularities in the propellant surface. X-Rays have been suggested for strand work, however, the sensitivity would probable be insufficient to resolve the surface of a small strand.

These techniques often have a limited sensitivity range so they are often used with a servo-positioning system that continuously positions the surface of the strand in the measurement volume [45,47,48] or sometimes the detector and source both follow the moving surface [50, 51].

3.3.2. Collimated Radioactive Beam [30,52] A radioactive beam is passed through the strand and the intensity of the emerging component is measured. A scintillation

probe is used as a detector and the resulting signal provides a continuous measure of the burning rate. Unfortunately, the sources introduce operational hazards for the test personnel.

3.3.3. Microwave Reflection [53-56] The principle of the microwave technique is illustrated in Figure 20. A continuous microwave beam is transmitted through the propellant and reflected back from the propellant burning surface. The reflected signal has a Doppler shift proportional to the surface regression rate. Present microwave techniques achieve greater resolution by monitoring the phase angle difference between the incidence and reflected microwave signal. Microwave systems are capable of measuring rapid, changes in the burning rate. The rate measured is an instantaneous rate.

The same principle could be applied by reflecting a wave (such as light or sound) off the burning surface through the gases. The variable physical properties of the gases and the diffuse nature of the burning surface currently make this approach less desirable.

3.3.4. Combustion Recoil [57,58] As the propellant burns, the weight of the remaining sample decreases. By measuring the force exerted at the base of the sample, the mass consumption rate can be measured and the burning rate determined by

$$\dot{r}_s = \frac{\dot{m}_t}{\rho_p A_s} \tag{14}$$

A propulsive force, however, is produced by the product gases that biases the measurement.

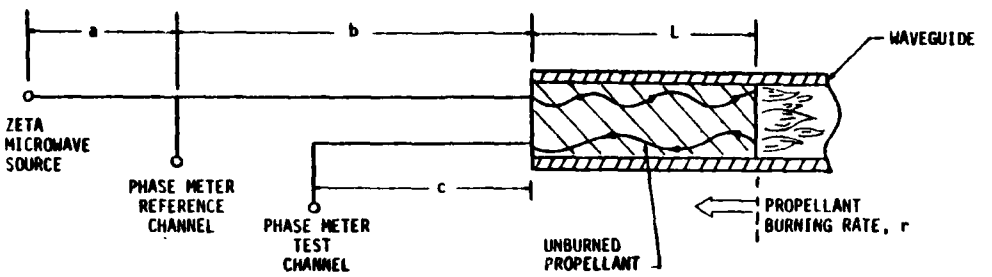

Figure 20. Principle of Microwave Reflection

3.3.5. Pressure-Time Trace [59,60] This method burns strands in a closed bomb to indirectly compute an expression for the burning rate. The pressure-time history of a strand burning in a sealed vessel is recorded. The pressure during the experiment increases and time derivatives of the pressure can be used to calculate the constants in the St. Robert's burning rate law

$$\dot{r} = cP^n \tag{15}$$

The analysis is based of a thermodynamic treatment of the closed system.

3.4. Summary of Experimental Techniques

Tables 1 and 2 presents a summary of the different methods employed for determining the burning rates of solid propellant strands. For purposes of comparison, a 25mm long, 6mm square, strand was assumed having a burning rate of 1.0 cm/sec. In Table 1, the discrete techniques are summarized. The ΔX column represents the estimated minimum separation distance of the sensors when action time is the independent variable. Table 2, compares estimated specifications for the continuous sensors. Resolution represents the minimum change in propellant surface height that the sensor can detect. Probe diameter represents the dimension of the minimum circular probe area showing how spatially local the measurement could be made. Range is the total distance over which the technique is sensitive.

Table 1.
Comparison of Discrete Measurement Techniques

Section	Technique	Type	ΔR_{min}	Δt	Accuracy	Remarks
3.2.1	Timing wires	Discrete	6 mm		Fair	All these techniques are appropriate for average measurements. The probes introduce combustion enhancement because of heat conduction. It is also difficult to precisely locate the probe positions. Any response time delays, that are not compensating amplify as the burn rate increases
3.2.2	Thermocouples	Discrete	6 mm		Fair	
3.2.3	Ionization or conductivity probes	Discrete	6 mm		Fair	
3.2.4	Laser beams	Discrete	3 mm		Good	Laser beams are bent by hot gases. Smoke attenuates beam. Beams are non-intrusive.
3.2.5	Pressure sensor	Discrete	25 mm		Fair	Threshold for triggering is imprecise in time
3.2.6	Acoustic Emission sensor	Discrete	12 mm		Good	Rugged accurate method of determining average burning rate
3.2.7	Strand measurement	Discrete	12 mm		Fair	Time consuming
3.2.8	Motion picture camera	Discrete/ continuous		1 msec	Very Good	Excellent time resolution. Provides qualitative view of combustion. Data analysis time consuming and not available in real time

Table 2.
Comparison of Continuous Techniques

Section	Technique	Resolution	ΔR	Range	Bandwidth	Accuracy	Remarks
3.2.8	Motion Picture Camera	20 μ	5 μ	12 mm*	2000 Hz	Good	Actually a high frequency discrete (see Table 1)
3.3.1	Tungsten Light	50 μ	2000 μ	2 mm**	200 Hz	Fair	Sample Heating
3.3.1	Laser Beam from side	50 μ	60 μ	.6 mm*	1000 Hz	Fair	Beam bent by gases. Small probe volume
3.3.1	X-ray	Unknown	6000 μ	24 mm*	Unknown	Poor	Poor resolution
3.3.2	Radioactive	Unknown	6000 μ	24 mm*		Unknown	Dangerous to operator
3.3.3	Microwave Reflection	.10 μ	6000 μ	25 mm+	2,000 Hz	Excellent	Excellent bandwidth. Instantaneous measure of larger portion of surface
3.3.4	Combustion Recoil	N/A	6000 μ	25 mm	10 Hz	Fair	Biased by propulsive forces of gases
3.3.5	Pressure-time Trace	N/A		25 mm		Unknown	Not used extensively in composites

* depends upon magnification
**can be extended with servo-positioning
+Gives an RMS average of surface (1.2 cm wave)

3.5. Conclusions

Clearly, of all the techniques surveyed, the only ones that are acceptable for measuring the microscopic burning rate fluctuations are high-speed photography and microwave reflection. High-speed photography has a sufficiently large bandwidth and small probe volume. There are some limitations however on the spatial resolution caused by limited depth of focus and the surface roughness of the burning front. Measurements can only be made at the edge of the strand which may not be representative of the actual combustion processes because of edge effects. Microwave reflection has enough resolution and bandwidth, but the probe volume is too large to isolate the burning rate fluctuations of single oxidizer crystals.

It would be desirable to develop a technique that can continuously measure the local deflagration of the propellant surface. Current state-of-the-art techniques do not provide a satisfactory method of measuring the local combustion phenomena.

4.0 TECHNIQUE DESIGN, ANALYSIS, AND TESTING

This chapter describes the development of a new optical instrument to measure the local movements of a solid propellant surface. The instrument, called a Laser Position Detector[61], uses a laser beam with a closed-loop tracking system to geometrically determine the surface height. The system also employs synchronous detection to measure in the combustion environment. This chapter describes the requirements, operating principles, analysis, and bench testing of the technique.

4.1. System Requirements

In this section, objective design requirements are specified for the performance of the measurement instrument. The highest objective is to measure the local, intermittent movements of the propellant so the requirements will be derived for this application. The requirements will be specified with classic terms and they will serve as guidelines for acceptable performance in the design, analysis, and the testing of the instrument.

4.1.1. Measurement Considerations The first consideration is describing the local movements of the propellant surface. Results of high-speed movie data, plotted in Figure 21, show that the propellant surface displacement has intermittent changes in slope. During the heating of large oxidizer crystals, the surface shows little displacement and this time is called the *rest period.* After the oxidizer ignites, the propellant burns displacing the surface at a much higher rate. This time is the *burn period.* The slope fluctuates between these high and low slopes as successive burn and

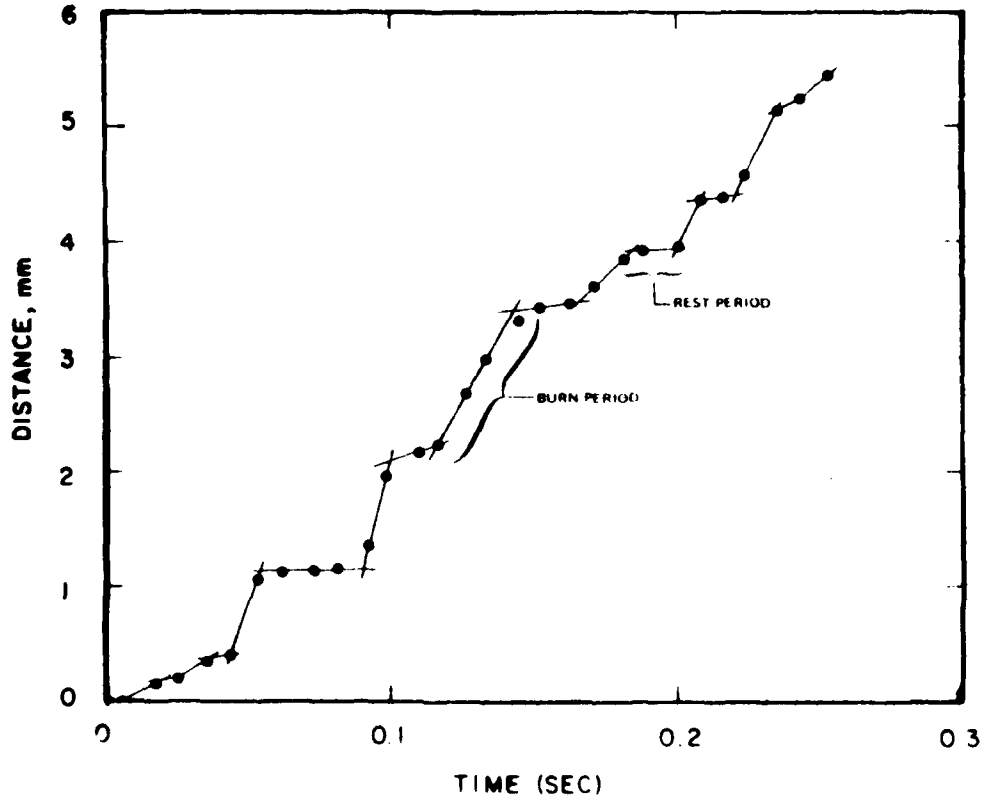

Figure 21. Experimental Burning Rate

rest periods occur during the combustion. *The objective of the measurement is to determine the duration of the burn and rest periods and the slope or rate during each period all to within ± 5 percent.*

Data averaged from high-speed motion picture measurements characterized the intermittent surface movements. Figure 22 shows typical values for the burn period, burn distance, rest period, and rest distance produced from the idealized curves. The displacement-time curve, in the top graph shows the surface moving an average of 0.010 in. during the rest period and 0.030 in. during a burn period. The duration of both the burn and the rest periods averaged to 25 msec. The idealized velocity (or rate) is shown is shown in the bottom graph. A square wave describes the idealized rate. The rate during the burn period of 1.20 in/sec and during the rest period 0.04 in/sec. Idealizing the surface motion will simplify the selection of transient performance requirements.

The second consideration is the hostile environment produced by the propellant combustion. For an optical instrument, portions of the light traveling through the combustion gases will be attenuated. Measurements of the smoke attenuation during an experiment [62] are plotted in Figure 23. These results show that, during an experiment, the smoke can block half of the beam power transmitted through the combustion gases. The combustion pressure also has an effect. Data from pulsed-laser experiments [63] is shown in Figure 24. The average laser intensity transmitted through the smoke and flames is reduced as the pressure of combustion increases.

The third consideration is the nature of the propellant surface. The surface often has an irregular shape that can produce angles up to 30 degrees off the horizontal. The oxidizer particles that are being observed are 300 to 600 microns in diameter.

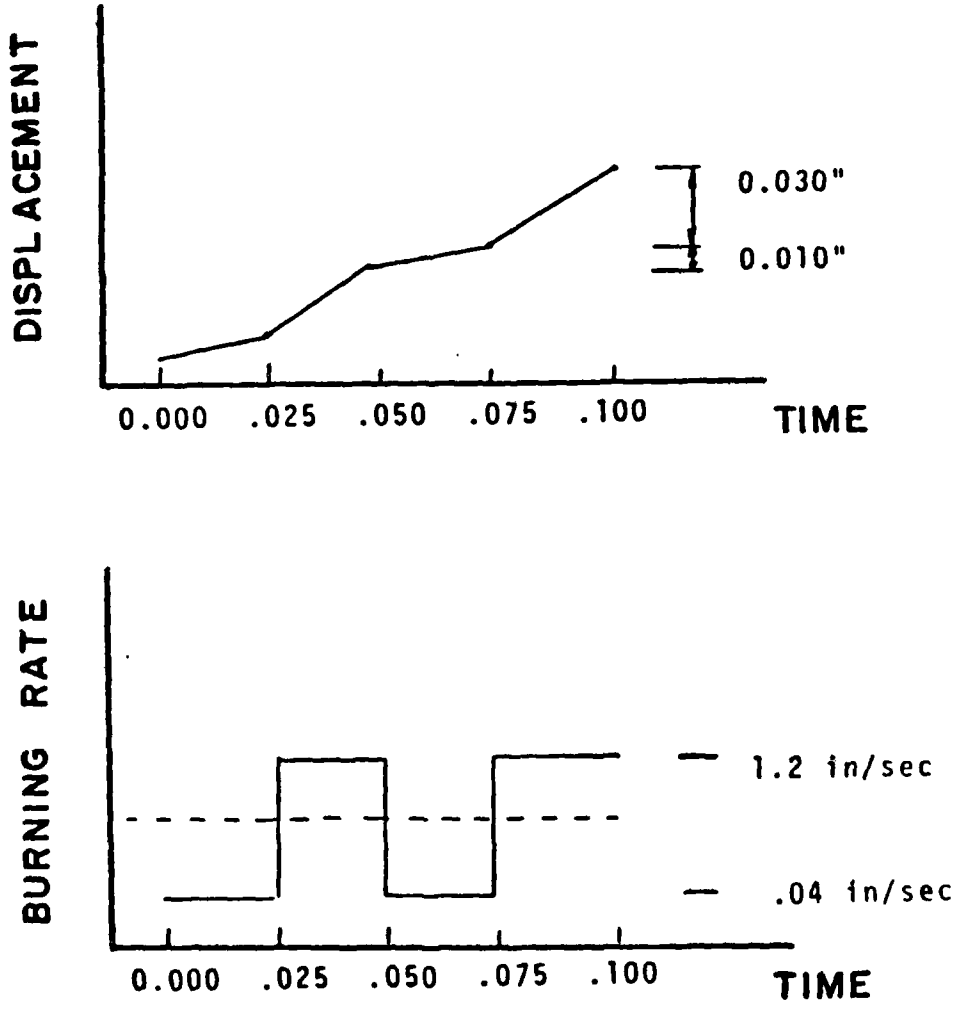

Figure 22. Idealized Intermittent Burning

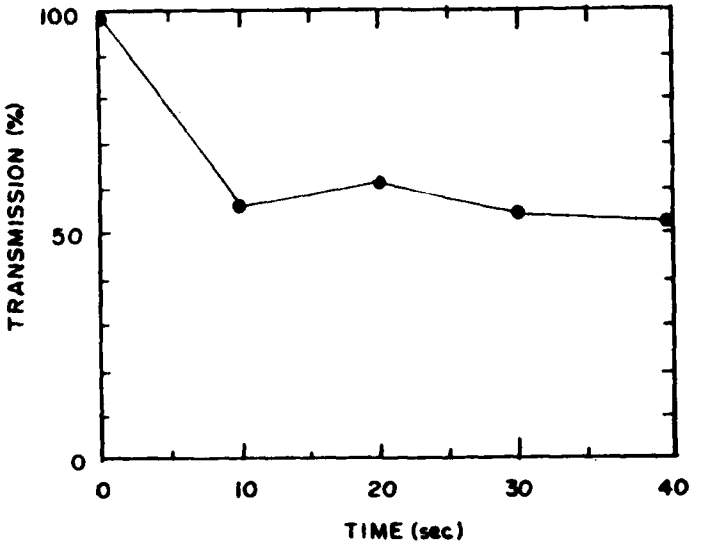

Figure 23. Transmission Reduction with Time [62]

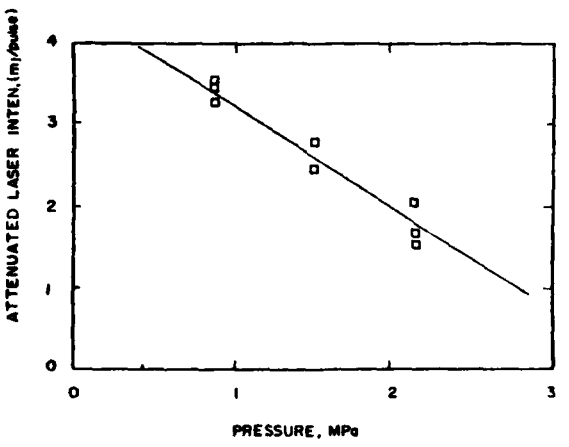

Figure 24. Transmission Reduction with Pressure [63]

The final consideration is the design technique. The system will be designed using experimentally determined transfer functions. Errors in estimating each transfer function could add through the system causing large miscalculations of phase for the total system. This will be accounted for by allowing 5 degrees of phase uncertainty for each component tested.

4.1.2. Specifications and Requirements The preceding considerations were converted into seven specifications. These specifications describe the steady-state and transient requirements for an instrument to measure the local, intermittent solid propellant burning. Table 3 lists the specifications, their required values, and the basis for calculating the requirement. The specifications are defined in the glossary at the beginning of this report. In addition, the instrument should have a probe diameter less than 400 microns.

4.2. System Description

An optical concept was adapted to approach the problem of continuous, local surface detection. A laser beam shines down on the surface at an angle θ from a horizontal reference line as illustrated in Figure 25. A spot appears on the surface as the light is *diffusely* reflected. As the surface moves from position 1 to position 2, the beam spot travels laterally a proportional distance x_e. Thus, the surface height change , y_s, may be determined by continuously measuring lateral position of the beam spot. A local displacement measurement is possible because the light is reflected off of an area the size of the beam spot. This concept has been applied extensively in optical gaging and machine vision.

This concept was modified to address the solid propellant measurement problem. The lateral movement of the spot had to be eliminated because solid propellants do not

Table 3
Minimum Performance Requirements- Intermittent Burning

SPECIFICATION	REQUIREMENT	BASIS
Resolution	≤ .003 in	10% of averaged burn distance
Rise Time	≤ 2 msec	10% of averaged burn or rest period
Settling Time	≤ 6 msec	≤ 3x rise time
Steady-State Error (velocity)	0	matching slope of the input
Minimum Gain Crossover Frequency	1000 to 1570 rad/sec	rise-time based analysis
Gain Margin	≥ 6 db	50% reduction in gain caused by smoke
Phase Margin	≥ 30°	5 deg. exp. error for 6 devices

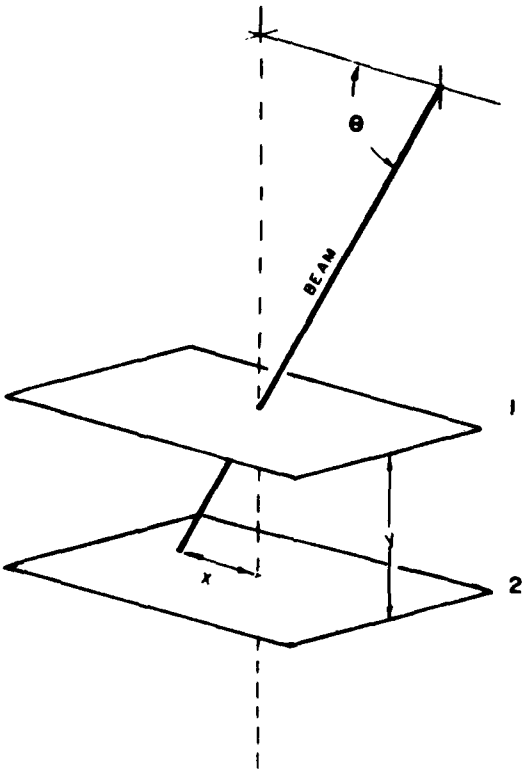

Figure 25. Geometric Height Sensing

burn in smooth, flat planes so the surface height ideally would be measured along a line perpendicular to the surface movement. Figure 26 shows how changing the incoming beam angle, θ, compensates for the lateral movement of the spot. Now, as the surface moves from position 1 to position 2, the beam angle increases to continuously center the spot on the vertical reference line. The surface height, Y_s, for this configuration is a trigonometric function of the beam angle, θ.

To carry out this concept, three subsystems are required that are symbolized in Figure 27. First, a beam scanner is needed to control the incoming beam angle so that the lateral error of the beam spot from the vertical axis can be eliminated as the propellant burns. Second, a sensor that measures the lateral misalignment of the beam spot from the vertical reference axis is required to produce an error voltage. Third, a controller or feedback link is necessary to modify the error signal from the sensor and transmit it to the beam deflector so that the beam angle can be adjusted to eliminate the lateral error. The system outlined is a closed-loop tracking system that will continuously measure the displacement of a local area of a surface.

The following sub-sections describe the principles and techniques used to carry out each of the functions just described.

4.2.1. Scanner The scanner controls the angular position of the incoming baser beam. Its function is to aim the beam at the point where a fixed vertical reference line intersects the moving propellant surface. Either an electro-mechanical beam scanner consisting of a mirror mounted on a galvonometer and a power amplifier, or an acousto-optic beam deflector consisting of a crystal and a RF amplifier, can control the angular position of a laser beam.

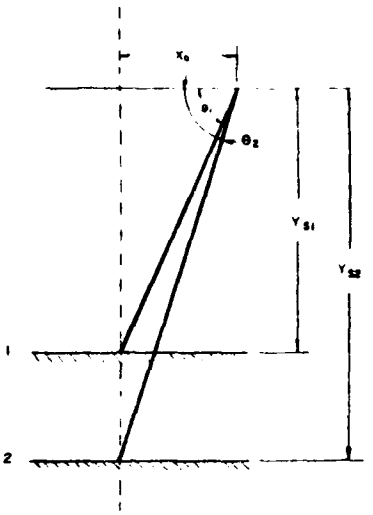

Figure 26. Surface Tracking

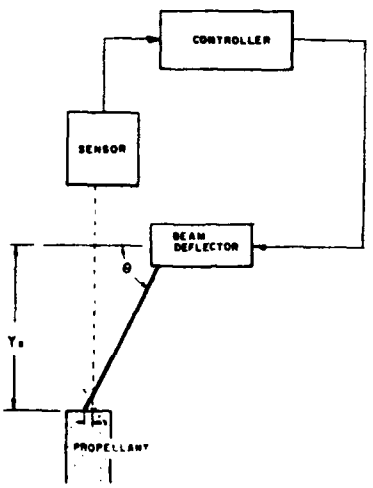

Figure 27. Outline of System

Measuring the scanner beam angle also determines the propellant surface height. The basic relationship for the surface height as a function of beam angle (from Figure 26) is

$$Y_s = X_s \tan(\theta) \tag{16}$$

assuming that there is no lateral error. This makes the surface height a unique function of the beam angle. In reality, however, the beam spot will not be located exactly at the intersection of the vertical axis of the detector and the propellant surface. Therefore, to account for finite lateral errors, it is necessary to describe a more general condition.

A coordinate system describes the configuration of the system. Figure 28 shows a fixed coordinate system, X-Y, with an origin at the point P. The beam angle, θ; the distance to the vertical axis, X_a; the distance to the propellant surface, Y_s; the distance to the point where the beam crosses the optical axis, Y_a; and the distance at which the beam strikes the propellant surface, X_s; are all measured in this coordinate system. Point A is a reference point having the fixed dimensions θ_o, $Y_a(\theta^o)$,and X_a. A line extending at the reference angle, θ^o, intersects the propellant surface at point P^o defining a reference lateral error, $X_s(\theta^o)$.

To express relations for the lateral error as a function of the propellant surface height and the beam angle, a local coordinate system, x-y, is defined at point A. In this local coordinate system, the lateral error is

$$x_e = x_s - x_a \tag{17}$$

Expressions for the reference lateral error, x_s, and the lateral beam compensation, x_a, are next derived from linearized relationships.

For a fixed beam angle, the beam spot moves laterally, x_s, when the propellant surface is displaced. The movement of this point, P^o, is linearized from point A

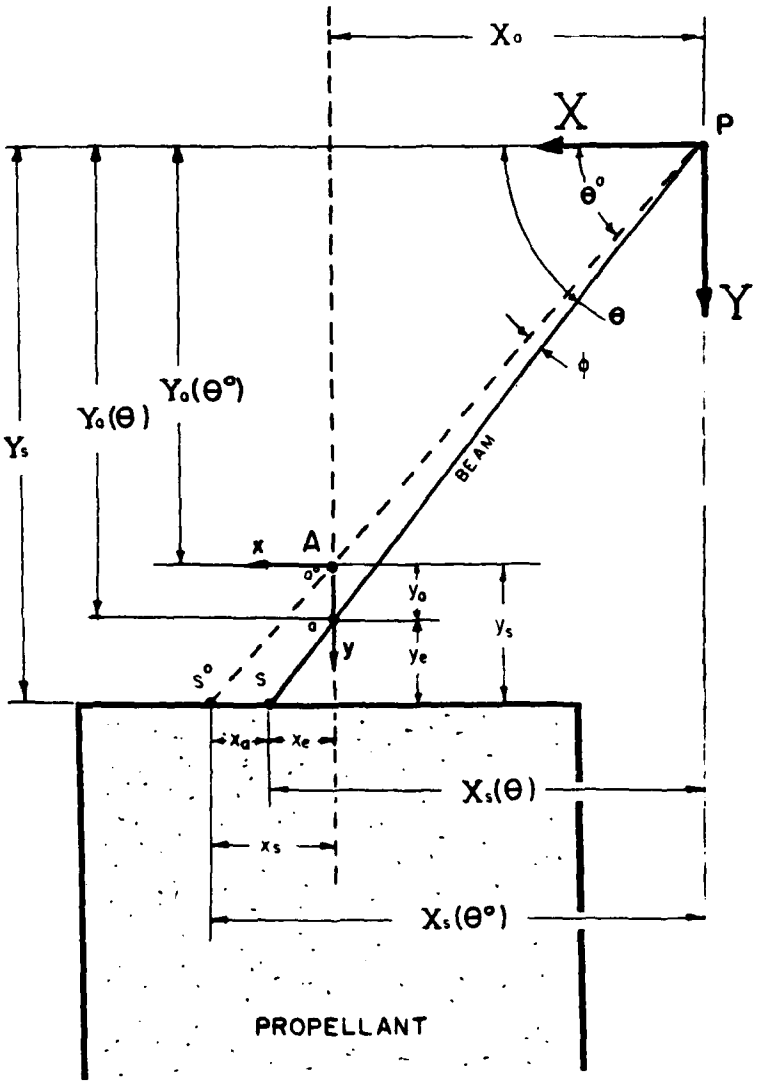

Figure 28. Coordinate System

$$X_s(\theta^o) = X_a + \left.\frac{\partial X_s}{\partial Y_s}\right]_o [Y_s - Y_a(\theta^o)] \tag{18}$$

Rearranging into local coordinates gives

$$x_s = X_s(\theta^o) - X_a = \left.\frac{\partial X_s}{\partial Y_s}\right]_o y_s \tag{19}$$

where the partial derivative is

$$\left.\frac{\partial X_s}{\partial Y_s}\right]_o = \left.\frac{\partial}{\partial Y_s}\left[\frac{Y_s}{\tan\theta}\right]\right]_o = \text{cotan}\theta_o \tag{20}$$

making

$$x_s = [\text{cotan}\theta_o]\, y_s \tag{21}$$

the linearized expression for the reference lateral error.

For a fixed surface height, the beam is deflected a lateral distance, x_a, when the beam angle changes. The expression for the beam intersection point is linearized about point A

$$X_s(\theta) = X_s(\theta^o) + \left.\frac{\partial X_s}{\partial \theta}\right]_o [\theta - \theta_o] \tag{22}$$

Rearranging into local coordinates gives

$$x_a = X_s(\theta) - X_s(\theta^o) = \left.\frac{\partial X_s}{\partial \theta}\right]_o \phi \tag{23}$$

where the partial derivative is

$$\left.\frac{\partial X_s}{\partial \theta}\right]_o = \left.\frac{\partial}{\partial \theta}\left[\frac{Y_s}{\tan\theta}\right]\right]_o = -Y_s \csc^2\theta_o \tag{24}$$

making

$$x_a = -[\csc^2\theta_o]\, \phi \tag{25}$$

the expression for the lateral compensation as a function of the local beam angle.

The linearized expression for the lateral error is the obtained by substituting equations 21 and 25 into equation 17

$$x_e = [\text{cotan}\theta_o]\, y_s - [\csc^2\theta_o]\, \phi \qquad (26)$$

Thus, a linearized expression has been derived showing how the initial geometry, the beam angle, and the propellant surface height are related to the lateral error of the beam spot from the vertical axis. This expression will be used later in the control system analysis.

4.2.2. Sensor The function of the sensor is to produce a voltage that is proportional to the lateral error, x_e, of the beam spot on the surface. The sensor consists of two parts; a detector that is sensitive to light coming from the propellant surface and an amplifier that recovers the signal of the laser spot from that of the noise produced by the combustion light.

The detector is an electro-optic device that measures the light emitted from a specific area of the propellant surface. Figure 29 shows that it consists of a lens, a pinhole, a laser line filter, and a photodiode. Laser light *diffusely* reflected from the propellant surface is collected by the lens and focused through a pinhole. The detector "looks" along its optical axis on a line through the center of the lens and the pinhole. The line filter admits only light at the laser wavelength. The diameter of the pinhole is slightly smaller than the diameter of the spot image. The energy of the light that passes through the pinhole is converted into a voltage by a photodiode and an amplifier located behind the pinhole.

The detector is sensitive to the lateral movements of the laser spot, x_e, from the optical axis. When the spot is positioned on the surface at the point of the detector's optical axis, the spot image is concentric with the pinhole allowing the maximum amount of light to pass through the pinhole to the detector. As the surface moves up or

down, the resulting lateral movements of the spot produce lateral movements of the spot image. This causes portions of the collected light to be blocked from the detector. Figure 30 illustrates a detector calibration curve showing the photodiode voltage plotted as a function of the lateral spot position.

For analysis, the central portion of this curve may be described empirically with an inverted parabola

$$V_{PD} = V_{max}(r) + \frac{1}{4a(r)} x_e^2 \qquad [-b < x < b] \tag{27}$$

The two coefficients in this expression are functions of the surface reflectivity, r, because a more reflective surface will produce a higher value of V_{max} and less contrast (larger values of "a"). Therefore, the lateral movements of the laser spot produce a detector calibration curve that is only a function of the surface reflectivity.

When the propellant is burning, the detector calibration curve is not solely influenced by the surface reflectivity. Figure 31 shows the detector voltage produced by light emitted from a burning strand. Light emitted from the reacting gases causes a large, time dependent increase in the detector voltage. Also, the soot, smoke, and flames in the gases attenuate some of the laser light decreasing the laser signal reaching the detector (shown previously in Figures 23 and 24). Equation 27 may be modified to account for these two influences

$$V_{PD} = \eta_c(t) \left[V_{max}(r) + \frac{1}{4a(r)} x_e^2 \right]_{sig} + \left[V_{flames}(t) \right]_{noise} \tag{28}$$

The combustion effectively lowers the laser signal and adds noise to the photodetector voltage. It is clear from this expression, that measuring the photodetector voltage during burning does not provide an accurate measure of the lateral position of the beam spot.

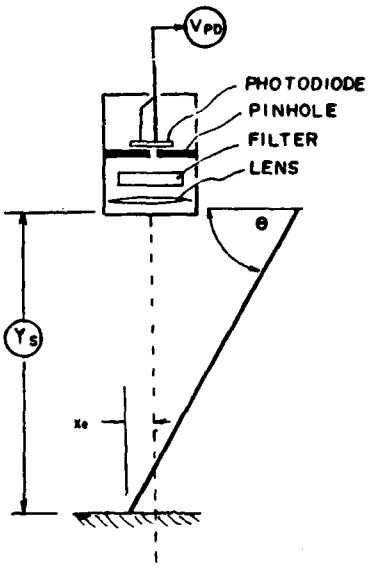

Figure 29. Detector Schematic

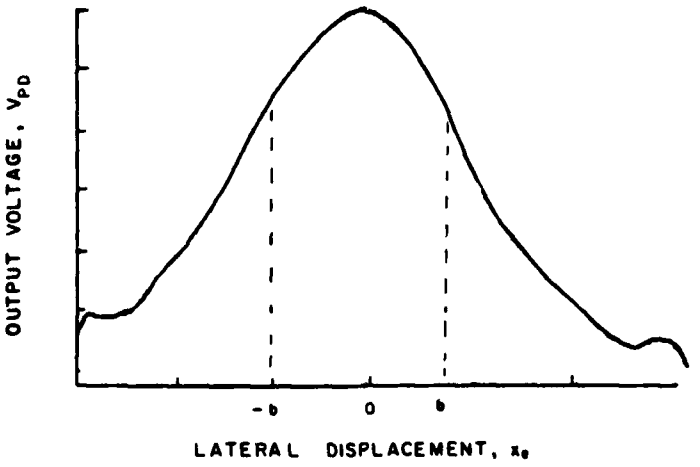

Figure 30. Detector Calibration Curve (No Combustion)

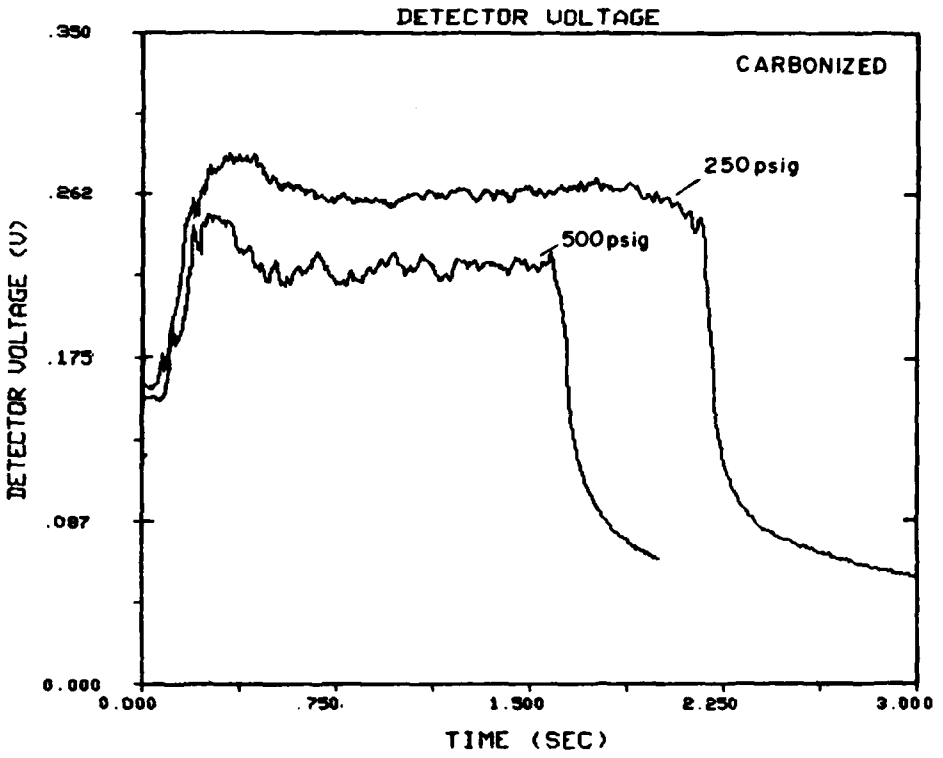

Figure 31. Detector Voltage Produced by Combustion Light

To recover the laser signal from the photodetector voltage synchronous detection is used. Common applications of synchronous detection use chopping of the laser beam. However, in this application, the incoming beam angle is deflected periodically at a carrier frequency, ω, such that a periodic movement of the spot on the surface occurs

$$x_e = b \sin(\omega t) + \bar{x}_e \tag{29}$$

With the laser spot periodically scanned, the detector now produces a time-dependent output that is derived by combining equations 28 and 29. The resulting expression, after a trigonometric substitution is

$$V_{PD} = \left[\eta_c(t) \left[V_{max}(r) + \frac{b^2}{8a(r)} + \frac{\bar{x}_e^2}{4a(r)} \right] + V_f(t) \right]_{low-freq} + \left[\left[\frac{b}{2} \frac{\eta_c(t)}{a(r)} \right] (\bar{x}_e) \right] \sin(\omega t) - \left[\frac{b^2}{8} \frac{\eta_c(t)}{a(r)} \right] \cos(2\omega t) \tag{30}$$

This equation has been grouped into three frequency components; a low-frequency component, carrier-frequency component, and double, carrier-frequency component. The terms of the low-frequency component result from the time-dependent combustion processes that are generally low frequency in nature (<200 hz). The magnitude of carrier-frequency component carries information about the lateral position of the spot. Its magnitude

$$V_{PD}\Big]_{\omega} = \left[\frac{b}{2} \frac{\eta_c(t)}{a(r)} \right] (\bar{x}_e) \tag{31}$$

is a linear function of the spot position. When the spot is centered on the optical axis ($\bar{x}_e = 0$), this magnitude is always zero.

Figure 32 show results of preliminary detector measurements converted into the frequency domain using a fast Fourier transform (FFT). Figure 32a shows an FFT of the measured flame emissions. The results, plotted with the DC component truncated, show little frequency fluctuations in the flame light in the frequency range below 200 hz. Figures 32c and 32d show FFT results of the detector voltage in the absence of combustion. Figure 32b shows the case when the lateral error is zero resulting in the minimal carrier frequency component. Figures 32c and 32d show the FFT for a lateral error of 2 and 4 mm respectively and the resulting increase of the carrier frequency component.

Synchronous detection extracts the magnitude of the carrier-frequency signal from the output voltage of the detector. A phase lock-in amplifier performs this function. The lock-in amplifier is synchronized with the carrier frequency of the beam scanning. The photodetector signal is then multiplied against a synchronized square wave and the output is averaged to produce a error signal that is proportional to the carrier-frequency amplitude

$$V_e = K_{PLA}\left[\frac{b}{2}\frac{\eta_c(t)}{a(r)}\right]\bar{x}_e(t)\cos(\alpha) \qquad (32)$$

The lock-in amplifier has an adjustable gain, K_{PLA}. The angle α is the phase angle between the lock-in reference channel and the input carrier. This angle is adjusted to 90 degrees to maximize the output. The unsynchronized, time-dependent noise is averaged out of the output signal with a low-pass filter.

Thus, a calibration curve for the lateral position of the spot can be extracted from the photodiode voltage by using beam scanning and synchronous amplification. While the slope of this curve is a function of the surface reflectivity and time, its origin is *always fixed*! The error voltage is

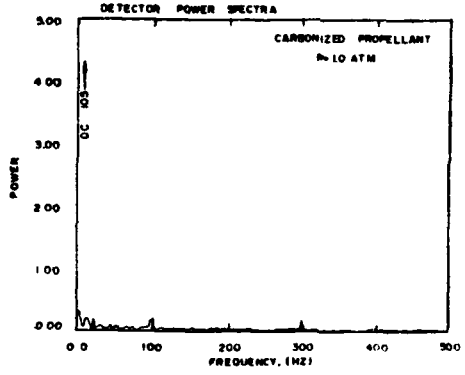

(a) FFT of Combustion Light (No Laser)

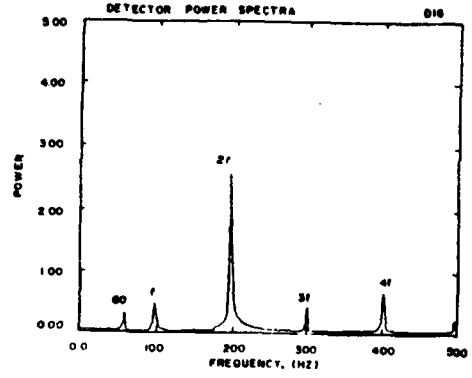

(b) FFT of Laser Light, $x_e = 0$ (No Combustion)

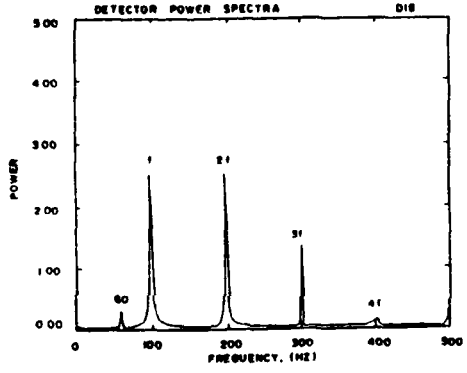

(c) FFT of Laser Light, x_e = 2mm (No Combustion)

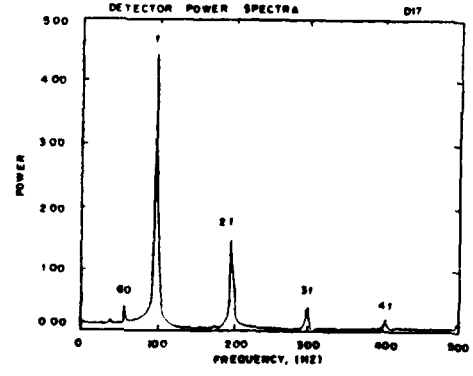

(d) FFT of Laser Light, x_e = 4mm (No Combustion)

Figure 32. FFT's of Detector Signal

$$V_e = K_{PLA} K_{PDL}(r,t)\, \bar{x}_e \qquad (33)$$

where the variable factors of the propellant, detector, and laser are lumped together in the factor K_{PDL}. The output, as plotted in Figure 33 for various surfaces, is then proportional to the local distance measured from the optical axis of the detector. This is the essence of this detection scheme. The time dependent factors of the combustion do not shift the *origin* of the calibration curve. They only change its slope within a certain range.

4.2.3. Controller The controller connects the output voltage of the sensor to the input voltage of the scanner. The controller must do two functions. First, it must produce a voltage for the scanner that eliminates the lateral error of the beam spot from the vertical reference line. Second, the controller must condition the sensor signal to compensate for any inadequacies in the transient response of the system. The following section describes an analysis of the control system to design this controller so that it will perform these two functions and meet the system requirements.

4.3. System Analysis

The system is analyzed using a block diagram and experimentally determined transfer functions. The analysis is used to design a controller to achieve the transient and steady-state requirements. Then, system response predictions are made with the controller added to the model.

Two scanners are analyzed for use in the system. For discussion, the configurations are called:

System-I Scanner is a galvonometer and mirror

System-II Scanner is an acousto-optic crystal

The analysis and results of System-I are described in detail while only the results for

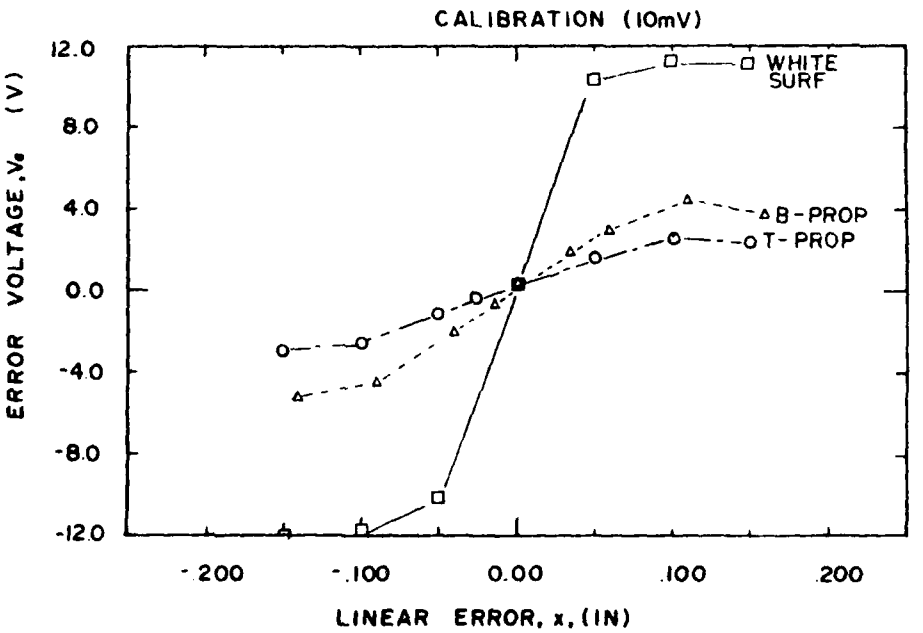

Figure 33. Sensor Calibration Curve

System-II are presented in this section of the report.

4.3.1. System Description System-I is sketched in Figure 34 to show the major components and their input-output variables. The input to the system is the propellant surface height, y_s, and the system output is the control voltage, V_c. The scanner consists of a galvonometer and a mirror that is controlled by the input voltage, V_c, to its amplifier. The parameters describing the geometry of the surface and beam angles were shown previously in Figure 28. The detector measures the lateral error of the beam spot from the vertical axis, x_e, and produces a voltage V_{PD}. The lock-in amplifier modifies the photodiode voltage into an error voltage, V_e, which is the input to the controller. A detailed list of the equipment appears in Appendix B.

Figure 35 shows the block diagram used to model the physical system. With this model, the propellant surface displacement, y_s, is the input and the beam crossing distance, y_a, is the output. (The actual measured output is the control voltage V_c.) Transfer functions are included for each component and for the geometric factors, K_1 and K_2. Using y_a as the output is a classic way to analyze the system and models the difference between the input and measured surface height.

Individual transfer functions will be determined by experiment and analysis. Table 4 lists the form of each transfer function, along with its respective input-output variables. The analysis in Section 4.2.1 determined the expressions for the geometric constants (equations 21 and 25). Note that the transfer function for the controller must still be designed.

4.3.2. Controller Design The system is analyzed to design a controller that will achieve the steady-state and transient performance requirements. A general expression for the controller is assumed

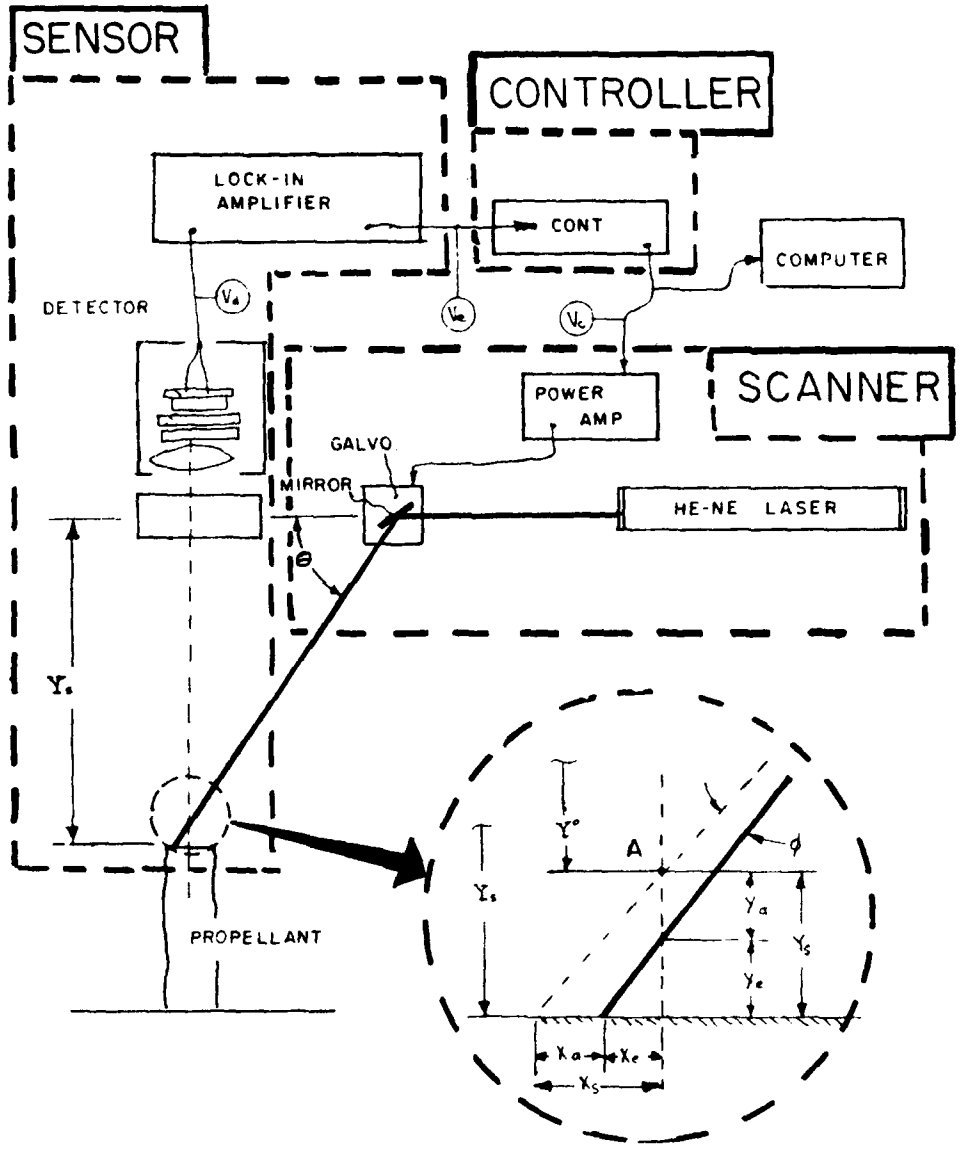

Figure 34. System Schematic

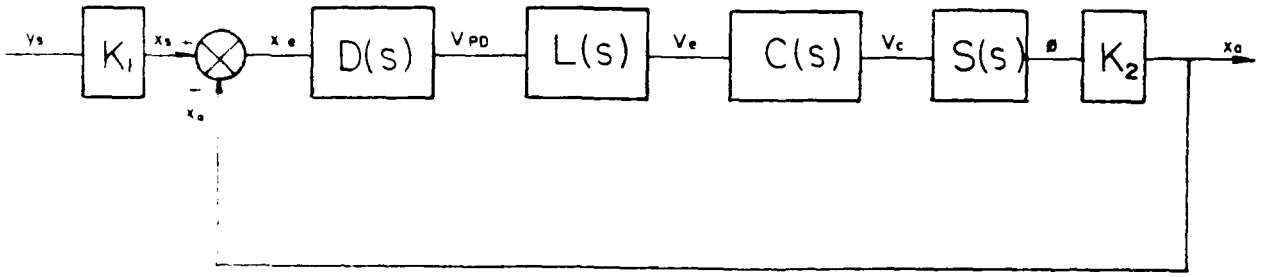

Figure 35. System Block Diagram

Table 4
Anticipated Transfer Functions

NAME	SYMBOL	OUTPUT/INPUT	TRANSFER FUNCTION
Detector	D(s)	$\frac{V_d}{x_e}$	$\frac{K_{PDL}(1/\tau_{PD})}{1/\tau_{PD} + s}$
Lock-in	L(s)	$\frac{V_e}{V_d}$	$\frac{K_{PLA}(1/\tau_{L1})(1/\tau_{L2})}{(s+1/\tau_{L1})(s+1/\tau_{L2})}$
Controller	C(s)	$\frac{V_c}{V_e}$	$C_{ss}(s)\left[\frac{N_c(s)}{D_c(s)}\right]$
Scanner-I	S(s)	$\frac{\phi}{V_c}$	$\frac{K_s(1/\tau_b)(\omega_n^2)}{(s+\frac{1}{\tau_b})(s^2+2\zeta\omega_n s+\omega_n^2)}$
Scanner-II	A(s)	$\frac{\phi}{V_c}$	$\frac{K_{AO}(1/\tau_{AO})}{1/\tau_{AO} + 1}$
Geometry	K_1	$\frac{x_s}{y_s}$	$\text{cotan}(\theta_o)$
Geometry	K_2	$\frac{x_b}{\phi}$	$-Y_s \csc^2(\theta_o)$

$$C(s) = C_{ss}(s)\left[\frac{N_c(s)}{D_c(s)}\right] \tag{34}$$

where $C_{ss}(s)$ is the compensation necessary to achieve the steady-state requirements and the bracketed quantity provides the compensation necessary to meet the transient requirements.

The first aspect of controller design is meeting the requirement of no steady-state errors for step inputs in burning rate. The position error for the system, assuming that the burning rate is the input is

$$\frac{\varepsilon(s)}{\dot{y}_s(s)} = \frac{x_e(s)}{\dot{y}_s(s)} = \frac{K_I}{1 + D(s)L(s)C(s)S(s)K_2} \tag{35}$$

Manipulation shows that the steady-state *velocity* error has an identical form

$$\frac{\bar{\varepsilon}(s)}{\dot{y}_s(s)} = \frac{K_I}{1 + D(s)L(s)C(s)S(s)K_2} \tag{36}$$

This means that the steady-state coefficient of the controller transfer function must have an integrating action since this is required to obtain zero steady-state error and integrating action is not present in the other components. So let

$$C_{ss}(s) = \frac{K_I}{s} \tag{37}$$

Substituting equations 34 and 37 into equation 36 and taking the limit as s goes to zero (time goes to infinity)

$$\lim_{s\to 0}\left[\frac{\bar{\varepsilon}(s)}{\dot{y}_s(s)}\right] = \lim_{s\to 0}\left\{\frac{s\,[D_c(s)]}{s\,[D_c(s)]+N_c(s)D(s)L(s)S(s)K_2}\right\} = 0 \tag{38}$$

shows that the steady-state error to a step input in velocity, $\dot{y}_s$, is zero when the controller has an integrating action.

The open-loop frequency response is now considered to design the transient compensation for the controller. The open-loop transfer function is

$$OLTF(s) = D(s)\,L(s)\,C(s)\,S(s)\,K_2 \tag{39}$$

The frequency domain characteristics of the open-loop system can be obtained using estimates of the transfer functions in equation 39. Experiments on each component (documented in Appendix A) were used to estimate the transfer functions and the results are listed in Table 5. The bar over the symbol indicates that each transfer function has been normalized by its gain. Substituting these expressions into equation 39 yields

$$OLTF = \bar{K}\left[\frac{N_c(s)}{D_c(s)}\right]\left[\frac{100(1900)(2513)(6250)(12{,}315)^2}{s(s+100)(s+1900)(s+2513)(s+6250)(s^2+739s+12{,}315^{2})}\right] \tag{40}$$

where the various forward path gains have been combined

$$\bar{K} = K_{PDL}\,K_{PLA}\,K_c\,K_s\,K_2 \tag{41}$$

The (s+100) pole in the denominator is from the lock-in amplifier and is the most significant component limiting the system response. This pole starts producing phase lags at 10 rad/sec, resulting in unsatisfactory performance.

To compensate for the lag of the lock-in amplifier the numerator of the controller is chosen as a lead compensator

$$N_c(s) = (s+100) \tag{42}$$

to cancel the lock-in pole and for simplicity the denominator is chosen as simply

$$D_c(s) = 1.0 \tag{43}$$

Combining the steady-state and transient compensation results (equations 34,37, 42, and 43) makes the controller transfer function

$$C(s) = \frac{K_c}{s}[s+100] \tag{44}$$

A controller with this transfer function should therefore achieve the steady-state requirements and compensate for the phase-lag of the slowest component in the system.

Table 5
Experimentally Estimated Transfer Functions

SYMBOL	DEF	TRANSFER FUNCTION
$\bar{D}(s)$	$\frac{D(s)}{K_{PDL}}$	$\frac{6250}{s + 6250}$
$\bar{L}(s)$	$\frac{L(s)}{K_{PLA}}$	$\frac{(10)(2513)}{(s + 10)(s + 2513)}$
$\bar{C}(s)$	$\frac{C(s)}{K_c}$	$\frac{1}{s}\left[\frac{N_c(s)}{D_c(s)}\right]$
$\bar{S}(s)$	$\frac{S(s)}{K_s}$	$\frac{(1900)(12,315)^2}{(s+1900)(s^2+739s+12,315^2)}$
$\bar{A}(s)$	$\frac{A(s)}{K_{AO}}$	$\frac{1,250,000}{s + 1,250,000}$

Figure 36 shows a controller designed to produce the desired transfer function. Figure 36a shows the block diagram. The incoming signal is modified by parallel, proportional and integral amplifiers whose outputs are summed together. This design produces the integral and lead compensation without amplifying high-frequency noise in the system. An additional amplifier is added after the summer for independent gain control. The transfer function from the controller block diagram is then

$$C(s) = \frac{K_b K_p (K_i/K_p + s)}{s} \tag{45}$$

where K_i/K_p is adjusted to cancel the lag of the lock-in amplifier. Figure 36b shows the electronic schematic actually used to build this controller.

4.3.3. System Performance Predictions The entire system is now analyzed with the controller included. The open-loop transfer function for System-I with compensation is

$$OLTF = \frac{\bar{K}(100)(1900)(2500)(6250)(12{,}315^2)}{s(s+1900)(s+2500)(s+6250)(s^2+239s+12{,}315^2)} \tag{46}$$

The system gain, $\bar{K}$, is assumed to be adjustable for the purpose of this analysis.

A Bode analysis of the open-loop system yields the gain margin and phase margin. The open-loop transfer function, shown in equation 46, was analyzed using the TOTALP [65] computer program that calculates both the amplitude ratio and phase lag as a function of frequency.

The program first computed the effect of system gain, $\bar{K}$, on the open-loop Bode plot. Figure 37 shows the results for two values of forward gain. The lower amplitude ratio curve represents a forward gain, $\bar{K}$, of 120 that meets the 1000 rad/sec gain crossover frequency represented at point A. The phase margin at this frequency is 32° as shown on the phase curve at 1000 rad/sec, and the gain margin is 7 db at 1660 rad/sec. The upper amplitude ratio curve represents a 6 db increase in gain to 240 to

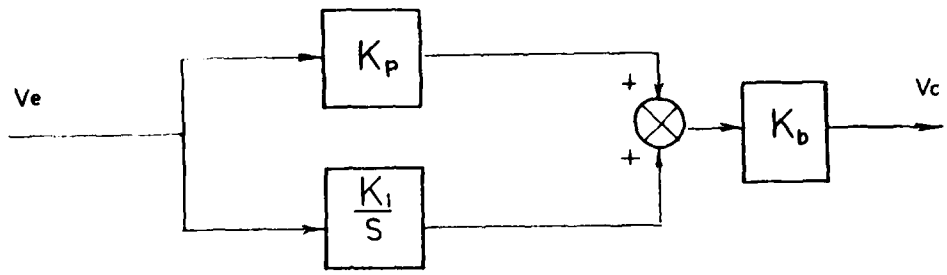

(a) Controller Block Diagram

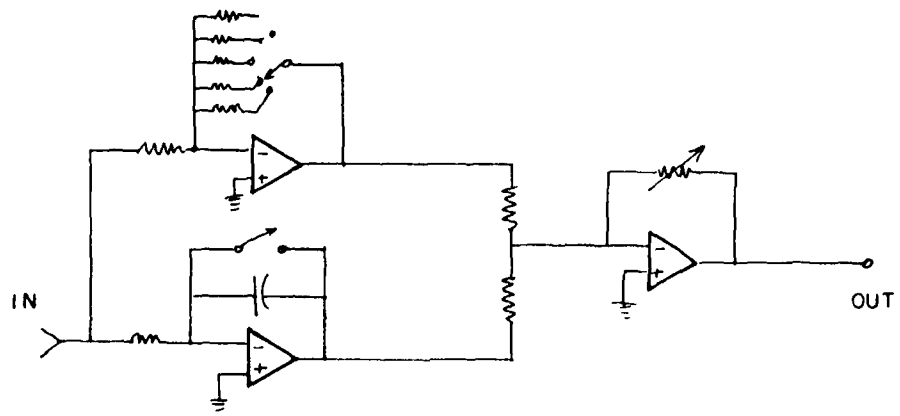

(b) Controller Electronic Schematic

Figure 36. Block Diagram - Controller

simulate the system operating before the smoke attenuates the beam and results in a crossing frequency of 1560 rad/sec, a phase margin of 4° and a gain margin of 1 db.

The closed-loop response to a step input is now evaluated for these two values of forward gain. Figure 38 shows the calculated step response: Figure 38a shows the response for a forward gain is 240; Figure 38b a gain of 120. The descriptive parameters are listed on the figure showing that the rise-time requirement is met, but the large overshoots resulting from the low closed-loop system damping, produces setting times much longer than are allowable.

This analysis shows that the system will not meet the performance requirements necessary for measuring the intermittent burning. The combined phase lags of the lock-in amplifier and detector lower the phase crossover frequency producing low gain and phase margins in the required frequency range.

System-I, although too slow to measure the intermittent burning of the propellant surface, can continuously measure the lower frequency movements of the surface. Lowering the forward gain to a value of 60 produces a rise time of 2 msec and a settling time of 6 msec. This gain represents the condition that produces the minimum settling time. The performance of this system could be improved with the addition of a lead-lag compensator.

Rather than designing additional compensation, an acousto-optic beam deflector was substituted for the galvonometer scanner. The entire analysis process was repeated using the the transfer function for the acousto-optic scanner (A(s) in Table 5). Figure 39 shows the calculated results of the closed-loop step response for two values of forward loop gain. The transient response requirements are met with this system

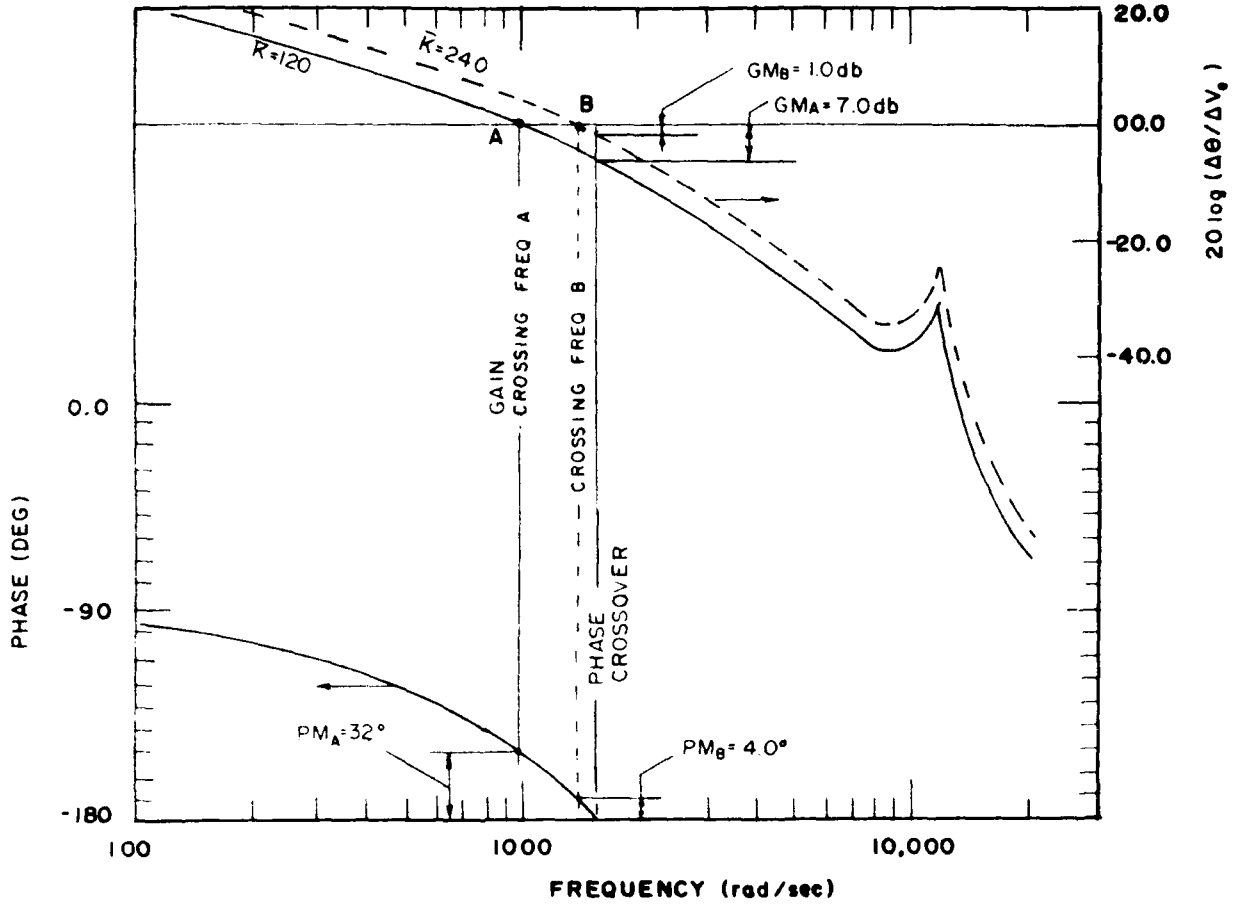

Figure 37. Open-Loop Predictions of Frequency Response: System-I

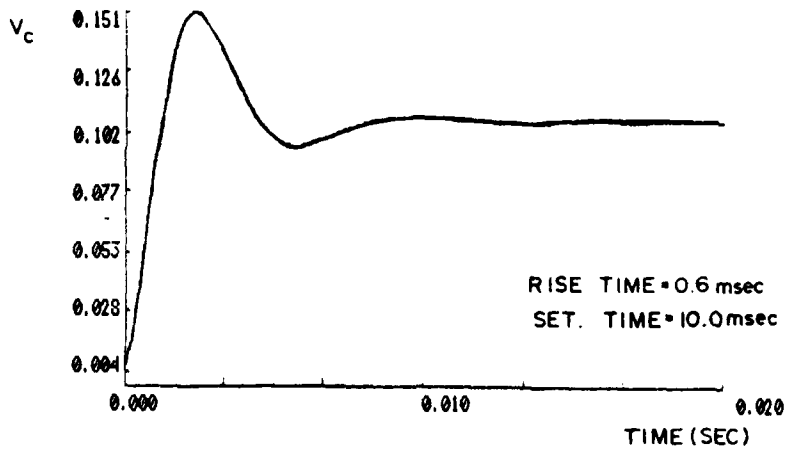

(a) Forward Gain is 240

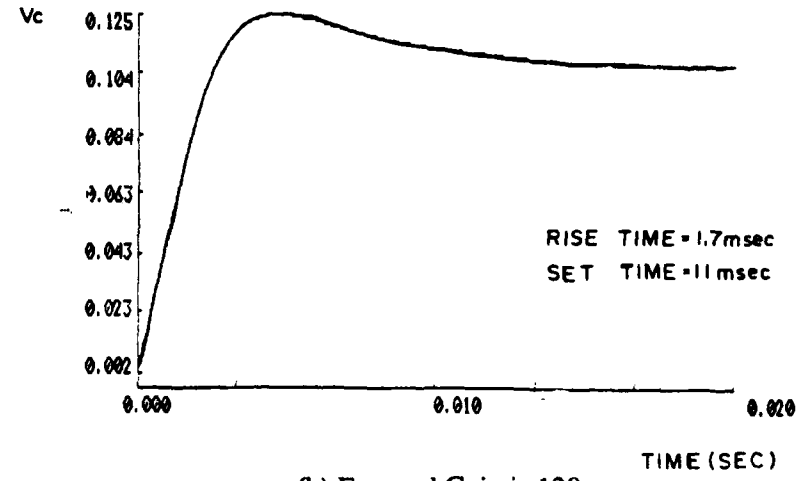

(b) Forward Gain is 120

Figure 38. Closed-Loop Prediction of Step Response: System-I

because of the lower phase lags of the acousto-optic beam deflector produce higher open-loop gain crossover frequency and resulting in larger system damping in the frequency range of interest.

4.3.4. Summary: Analysis

Results of both analyses are summarized in Table 6 along with the requirements established in Section 4.1. System-I predictions represent the system with a galvonometer scanner while System-II predictions are for a system with an acousto-optic beam deflector. The range of values for each prediction are for a 6db change of forward gain to simulate the variations caused by the propellant smoke. The lower value of gain was set by matching the 1000 rad/sec gain-crossover-frequency requirement for the open-loop analysis. System-I does not meet the requirements for the intermittent burning measurement. *Lowering its gain, however, will make it a useful system to measure the lower frequency variations in surface position and the average burning rate of the propellant strands*. System-II predictions meet or exceed all the specified requirements for the intermittent burning measurement.

4.4. System Testing

The Laser Position Detector system was constructed for bench testing. Special experiments were designed to determine the static and the transient performance of the actual system as a function of system forward gain. This section describes the approach and the results of testing the closed-loop system. Additional details of this testing are presented in Appendix B.

4.4.1. Test Configuration To test the system, controlled inputs must be applied to the system while measuring the output. A step input is required for the rise-time and settling time measurements while harmonic inputs are necessary to determine the

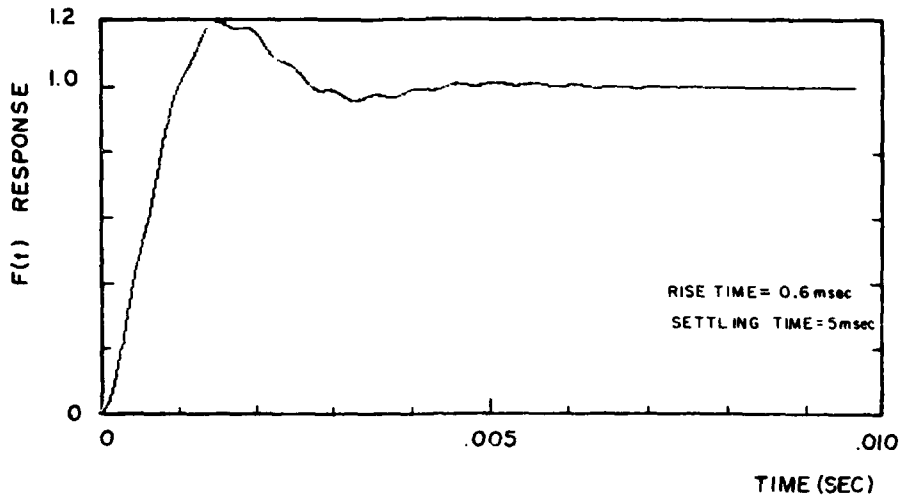

(a) Forward Gain, $\bar{K}$, is 280

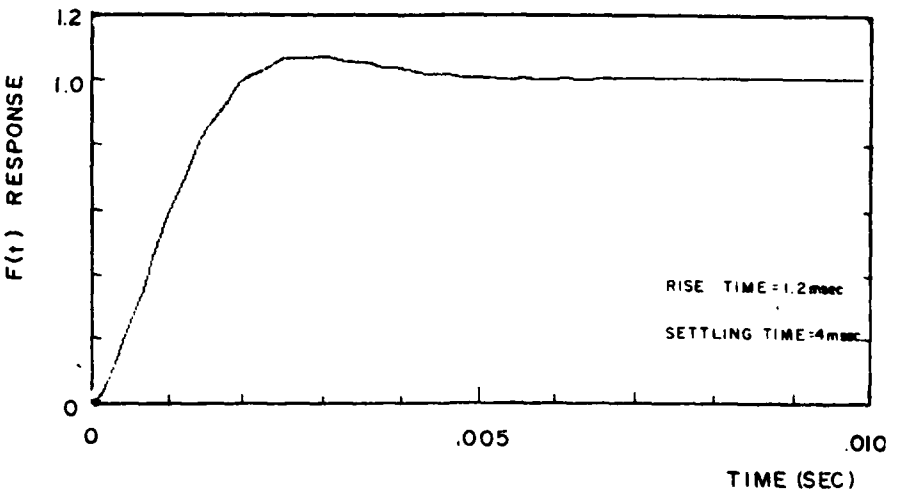

(b) Forward Gain, $\bar{K}$, is 140

Figure 39. Closed-Loop Prediction of Step Response: System-II

Table 6
Transient Performance Predictions

SPECIFICATION	REQUIREMENT	PREDICTION-I Galvonometer	PREDICTION-II AO Crystal
Rise-Time	≤2 msec	1.1-0.7 msec	1.2 - 0.6 msec
Settling Time	≤6 msec	12-75 msec	4-5 msec
Steady-State Error	0	0	0
Minimum Gain Crossover Freq.	≥ 1000 - 1570 rad/sec	1000 - 1560 rad/sec	1000-1700 rad/sec
Gain Margin	≥ 6 db	7 - 1 db	16-10 db
Phase Margin	≥ 30°	32–4°	60–40°

frequency response. Controlling the displacement of the input target to produce step inputs or harmonic inputs with controlled frequency and amplitude is a difficult task. A step movement with a rise time of 1 microsecond or harmonic vibrations at frequencies up to 1000 hz would be required.

An alternative technique was devised for producing a system input. Figure 40 shows the System-I model rearranged with the control voltage as the output and an additional input in the feedback path. This input represents the acousto-optic beam deflector also placed in the path of the laser beam. Figure 41 shows the optical arrangement with the acousto-optic deflector in series with the galvonometer scanner. The acousto-optic beam deflector produces a controlled addition, $\Delta\phi$, to the beam angle ϕ. The beam deflector has a rise time of 1 microsecond and has a bandwidth from 0 to 10,000 hz. Using the acousto-optic deflector to perturb the system would simulate movements of the test surface by producing lateral movements of the beam spot. This eliminates the necessity of moving the test target.

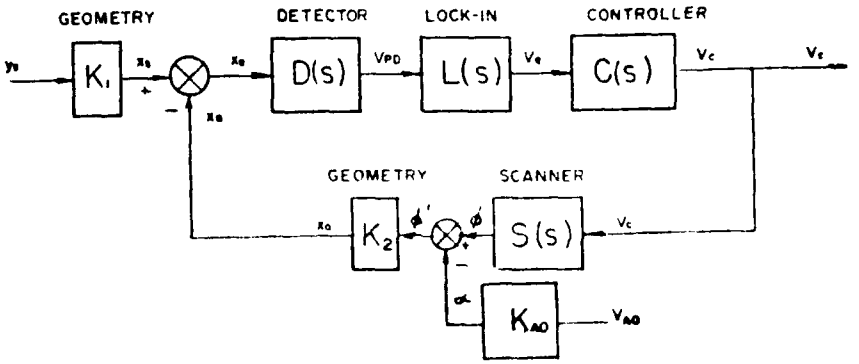

Figure 40. Feedback Perturbation for Testing

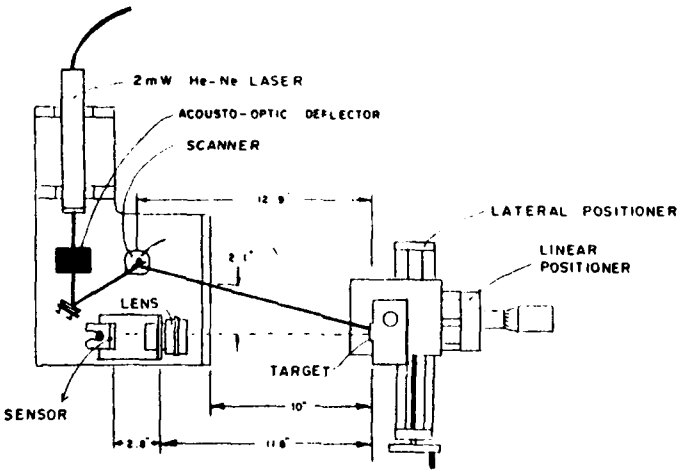

Figure 41. Arrangement of the Optical Components

Figure 42 shows the system model rearranged into what will be called the test system model. The voltage controlling the acousto-optic beam deflector, V_{AO}, is now the system input while the control voltage, V_c, as the output. The input can now be easily controlled using a function generator to produce step or sin inputs.

Before proceeding, the relationship between the actual system and the test system must be established to interpret the results. Considering x_s as the input for the actual system the closed-loop transfer function is

$$CLTF_A = \frac{V_c}{x_s} = \frac{\bar{K}D(s)L(s)C(s)}{1 + \bar{K}K_2D(s)L(s)C(s)S(s)} \tag{45}$$

Similarly, the closed-loop transfer function for the test system is

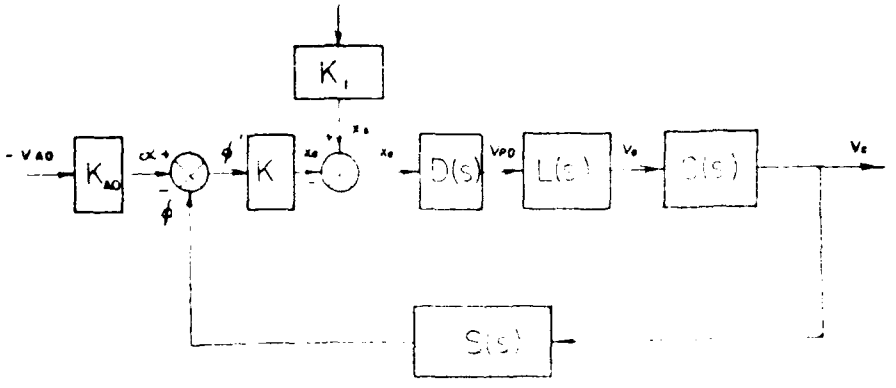

Figure 42. Test-System Model

$$CLTF_T = \frac{V_c}{V_{AO}} = \frac{K_{AO}\bar{K}K_2D(s)L(s)C(s)}{1 + \bar{K}K_2D(s)L(s)C(s)S(s)} \quad (46)$$

The ratio of the two system transfer functions is simply

$$\frac{CLTF_A}{CLTF_T} = \frac{1}{K_2K_{AO}} \quad (47)$$

Meaning that the test system will display a transient response identical to that of the actual system. System stability, rise-time, and settling time should not be altered by using the beam deflector to perturb system. The system resolution is estimated by measuring the minimum and maximum values of indicated output of the system for a stationary target.

4.4.2. Measured Frequency Response

Figure 43 shows the the measured and predicted Bode plots for System-I. The measured results represent the closed-loop test system with each curve representing a 6db change in system forward gain. The predicted results represent calculations using the test system block diagram and the experimentally estimated transfer functions for 6db increments in forward gain. The gain for the test system was calibrated at one point for comparison with the model. This was accomplished by adjusting the various amplifiers to to match the phase lag at 100 hz of -30 degrees predicted by the model for case "c". This is shown as the "calibration point" in Figure 43. Then the test system gain was changed in 6db increments for the other cases.

The results show excellent agreement with the predictions based on the experimentally determined transfer functions. This agreement confirms the accuracy of the system model and the previous predictions made for System-I.

Figure 44 shows the results for similar testing of System-II. In this case the acousto-optic deflector was used both to control the beam for surface tracking and to

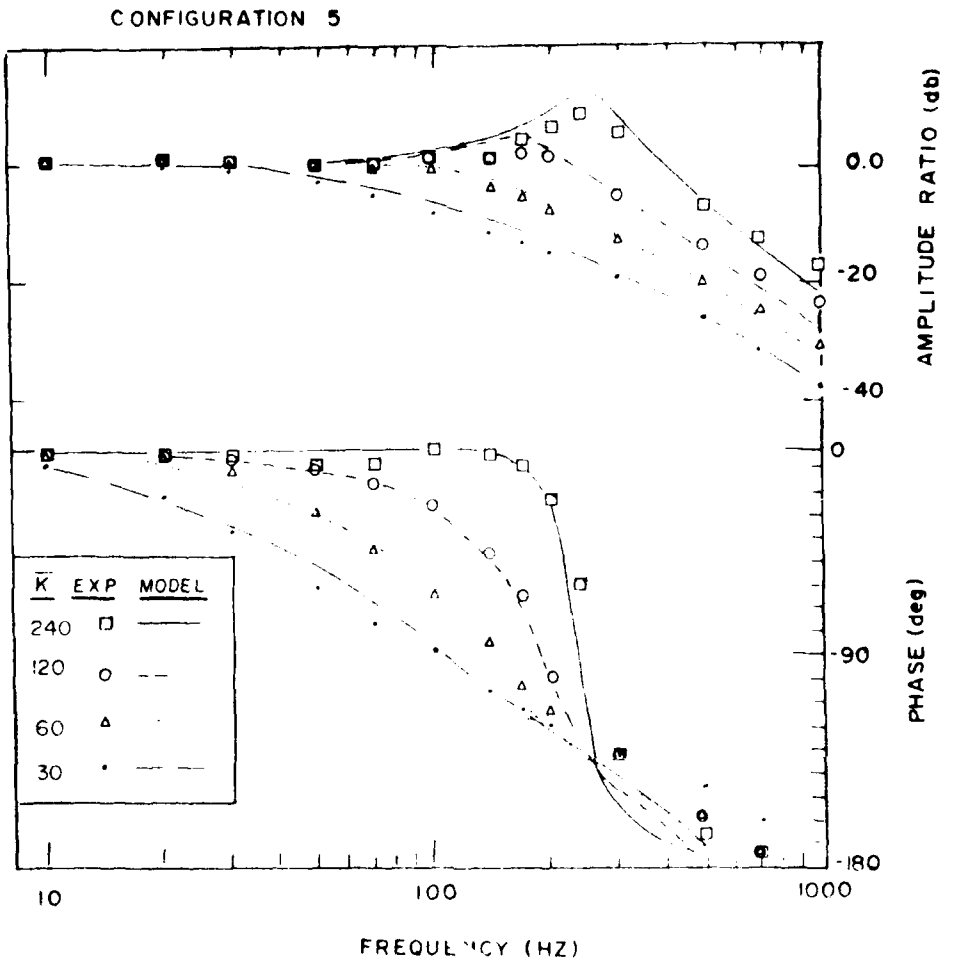

Figure 43. Closed-Loop Frequency Response-System-I

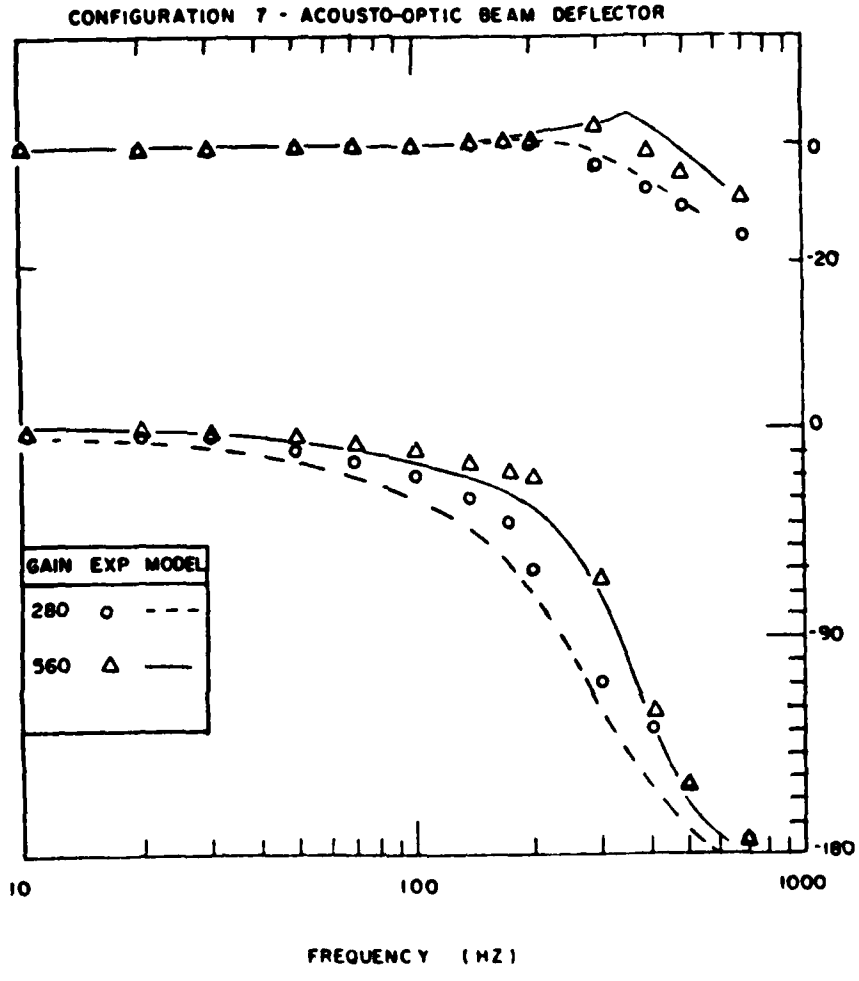

Figure 44. Closed-Loop Frequency Response-System-II

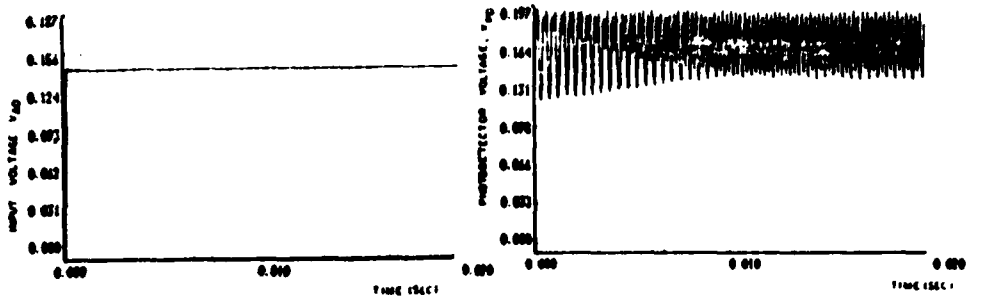

(a) Input Voltage

(b) Detector Voltage, V_{PD}

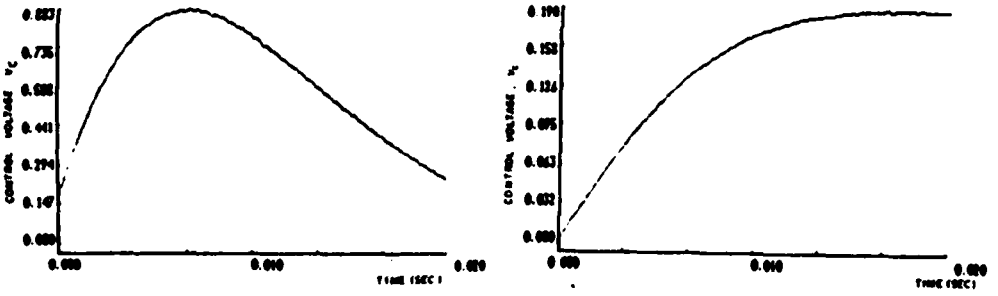

(c) Error Voltage, V_e

(d) Control Voltage, V_c

Figure 45. Response of Various Voltages to a Step Input

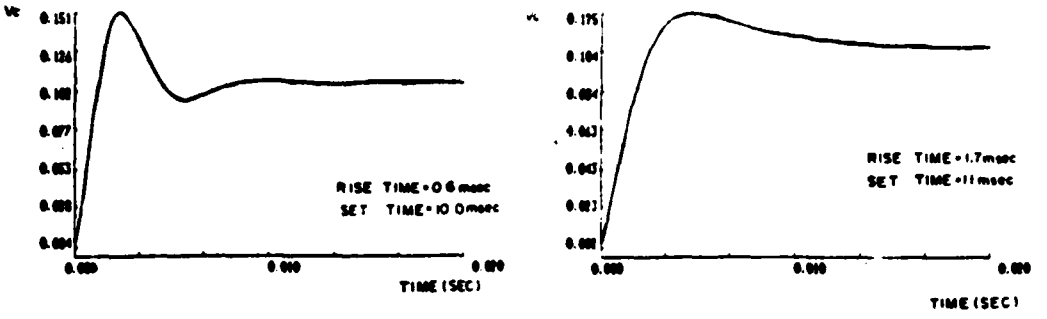

(a) Forward Gain, $\bar{K}$, is 240 (b) Forward Gain, $\bar{K}$, is 120

Figure 46. Measured Closed-Loop Response-System-I

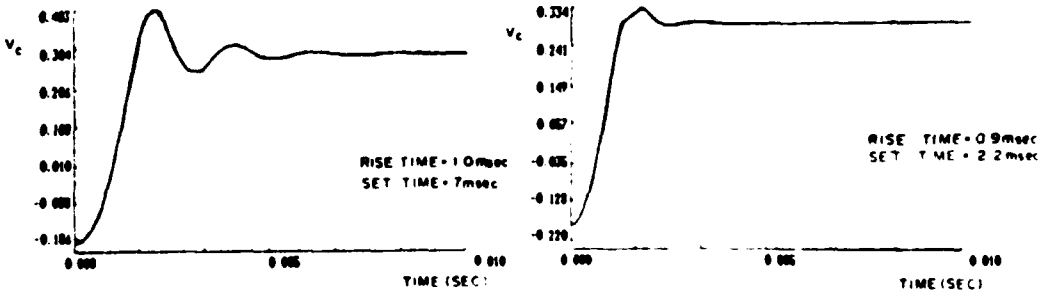

(a) Forward Gain, $\bar{K}$, is 280 (b) Forward Gain, $\bar{K}$, is 140

Figure 47. Measured Closed-Loop Response-System-II

The estimated rise time and settling times are shown in the figures. Figures 47a and 47b show similar results for System-II.

These results show the actual response of the system. The results for System-II confirm that it has adequate transient performance to measure the intermittent combustion of the solid propellant burning surface.

4.4.4. Summary: Measurements Experimental measurements of the closed-loop system response showed excellent agreement with the predictions made in the previous section. The testing confirms that System-II, using an acousto-optic beam deflector has adequate performance to meet all specified requirements. The results of the measurements are outlined in the chapter summary that immediately follows.

4.5. Summary: Design, Analysis, and Testing

Two configurations of the Laser Position Detector have been designed and tested that will continuously measure the local area of the burning surface. Table 7 summarizes the predicted and measured performance for System-I. System-I uses a galvonometer and mirror as the beam scanner and it has adequate resolution and frequency response to measure the low-frequency transient nature of the burning surface displacement. The galvonometer has a large angular range making it possible to measure the surface height over a 3 inch range. It should be a useful system for continuously measuring the low-frequency, transient features of the propellant burning.

System-II uses an acousto-optic beam deflector to control the beam and it has adequate frequency response to detect the intermittent burning of the propellant surface. Furthermore, it maintains specifications over gain reductions of 6db (50%) to compensate for the effects of propellant smoke on the instrument forward gain. Table 8 summarizes the specifications, predictions, and the measurements for System-II. This

system has sufficient resolution and bandwidth to measure the local, intermittent burning of the solid propellant surface. It has an experimentally measured range of 0.6 inches.

Table 7
Results for System-I
(Galvonometer Scanner)

SPECIFICATION	PREDICTION	MEASUREMENT
Resolution	NA	0.003 in.
Rise Time	2.3-1.0 msec	1.7-0.6 msec
Settling Time	7-10 msec	11-10 msec
Steady State Error	0	0
Bandwidth	160-250HZ	150-230HZ

Table 8
Summary of Development: System-II
(Acousto-Optic Scanner)

SPECIFICATION	REQUIREMENT	PREDICTION	MEASUREMENT
Resolution	.003	NA	.001
Rise-Time	≤2 msec	1.2 - 0.6 msec	1.0 - .9 msec
Settling Time	6 msec	4-5	2-7 msec
Steady-State Error	0	0	0
Minimum Gain Crossover Freq.	≤ 1000 - 1570 rad/sec	1000 - 1700 rad/sec	-
Gain Margin	≤ 6 db	16 - 10 db	-
Phase Margin	≤ 30°	60–40°	-

5.0 INSTRUMENT TESTING: COMBUSTION ENVIRONMENT

With the instrument meeting the static and transient requirements on the bench, the next problem is to access he effect of the propellant environment on the performance. The three issues that must be settled are:

(1) Gain Reduction	How much does the combustion products reduce the instrument forward gain?
(2) Resolution	How much does the combustion environment perturb the system output?
(3) Objective	Can the instrument measure the position of the propellant surface?

Answering the first question will determine the effect of the propellant environment on the system performance and define the range of pressures over which the measurement can be made. It will also provide the information that is necessary to pre-set the forward gain so that smoke attenuation reduces the gain into on optimum range during an experiment. Answering the second question will tell if the combustion environment will allow the resolution necessary the measurement of the local, intermittent burning. Answering the third question, of course, will determine the usefulness of the system for propellant research.

5.1. Experimental Facility

A laboratory, capable of performing experiments on propellants strands at pressure levels from -5.0 psig to 900 psig, was constructed to evaluate the measurement technique. The laboratory consists of a test cell and a separate control room. The test cell contains a low-pressure test rig, a high-pressure test rig, and a high-pressure nitrogen system. High-pressure experiments are run remotely from a control room that also contains a data acquisition system. A brief description of the equipment is presented in the following subsections.

5.1.1. Low-Pressure Test Rig The Laser Position Detector was mounted on the top of a Pyrex combustion vessel for the low-pressure combustion experiments. Figure 48 shows the configuration consisting of a 15.2 cm Pyrex pipe cross (Corning) with aluminum plates covering each of the four openings. The top plate supports the optical equipment and contains two 4.5 cm (1.75 in.) Pyrex viewing windows. The optics are arranged as shown previously in Figure 41. The propellant strands are supported and ignited on a removable assembly (the base cap of the high-pressure bomb; discussed Section 5.1.3). The entire chamber is continuously purged with nitrogen injected in the bottom flange through a regulated valve. The nitrogen and combustion products are drawn out of the combustion bomb through the top flange with a Duo-Seal vacuum pump. The Pyrex vessel allows direct observation of the propellant combustion as well as the alignment and operation of the Laser Position Detector.

5.1.2. High-Pressure Test Rig Figure 49 shows a photograph of the high-pressure test rig. It consists of a high-pressure combustion vessel, an optics holder, and a high-speed motion picture camera.

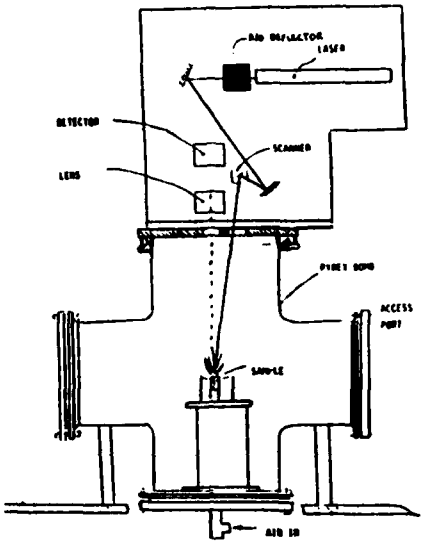

Figure 48. Low-Pressure Vessel and Optics

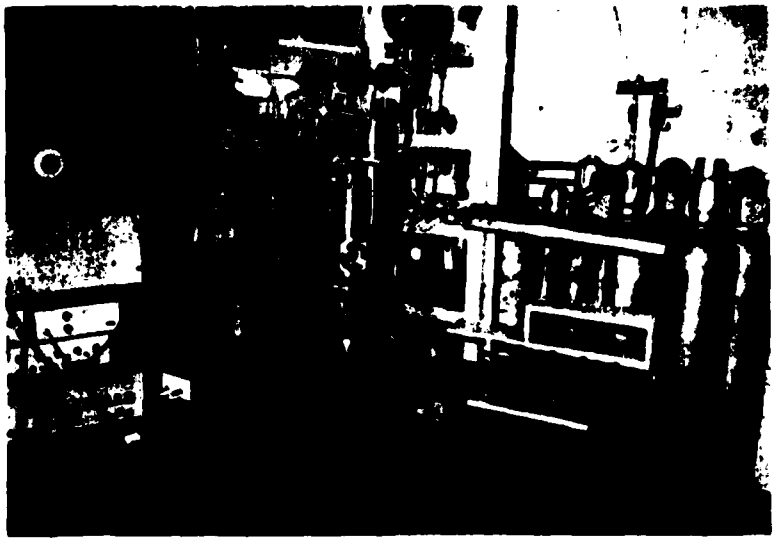

Figure 49. High-Pressure Test Rig

Each component is attached to a plate that bolts into channels that are attached to a steel beam. The channels allow the plates to slide horizontally and to be fastened at various locations.

The electronics for the instrumentation are mounted on a rack beside the table. The rack also holds a panel connected to the computer data acquisition system in the control room. A nitrogen pressure/purge system routes gas from bottles in the test cell to the combustion bomb. The gas system is controlled remotely from the control room.

5.1.3. High-Pressure Combustion Bomb Figure 50 shows a cross-sectional drawing of the high-pressure combustion bomb. The inner diameter of the bomb is 2.5 inches. The bomb is constructed out of 316 stainless steel and consists of a top cap, chimney, body, and base cap. These four sections are held together with threaded surfaces and sealed with O-rings. The vessel, adapted from [66], can be pressurized to 2000 psig.

The internal pressure and gas flow is controlled with nitrogen through openings in the base cap and top cap. Pressurized nitrogen enters the base cap where it is diffused by passing through a sintered plate and then a porous plate. The nitrogen passes by the sample carrying the combustion products away from the sample. The nitrogen and some of the exhaust products exit through two holes in the top cap that are connected to an exhaust line. The chimney allows accumulation of smoke recirculating from the exhaust holes. The exhaust is passed through an orifice plate that controls the mass flow, then it is routed out of the cell. A complete description of the presure system is presented in Appendix D.

Five quartz window permit optical access to the vessel. The two windows, shown in Figure 50, allow entrance and measurement of the laser beam used to measure the surface height. Three additional windows are placed in the bomb body for viewing the

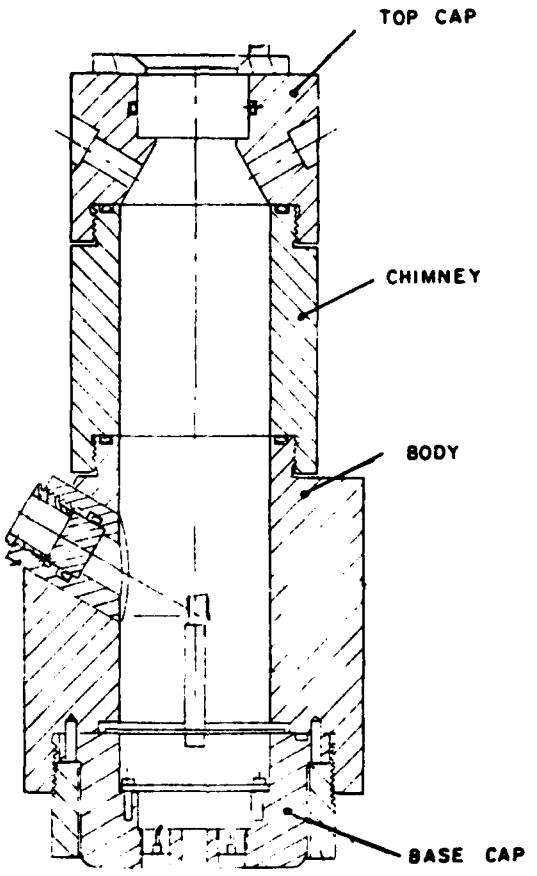

Figure 50. High-Pressure Bomb

side of the propellant with an high-speed motion picture camera.

Drawings showing the dimensions and layout of the high-pressure combustion bomb are in Appendix C.

5.1.4. Optics Figure 51 shows the Laser Position detector and combustion bomb arrangement for the high-pressure rig. The optics are held in place an a vertical aluminum plate. Laser light from a 10 mW He-Ne laser is passed through a beam expander, deflected with an acousto-optic crystal, focused with a 254mm lens, and pointed with a galvonometer scanner. The beam enters the bomb through a 0.75 in diameter quartz window mounted in the bomb body at a 60 degree angle from the vertical axis. The detector and collection optics are positioned above a 1.0 inch diameter window in the top cap.

5.1.5. Electronics A computer data acquisition system monitored the instrumentation during the experiments. A 15-channel coaxial cable running from the test cell to the computer transmitted the voltage signals to an HP 3852A data acquisition system equipped with a multiplexer and a high-speed voltmeter. The digitized results were transferred to an HP Vectra which reduces the data and makes the plots.

5.2. Gain Reduction Experiments

This section describes experiments to determine the actual loss of system forward gain, $\bar{K}$, caused by the propellant combustion. System-I is used for the testing.

The first task is to calibrate the system gain to a reference value. This can be accomplished by combining the closed-loop frequency response data with the test system model. Previous testing (see Figure 43) showed that between 50 and 200 hz, the phase lag of the closed-loop system is a strong function of the system gain. This

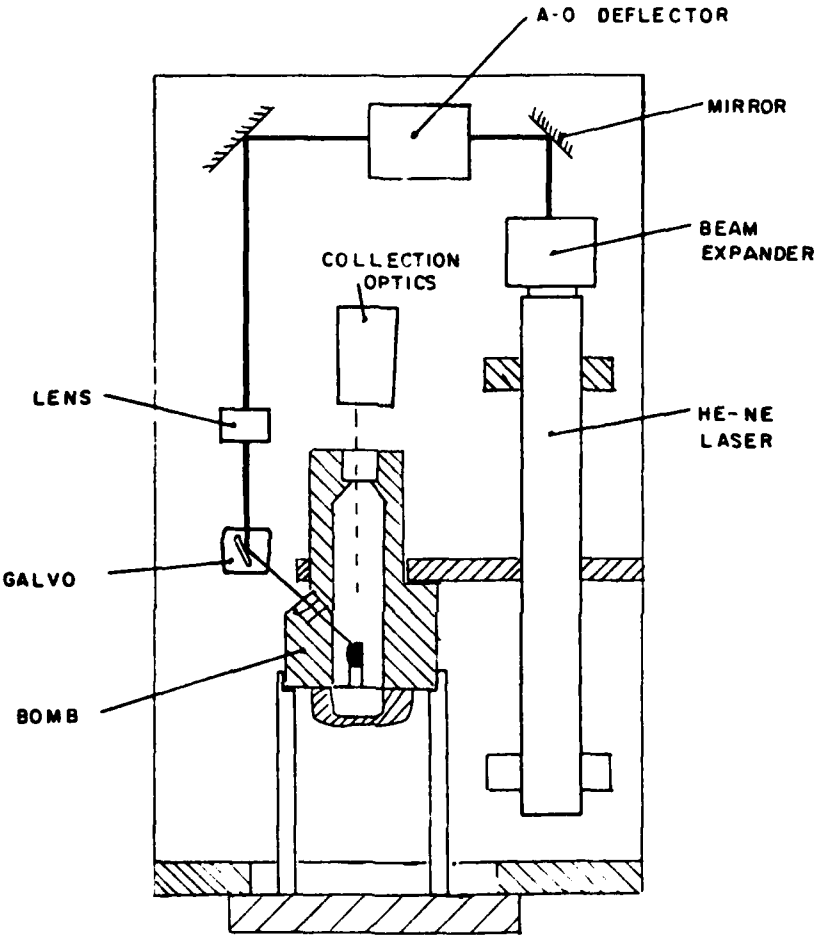

Figure 51. High-Pressure Bomb and Optics

relationship as predicted by the model is plotted in Figure 52. The x-axis represents the phase lag between the output and the input while the y-axis represents the system gain. The curve shown is for an input frequency of 100 hz. Also shown in the plot are four measured points from the previous testing with the point A being the condition at which the model and the measurements were matched. These relationships describe the system forward gain as a function of phase lag

$$\bar{K} = \bar{K}(\phi_f) \tag{45}$$

where the phase is determined at a known excitation frequency, f.

The system gain is adjusted to a desired value with the instrument gains. The system gain is

$$\bar{K}(\phi_{fcal}) = K_{PDL_{cal}} K_{PLA} K_b K_s K_2 \tag{46}$$

The first gain, $K_{PDL_{cal}}$ accounts for the combined influences of the propellant, detector, and the laser and is constant during the calibration. The scanner gain, K_s and the geometric gain, K_2 are also constant. The lock-in and scanner gain K_{PLA} and K_b may be varied and are adjusted to calibrate the system forward gain.

With the system calibrated to a known gain, the only parameter that can change during the experiment is K_{PDL}. The gain reduction during the experiment is then

$$\frac{\bar{K}(\phi,t)}{\bar{K}(\phi)_{cal}} = \frac{K_{PDL}(t) K_{PLA} K_b K_s K_2}{K_{PDL_{cal}} K_{PLA} K_b K_s K_2} \tag{47}$$

where the time dependency has been added to represent variations caused by the combustion. This expression shows that the gain loss can be determined by measuring the system phase lag before and during the experiment.

The experiments were conducted with a special constant-height sample holder. The holder, drawn in Figure 53, supports a 6 mm cubic sample. A 2 mm stainless steel dowel pin is press-fit in the holder and passes through a hole drilled in the sample. A

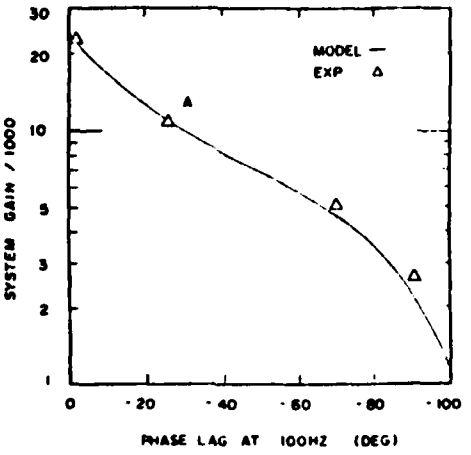

Figure 52. Gain-Phase Relationship

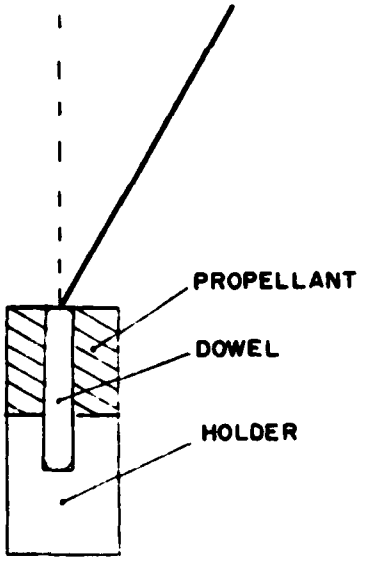

Figure 53. Constant-Height Sample Holder

nichrome ignition wire circles the top surface of the propellant and connects with the two ignition posts.

This holder allows the laser beam to be focused on the top of the steel pin while the propellant burns around it. This provides a fixed surface height so that any output perturbations are caused by the 100 hz driving signal and the propellant gases.

The results of phase measurements for one experiment are shown in Figures 54a and 54b. The Lissajous figures are a result of plotting the input sin wave signal on the x-axis and the instrument output signal on the y-axis. The phase lag is given by

$$\phi = \sin^{-1}(\Delta V_y/\Delta V_{out}) \tag{48}$$

where the voltages, shown in the figure, are measured by the computer. Figure 54a shows that the phase lag before the experiment is -21 degrees corresponding to a system gain of 125 (from Figure 52). The phase during the experiment dropped to -56 degrees, as shown in Figure 54b, showing that the system gain has dropped to 69. This makes the gain reduction ratio, $\bar{K}_2/\bar{K}_1$, have a value of 0.66. Table 9 shows the results for several experiments showing that the system gain can drop by 25 to 50 percent (-2.5 to 6.0 db) during an experiment at atmospheric pressure. The results mean that the combustion reduces the system gain as anticipated.

The gain reduction measurement experiment was repeated for higher pressures. System-I was rearranged to operate on the high-pressure combustion rig. The data acquisition system was also modified so that the system output could be continuously monitored during the experiment making it possible to calculate the system gain as a function of time.

Figure 55 shows the results for two pressures. Figure 55a shows the gain reduction ratio as a function of time for an experiment at 125 psig. After ignition, the combustion products reduce the gain by 18 db in 0.4 sec. At 250 psi, the reduction is

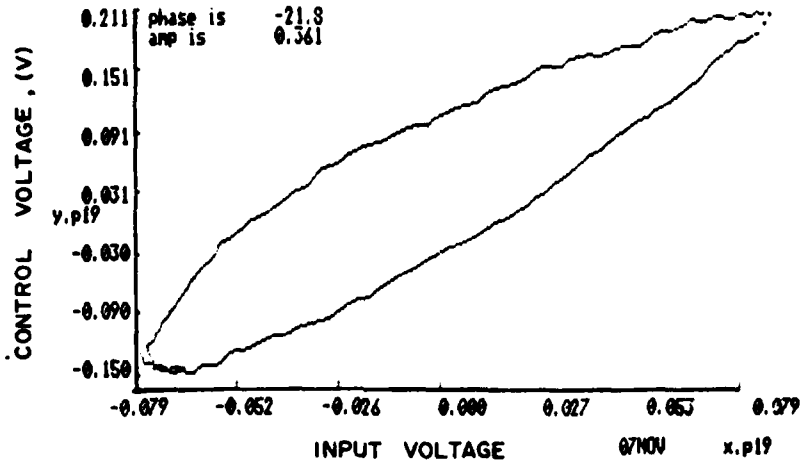

(a) Lissajous Figure without Combustion

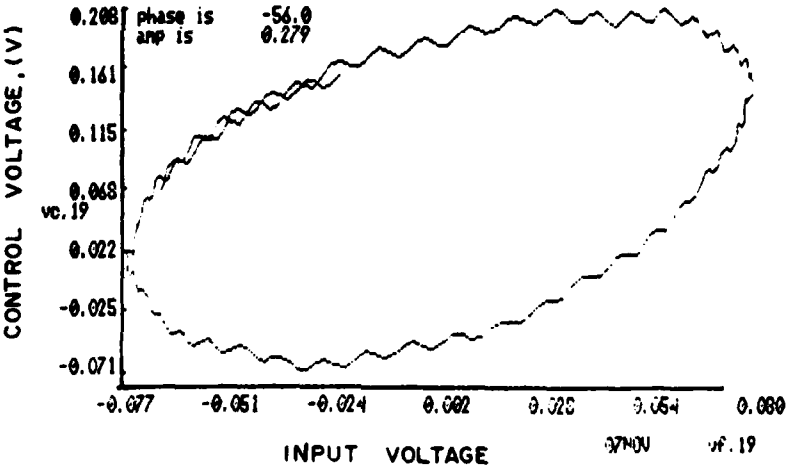

(b) Lissajous Figure with Combustion

Figure 54. Lissajous Figures

Table 9

System Gain Measurements-
Atmospheric Pressure

NO COMBUSTION		COMBUSTION		RATIO	db
ϕ_1	$\bar{K}_1$	ϕ_2	$\bar{K}_2$	$\bar{K}_2/\bar{K}_1$	$20 \log(\bar{K}_2/\bar{K}_1)$
−21°	125	−45°	63	0.50	-6.0db
−21°	125	−34°	94	0.75	-2.5db
−21°	125	−36°	94	0.75	-2.5db
−25°	115	−42°	84	0.73	-2.7db
−30°	105	−56°	69	0.66	-3.6db

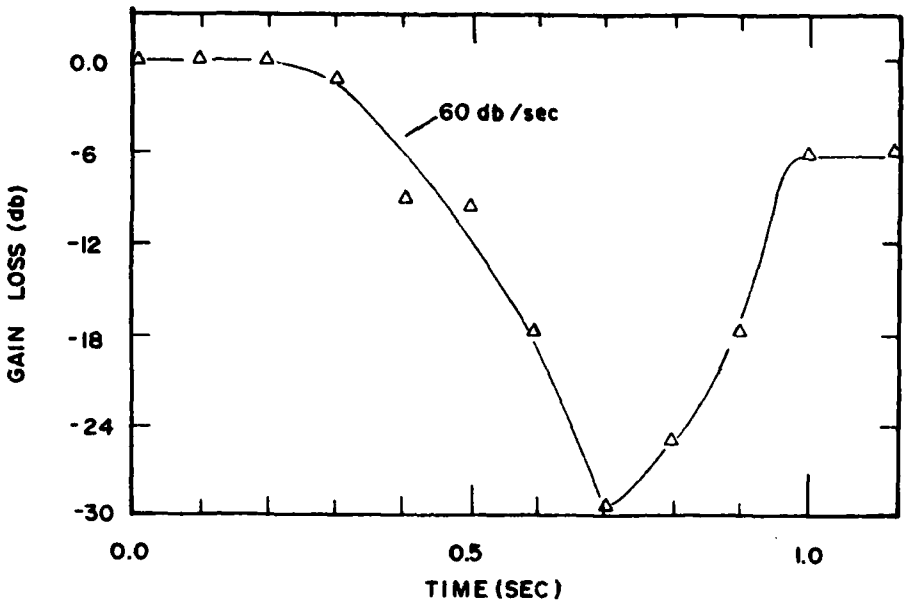

(a) Pressure is 125 psig

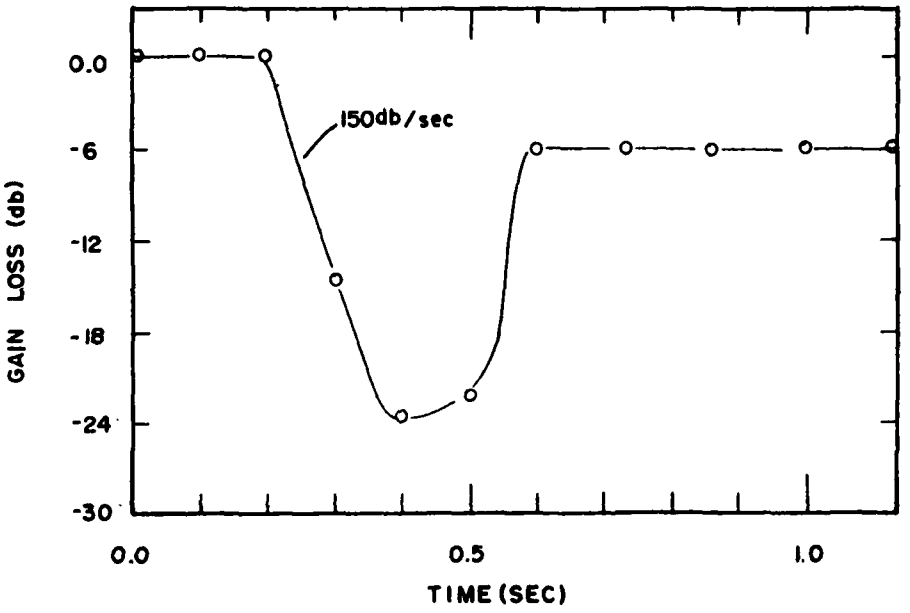

(b) Pressure is 250 psig

Figure 55. Gain Reduction as a Function of Pressure

much faster because the sample is burning faster producing smoke at a higher rate. Figure 55b shows the results for the 250 psig experiment. In this case, the gain is reduced 23 db during the burn. At 500 psig the system looses "lock" on the surface meaning the laser spot drifts from the target. These results show that the combustion products do alter the system forward gain beyond what was anticipated.

Since the instrument is designed to meet specifications over gain losses of 6db, the gain loss characteristics determine the time window over which the instrument will be performing above its requirements. At 125 psig this time period is .25 sec; at 250 psig it is .15 sec.

5.3. Resolution Experiments

Since the combustion gases were observed to perturb the laser beam, experiments were performed to determined the amplitude deviations of the output caused by the combustion gases perturbations. The amplitude of the perturbations will be considered the minimum resolution of the instrument. The constant-height sample holder was used for these measurements, however, the instrument was not perturbed with the 100 hz sin wave as in the gain measurement experiments. Thus, during the burn, the beam was focused on a fixed surface height making any fluctuations in the output voltage the result of the hot gas flow or other noise.

Figure 56 shows representative plots of the measured displacements as a function of time for the constant-height experiment. Figure 56a shows an atmospheric pressure measurement. At ignition, a large spike occurs from the ignition wire crossing the beam path. Then the output increases to an apparent surface height of about 0.140 inches with large amplitude fluctuations. After about 6 seconds, the fluctuations decrease and the apparent surface height lowers to about 0.040 inches and has small

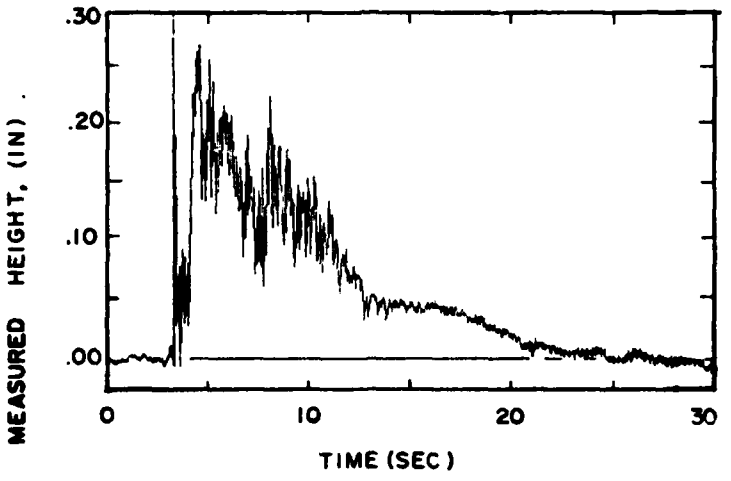

(a) Output Perturbations Caused by the Gases-0 psig

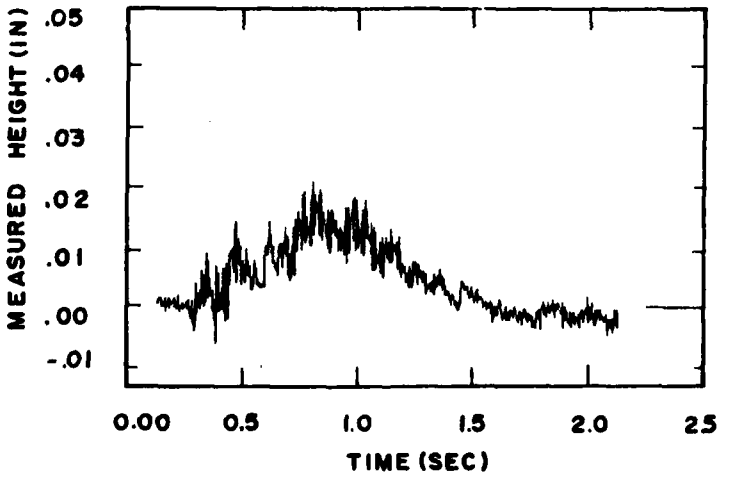

(b) Output Perturbations Caused by the Gases-250 psig

Figure 56. Output Perturbations Caused by Combustion

(0.010 in.) perturbations. At the burn out, the measured surface height returns to its original value. Figure 56b shows a measurement taken at 250 psig. At ignition, the output increases to an apparent surface height of about .003 inches and has small (0.001 in.) perturbations. At the burn out, the measured surface height returns to its original value.

This behavior results from the hot gases above the surface bending the laser beam as illustrated in Figure 57. The hot gases have a lower refractive index than the surrounding nitrogen. Thus as the beam enters the hot gas its angle is changed. This is the cause of the *offset* in the measured surface height. The offset for the high pressure experiment is lower because the beam enters the gases at an angle closer to the normal of the interface. The *fluctuations* in the measured height are caused by the shear turbulence at the boundary between the hot and cool gases. During the first part of the experiment, the location of the boundary between the hot and cool gases fluctuates because of the surface is burning unevenly after the hot-wire ignition. Then, the surface assumes a flat even burn still producing a offset but having much smaller fluctuations.

After the initial fluctuations of the output, the results of the resolution experiments show two characteristics important to the instrument performance. The first is a mean offset in apparent surface height. This reduces the accuracy of the surface height measurement, causing differences in the actual and measured surrface height. Because the magnitude of the offset doesn't change rapidly with time, it does not defeat the objectives of the measurement. The duration of burn or rest periods could still be precisely measured even with an offset present. The high-frequency fluctuations in the output are what establishes the resolution of the measurement. From these results, the minimum resolution is estimated from .001 to .014 inches with the sample burning. The resolution improves as the system gain is lowered because it reduces the system

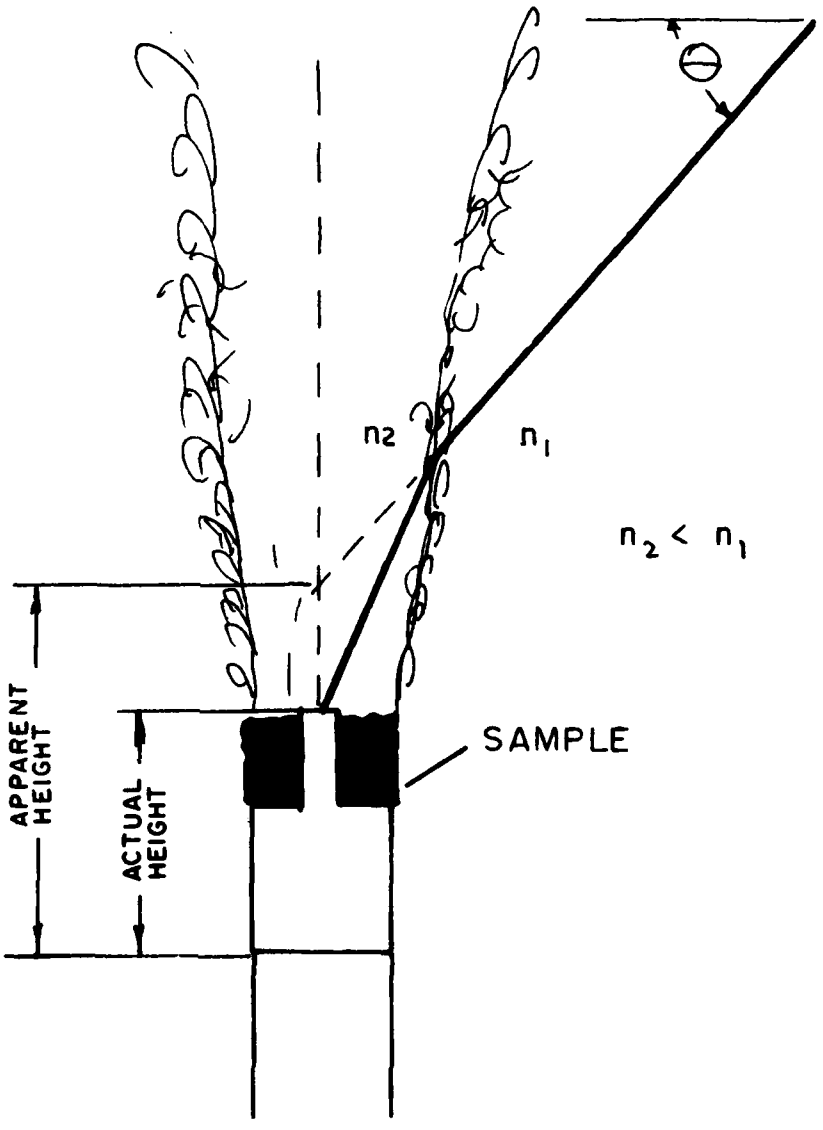

Figure 57. Effect of Gases on Measured Surface Height

bandwidth. This tends to filter out the high-frequency fluctuations. The source of the disturbance is apparently a turbulent sheer layer between the combustion products and the purge gases.

5.4. Propellant Surface Height Measurement

The objective of the instrument is to measure the surface displacement of a burning propellant surface. From the results of the previous analysis and testing, proper gain selection and control of the purge gases around the sample were considered two important factors to explore to find the conditions for achieving optimum performance. Measurements of the surface height was attempted at pressure levels from ATM to 500 psig.

5.4.1. Atmospheric Experiments The low-pressure test rig was used to perform experiments at atmospheric pressure. A 6x6x20mm propellant sample, inhibited on the outer faces to prevent side burning was ignited with a nichrome wire. The system forward gain was calibrated before the experiment using the gain-phase relationship.

Figure 58 shows the results for atmospheric pressure measurements. The system gain was pre-set to a value of 30 resulting in a bandwidth of approximately 20hz. An x-y plotter directly recorded the output as a function of time. Figure 58a shows the results for the case when the sample burns unevenly after the ignition. The Laser Position Detector tracks the surface during the entire burn. During the first 7 seconds, the output fluctuates because of the turbulent shear layer perturbing the beam angle. After the ignition transient, the instrument measures the displacement of the surface and even shows some indication of intermittent burning. Figure 58b shows results for a similar experiment in which the propellant surface burned much more evenly during the ignition transient. In this curve, the slope changes during the second half of the burn

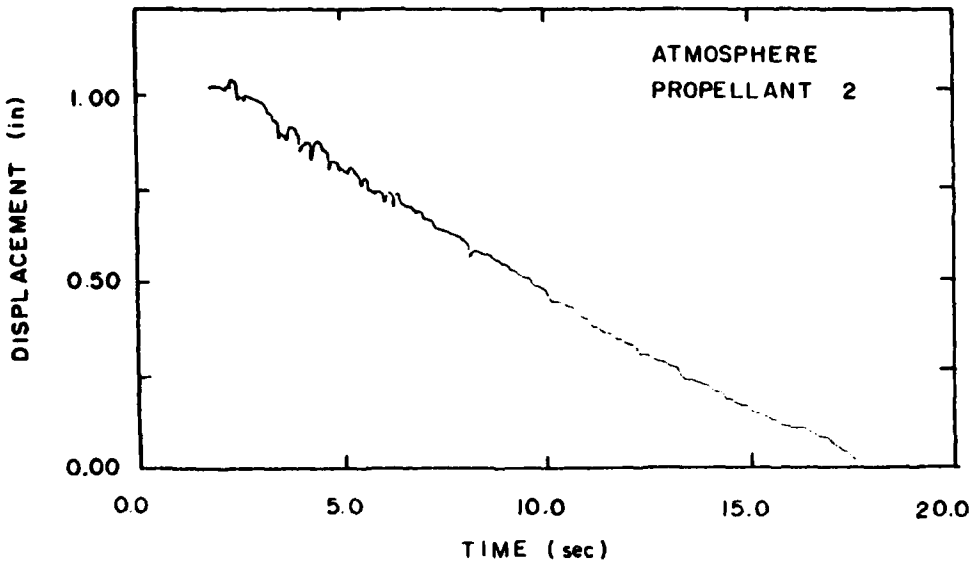

(a) Uneven Burning Surface-Bandwidth is 20 hz

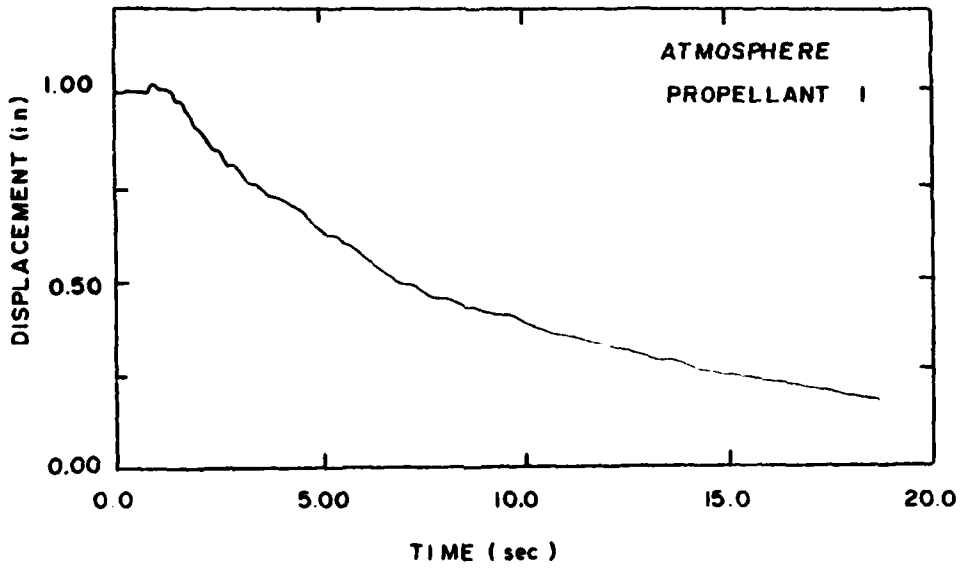

(b) Even Burning Surface-Bandwidth is 20 hz

Figure 58. Propellant Surface Height Measurements-Atmospheric Pressure

revealing a lowering of the burning rate. These results also show indications of intermittent movements of the propellant surface. Detection of intermittent burning at this low gain is apparently possible because the low pressure slows the surface movements significantly from the 1000 psi conditions used to derive the specifications.

Figure 59 shows surface height measurements made with a higher value of forward gain and recorded with the digital data acquisition system. Figure 59a shows results for a system gain pre-set to a value of 120. This gives the system an initial bandwidth of about 230hz. The output has fluctuations throughout the entire burn. It was observed that the purge gases were causing the gas zone above the strand to swing back and forth. The increased bandwidth caused by the gain increase now makes the instrument sensitive to the beam angle perturbations induced by these movements.

Several modifications were tried to reduce the flame/purge-air interaction at atmospheric pressure. Lowering the purge flow, changing the sample from square to round, water leaching the outside of the sample rather than using inhibiter, placing a 4 inch concentric ring around the sample holder to straighten the purge flow, and different type samples were attempted to reduce the oscillations. Still, the movements of the turbulent shear layer perturbed the beam angle as the sample burned. Finally, the vacuum system was shut off and only a small amount of purge air blown over the viewing windows to prevent moisture accumulation. Figure 59b shows the results without purge air flowing past the sample. After the initial ignition transient, the surface displacement is measured without perturbations. Evidently, the purge flow around the sample and the vacuum pump exhaust system produced the perturbations in the shear layer for these low-pressure experiments.

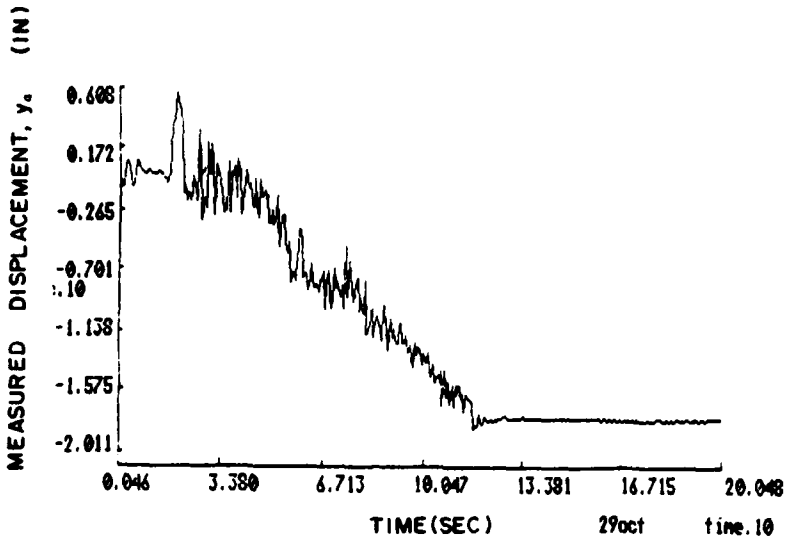

(a) High Purge-Bandwidth set at 230 hz

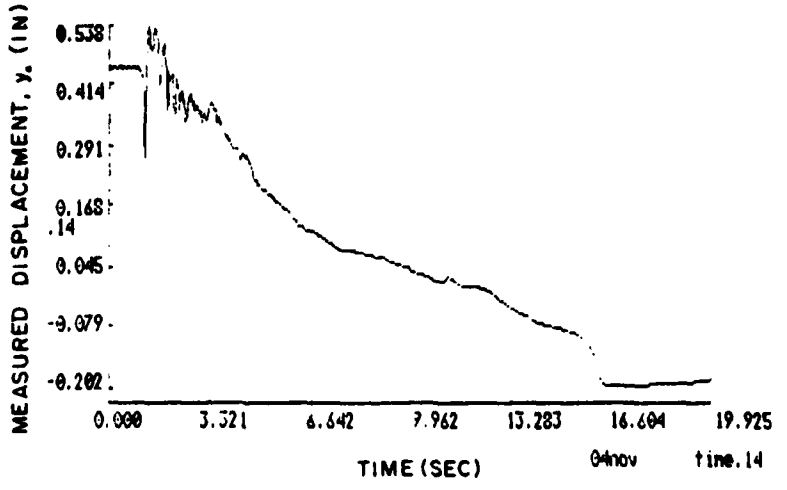

(b) Low Purge-Bandwidth set at 230 hz

Figure 59. Propellant Surface Height Measurements-Atmospheric Pressure

5.4.2. High-Pressure Experiments The high-pressure rig was set-up to make propellant surface height measurements using a System-I configuration. The sample size was reduced to 3x6x6mm to lower the amount of smoke generated by the propellant. In addition, a few experiments were performed using the laser position detector and a high-speed movie camera to simultaneously record the propellant surface height.

Figure 60 shows the results of Laser Position Detector measurements at 250 psig. Figure 60a shows the entire experiment. The laser device was pre-set to give it a bandwidth of approximately 200 hz. The output rises at ignition because of the difference in gas densities. After the ignition transient, the system followed the surface displacement with small perturbations in the output caused by the product gases. Figure 60b shows the middle portion of the burn enlarged. Some characteristics of the intermittent burning could be inferred from the trace.

Figure 61 shows a comparison of simultaneous optical and photographic measurements made of a strand burning at 250 psig. The photographic measurement was made with an NAC-E10 16 mm high-speed movie camera recording at 400 frames per second. The camera had a total magnification of 1.0 and was focused on the front edge of the sample. The laser spot was focused on the center of the sample to obtain the least amount of perturbations from the shear layer. The comparison shows the same general trends in surface height. The center of the sample where the Laser Position Detector measured was observed to burn lower in the films. Since the camera was on loan for a short period, additional experiments to make a better comparison were not possible.

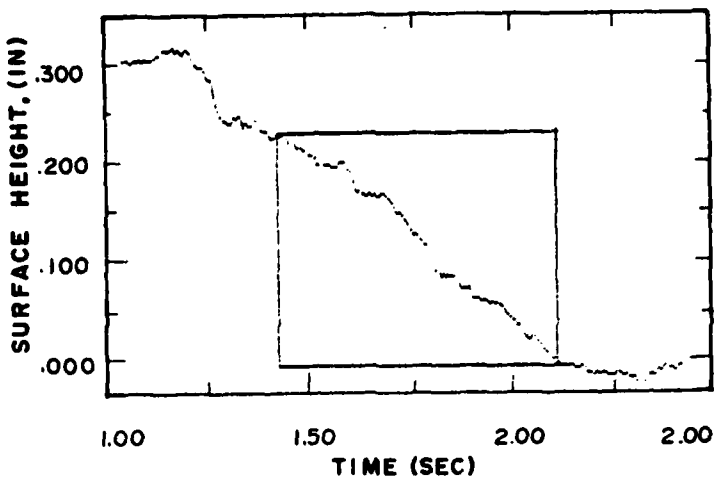

(a) Entire Experiment

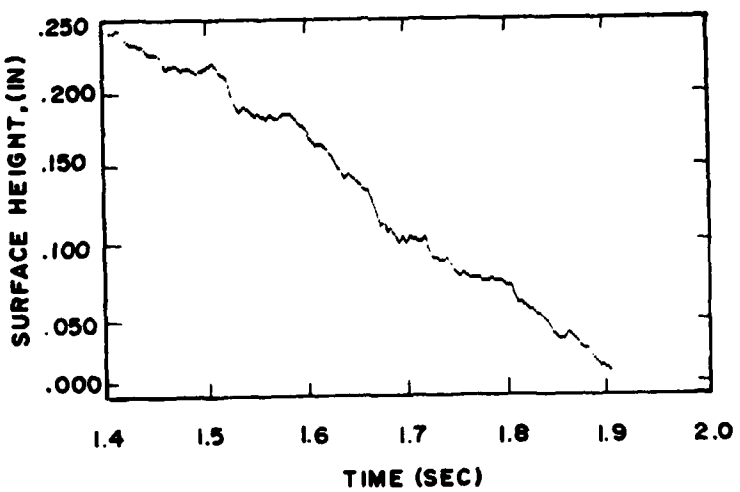

(b) Enlarged View of Latter Portion

Figure 60. Propellant Surface Height Measurements- 250 psig

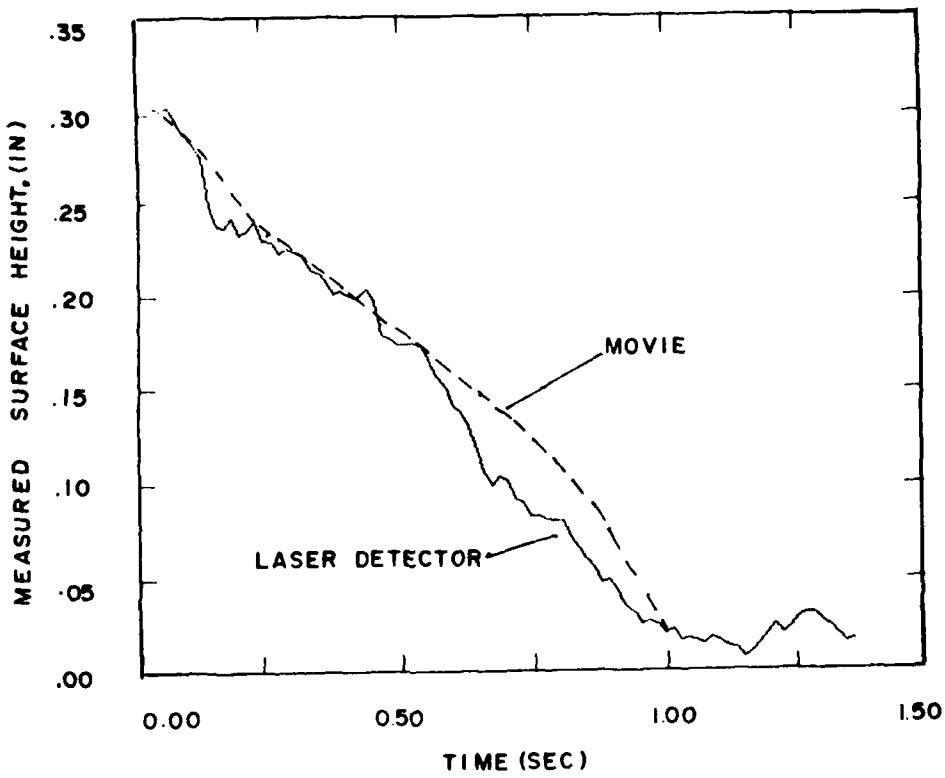

Figure 61. Comparison of Optical and Photographic Surface Height Measurements

5.5. Discussion of Results: Combustion Measurements

The results of the combustion experiments are summarized in Table 10.

The gain reduction experiments showed that, during an experiment, the combustion products reduce the system gain significantly. The atmospheric combustion experiments showed gain losses up to 6db during an experiment while at pressures of 250 psig the gain is reduced up to 23 db. The drop is caused by the smoke and other combustion products attenuating portions of the laser signal reaching the detector. Another possible cause is the beam being deflected perpendicularly to the plane in which the scanner rotates it. This moves the spot image out of the pinhole and reduces the signal reaching the detector. Focusing the beam to smaller and smaller spots on the surface would tend to amplify this effect.

The gain reduction lowers the system bandwidth during the experiment. For atmospheric experiments, the gain loss can be compensated for because the system was designed to operate over a 6 db loss of gain. However, at the higher pressures, the gain loss reaches 6 db in 0.1 to 0.3 seconds. This means the short period at the beginning of the burn is the time when the system has sufficient bandwidth to measure the higher frequency intermittent burning.

The resolution experiments showed that the density difference between the hot combustion products and cool purge gases cause refractive index gradients that bend the laser beam. As the beam is bent, the control system compensates to keep the spot centered under the detector. This creates apparent offsets in surface height. A mean shift from 0.003 to 0.015 inches is caused by the refractive index difference. Higher frequency, lower-amplitude oscillations are produced as the interface between the hot and cool gases is disturbed by shear turbulence. These disturbances result in a minimum resolution between 0.001 to 0.010 inches depending upon the angle of the

Table 10
Combustion Measurements

MEASUREMENT	Opsig	125 psig	250 psig
Gain Loss (Max)	6db	30db	24db
Gain Loss (Rate)	-	60 db/sec	150 db/sec
Accuracy	0.014 in	-	0.003 in
Resolution	0.010 in	-	0.001 in
Continuous Measurement	YES	YES	YES

beam relative to the flow. Beam angles more perpendicular to the flow are disturbed less.

The results of the propellant surface height experiments show that a local position of the propellant surface can be continuously measured at pressure levels from 0 to 250 psig. Above this pressure, smoke attenuation blocks the beam. The output is perturbed by the combustion products to a greater extent during the initial portions of the burn. Then the perturbations are reduced in amplitude and some evidences of intermittent burning are observed. The reduction of the disturbances results from the surface assuming a smooth shape after the ignition transient and the reduction of bandwidth caused by the increase in smoke. Although the bandwidth is lowered by the smoke, some evidences of intermittent burning were detected. Apparently some intermittent movements of the burning surface occur at lower frequencies than anticipated. Therefore, the instrument is found most suitable for measureing the lower frequency, transient nature of the surface displacement (< 50 hz). Although the instrument has sufficient bandwidth and resolution, the combustion environment prevents more accurate measurements.

5.6. Recommendations

The main difficulty of making an optical measurement in the combustion environment is the properties of the combustion gases. The smoke attenuation could be compensated for over a broader range by using a more powerful laser and programing the intensity to increase after the propellant has ignited. The intensity of the laser can be controlled with the acousto-optic crystal.

The instrument could find applications to other disciplines where precise measurements are required in a hostile environment or on surfaces that have changing reflectivity. Possible applications would include measuring the erosion rate of ablative material; surface height for servo-controlled propellant strand burners; non-steady surface height in water table studies (some opacificier would have to be added to the water.)

Basically, the instrument can continuously measure the position of a diffusely reflected spot. Changes in the level of the detected signal only change the time response of the instrument. The instrument could be used for propellant research studies at pressure levels from 0 to 250 psig on non-aluminized propellants.

PART III

COMBUSTION STUDIES

6.0 MATERIALS AND METHODS

This chapter describes the materials and methods used in the experimental research investigation concerning the effect of oxidizer particle size distribution on the combustion of wide distribution solid propellants. The background for this research has been presented in Chapter 2.

6.1. Propellant Formulations

Two influences are believed to cause departure of wide distribution propellants from predicted burning rates. They are: (1) control of the ballistics by the fine - AP/binder (pocket propellant) matrix and; (2) local intermittent burning related to the mass fraction of the coarse oxidizer particles. These two influences are investigated with AP/HTPB propellant formulations and two different binder curatives.

To design propellants having controlled pocket propellant chemistry, and controlled solids loading, equations were derived to describe the relationship between volume fraction of coarse oxidizer, V_c/V_t; total solids level, α_t; and the oxidizer-to-fuel ratio of the pocket propellant, OF_p. Figure 62 shows the resulting propellant formulation chart. The x-axis represents the volume fraction of the coarse oxidizer (ratio of volume of coarse material to the total volume). The y-axis represents the total solids level (oxidizes mass fraction) propellant. The curves plotted on the chart are lines of constant pocket propellant oxidizer-to-fuel ratio (OF_p). The equations used to produce this chart are derived in Appendix E.

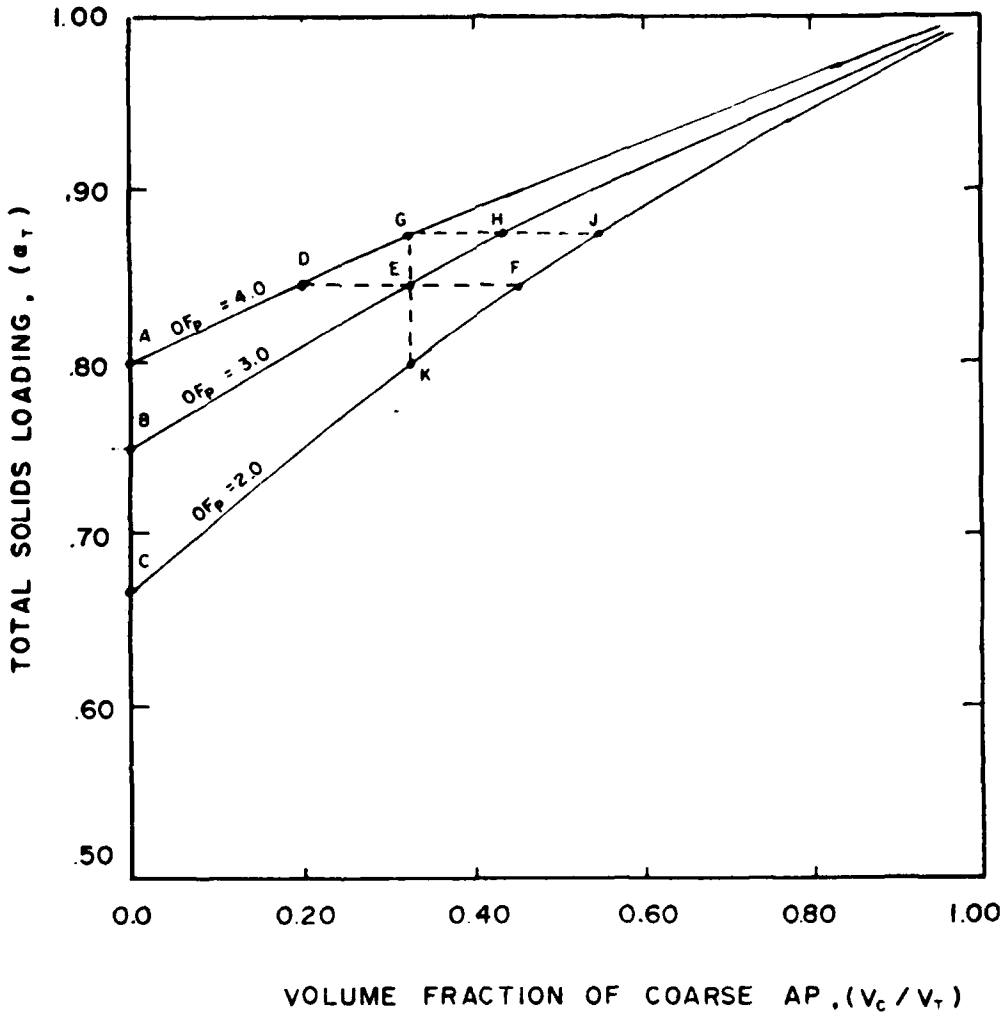

Figure 62. Composition Diagram for Wide Distribution Propellants

Propellants will be described in sets. A set is a series of propellants having one characteristic of its oxidizer size distribution controlled. For example, line G-H-J in Figure 62, represents a set of propellants having a constant, 87%, total solids level.

Each propellant set in this investigation was formulated twice. The propellants formulated are divided into two series according to their binder composition. Table 11 shows that the Series-I propellants have an IPDI (isophoron diisocynate) cured HTPB binder; Series II a DDI (dimeryl diisocynate) cured HTPB binder. A constant NCO/OH ratio was maintained in each binder to produce an approximately constant density of urethane linkages.

6.1.1. Pocket Propellant Formulations. Monomodal propellants were formulated using 16μ AP at oxidizer-to-fuel levels of 2.0 to 4.0 (line A-B-C in Figure 62). Their formulations are listed in Table 12 along with the identification designators for the Series-I and Series-II binders (Note that the letters correspond to the points in Figure 62). These formulations represent the pocket propellants of wide distribution formulations. (Pocket propellant described in Section 2.1.1).

These propellant formulations will be used to determine the ballistic properties of the fine-AP/binder matrix in the absence of coarse oxidizer particles that would introduce chemical heterogenity at the surface. These six compositions (3 solids levels x 2 binders) will then be the basis for formulating additional sets of bimodal analogue propellants (i.e. having analogous pocket propellants). Equations to formulate the analogue propellants are derived in Appendix E.

6.1.2. Constant Volume Fraction Analogue Formulations. A second set of bimodal propellants controlled pocket propellant chemistry and *constant volume fraction* of coarse particles. These propellants are represented by points G-E-K on the formulation

chart and the compositions are listed in Table 13. Three types of coarse particles were used: 400μ AP used in the bimodal analogue formulations; 400μ NaCl used as an inert surrogate for the coarse AP; and 600μ AP included for initial studies with the Laser Position Detector (Section 5.4).

Replacing the coarse AP with salt at a constant volume fraction simulates the physical heterogenity of the surface and the thermal absorbtion of the coarse AP without the production of reactive species that can interact with the pocket propellant decomposition products. While it is not an exact analogy thermally, it could show some of the interactions of the coarse oxidizer and the products of the pocket propellant.

6.1.3. Constant Total Solids Analogue Formulations. Bimodal propellants were formulated having controlled pocket propellant chemistry and constant total solids level. Conceptually, this is achieved by mixing coarse oxidizer into each pocket propellant formulation until a specified total solids level is reached.

Formulations producing an 84% total solids propellant are shown at points D-E-F on Figure 62 and their compositions are listed in Table 14. Table 15 lists 87% total solids level propellants (Points G-H-J in Figure 62).

6.1.4. Trimodal Application Formulations. The final set of propellants contain a trimodal oxidizer particle size distribution. The propellents contain an 87% total solids loading and have the previously mentioned Series I and Series II binder compositions.

These propellants were selected because previous studies have shown that they display intermittent combustion and they represent compositions more typical of those used in actual applications. Their formulations are listed in Table 16.

Table 11

Series I and II - Binder Compositions

INGREDIENT	SERIES I % BINDER	SERIES II % BINDER
R-45M (HTPB)	66.3	59.9
IPDI	5.0	-
DDI	-	11.4
DOA	25.5	25.5
HX-752	1.2	1.2
Agerite White	2.0	2.0

Table 12

Monomodal Pocket Propellants

DESIGNATORS		OF_p	16 μ AP	BINDER
1PDI	DDI	-	Wt. %	Wt. %
A-I	A-II	4.0	80.0	20.0
B-I	B-II	3.0	75.0	25.0
C-I	C-II	2.0	66.7	33.3

Table 13

Coarse Volume Fraction $V_c/V_t = 0.305$

Bimodal Analogue Propellants

DESIGNATOR		OF_p	COARSE	COARSE	16μAP	BINDER
IPDI	DDI		MATERIAL	Wt %	Wt %	Wt %
G-I	G-II	4.0	400 μ AP	35.0	52.0	13.0
G-I-400S	G-II-400S	4.0	400 μ NaCl	37.4	50.1	12.5
G-I-600A	G-II-600A	4.0	600 μ AP	35.0	52.0	13.0
E-I	E-II	3.0	400 μ AP	36.0	48.0	16.0
E-I-400S	E-II-400S	3.0	400 μ NaCl	38.4	46.2	15.4
E-I-600A	E-II-600A	3.0	600 μ AP	36.0	48.0	16.0
K-I	K-II	2.0	400 μ AP	37.6	41.6	20.8
K-I-400S	K-II-400S	2.0	400 μ NaCl	40.1	39.9	20.0
K-I-600A	K-II-600A	2.0	600 μ AP	-	-	-

6.2. Propellant Preparation

6.2.1. Propellant Ingredient Properties. Detailed properties for both the oxidizer and binder were documented for all the ingredients. Table 17 summarizes the average diameter and mode widths that describe each oxidizer mode. The results were obtained by optimizing a long-normal distribution function to experimentally measured mass distribution data. Appendix F contains additional properties including SEM photographs of the oxidizer, mass distribution data, binder ingredients descriptions, and thermodynamic properties of the ingredients.

6.2.2. Propellant Mixing, Casting, and Cutting. The monomodal and bimodal propellants were mixed is 600 gram batches using a Baker-Perkins mixer. A special process was developed to speed the production by making gallon batches of each pocket propellant, then adding the coarse material and curative to pint portions of this mix. A description of the mix procedure is shown in Appendix E. Each batch was vacuum cast into a 4 in. cube and cured for 7-10 days.

The trimodal propellants were mixed in 4000 gram batches using a gallon-size mixer. These propellants were vacuum cast into cartons and cured for 12 days.

Propellant strands were prepared from the castings as described in Figures 63 and 64. The monomodal and bimodal propellants, cast from pint mixes were prepared according to Figure 63. The trimodal application propellants, cast from gallon mixes were prepared according to Figure 64. In both cases, the castings were cut and milled into 0.25 inch slabs. Then selected slabs were cut into 0.25x0.25 inch strands using a special cutting tool. The figures also show the labeling system used to describe the position that the strand was located in the original casting.

Table 14

84% Total Solids - Bimodal Analogue Propellants

DESIGNATOR		OF_p	16 μ AP	400 μ AP	BINDER
IPDI	DDI		Wt %	Wt %	Wt %
D-I	D-II	4.0	64.0	20.0	16.0
E-I	E-II	3.0	48.0	36.0	16.0
F-I	F-II	2.0	32.0	52.0	16.0

Table 15

87% Total Solids - Bimodal Analogue Propellants

DESIGNATOR		OF_p	16 μ AP	400 μ AP	BINDER
IPDI	DDI		Wt%	Wt%	Wt%
G-I	G-II	4.0	52.0	35.0	13.0
H-I	H-II	3.0	39.0	48.0	13.0
J-I	J-II	2.0	26.0	61.0	13.0

Table 16

87% Total Solids - Trimodal Application Propellants

DESIGNATOR		OF_p	V_f/V_T	400 μ AP	25 μ AP	2 μ AP	BINDER
IPDI	DDI			Wt %	Wt %	Wt %	Wt %
L-I	L-II	3.76	0.28	38.0	10.0	39.0	13.0
M-I	M-II	3.54	0.30	41.0	10.0	36.0	13.0
N-I	M-II	3.31	0.31	44.0	10.0	33.0	13.0
O-I	0-II	3.08	0.32	47.0	10.0	30.0	13.0
P-I	P-II	2.85	0.33	50.0	10.0	27.0	13.0

Table 17

Results of Particle Size Distribution Analysis

NOMINAL DIAMETER	$\bar{D}$ μ	σ	ANALYSIS
2	9†	1.60	suspension
16	20	1.80	suspension
25	21	1.60	suspension
400	400	1.10	SIEVE
400s*	355	1.05	SIEVE
600	614	1.10	SIEVE
SALT*	355	1.05	SIEVE

† SEM photographs showed that the 2 μ material was lumped together into larger masses (Appendix D).

* These materials were pre-sieved between a 417 μ upper and a 351 μ lower screen.

6.3. Average Ballistic Properties

The average burning rate as a function of pressure was determined at pressure levels from 125 to 2000 psig using an acoustic emission method. A sound sensor mounted externally on the combustion bomb detects an acoustic signal presumably created by the thermal fracture or deflagration of the oxidizer. The system monitors the time required for the strand to be consumed at a fixed pressure.

A hole was drilled through each strand to insert an ignition wire. A metal jig controlled the distance between the end of the strand and the wire. The strands from the pint mixes were cut to 2.1 inches with the igniter wire being 2.0 inches from the end. The strands from the gallon mixes were cut to 3.1 inches with the wire placed 3.0 inches from the end. The strands were inhibited on the outer surface by dipping them in a polymer.

Because of the heterogeneous nature of the propellant, the casting process could distribute the particles anisotropically throughout the casting. To determine if casting biases were present, strands from distributed locations in the carton were tested at constant pressure levels of 1000 psi. Additional pressures were specified to obtain the other burning rates. The testing pressures of the various strands are also shown in Figures 63 and 64.

The data for each propellant and pressure level are then averaged to determine the ballistic properties.

6.4. Local Burning Rate

High-speed motion pictures of propellants were taken at the AFAL. A Hycam camera recorded the burning of a 1/8x1/4x1/4 inch strand. The strand was illuminated with a 2000 watt Xenon light source and inhibited on the three sides away from the

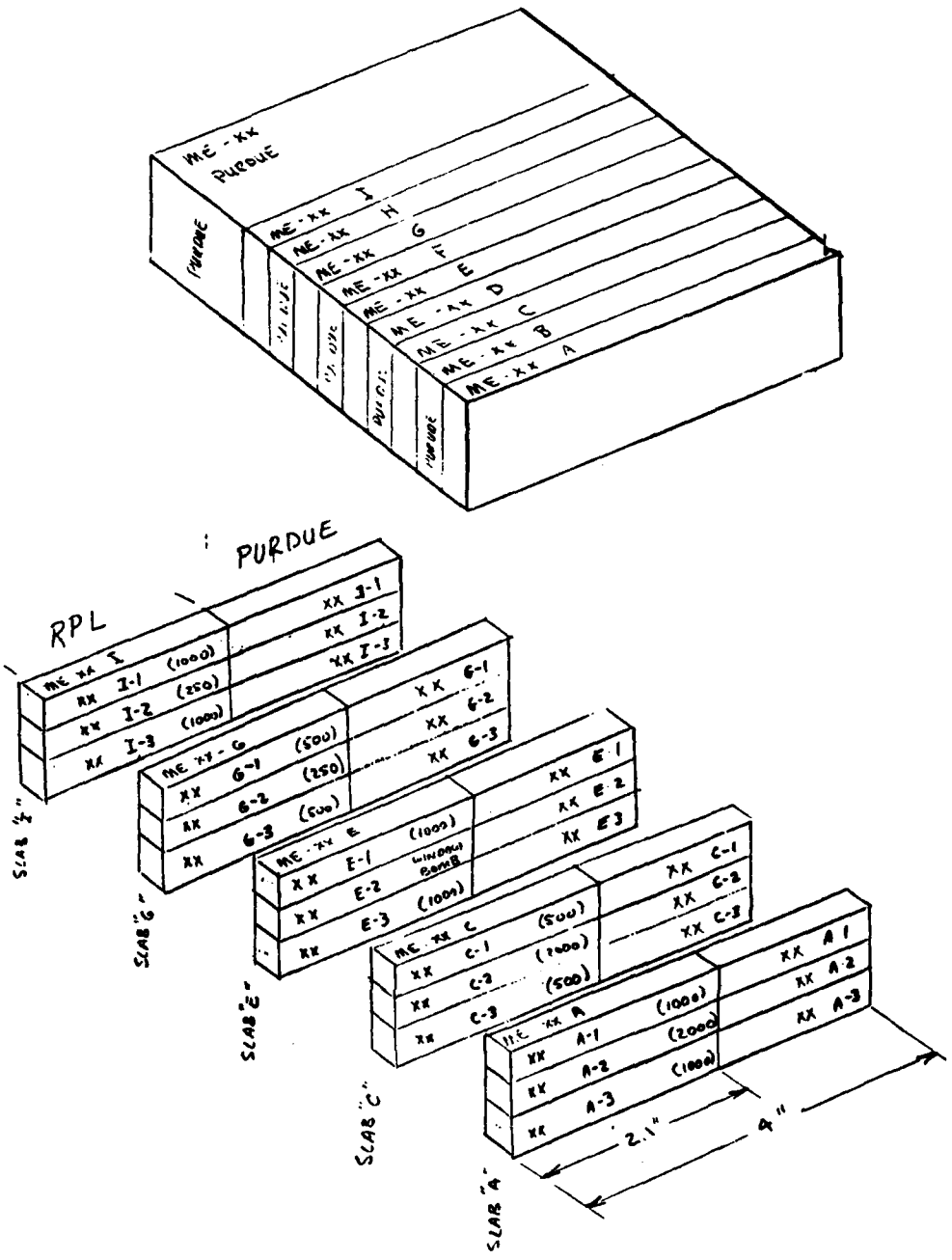

Figure 63. Strand Cutting Diagram for Pint Castings

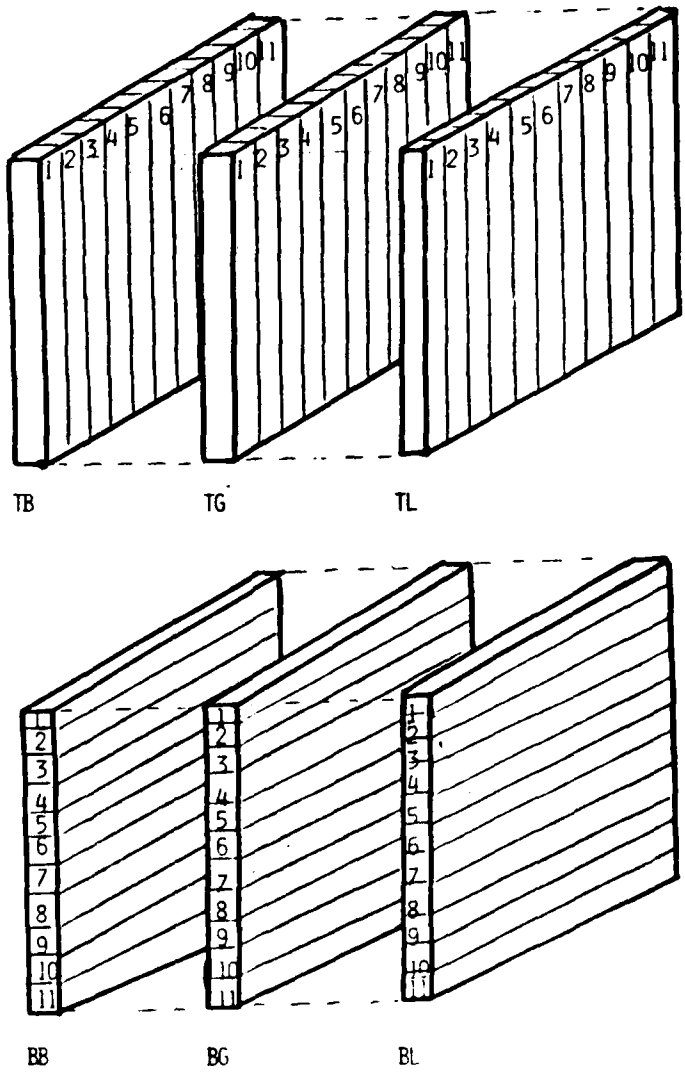

Figure 64. Strand Cutting Diagram for Gallon Castings

camera. The camera recorded the burning at 2000-3000 frames per second. The combustion vessel produced pressure levels from 250 to 1000 psi and is similar to the design described in Appendix C.

6.5. Propellant Surface Structure Examination

Propellants G-I and G-II were extinguished during combustion so that the surface could be examined under a scanning electron microscope (SEM). Pressure levels from 250 to 1000 psia were examined.

Figure 65 shows the experimental set-up. This arrangement allows the extinguishment of a sample after a fixed burning distance insuring that steady-state combustion has been established. The combustion vessel has two 1.0 in. diameter windows that lie on a horizontal axis with the propellant burning surface. A 2 mW (red) He-Ne laser is transmitted into the chamber where it is blocked by the propellant strand. After ignition, the propellant burns past the level of the laser beam allowing the beam to pass through the bomb and enter a detector. The detector activates a trigger circuit that connects a 24 volt DC power supply into a nichrome that melts the mylar disk in the top of the vessel. The stack of disks then ruptures causing the extinguishment.

The extinguished samples were prepared for examination two ways. First, a portion of the sample was sectioned off for examination of the original extinguished surface. Second, the remainder of the sample was soaked in water for 5 min and dried in heated air to remove the AP from the extinguished surface. This allows closer examination of the binder flow details around the edges of the particles.

The surface structure was examined using a JEOL-JSM-840 scanning electron microscope (SEM). Both type samples were coated with gold palladium and mounted

on conductive glue for examination under the SEM. Magnifications of from 50x to 2000x were employed to obtain detailed images of the extinguished surface structures.

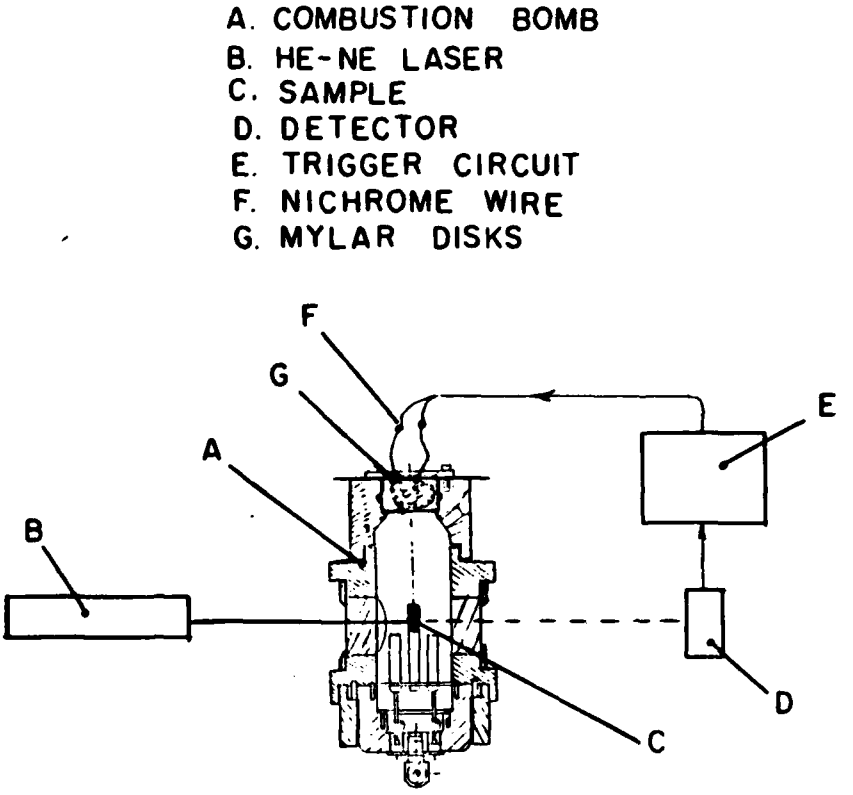

Figure 65. Propellant Extinguishment Experiment

7.0 RESULTS AND DISCUSSION

This chapter presents the results of the burning rate measurements, high-speed photography observations, and SEM photographs of the extinguished surfaces. All the ballistic and photographic results are presented first. Then, a discussion of the ballistics follows. Most of the detailed discussion is for the IPDI propellants since most of the pocket propellant of the DDI cured propellants self-extinguished. Next, the SEM photographs are presented and discussed. Combustion mechanisms are then postulated from the results.

7.1. Burning Rate Survey

Figures 66 and 67 show example results for the pint-casting and gallon-casting burning rate survey. Figure 66 shows the results for similar bimodal propellants having different binder curatives. Figure 66a shows that propellant G-I has an average burning rate of 0.443 inches per second at 1000psi and a standard deviation of 0.021 inches per second. The burning rates of the strands do not vary significantly as a function of their original position in the casting. Evidently the quick-cure technique prevented settling of the oxidizer particles. Figure 67 shows similar results for a pint-cast DDI propellant. Generally the standard deviations for the monomodal and bimodal propellant burning rates were from 1 to 5% of the average rate. Detailed results for the monomodal and bimodal propellants are listed in Appendix G.

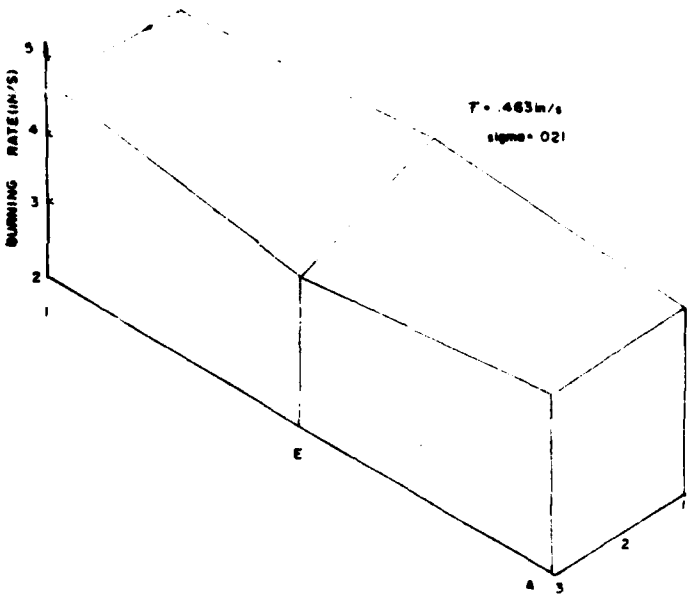

(a) Propellant G-I, 1000psi

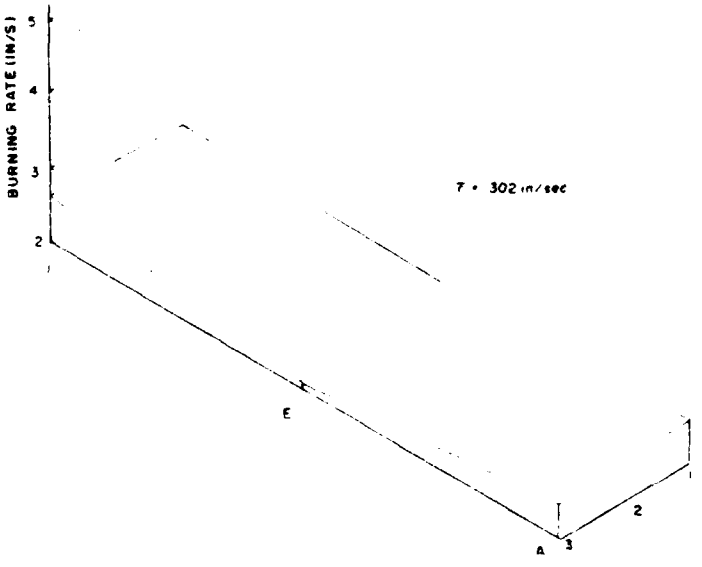

(b) Propellant G-II, 1000psi

Figure 66. Burning Rate Survey - Pint Casting

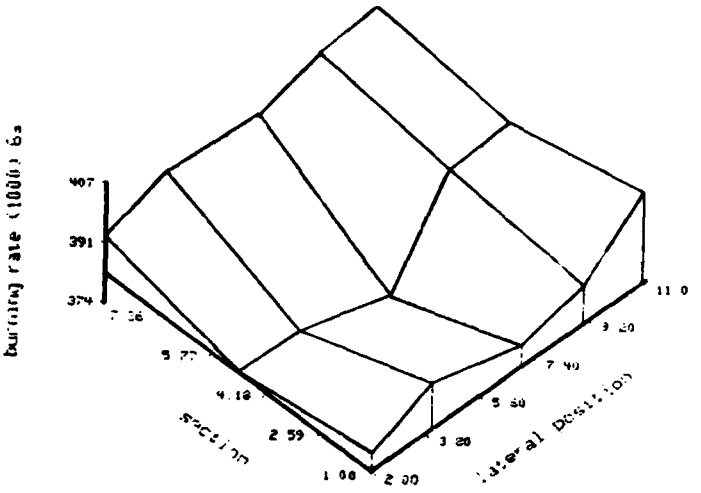

(a) Propellant L-I, 1000psi

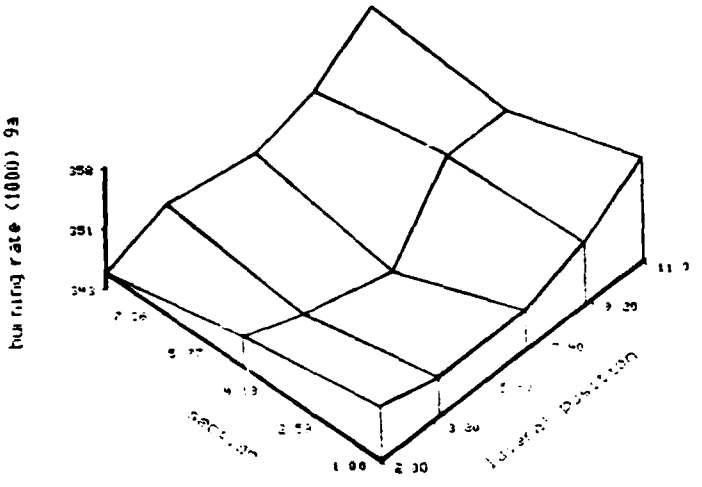

(b) Propellant L-II, 1000psi

Figure 67. Burning Rate Survey - Gallon Casting

Figure 67 shows example results for taken from the top half of the gallon mix casting. The survey shows a depressed burning rate in the central portion of the casting. This was a general trend for most of the castings and differences of 20-30% between the maximum and minimum measured rate for one casting were not uncommon. Detailed results for the trimodal burning rate survey are tabulated in Appendix H.

7.1.1. Average Burning Rate The average burning rate results as a function of pressure and propellant formulation are listed in Tables 18 to 24 and plotted in Figures 68 to 74. These results represent the averages for several experiments at each condition. The tables and figures are grouped by propellant sets in the following order

- pocket propellants
- constant volume fraction propellants
- constant total solids propellants
- trimodal application propellants

The original data are presented in Appendix G and Appendix H.

7.1.2. Photographic Observations Tables 25 to 30 summarize observations made from the high-speed films. The observations were made on the monomodal and bimodal propellants burning burning at 1000psi. No observations for the DDI propellants were noted because they extinguished in the strand bomb. The observations are broken down into six categories. The "burning rate" was measured from the projected image. The "flame cover" describes the extent of the propellant surface covered with a luminous flame. The "smoke" describes the extent of dark colored smoke observed above the propellant surface. The "surface roughness" is an estimate of the amplitude of the propellant surface roughness at an instant of time. The "binder

Table 18

Average Burning Rate - Pocket Propellants

PROPELLANT DESIGNATOR	BURNING RATE (in/sec)				
	125 psi	250 psi	500 psi	1000 psi	2000 psi
A-I	--	.186	.248	.363	.535
B-I	--	.152	.189	.245	.364
C-I	EXT.	.078	EXT.	EXT.	--
A-II	.121	.164	EXT.	EXT.	--
B-II	EXT.	EXT.	EXT.	EXT.	--
C-II	EXT.	EXT.	EXT.	EXT.	--

Table 19

Average Burning Rate - Constant Volume Fraction Propellants, 400 μ AP - Coarse Fraction

PROPELLANT DESIGNATOR	BURNING RATE (in/sec)				
	125 psi	250 psi	500 psi	1000 psi	2000 psi
G-I	--	.201	.279	.443	.641
E-I	--	.163	.232	.322	.463
K-I	.081	.121	.180	.249	--
G-II	.135	.177	.208	.301	--
E-II	.104	.133	.EXT.	.200*	--
K-II	.075	.099*	EXT.	.011*	--

*Some Samples Extinguished

Table 20

Average Burning Rate - Constant Volume Fraction Propellants, 400 μ NaCl - Coarse Fraction

PROPELLANT DESIGNATOR	BURNING RATE (in/sec)				
	125 psi	250 psi	500 psi	1000 psi	2000 psi
G-I-400S	--	.207	.315	.520	.783
E-I-400S	--	.150	.225	.379	.596
K-I-400S	EXT.	.060	.097	.175	--
G-II-400S	.095	.165	.121	.195	--
E-II-400S	.049	.061	.066	.102	--
K-II-400S	EXT.	.045*	EXT.	.077*	.067*

Table 21

Average Burning Rate - Constant Volume Fraction Propellants, 600 μ AP - Coarse Fraction

PROPELLANT DESIGNATOR	BURNING RATE (in/sec)				
	125 psi	250 psi	500 psi	1000 psi	2000 psi
G-I-600	--	.230	.291	.467	.726
E-I-600	--	.171	.241	.349	.449
G-II-600	.134	.180	.218	.323	--
E-II-600	.132	.132	.163	.234	--

*Some Samples Extinguished

Table 22

Average Burning Rate - 84% Total Solids Propellant

PROPELLANT DESIGNATOR	BURNING RATE (in/sec)				
	125 psi	250 psi	500 psi	1000 psi	2000 psi
D-I	--	.188	.261	.385	.580
E-I	--	.163	.232	.322	.463
F-I	.093	.144	.206	.278	--
D-II	.128	.164	.190	.259	--
E-II	.104	.133	EXT.	.200*	--
F-II	.092	.120	.155	.209	--

Table 23

Average Burning Rate - 87% Total Solids Propellant

PROPELLANT DESIGNATOR	BURNING RATE (in/sec)				
	125 psi	250 psi	500 psi	1000 psi	2000 psi
G-I	--	.201	.279	.443	.641
H-I	--	.171	.241	.357	.497
J-I	.094	.140	.227	.311	--
G-II	.135	.177	.208	.302	--
H-II	.130	.151	.188	.251	--
J-II	.108	.136	.191	.261	--

Table 24

Average Burning Rate - 87% Total Solids, Trimodal Application Propellants

PROPELLANT	AVERAGE BURNING RATE (in/sec)				
DESIGNATOR	125 psi	250 psi	500 psi	1000 psi	2000 psi
L-I	-	.197	.347	.536	1.253
M-I	-	.188	.343	.464	.988
N-I	-	.173	.259	.410	.866
0-I	-	.178	.245	.390	.630
P-I	-	.155	.229	.347	.540
L-II	-	.225	.226	.294	.446
M-II	-	.249	.213	.282	.438
N-II	-	.186	.204	.299	.402
O-II	-	.163	.201	.290	.328
P-II	-	.157	.204	.282	.316

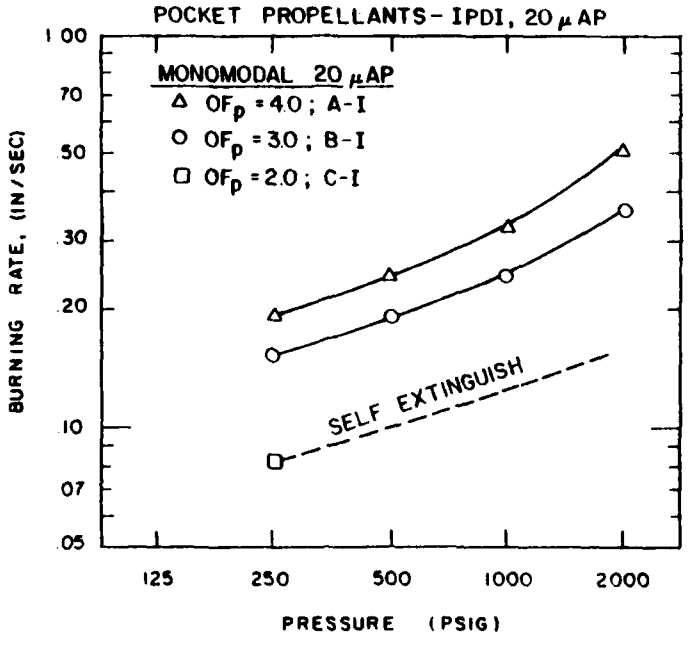

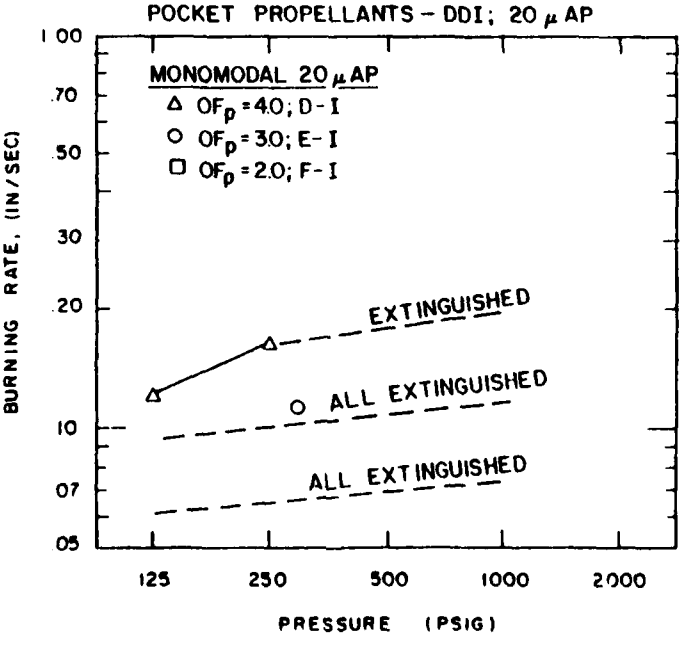

Figure 68. Pocket Propellant Ballistics

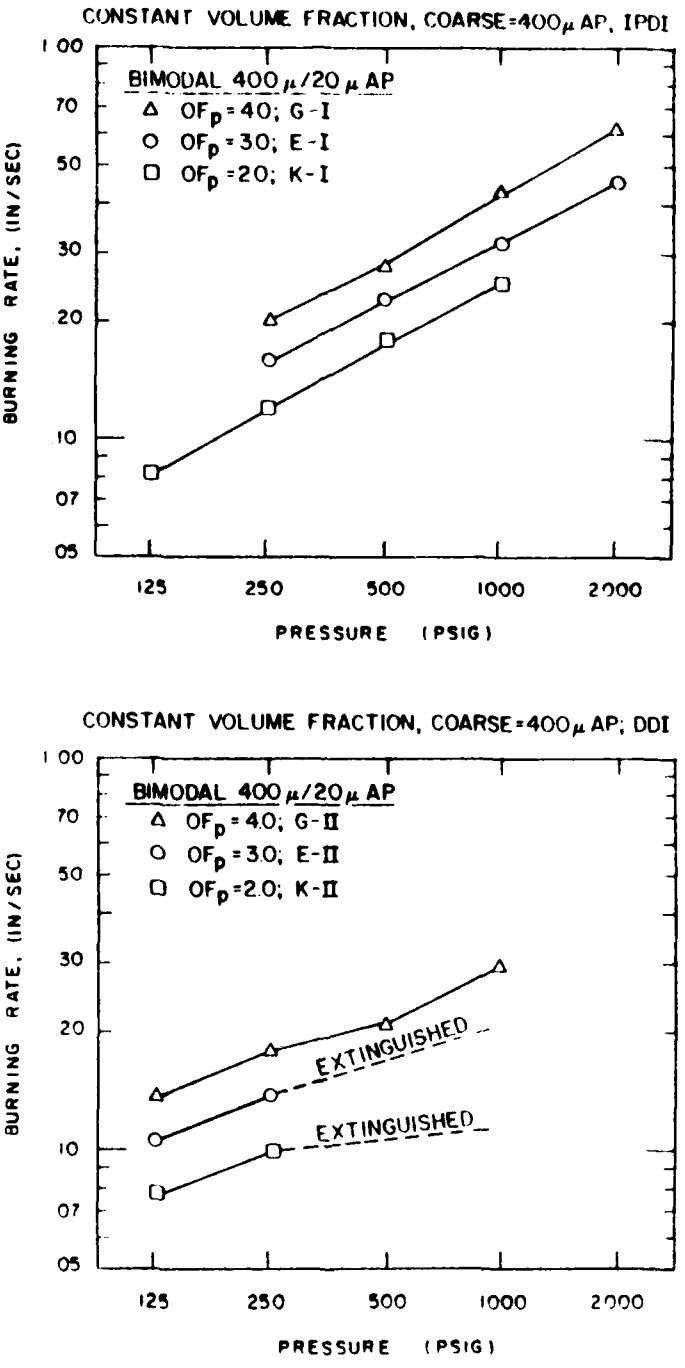

Figure 69. Constant Volume Fraction, 400μ AP, Ballistics

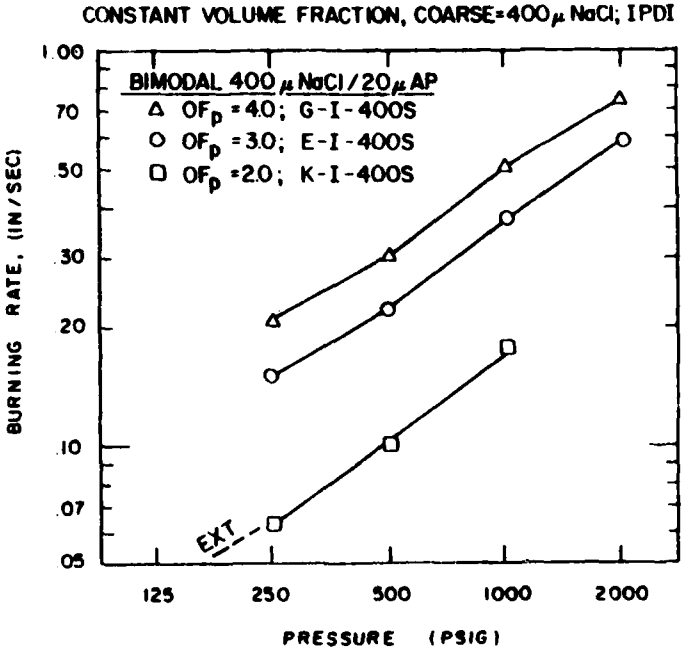

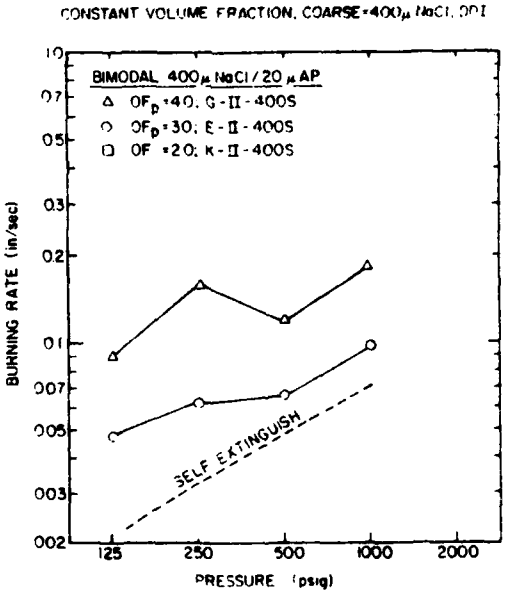

Figure 70. Constant Volume Fraction, 400μ NaCl, Ballistics

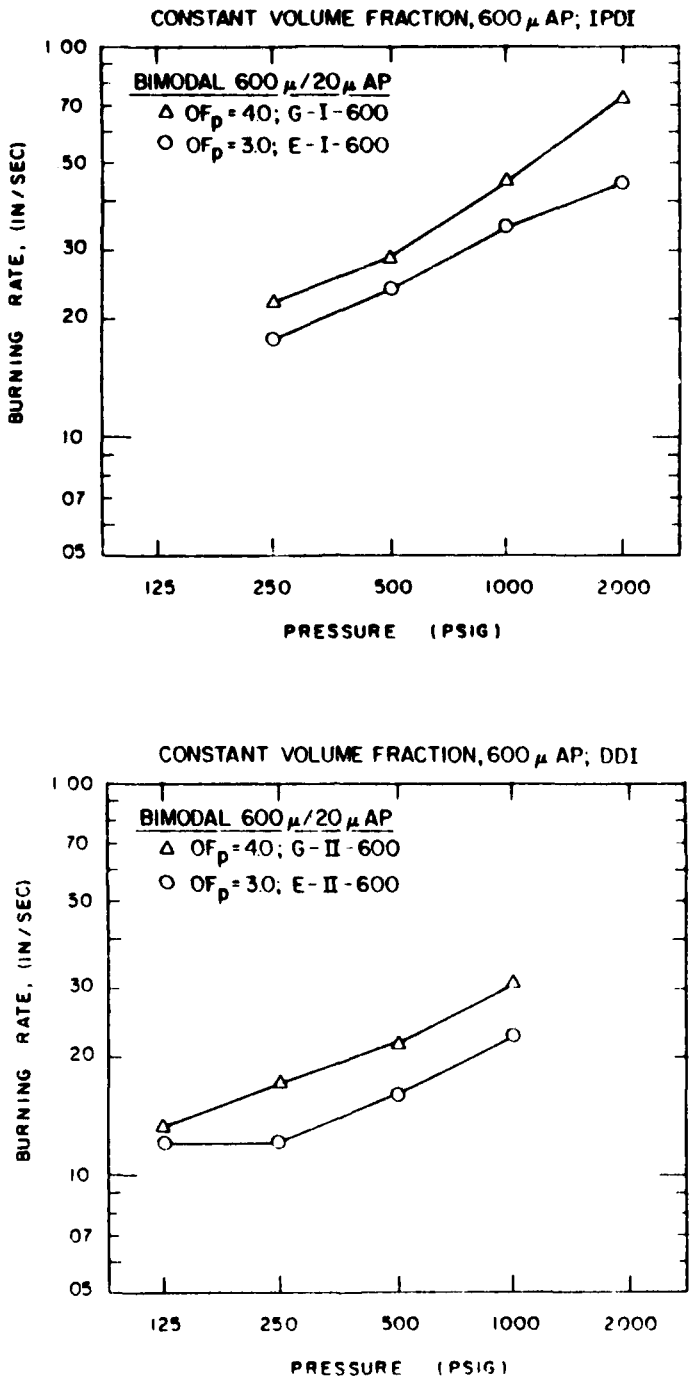

Figure 71. Constant Volume Fraction, 600μ AP, Ballistics

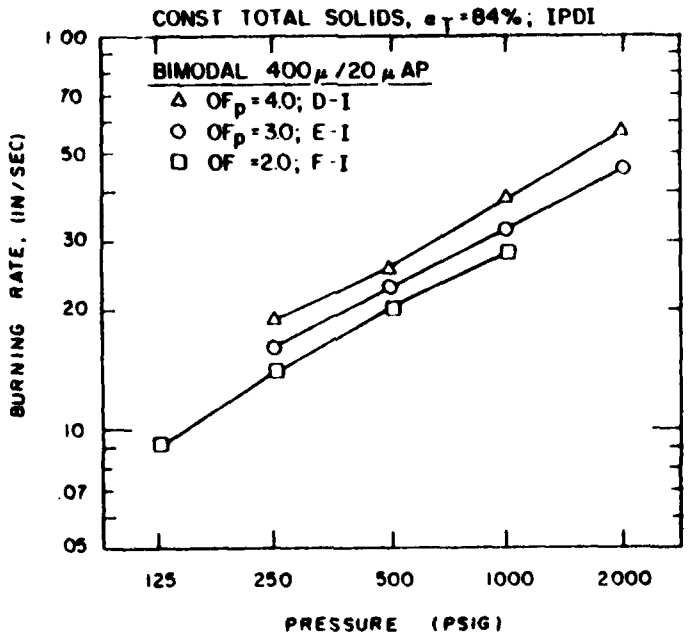

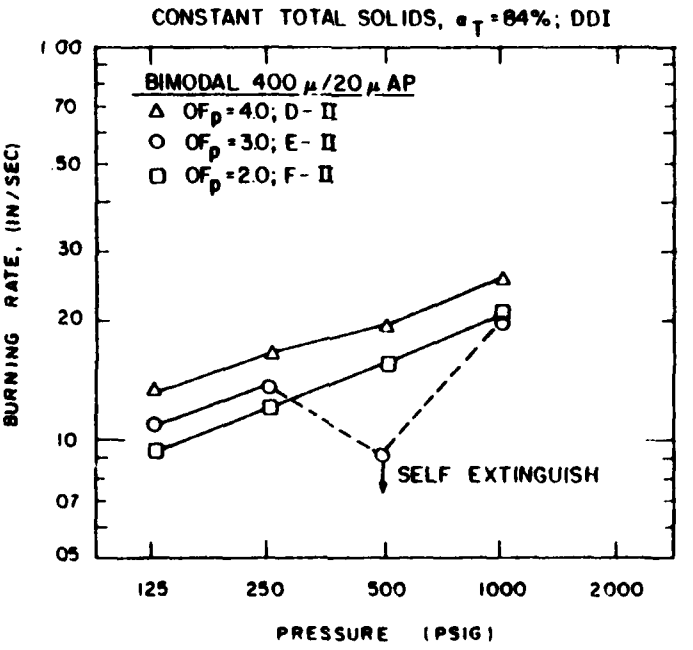

Figure 72. 84% Total Solids Ballistics

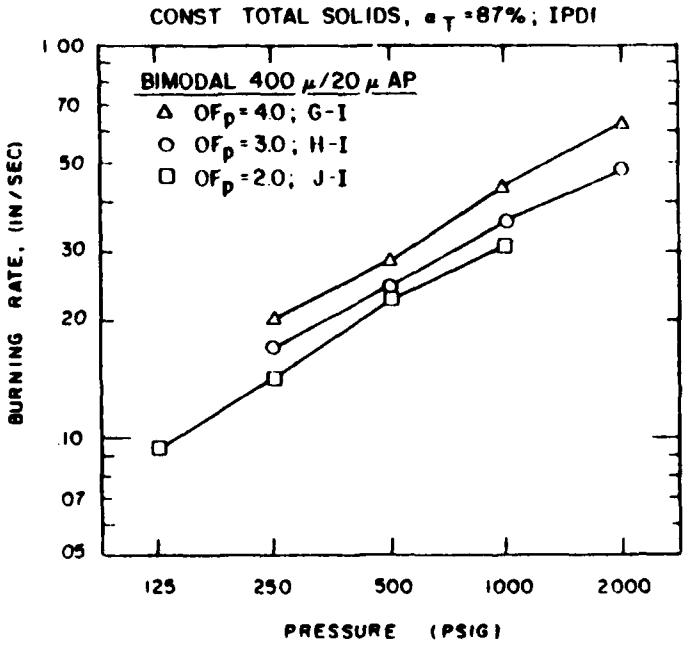

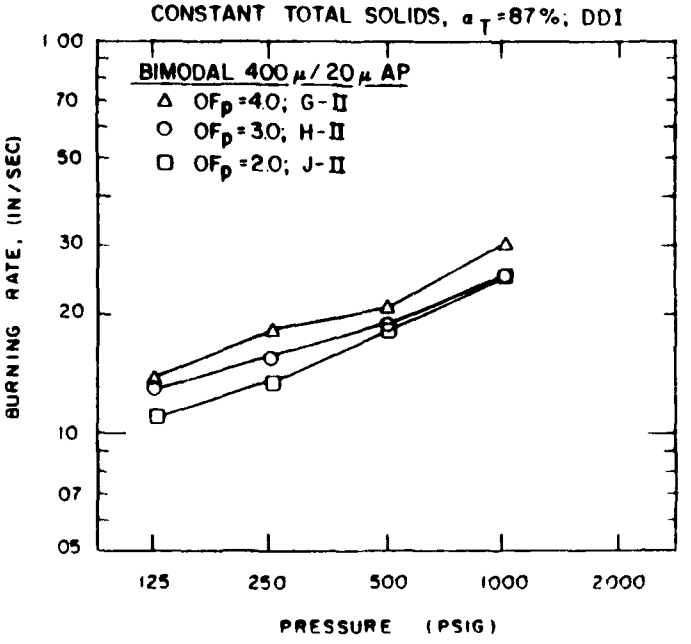

Figure 73. 87% Total Solids Ballistics

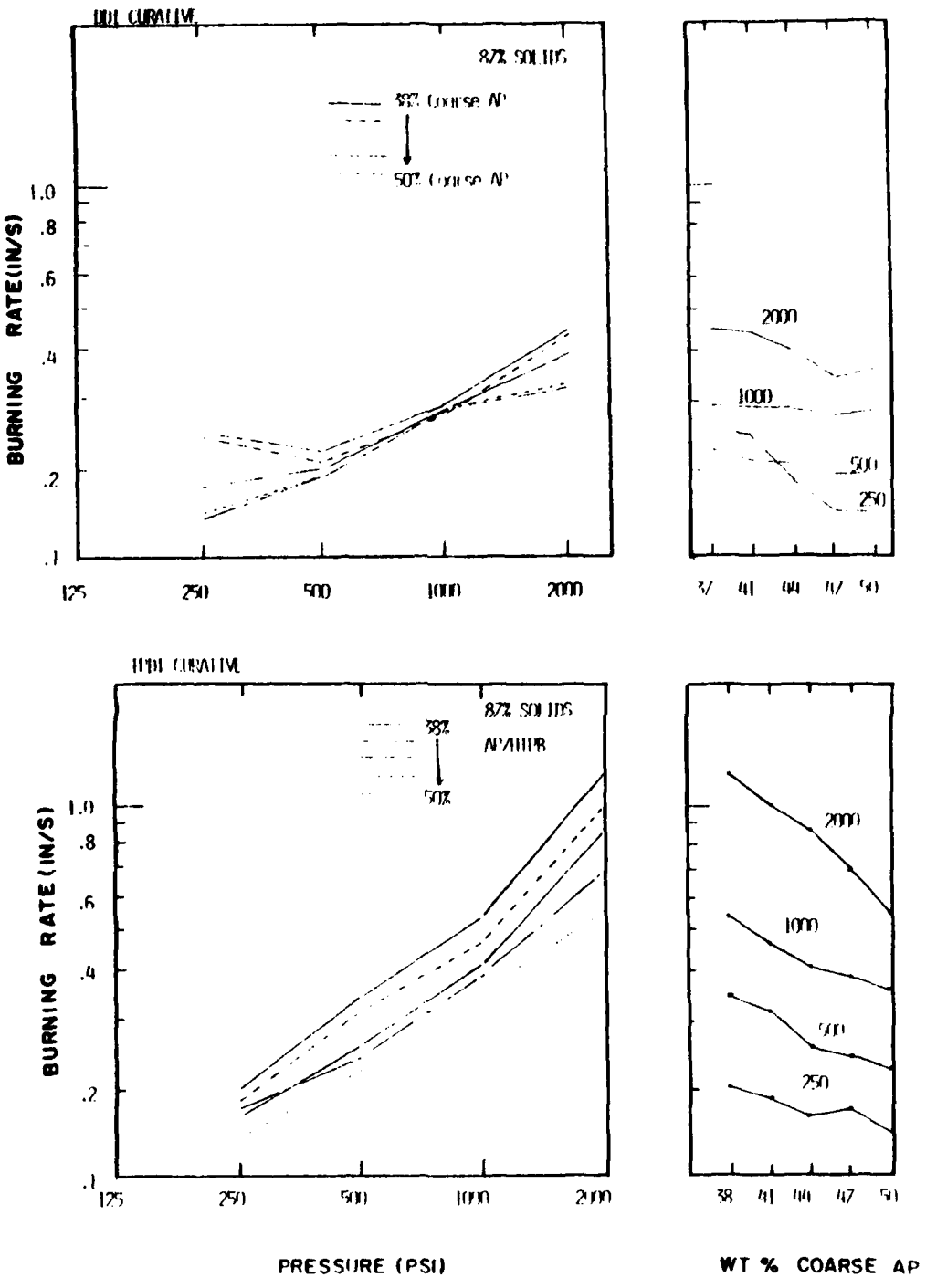

Figure 74. Trimodal Application Propellant Ballistics

Table 25

Motion Picture Results-Pocket Propellants, 1000psi,IPDI

OBSERVATION	$OF_p = 4.0$ A-I	$OF_p = 3.0$ B-I	$OF_p = 2.0$ C-I
$\dot{r}_{1000}$ (in/sec)	.34	.22	EXT.
flame cover	total	total	--
smoke	little	some	--
surface roughness	+–50μ	±100μ	--
binder flow	little 25%	much* 60%	--
coarse particles	--	--	--
comments		*100–200μ thick 200–600μ wide beads of binder	--

Table 26

Motion Picture Results-Constant Volume Fraction, 400 μ AP, 1000 psi, IPDI

OBSERVATION	$OF_p = 4.0$ G-I	$OF_p = 3.0$ E-I	$OF_p = 2.0$ K-I
$\dot{r}_{1000}$ (in/sec)	.44	.26	.21
flame cover	total	total	total
smoke	little	little	little
surface roughness	±100μ	±100μ	±100μ
binder flow	10%	40%	40%
coarse particles	not ejected	not ejected	not ejected
comments			

Table 27

Motion Picture Results-Constant Volume Fraction, 400 μ NACl, 1000 psi, IPDI

OBSERVATION	$OF_p = 4.0$ G-I-400S	$OF_p = 3.0$ E-I-400S	$OF_p = 2.0$ K-I-400S
$\dot{r}_{1000}$ (in/sec)	.52	.26	.15
flame cover	total	total	partial
smoke	some	some	much, black**
surface roughness	±350μ	±250	±200
binder flow	?	?	?
coarse particles	ejected*	ejected	few ejected
comments	*salt protudes above burning surface before ejecting		**flame sporadic over surface

Table 28

Motion Picture Results-Constant Volume Fraction, 600 μ AP, 1000 psi, IPDI

OBSERVATION	$OF_p = 4.0$ GI-600	$OF_p = 3.0$ EI-600
$\dot{r}_{1000}$ (in/sec)	.38	.34
flame cover	total	total
smoke	little	some black
surface roughness	±150–200	±150–200
binder flow	little 5%	40%
coarse particles	not ejected	not ejected

Table 29

Motion Picture Results-84% Solids Propellants, 1000 psi, IPDI

OBSERVATION	$OF_p = 4.0$ D-I	$OF_p = 3.0$ E-I	$OF_p = 2.0$ F-I
$\dot{r}_{1000}$ (in/sec)	.34	.26	.23
flame cover	total	total	total*
smoke	little	little	little
surface roughness	±100μ	±100μ	±100μ
binder flow	15%	40%	15%
coarse particles	not ejected	not ejected	not ejected
comments			*turbulent flame zone

Table 30

Motion Picture results-87% Solids Propellants, 1000 psi, IPDI

OBSERVATION	$OF_p = 4.0$ G-I	$OF_p = 3.0$ H-I	$OF_p = 2.0$ J-I
$\dot{r}_{1000}$ (in/sec)	.36	.27	.31
flame cover	total	total	total
smoke	little	little	very little
surface roughness	±100μ	±150μ	±300μ
binder flow	10%	20%	15%
coarse particles	not ejected	not ejected	not ejected
comments			

flow" is an estimate of the percentage of the surface edge covered with molten binder at an instant in time. The "coarse particles" category shows whether or not the coarse particle were ejected from the propellant surface during the combustion.

7.2. Ballistic Results - Overview

The ballistic results did reveal anomalous burning rates of the wide distribution propellants. First of all, using the Petite Ensemble Model as a basis of comparison shows that the burning rates are very much lower than predicted. Figure 75 shows a correlation between the predicted and measured burning rates. The model over-predicted the burning rates generally from 40 to 280 percent. A consistent difference can be seen between the IPDI binder and DDI binder propellants. The IPDI binder propellants had higher measured burning rates which resulted in better comparison with the model. While this comparison shows low burning rates and a distinction between the binders, an examination of the data was first made rule out a repetitive experimental error that would produce the low burning rates.

7.2.1. Accuracy of the Data Since the majority of the ballistic results are based on the acoustic emission detection system, it would be possible that the low rates could be caused by some error here. This can be quickly addressed by comparing the acoustic emission results with burning rates determined with another technique. A comparison of the acoustic emission burning rates with the burning rates derived from the motion pictures shows that the rates determined in the motion pictures are even lower than the acoustic emission results. So the acoustic emission measurements are probably not too low.

Since the samples were taken from distributed locations in the casting, the effect of casting flow possibly biasing the burning rates is ruled out. The results for the

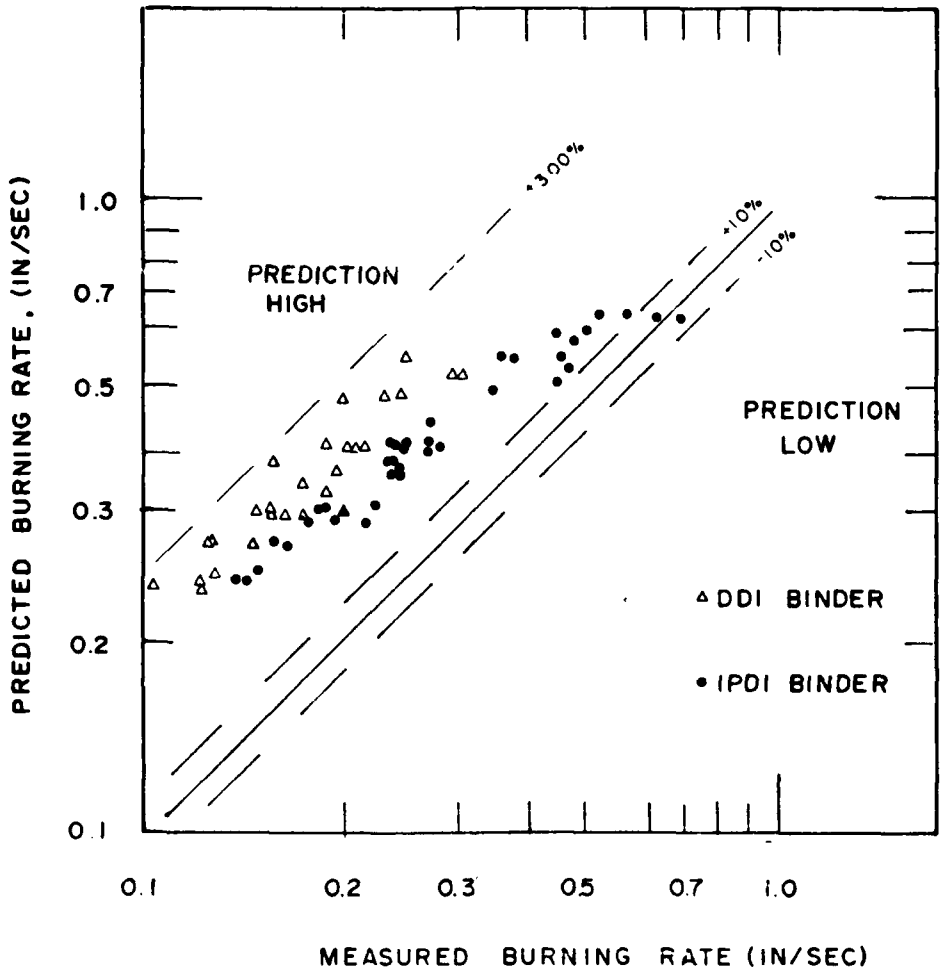

Figure 75. Comparison Between PEM Predictions and Experimental Burning Rates

monomodal and bimodal burning rate surveys show that the standard deviation of the propellant rates were generally only 1-4 percent of the average burning rates. The trimodal burning rate survey did show some significant casting flow effects with a generally suppressed burning rate in the middle of the carton. However, the 20-30 percent variation in rates across the casting cannot account for the 240% difference in the predicted and measured values.

Comparing the results from this study with results of similar propellants from other investigations was done as a final check of the burning rate accuracy. The trimodal propellants formulations were duplicated from a program by Miller [66]. Figure 76 shows a comparison of the experimentally measured burning rate at 1000 psi as a function of coarse oxidizer concentration. These results for the trimodal application propellants show that the current results agree with the past measurements within 0 to 40 percent, and differences here are most probably a result of variations in the oxidizer lots used to formulate the propellants. Figure 77 shows a comparison between a monomodal propellant from this study and an identical formulation investigated by Matson [67] showing close agreement between the burning rate results.

It is therefore concluded, that the burning of these series of propellants is greatly suppressed by a combustion mechanism not accounted for in the current burning rate model. An analysis of the data to propose mechanisms is discussed later.

7.2.2. Intermittent Combustion Intermittent combustion of the type noted in previous results was not detected either with high-speed photography or the Laser Position Detector. Several films of the trimodal propellants were analyzed and no burn period-rest period phenomena were observed. Similar measurements on the bimodal propellants shows occasional rest periods or times when the surface showed little regression, but in general the burning was in a more continuous fashion. Camera

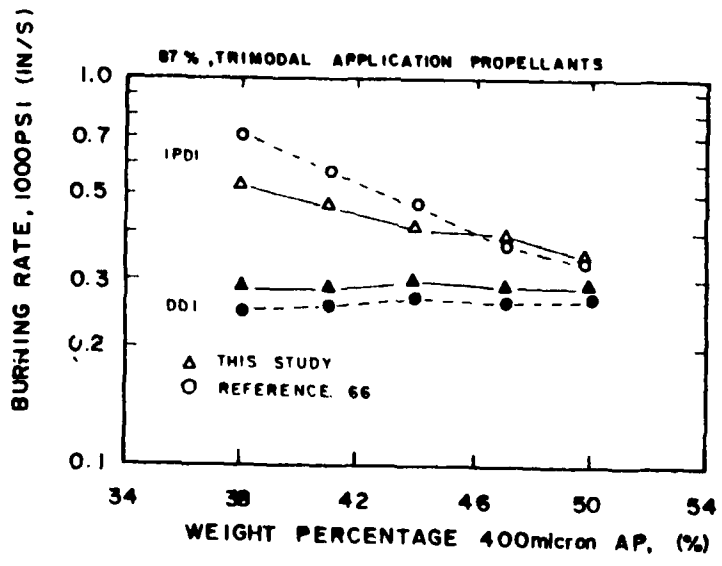

Figure 76. Comparison of Trimodal Propellant Burning Rates

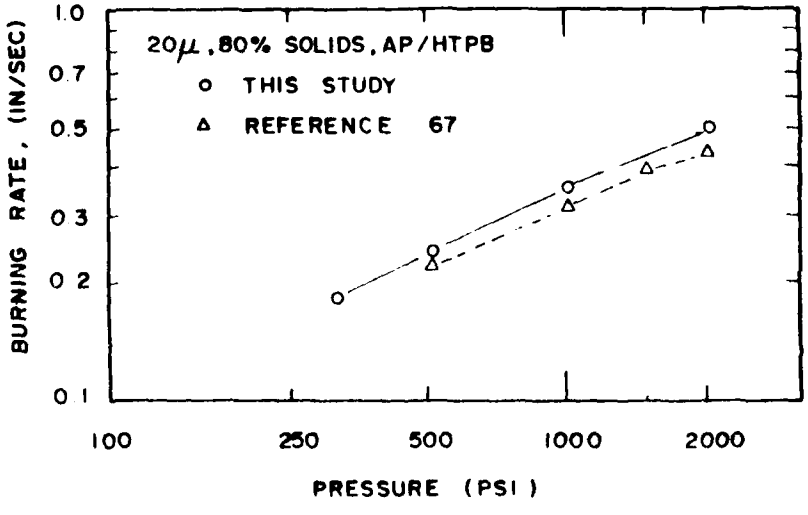

Figure 77. Comparison of Monomodal Propellant Burning Rates

vibrations, although corrected to a certain extent, made this measurement difficult.

7.2.3. Propellant Extinguishment Propellant strands would sometimes extinguish during a burn and more often fail to ignite. The tendency to extinguish followed the solids loading of the pocket propellant, with lower solids producing more frequent extinguishment. The DDI curative increased the probability of extinguishment.

Another factor that promoted extinguishment was the propellants ambient environment. The DDI cured propellants that burned in the acoustic emission tests failed to sustain combustion in the window bomb. Evidently the nitrogen purge flow combined with a smaller sample size produces the extinction.

7.2.4. Outline of Discussion In the view of the general characteristics of the ballistic measurements, the discussion will be based on the effect of propellant composition on the burning rates. Measurements of the local, intermittent burning were not attempted for systematic formulation studies since preliminary measurements and motion picture results did not reveal the intermittent burning for the bimodal formulations.

The majority of the discussion will be limited to the pocket propellants and the IPDI cured constant volume fraction propellants. General comments are made on the constant total solids and the application propellants.

7.3. Pocket Propellant Ballistics-Discussion

The pocket propellants simulate the combustion of the fine-AP/binder matrix that exists in bimodal, wide distribution propellants, without any of the influences of the coarse oxidizer particles. That is, they isolate the fine-AP/binder matrix from the additional oxidizing species that could be provided by the coarse particles and the geometric obstructions produced by the lower burning rates of the coarse particles.

Thus, the burning rates of the pocket propellants serve as a baseline for determining the extent of chemical and physical interactions produced by adding the coarse material.

7.3.1. Effect of Solids Level - IPDI The burning rate results for the pocket propellants show that lowering the solids level lowers the burning rate to the point of extinction. A general reduction of the burning rate is expected from the reduced adiabatic flame temperature as the total solids level is lowered. Propellants A-I and B-I (OF_p 4.0 and 3.0 respectively) burn over the entire pressure range investigated while the OF_p of 2.0 propellant, C-I, can only sustain combustion at 250 psi. Thus, there is a point between an O/F ratio of 3.0 and 2.0 that the propellant will self-extinguish.

The self-extinguishment can be explained in terms of the packing statistics of the oxidizer particles. As an oxidizer particle burns, the primary flame heats the adjacent binder. The resulting binder pyrolysis products then react with the oxidizer decomposition products sustaining the primary flame. However, as the oxidizer particle burns out, there are no oxidizing species to sustain the primary flame leaving no direct energy source to sustain the surface temperature of the binder. This causes the pyrolysis of the binder to slow and possibly stop leaving a layer of binder on the propellant surface that must be removed for the combustion to continue. For the lower solids propellants, the interparticle distance is much larger decreasing the number density of oxidizer particles exposed on the surface and increasing the thickness of binder that must be penetrated to encounter the next particle.

Burning through the interparticle binder is a non-linear function of the penetration thickness. Strahle [12] proposed an expression for the time to burn through the interparticle binder is

$$t_b = \frac{k\Delta_i}{\bar{r}} \exp\left[\frac{\Delta_i r_b}{\alpha_{THERM}}\right] \quad (49)$$

This expression says that the binder burnthrough time increases exponentially with increasing interparticle distances and decrease, Δ_i, with increasing average propellant burning rate. Thus the extinction could be caused by the inability of the low temperature flame to uncover sufficient oxidizer to sustain the combustion.

The motion picture results support the proposition that unburnt binder remains on the surface of the propellant even in the pocket propellant formulations that did burn. Shortly after the strand ignited, small beads could be easily seen forming along the edge of the burning surface. The beads were a black liquid and generally 100 to 200 microns in thickness. Since the front of the sample was uncoated, it is assumed this material is molten binder. The motion pictures also indicated an increase in the amount of liquid binder flow as the solids level is lowered. The fraction of the front edge covered by the liquid binder increased from 25 to 60 percent when the solids level is lowered from 4.0 to 3.0. If the characteristics of the binder allow a liquid phase rather than a solid phase as the local surface cools, then this unburned binder could accumulate and flow on the surface. The observed covering of the front edge, while not an absolute indication of the condition of the burning surface, does show the tendency of the fuel-rich pocket propellants to produce local, binder covered areas on the burning surface.

Figure 78 shows the effect of the proposed mechanism. Figure 78a shows the percent of the surface covered with molten binder as a function of OF_p. Assuming there is a certain critical level of covering above which the surface is extinguished, the propellant should extinguish between an oxidizer-to-fuel ratio of 3.0 to 2.0. This is the case as shown in Figure 78b. In this graph the measured burning rate divided by the predicted burning rate at 1000 psi is plotted as a function of OF_p. The results imply that

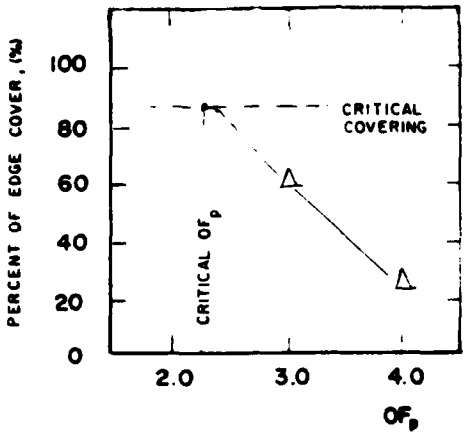

(a) Effect of OF_p on Binder Covering

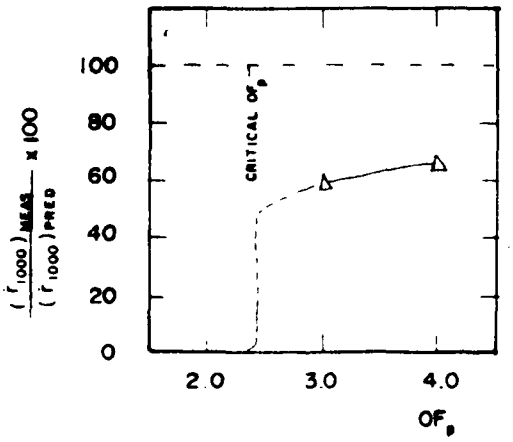

(b) Effect of OF_p on Burning Rate

Figure 78. Proposed Influence of Binder Cover

the unburnt binder could be the mechanism that causes the suppression of the burning rate observed when compared to the theory.

7.3.2. Effect of Binder Ingredients The DDI cured pocket propellants generally extinguished over the pressure ranges investigated. The effect of curing agent is not predicted in the model because binder is given a subordinate role in the combustion processes being constrained to deflagrate at a fixed ratio based on the oxidizer burning rate. The suppressing effect of the DDI first of all shows that near surface or subsurface reactions are influenced by the binder ingredients. It also shows some independence of the binder pyrolysis from the oxidizer deflagration.

Comparing the ballistic results of this research with those from other programs shows a significant influence of the binder ingredients on the low-solids, pocket propellant burning rate. The implication is that the properties of the binder have an active role in the rate-controlling combustion processes. The possibility of liquid layers and surface reactions could argument the anticipated burning rates even with the addition of non-reactive binder ingredients.

The binder curative and plasticizer used in this study contribute to the general burning rate suppression of the fuel-rich pocket propellants. Figure 79 shows a "comparison" of burning rate - pressure data for HTPB propellants that all contain 20μ AP oxidizer. The curves show the peculiar trend that the burning rate decreases for increased total solids level. The suppression of the rate however is produced by variations in the binder ingredients. The top two curves represent monomodal, 20μ propellants with different binder curatives. The fastest burning propellant comes from results by Schmidt (68) and contains an MDI curative with no plasticizer. The 73% solids propellant comes from results by King (69) and the binder contains an IPDI curative with no plasticizer. The bottom two curves show the results of this

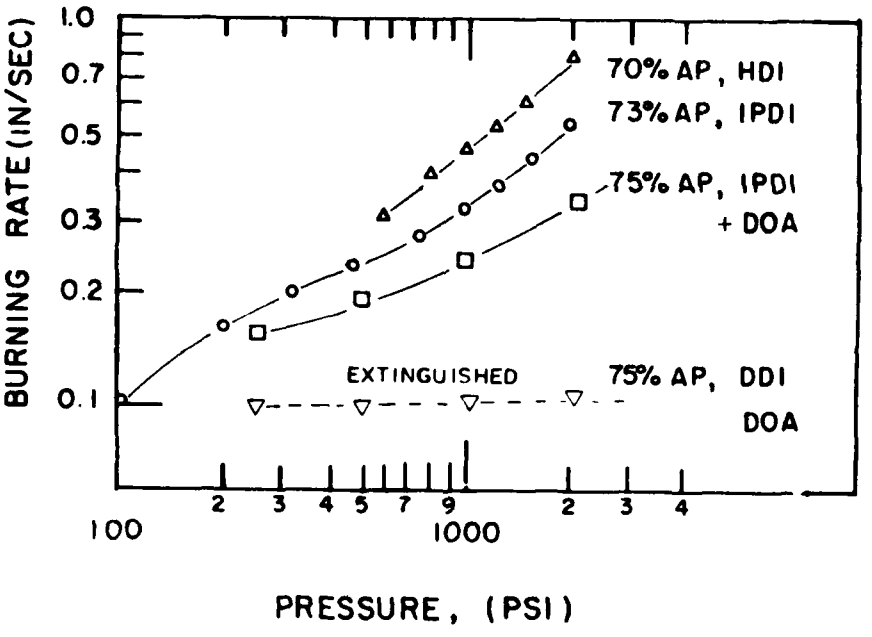

Figure 79. Effect of Binder Ingredients on Ballistics

investigation representing plasticized IPDI and DDI cured binders. It is evident from this comparison that addition of non-energetic ingredients in the binder could have a dominant influence on the combustion. Plasticizer seems to add additional rate suppression to the propellant.

The plasticizer is included in propellants mainly as a processing aid to insure complete mixing and ease of casting. It always maintains its liquid state even after the propellant is cured. Past studies by Schmidt (68) on fuel-rich pocket propellants having 9μ AP have shown that addition of plasticizer to the binder suppresses the burning rate and can even cause extinguishment in intermediate pressure regimes. The plasticizer does not change the adiabatic temperature of the combustion products since it is thermodynamically similar to the polymer binder. Therefore, it must influence combustion mechanisms near the propellant surface. The observation of liquid binder flow off the edge of the burning surface could be produced or enchanced by the plasticizer.

The difference in curative between IPDI and DDI can be explained based on the results of Miller (70). Differential Thermal Analysis and Differential Scanning Calorimetry studies have revealed that the binder decomposes in a three step process:

(1) depolymerization of the urethane linkages

(2) crosslinking through double bonds in the HTPB

(3) decomposition

The initial depolymerization of the IPDI cured binders was found to be much more energetic. Further, results suggest that this energetic breakup produces reactive species that would immediately promote combustion. The DDI binder, in contrast, has a much less energetic initial depolymerization which does not produce reactive species.

7.3.3. Pocket Propellants-Conclusions

All of the results, past and present, show that the binder plays a dominant role in fuel-rich-pocket propellants. The addition of plasticizer and changing of curative reduce the burning rate of otherwise identical propellants. The results point to surface mechanisms which alter the combustion. Since the thermodynamic differences of the additives are minimal, the binder changes must influence surface mechanisms though a liquid melt layer, or a change in the surface temperature at which reactive species are released from the binder.

The dominance of the binder is also increased by the low-solids nature of the pocket propellants. This means that the binder decomposition reaction cannot be constrained to follow the deflagration of the oxidizer. It can act more independently, which would explain the over-prediction of the burning rate with the PEM.

The ballistics results for the current research show the IPDI and DDI cured binders with plasticizer causes greater burning rate suppression when compared to other

curative and plasticizer levels. Therefore it is concluded that the fuel-rich pocket propellants in this study have a greatly suppressed burning rate owing to the curative type and plasticizer used in the binder. The results of the motion picture studies suggest that a possible mechanism for the general suppression is liquid binder flow on the surface of the propellant. Total solids level also has an influence by changing the flame temperatures and increasing the inter-particle distance between the AP particles in the solid phase.

Therefore, the pocket propellants have combustion mechanisms unique to their low-solids characteristics. While these experiments isolated the combustion mechanisms from interactions that would be present in the bimodal, analogue formulations, they reveal that the surplus of binder causes sensitivity to the binder ingredients and tendencies toward propellant extinction not predicted by the current model.

7.4. Constant Volume Fraction Ballistics-Discussion

The constant volume fraction propellant sets were formulated to determine the thermal effect of the coarse oxidizer on the burning rate of the propellants. Past studies had indicated that the coarse particles do not receive sufficient energy from the pocket propellant so they act mainly as a thermal heat sink and just lower the average burning rate of the propellant. The addition of both reactive (AP) and non-reactive (RDX) coarse material has shown this effect.

The results for this study, however, show an increase in the burning rate of the propellant when the coarse material is added to the pocket propellant. Figures 80, 81, and 82 show ballistic results for adding either 400μ AP or 400μ NaCl to pocket propellants having an OF_p of 4.0, 3.0, and 2.0.

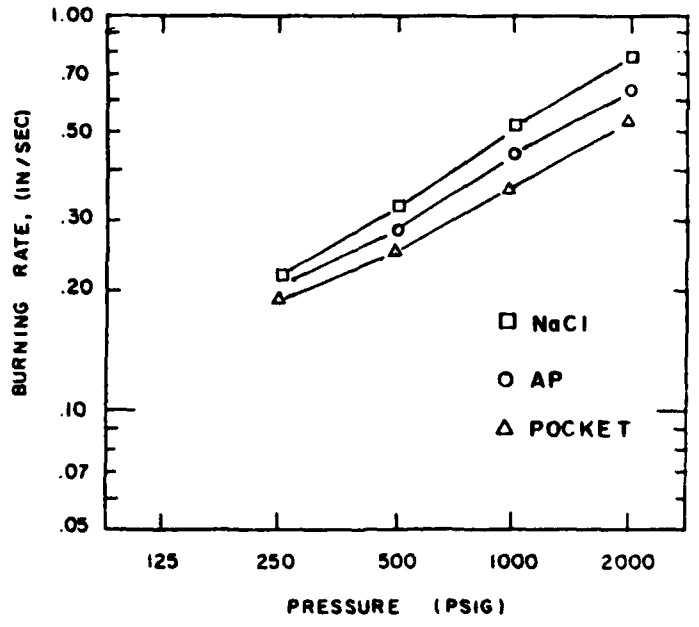

Figure 80. Effect of Adding 400μ AP or NaCl to Propellant A-I, $OF_p = 4.0$, IPDI Curative

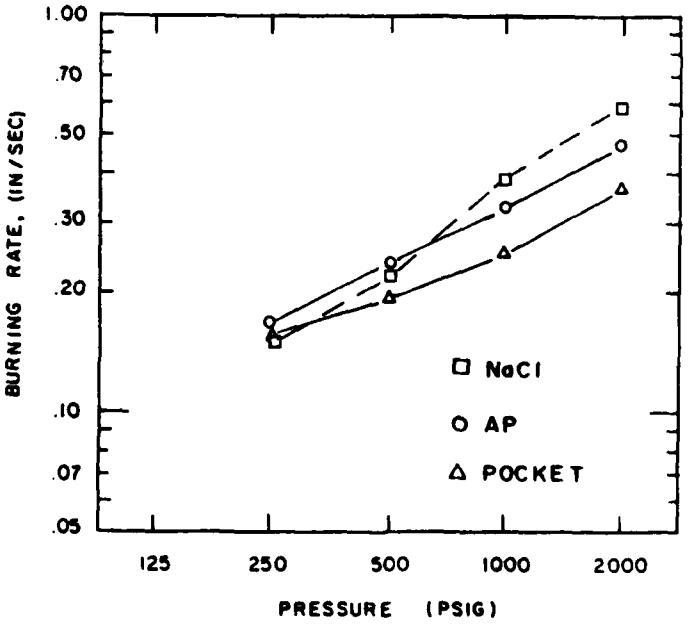

Figure 81. Effect of Adding 400μ AP of NaCl to Propellant B-1, $OF_p = 3.0$, IPDI Curative

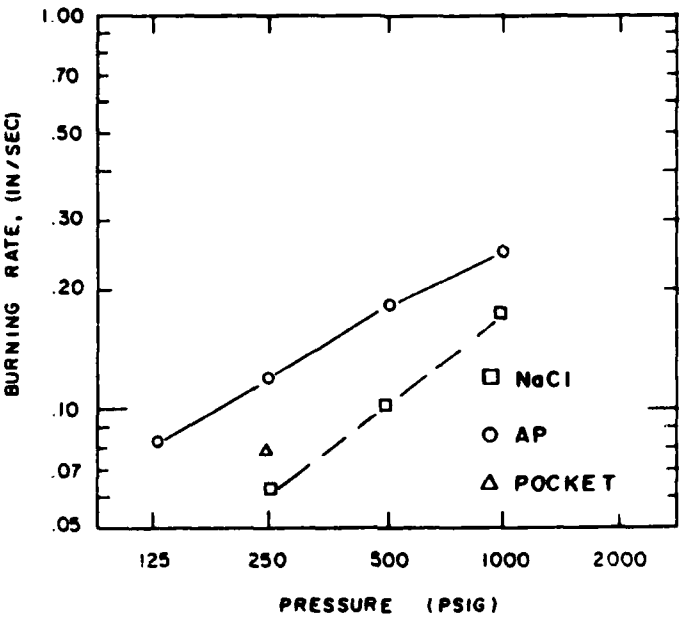

Figure 82. Effect of Adding 400μ AP of NaCl to Propellant C-I, $OF_p = 2.0$, IPDI Curative

7.4.1. Constant Volume Fraction, 400 micron AP Propellants The results in Figures 80, 81,and 82 show that adding coarse AP to a constant volume fraction loading of 0.305 increases the pocket propellant burning rate in all cases. Figures 80 and 81 show a significant increase above 250psi while Figure 82 shows that pocket propellant C-I only burns at 250psi.

Conventional theory would predict two effects of adding the coarse AP. First, an increase in the burning rate of the fine AP particles resulting from the increased total solids level. The oxidizer-to-fuel ratio of the pocket propellant is raised to the that of the total propellant.

Second, a decrease in the average propellant burning rate resulting from the relatively slow burning of the coarse AP particles. The net effect of these two components is only a slight increase in the predicted propellant burning rate. This increase becomes greater as the OF_p is lowered.

These results show, however, that the rate increases significantly with the addition of coarse AP at all OF_p levels. This can be explained in terms of the pocket propellant. It has been concluded, that these pocket propellants burn well below predicted values because of the dominance of binder mechanisms. Adding the coarse material could defeat these mechanisms by (1) establishing a primary flame around the edge of the coarse particle that would supply energy to burn through the inter-particle binder in the pocket propellant; (2) moving the rate controlling combustion mechanisms to the coarse particles.

The photographic results at 1000 psi showed that none of the coarse particles were ejected from the surface before they burned. The films did show more covering of the front edge of the sample with molten binder as the OF_p was reduced indicating that binder flow, characteristic of the pocket propellants, exists in the bimodal analogue propellants.

7.4.2. Constant Volume Fraction, 400 micron NaCl Propellants Figures 80, 81, and 82 also show the analogue propellants containing 400μ salt added at a constant volume fraction to the pocket propellants. Salt was used as a non-reactive surrogate for the coarse AP.

These results are most unusual because they show a dramatic increase in the pocket propellant burning rate with the addition of salt to the pocket propellant. (Even the DDI cured pocket propellants which generally extinguished, burn when the coarse

NaCl was added.) It was anticipated that the salt would lower the burning rate by absorbing energy from the gas and solid phase. Instead, the burning rate increased, and in some instances, it increased more than the propellants having the coarse AP material.

The burning rate cannot be increased by a increase in the local oxidizer-to-fuel level, because the decomposition products of the salt are non-reactive. This means that some surface phenomena must be changed by the addition of the salt. The motion pictures, taken at 1000psi, showed the coarse salt particles emerging from the propellant and being ejected front the surface for the propellants having OF_p of 4.0 and 3.0. The figures show that in this case the propellant burns faster than the pocket propellant and faster than the corresponding propellant with coarse AP. The salt particles were not ejected at 1000psi for the OF_p of 2.0 propellant resulting in a burning rate higher than the pocket propellant rate but lower than the corresponding AP propellant.

The salt could enhance the burning rate by three possible mechanisms: (1) Ejection from the surface exposing greater areas of fine AP; (2) Allowing the burning front to burn in the crack between the salt particle and the pocket propellant; or (3) A catalytic effect. The first mechanism was noted in the films. The particle ejection could decrease the suppressing mechanisms caused by the excess binder on the surface of the the pocket propellant. This would expose fine AP particles that would regain the control of the combustion processes. The second mechanism is included because some rate enhancement was noticed around the coarse AP particles as the propellant burned. That is the the burning front would move into the area around the coarse AP particle below the mean burning surface height. In this case the combustion products of the propellant could heat the salt. The third mechanism is the catalytic effect. This would be the lowering of the activation energy of the the binder or the oxidizer. This

possibility is unlikely since catalysts tend to be materials having good conductivity making then ion donors.

7.4.3. Conclusions-Constant Volume Fraction Propellants The addition of coarse material (reactive or non-reactive) to these wide distribution propellants does not reduce the burning rate as expected. What it does is reduce the rate-suppressing mechanisms related to the excess binder in the pocket propellant. The addition of coarse AP could supply additional heat to the surface necessary to burn through the interparticle binder. This comes from the primary flame around the circumference of the coarse particle. The most likely mechanism for the rate enhancement of the propellants with salt added is the exposure of fine AP particles on the surface by the ejection of the salt.

7.5. Constant Total Solids Ballistics - Discussion

Figures 83, 84, and 85 show the ballistic results for the constant total solids, bimodal analogue propellants compared to their respective pocket propellants. These results show the same trends as the constant volume fraction propellants. In all cases, adding the coarse AP increased the burning rate of the pocket propellant. The 87% propellants burned faster that the 84% propellants except for the OF_p of 2.0 analogue propellant at lower pressures. The discussion applied to the constant volume AP analogue propellants applies to these propellants as well.

These results are in contrast to previous results by Miller [71] who added coarse material to 12μ, pocket propellants. These pocket propellants had a much higher burning rate than did the pocket propellants in this study. Addition of the coarse material lowered the propellant burning rate. The current study evidently has greatly suppressed pocket propellant burning rates because of the DOA plasticizer and the IPDI curative.

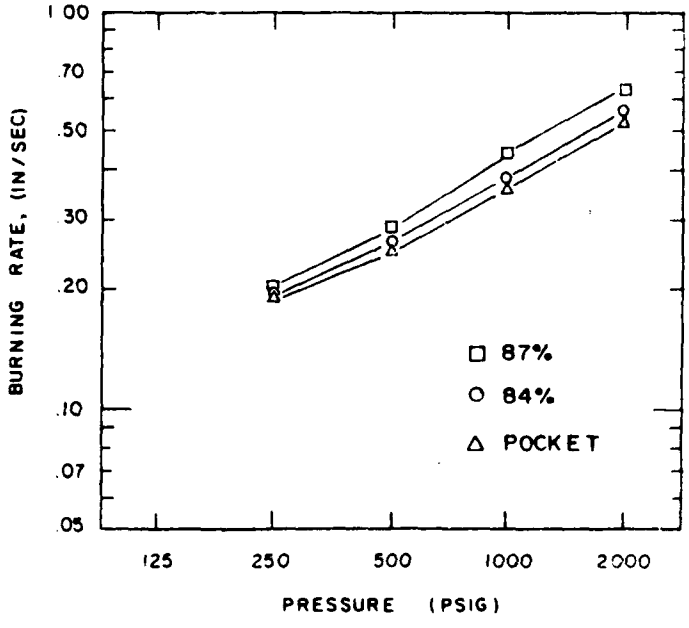

Figure 83. Constant Total Solids Propellants, $OF_p = 4.0$, IPDI

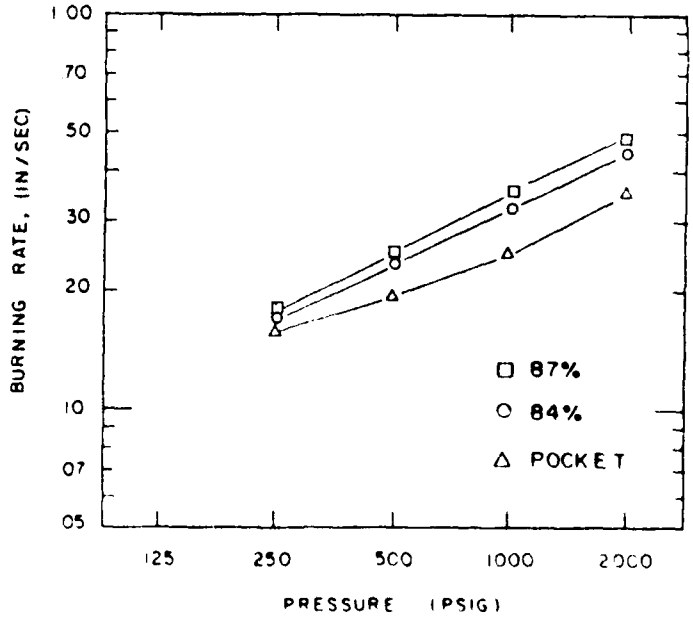

Figure 84. Constant Total Solids Propellants, $OF_p = 3.0$, IPDI

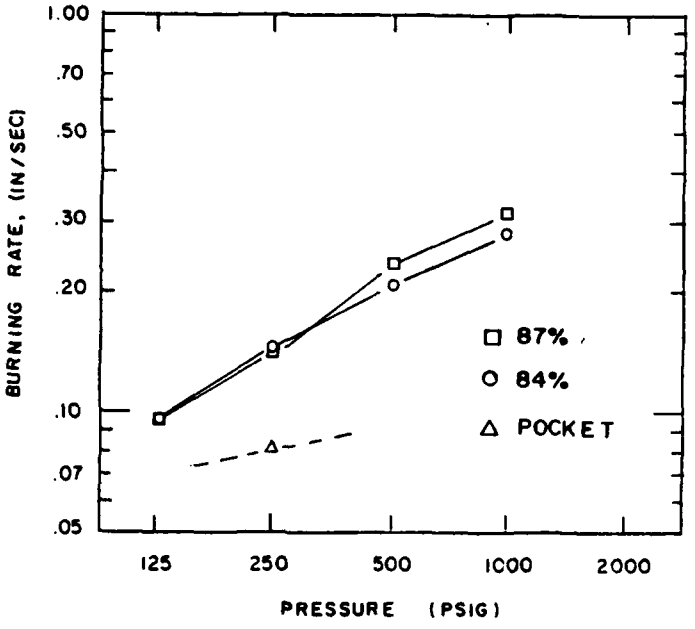

Figure 85. Constant Total Solids Propellants, $OF_p = 2.0$, IPDI

7.6. Propellant Surface Characteristics

The results of the average ballistic properties have shown that the low burning rate of the pocket propellants cannot be completely explained by the chemical partitioning of the oxidizing species. The addition of reactive (AP) or non-reactive (NaCl) increases the pocket propellant burning rate. This indicates that the rate suppressing mechanisms are not in the gas phase but rather are related to a surface mechanism.

Observations of the high-speed motion pictures showed that beads of molten binder flow off of the burning surface during the propellant combustion. Figure 86 shows a correlation between the estimated binder covering measured from the films, and the ratio of the measured to the predicted burning rate. This graph suggests that the rate suppressing mechanism unaccounted for in the model is strongly related to the flow of molten liquid binder on the propellant surface.

The average ballistic results also indicate that the binder curative changes the the propellant burning rate for propellants having identical oxidizer particle size distributions. Figure 87 shows the Series-I (IPDI) and Series-II (DDI) measured burning rate correlation. These results show that the DDI curative produces a 30 to 70 percent drop in the propellant burning rate. Since the thermodynamic properties of the two binders are very similar, these results also suggest that some surface mechanisms could be the cause of the binder curative effect.

Therefore, the structure of the burning surface was examined in detail. Propellants G-I and G-II, whose ballistic properties are plotted in Figure 88, were selected for the experiments. Propellant samples were extinguished at pressure levels from 250 to 1000 psig. Details of the experiments and the sample preparation were presented in Section

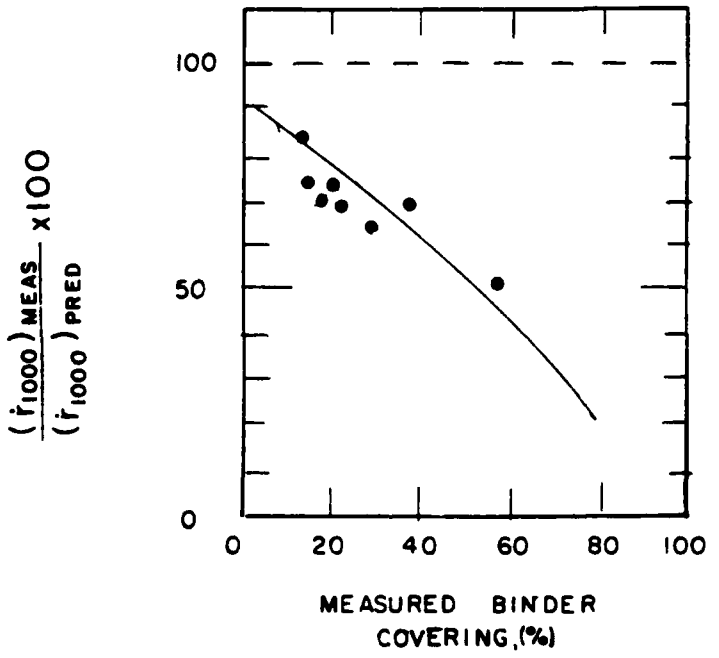

Figure 86. Binder Covering Correlation

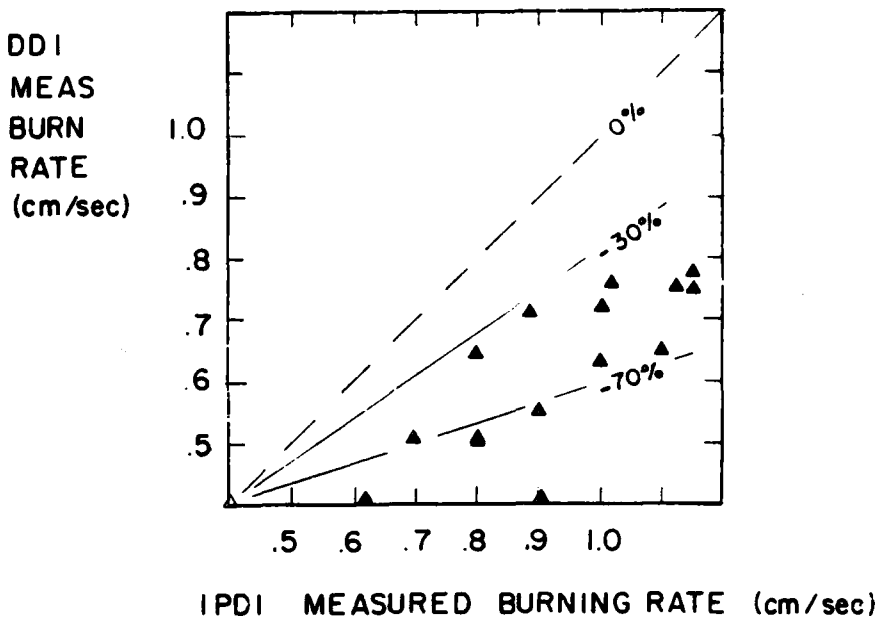

Figure 87. Comparison of Series-I and Series-II Burning Rates

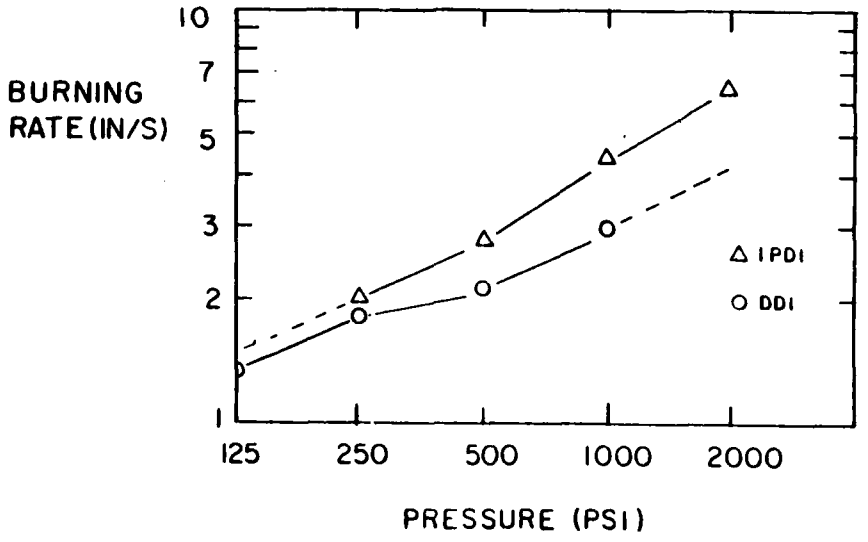

Figure 88. Ballistic Results, G-I and G-II

6.5. The extinguished surfaces were examined under a scanning electron microscope (SEM).

7.7. Propellant Surface Characteristics-Results

Figures 89 to 104 show example SEM photographs of the extinguished surfaces of propellants G-I and G-II. All samples extinguished by the depressurization of the the combustion vessel and did not self extinguish. The bursting mylar depressurization technique worked well, however, the sample holder had to be modified to prevent the sample from leaving the combustion bomb during depressurization.

7.7.1. Surface Structure - 1000 psig Figures 89 and 90 show low-magnification pictures of the extinguished surface for propellants G-I and G-II respectively. The 400μ coarse AP particles can easily be seen exposed on the surface for both propellants. Around the circumference of most of the coarse particles, an thin, dark band can be seen. The darker portions of the picture are interpreted as areas of binder because of the properties of the materials. The exposed portions of the coarse particles has a flat, porous texture for the IPDI propellant while the DDI propellant produces a concave shape on the exposed surface. The fine-AP/binder matrix between the coarse particles shows a different surface texture for these two cases. The IPDI propellant shows 50 to 80 micron craters in the pocket propellant separated by thin ridges. The pocket propellant of the DDI propellant has a rougher texture in which the outline of the fine particles is much more evident.

Figures 91 and 92 show close-up photographs of individual coarse oxidizer particles for the 1000psig experiments. Figure 91 shows a coarse particle for the G-I, IPDI propellant. The dark areas around the outer edge indicate that binder partially covers the outer edge and some areas on the central region. The exposed surface

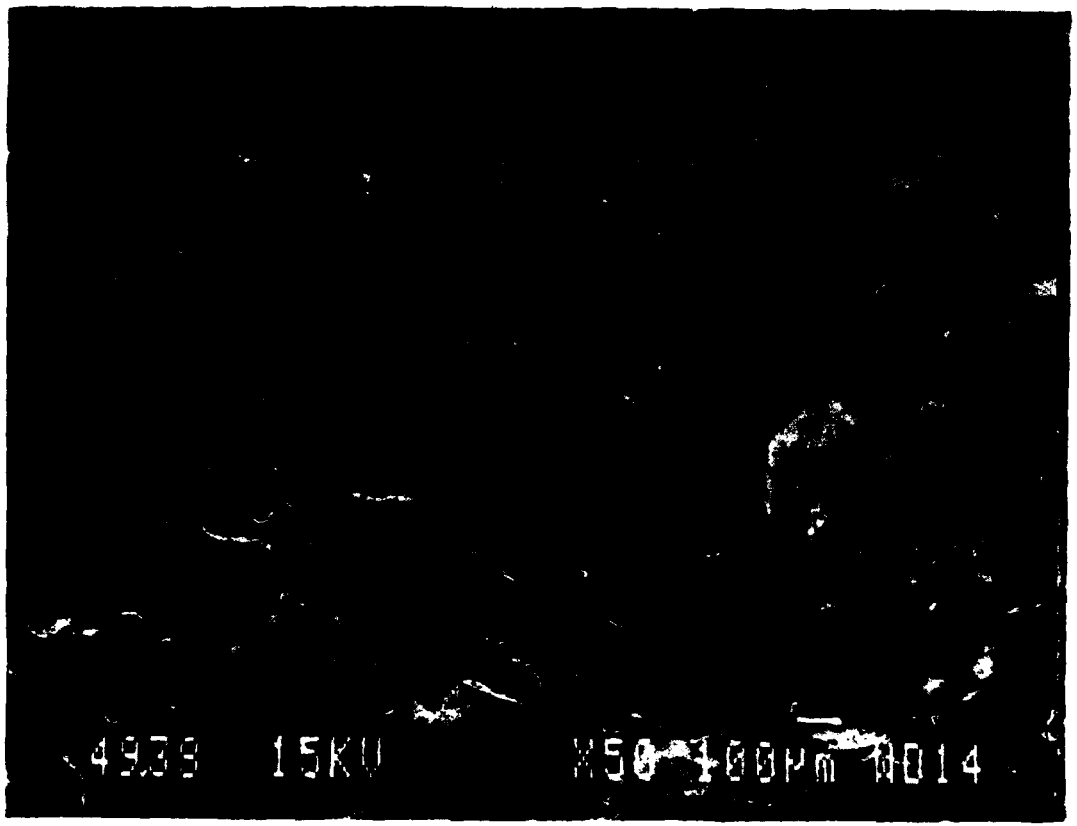

Figure 89. Extinguished Surface, G-I, 1000psig

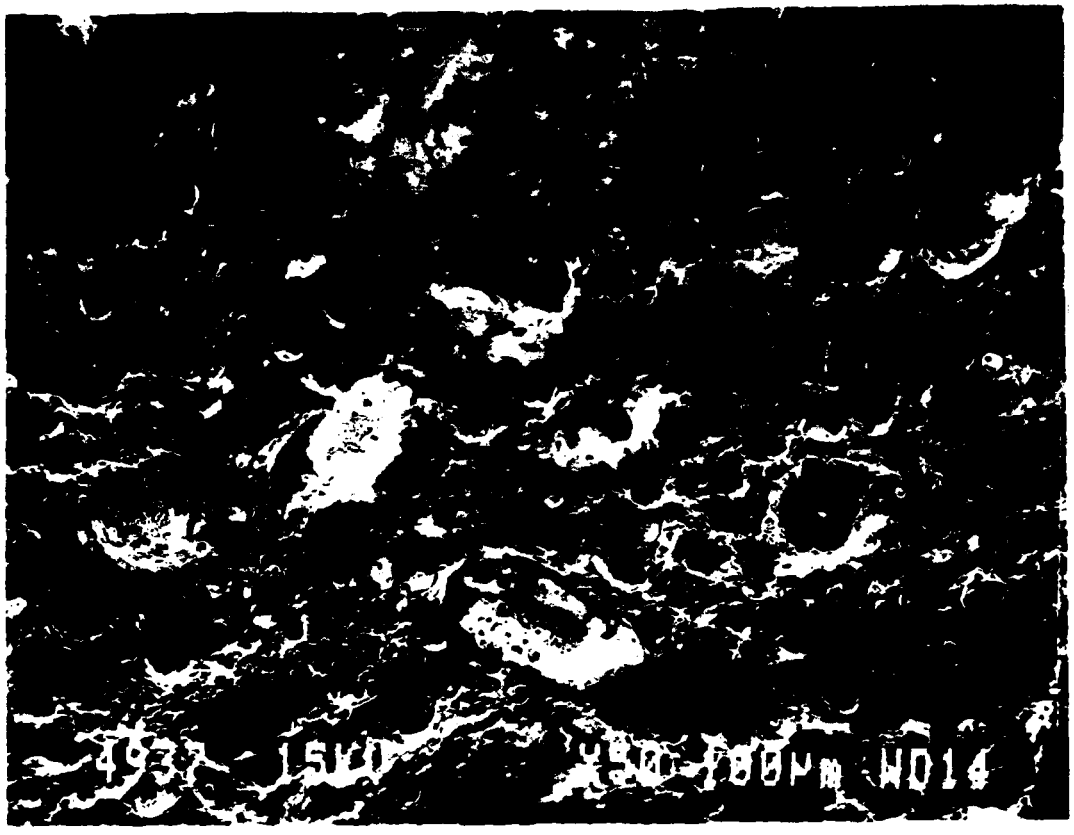

Figure 90. Extinguished Surface, G-II, 1000psig

Figure 91. Coarse AP Particle, G-I, 1000psig

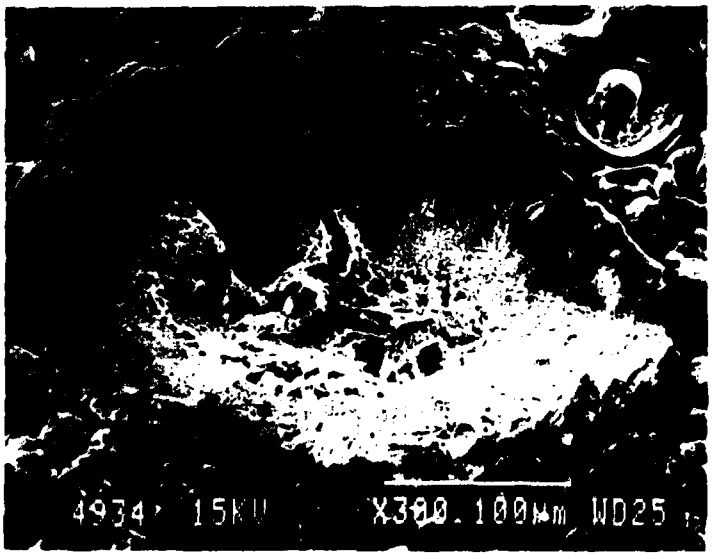

Figure 92. Coarse AP Particle, G-II, 1000psig

appears flat and rough in texture. Some areas show patches of surface holes in the AP that are 5 to 20 micron in diameter and are often accompanied by larger surface cracks. The area in the pocket propellant around the coarse particle shows light colored patches where where the fine oxidizer has apparently been exposed. Much of the fine oxidizer is still covered with binder. The exposed portions of the fine particle show similar characteristics to the exposed portion of the coarse AP particle.

Figure 92 shows a close-up photograph of a coarse AP particle for the DDI propellant extinguished while burning at 1000psig. The surface of this particle is depressed in the middle. The exposed central region is much more porous than the previous case indicating perhaps a liquid layer of AP. The outer circumference is covered with a dark band indicating a thin layer of binder cover.

7.7.2. Surface Structure - 250psig Figures 93 to 99 show example SEM photographs of propellant surfaces extinguished while burning at 250psig. Figures 93 and 94 show low-magnification pictures of propellants G-I and G-II respectively. These pictures show more binder covering over the coarse particles than the previous 1000psig cases.

Figures 95, 96, and 97 show details of a coarse particle for the IPDI propellant. Figure 95 shows that only a portion of the center and some areas around the edge of this 400μ AP particle are exposed. The rest of the surface is covered with a thin layer of binder. Figures 96 and 97 show enlargements of the central AP region and the binder-covered region.

Figures 98 and 99 show similar results for the DDI-cured propellant. Figure 98 shows a two distinct regions on the surface of the coarse AP: an uncovered region; and a covered region. The cross-sectional diameter of this particle is approximately 400μ while the central, exposed region is only about 150μ in diameter. The central region

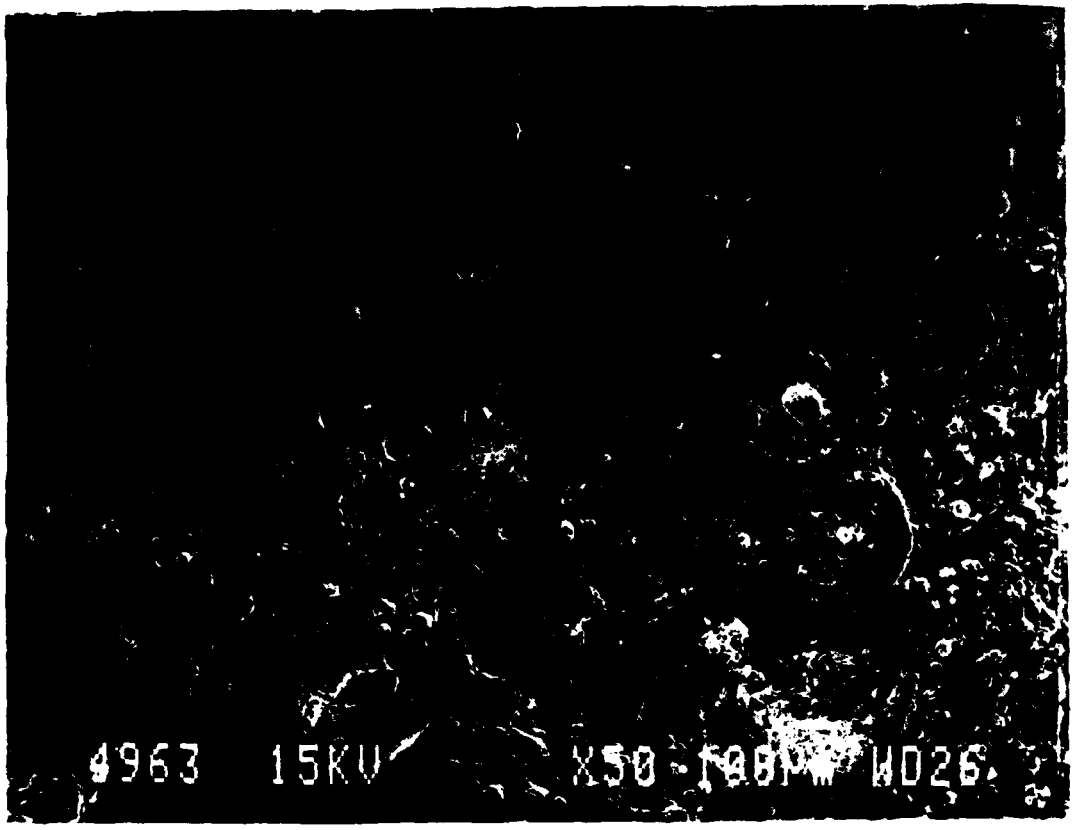

Figure 93. Extinguished Surface, G-I, 250psig

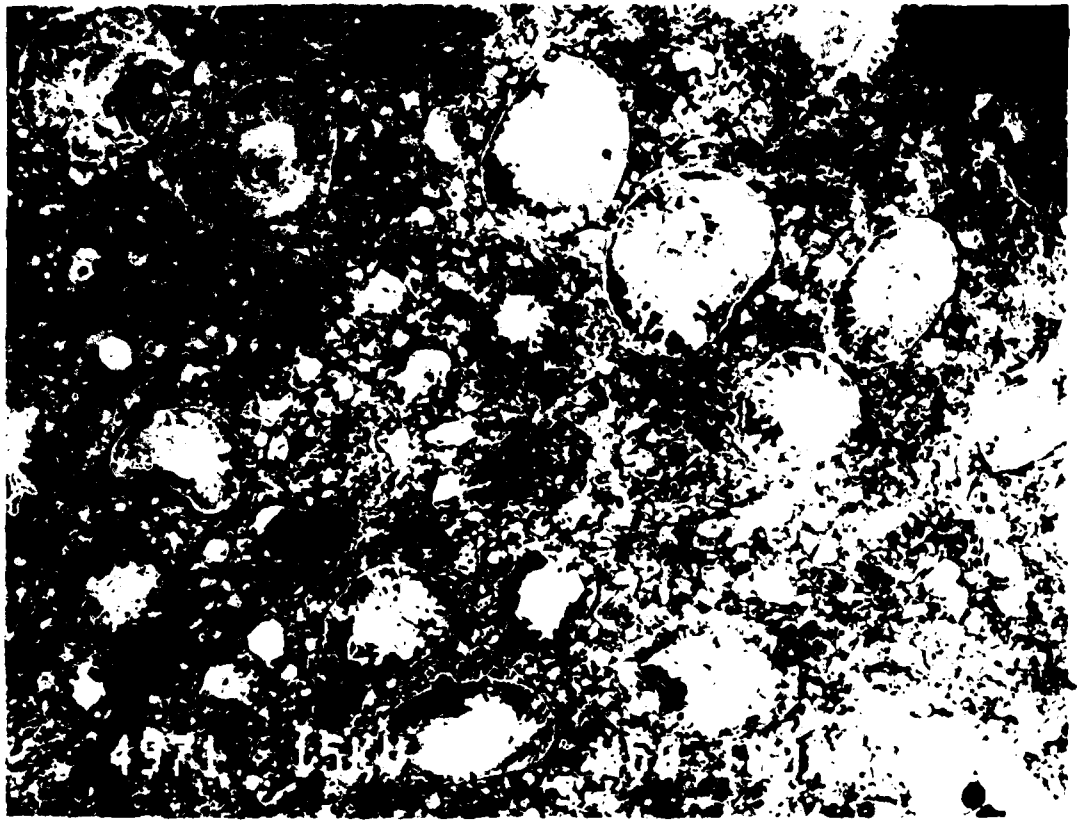

Figure 94. Extinguished Surface, G-II, 250psig

Figure 95. Coarse AP Particle, G-I, 250psig

Figure 96. Enlargement of Central AP Region of Figure 95.

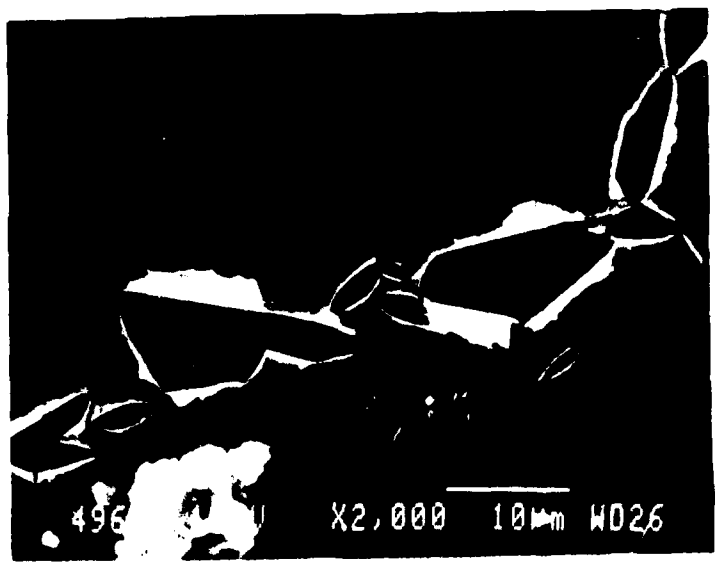

Figure 97. Enlargement of Binder-Covered Region of Figure 95

Figure 98. Coarse AP Particle, G-II, 250psig

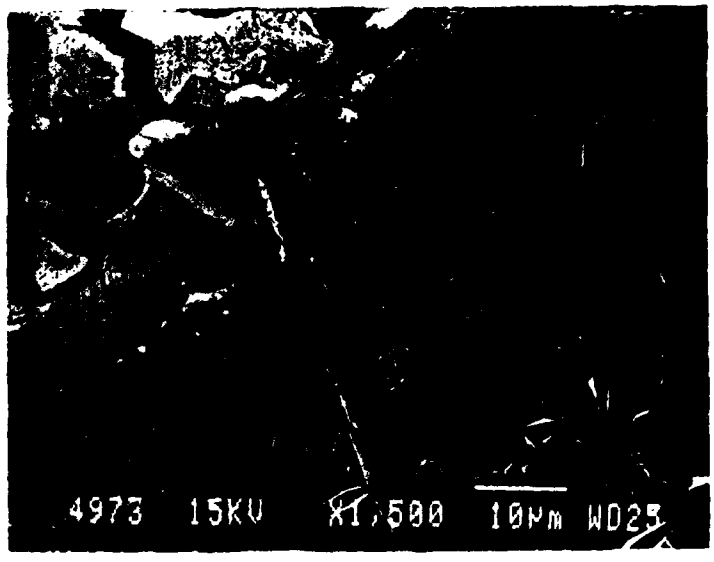

Figure 99. Enlargement of Figure 98

Figure 98. Coarse AP Particle, G-II, 250psig

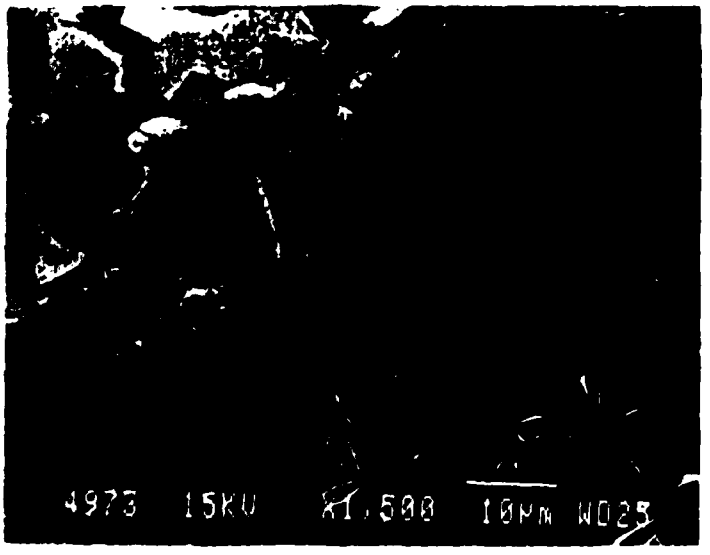

Figure 99. Enlargement of Figure 98

has an a rough texture protruding above the adjacent binder-covered surface. Figure 99 shows a enlargement of the interface between the central and binder-covered area of the surface. The outer edge of the particle has a light shade indicating that a rim of AP is exposed around the circumference. If a cross-section of this particle were viewed, the surface of the AP might look like a straw hat with a raised center, a binder-filled brim, and an outer edge that flares back up.

7.7.3. Partially Burnt Coarse Particles Figure 100 shows a coarse particle in which the outer binder-covered region is still intact and the central region has burned away. The hole is roughly 150μ in diameter. The remaining portion of the particle shows both covered and uncovered surfaces. Figure 101 shows a similar case except only a crescent shaped portion of the 400μ particle remains. The fine particles beneath this area are exposed to varying degrees.

7.7.4. Water-Soaked Samples Figures 102, 103, and 104 show results of samples that were soaked in water to remove the AP after extinguishment. Figure 102 shows the rim of the binder that surrounded a coarse AP particle. Figure 103 shows an enlargement of the edge revealing evidence of a liquid layer. Figure 104 shows a thin binder covering that remains after the AP beneath has been removed.

7.8. Effect of Binder Covering the Oxidizer-Discussion

Exposed AP particles have two types of of surface characteristics; An area where a layer of binder covers the surface (Region-I) and an area where the surface of the oxidizer is exposed (Region-II). Figure 105 shows the a sketch of an oxidizer particle with the two regions labeled. Regions-I and II were observed for both IPDI and DDI curred propellants. The Region-I covering is easily seen on the coarse particles at pressure levels from 250 to 1000 psig and generally appears as a washer-shaped layer

Figure 100. Coarse AP Particle Burnthrough, G-II, 500psig

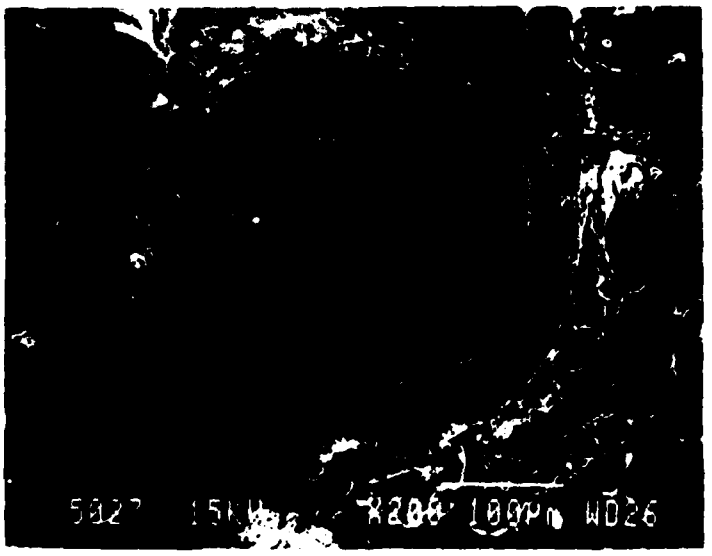

Figure 101. Coarse AP Particle Burnthrough, G-II, 1000psig

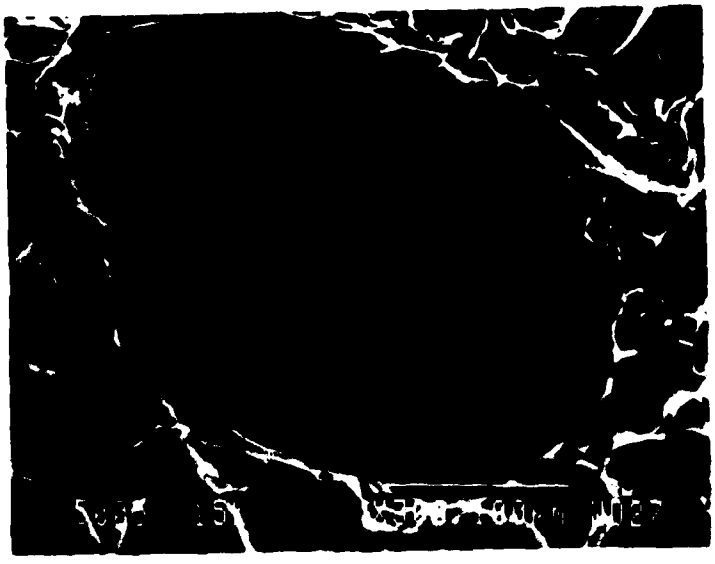

Figure 102. Water-Soaked Surface, G-I, 250 psig

Figure 103. Enlargement of Figure 102

Figure 104. Water-Soaked Surface, G-I, 500psig

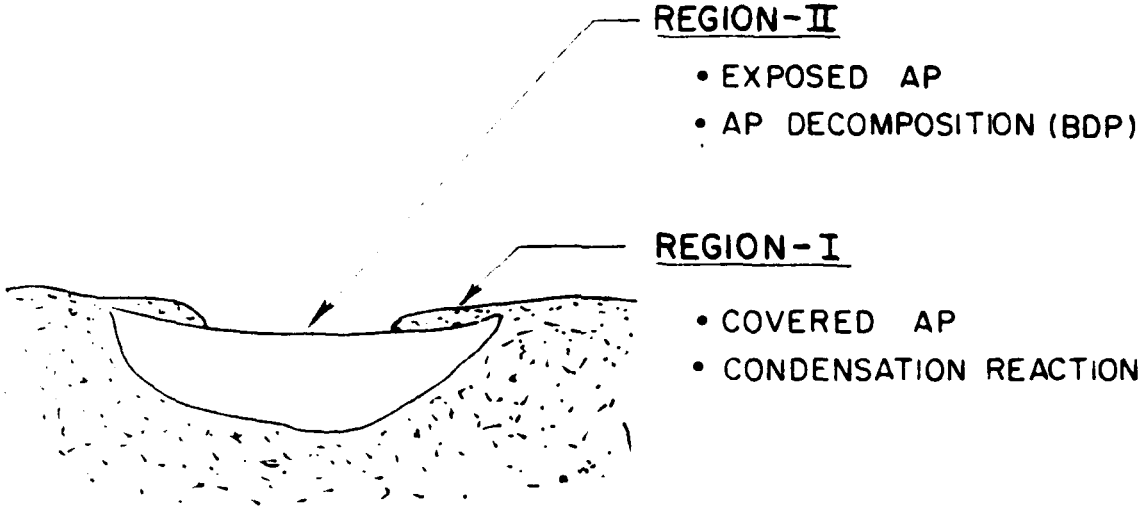

Figure 105. Two Regions of the Exposed AP Surface

covering the particle surface from its outer edge to an opening over the center. The covering has a smooth texture suggesting a liquid state could have existed over the AP. In Region-II (uncovered part) the oxidizer surface is exposed and has a porous texture.

Obviously, when the surface of an AP particle is covered with the molten binder, some phenomena are different from uncovered burning. In the case of an AP particle covered with binder, the gaseous AP decomposition products cannot rapidly enter the flame zone because they have to first pass through the layer of molten binder. This increases the concentration of AP decomposition products above the covered AP surface to higher mole fractions than occur above the uncovered AP surface. This increases the reverse condensation reaction of the products back to the liquid state. This reverse reaction has to be considered even at low pressures.

The effect of the reverse reaction is a lowering of the burning rate of the covered portion of the oxidizer. Wengan [72] has developed a physiochemical model describing the mass flux of the AP particle covered with molten binder

$$\dot{m}_{ox_I} = \frac{A^I_{ox}}{1-G} \exp(-E_{ox}/RT^I_s) \left[1 - \frac{P \exp(\frac{q}{R^o T^I_s})}{B_1(1 + \frac{G}{1-G} \frac{W_{AP}}{W_G})} \right] \tag{52}$$

This expression modifies the Arrhenius decomposition expression to account for the burning rate reduction that occurs when the gaseous AP decomposition products must bubble through the molten binder covering. Calculations with this expression show that the burning rate of the covered portion of the particle is lower than the uncovered area. Further, the expression shows that increasing pressure levels further reduce the burning rate and could even result in local or total extinguishment of the propellant surface.

The expression for calculating the propellant burning rate is with this model is

$$\dot{m}_t = \frac{\gamma}{\alpha} \dot{m}_{ox_I} + \frac{1-\gamma}{\alpha} \dot{m}_{ox_{II}} (S_{ox}/S_o) \tag{51}$$

The first term is the total mass flux for Region-I while the second is for Region-II. The propellant burning rate then depends upon the fraction of the exposed oxidizer particles covered with molten binder γ -especially the fine particles. Greater covering fractions would further reduce the propellant burning rate. The value of the covered area fraction will depend upon the fluidity of the molten binder and the roughness of the burning surface.

Figure 106 shows the calculated effect of the binder covering on the propellant burning rate. The top curve corresponds to the case were γ is zero meaning that there is no liquid binder covering the oxidizer surface. This corresponds to the PEM calculations based on the traditional multiple flame model. The bottom curve represents the situation where the burning surface is completely covered with molten binder ($\gamma = 1.0$). This curve shows a dramatic decrease in the magnitude of the propellant burning rate. It also show a pressure-dependent reduction in the burning rate exponent. The intermediate curve shows a general condition where the oxidizer surface is partially covered.

The binder covering mechanism explains the the observed burning behavior of the wide distribution propellants. The SEM photographs showed a significant fraction of the oxidizer surface covered with binder. This explains the overprediction of the burning rate by the PEM. Furthermore, the covering fraction was qualitatively observed to be less at 1000 psig when compared to the 250 psig surfaces. Again, this correlated with the burning rate results because the measured and calculated values correlated much better at the higher pressures (higher burning rates in Figure 75).

The difference in binder covering caused by the curative change could not be quantitatively measure with the SEM photographs. It is possible that this could be a

$$\dot{m}_t = \frac{\gamma}{\alpha}\,\dot{m}_{ox_I} + \frac{1-\gamma}{\alpha}\,\dot{m}_{ox_{II}}(S_{ox}/S_o)$$

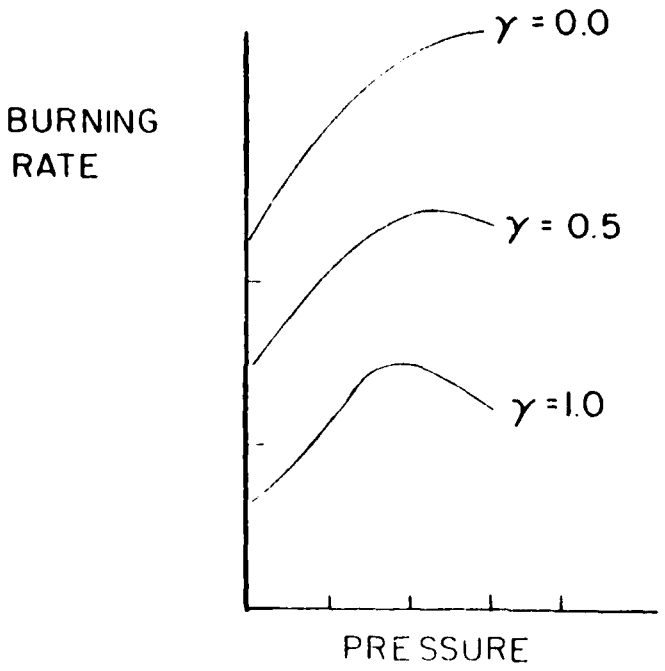

Figure 106. Predicted Effect of Molten Binder Covering

mechanism that contributes to the curative induced burning rate changes. The effect would come through the influence of the binder curative on the fluid properties of the molten binder.

The motion picture results suggest that the extent of the binder flow is related to the oxidizer-to-fuel ratio of the pocket propellant; both for the monomodal and the bimodal analogue formulations. Decreasing the oxidize-to-fuel ratio of the pocket propellant produces a marked increase in the observed binder flow.

To obtain a quantitative measurement of the extent of binder covering on the extinguished propellant surface, measurements should be made with an X-ray, photoelectron spectroscopy technique of Auger spectroscopy.

7.9. Combustion Mechanisms - Summary

This experimental research of wide distribution propellants has shown that the heterogeneity of the propellant ingredients produces several unique combustion mechanisms at the propellants surface.

7.9.1. Pocket Propellant Mechanisms First, since the pocket propellant is isolated from the coarse AP, it must deflagrate in fuel-rich conditions. This makes it very sensitive to the properties of the binder. The deflagration expressions for, the oxidizer and binder are generally assumed

$$\dot{m}_{ox} = A_{ox}\exp\left(\frac{-E_{ox}}{RT_{ox}}\right) \tag{52}$$

$$\dot{m}_{b} = A_{b}\exp\left(\frac{-E_{ox}}{RT_{b}}\right) \tag{53}$$

For the burning propellant, the equation of mass continuity can be written as

$$\dot{m}_t = \dot{m}_f(S_f/S_o) + \dot{m}_{ox}(S_{ox}/S_o) \quad (54)$$

On the right side of the equation, the first term represents the fuel mass flow and the second term represents the oxidizer mass flow. This equation can be simplified by requiring that the ratio of oxidizer and fuel consumed over a long period of time is equal to the oxidizer-to-fuel weight ratio of the propellant formulation. The expression for the average propellant mass flux then becomes

$$\dot{m}_t = (\dot{m}_{ox}/\alpha)(S_{ox}/S_o) = [\dot{m}_f/(1-\alpha)](S_f/S_o) \quad (55)$$

Generally, for higher solids propellants, the first expression in equation 54 has been used to calculate the burning rate of the propellant. This implies that the deflagration of the oxidizer is the dominant mechanism. However, for these fuel-rich pocket propellants, the second expression may be more applicable. That is, the combustion control shifts to the binder deflagration characteristics.

Results from this study, show that a combustion model assuming the dominance of the oxidizer, overpredicts the burning rate of the pocket propellants. Also, changing the binder ingredients has significant effects on the propellant burning rate. Both of these obse tions are consistent with the dominance of the binder deflagration.

7.9.2. Binder Flow Mechanism

The rate suppressing mechanism of wide distribution propellants is the presence of a liquid binder layer that covers the portion of the AP particle exposed at the burning surface. Results of this investigation have shown that a thin layer of liquid binder covers portions of the exposed AP surface even for formulations with high pocket propellant oxidizer-to-fuel ratios. Results from calculations accounting for the binder covering are consistent with the experimentally measured burning rate results.

The difference in the measured and predicted burning rate is related to the extent of the oxidizer surface covered with binder. The covering is enhanced by lowering the oxidizer-to-fuel ratio of the pocket propellant and for the two propellants investigated, the covering fraction increased at lower pressures. The binder flow may increase the burning in the central uncovered portion of the coarse AP by reducing the apparent diameter of the exposed AP (It burns more like an equivalent smaller-sized particle). So then, as the coarse fraction of a given propellant formulation is increased, the oxidizer-to-fuel ratio of the pocket propellant decreases. This produces a greater fraction of the burning surface that is covered with the liquid binder layer. This combustion mechanism explains the current discrepancy (see Figure 12) in model predictions and experimental results.

8.0 SUMMARY AND CONCLUSIONS

This experimental investigation of wide distribution propellants has focused on two major areas: (1) the development of an optical technique to continuously measure the local surface deflagration of a burning propellant strand, and; (2) combustion studies of wide distribution AP/HTPB propellants. The objective of the research was to establish a systematic data base to isolate combustion mechanisms unique to this type of propellant and provide a basis for combustion modeling.

8.1. Instrument Development

8.1.1. Summary An optical technique was developed to measure the local, intermittent deflagration, characteristic of certain wide distribution propellants. The technique, called a Laser Position Detector, was designed, developed, and tested producing a new tool for solid propellant research. The Laser Position detector uses a laser beam, synchronous detection, and a closed-loop tracking system to geometrically track the local surface height of a propellant strand.

Specifications were developed from photographic data to establish requirements for the instrument performance. The control system was then developed to meet these specifications having a bandwidth above 150hz and the ability to compensate for gain reductions of 50% induced by the propellant smoke. The instrument achieved all the desired specifications when tested on the bench.

Experiments on burning propellant strands demonstrated that the Laser Position Detector can continuously measure the local surface position at pressure levels from 0 to 250 psig. The combustion gases limit the measurement resolution to values from 0.001 to 0.010 inches depending on the pressure level. Experiments also determined that combustion products can reduce the beam transmission up to 90% during the experiment lowering the instrument bandwidth below the designed operating conditions.

8.1.2. Conclusions The Laser Position detector is a useful tool for measuring the local movement of the propellant surface. Smoke attenuation currently limits the measurements to pressures below 250psig and reduces the system bandwidth to about 50hz. This makes the instrument most applicable for use in conjunction with spectroscopic diagnostics where the precise distance between the local propellant surface and the diagnostic's probe volume is required. The instrument could also be used to measure the low-frequency transient movement of the burning surface. Further development could increase the usable pressure range. The main difficulty is the hostile optical properties of the propellant combustion products.

8.2. Combustion Studies

8.2.1. Summary The combustion studies were concerned with the ballistic properties of wide distribution propellants. One set of monomodal, five sets of bimodal, and one set of trimodal propellants were formulated. Each set contained an HTPB-DOA plasticized binder and duplicate formulations were cast with either an IPDI or a DDI curative. The monomodal propellants simulate the pocket propellant (fine-AP/binder matrix) of wide distribution propellants and oxidizer-to-fuel ratios from 2.0 to 4.0 were investigated using 20 micron AP. Bimodal, analogue propellants (ie. having analogous

pocket propellants) were formulated by adding coarse (400 micron) material to achieve either a constant volume fraction of the coarse material, or a constant total solids loading. The trimodal propellants extended the data base into more application oriented formulations.

Ballistic measurements were taken at pressure levels from 125 to 2000psig. Table 31 summarizes the ballistic properties at 1000psig for selected monomodal and bimodal propellants.

High-speed photographs and examination of extinguished propellant surfaces showed evidence of molten liquid binder flowing on the propellant surface. This was indicated by beads of binder flowing off the burning surface in the window bomb movies and thin layers of binder covering portions of the oxidizer particles on the extinguished surface. The binder flow increases significantly as the oxidizer-to-fuel ratio of the pocket propellant is lowered.

8.2.2. Conclusions Wide distribution propellants have three unique combustion mechanisms.

Binder Flow

This study has shown that molten binder flow over the propellant burning surface is a dominant combustion mechanism for wide distribution solid propellants. The fuel-rich, low-temperature region of the pocket propellants allows the formation of a thin layer of liquid binder that flows over portions of the exposed oxidizer particles. Calculations with a physiochemical model show that the binder covering reduces the oxidizer burning rate over 50 percent.

Table 31
Summary of Ballistic Measurements

PROPELLANT DESIGNATOR*	CONTROLLED PROPERTIES			OXIDIZER WEIGHT FRACTION			BALLISTIC RESULTS			
				400μAP	400μNaCl	16μAP	IPDI		DDI	
	V_f/V_T	α_T	OF_p	$\bar{D}$ = 355μ σ = 1.05	$\bar{D}$ = 355μ σ = 1.05	$\bar{D}$ = 20μ σ = 1.8	r_{1000} (cm/sec)	n_{1000}	r_{1000} (cm/sec)	n_{1000}
A-I	0	.800	4.00		-	0.800	.922	.61	EXT.	-
B-I	0	.750	3.00	-	-	0.750	.622	.47	EXT.	-
C-I	0	.670	2.00	-		0.670	EXT	-	EXT.	-
G-I	.305	.870	4.00	.350		.520	1.13	.60	.767	.54
E-I	.305	.840	3.00	.360	-	.480	.818	.50	.508**	-
K-I	.305	.792	2.00	.376	-	.416	.632	.47*	.028**	-
G-I-400S	.305	.875	4.00		.374	.501	1.32	.66	.495	.69
E-I-400S	.305	.846	3.00	-	.385	.462	.963	.60	.305	.63
K-I-400S	.305	.800	2.00	-	.401	.399	.445	.85*	.183**	-
D-I	.169	.84	4.00	.200	-	0.640	.978	.58	.658	.45
E-I	.305	.84	3.00	.360	-	0.480	.818	.49	.508**	-
F-I	.441	.84	2.00	.520	-	.320	.706	.43	.531	.43
G-I	.305	.87	4.00	.350	-	.520	1.13	.60	.767	.54
H-I	.419	.87	3.00	.480		.390	.907	.53	.638	.42
J-I	.532	.87	2.00	.610	-	.260	.790	.45	.662	.45

* Designators for series "I" are shown (IPDI binder)

** Some samples extinguished. Data shown are for samples that burned

This explains the differences in the predictions made with the PEM combustion model and the experimental results for wide distribution propellants.

The fraction of the AP burning surface covered with the molten binder determines the magnitude of the propellant burning rate suppression. Experimental evidence suggests that lowering the oxidizer-to-fuel ratio of the pocket propellant increases the binder covering fraction. The SEM's also show that the binder covering fraction varies with the combustion pressure.

The SEM photographs lack sufficient resolution to quantitatively measure the differences in binder covering fraction from case-to-case. It is recommended that X-ray photoelectron spectroscopy or another suitable technique be used to measure the binder covering fraction of extinguished surfaces as a function of pressure and propellant composition.

Dominance of Pocket Propellants

The physical heterogeneity of the propellant causes the fine particle to burn in very fuel-rich conditions.

Dominance of Binder Reactions

The fuel-rich nature of the pocket propellants makes them less sensitive to the deflagration of the fine oxidizer particles and more sensitive to binder ingredient changes. This in general produces lower burning rates than anticipated.

LIST OF REFERENCES

[1] Beckstead, M.W., "Combustion Calculations for Composite Solid Propellants," Proceeding of the 13th JANNAF Combustion Meeting, CPIA Publication 281, Vol.II, pp. 299-312, December 1976.

[2] Condon, J.A. and Osborn, J.R., The Effect of Oxidizer Particle Size Distribution on the Steady and Non-Steady Combustion of Composite Propellants, AFRPL-TR-78-17, Air Force Rocket Propulsion Laboratory, Edwards AFB, CA., June, 1978.

[3] Renie, J.P., Condon, J.A., and Osborn, J.R., "Oxidizer Size Distribution Effects," Proceedings of the 14th JANNAF Combustion Meeting, CPIA Publication 292, Vol. I, pp. 325-339, December 1977.

[4] Crump, J.E., Combustion of Solid Propellants and Low Frequency Combustion Instability, Progress Report 1, 1 April, 30 September 1967, Naval Weapons Center, China Lake, CA, p 52., April 1968.

[5] Osborn, J.R., Combustion of Solid Propellants, Class Notes-A&AE 539, School of Aeronautics and Astronautics, Purdue University, W. Lafayette, In, 47907. May 1986.

[6] Hermance, C.E., "A Model of Composite Propellant Combustion Including Surface Heterogeneity and Heat Generation," AIAA Journal, Vol.4, pp. 1629-1637, September 1966.

[7] Beckstead, M.W., Derr, R.L. and Price, C.F., "A Model of Composite Propellant Combustion Based on Multiple Flames," AIAA Journal, Vol. 8, pp. 2200-2207, December 1070.

[8] Cohen, N.W., Price, C.F., and Strand, L.D., Analytical Model of Combustion of Multicomponent Solid Propellants, AIAA Paper 77-927, July 1977.

[9] Glick, R.L. and Condon, J.A., "Statistical Analysis of Polydisperse, Heterogeneous Propellant Combustion: Steady-State," Proceedings of the 13 JANNAF Combustion Meeting, CPIA Publication 281, Vol.II, pp. 313-345, December 1976.

[10] Miller, R.R., Hartman, K.O., and Myers, R.B., "Prediction of Ammonium Perchlorate Particle Size Effects on Composite Propellant Burning Rate," Proceedings of 26th JANNAF Solid Propulsion Meeting, CPIA Publication 196, Vol. I, pp. 567-591, May 1970.

[11] Condon, J.A. and Osborn, J.R., The Effect of Oxidizer Particle Size Distribution on the Steady and Non-Steady Combustion of Composite Propellants, AFRPL-TR-78-17, Air Force Rocket Propulsion laboratory, Edwards AFB, CA., June, 1978.

[12] Strahle, W.C., "Some Statistical Considerations in the Burning of Composite Propellants," AIAA Journal, Vol.16, pp.843-847, August 1978.

[13] King, M.K., An Analytical and Experimental Study of the Erosive Burning of Composite Propellants, Part A, AFOSR-TR-78-0060, Atlantic Research Corp., Alexandra, Va. November, 1977.

[14] Miller, R.R., Donohue, M.T., Yount, R.A., and Martin, J.R., Control of Solids Distribution in HTPB Propellants, AFRPL-TR-78-14, Air Force Rocket Propulsion laboratory, Edwards AFB, CA., April, 1978.

[15] Miller, R.R., "Control of Solids Distribution-I : Ballistics of Non-Aluminized HTPB Propellants," 13th JANNAF Combustion Meeting, CPIA Publication 281, Vol. II, September 1976.

[16] Miller, R.R., "Anomalous Behavior of Reduced Smoke Propellants with Wide AP Distributions," CPIA Publication NO.297, Vol.II, Feb 1979.

[17] Foster,R.L. and Miller, R.R., The Influence of the Fine AP/Binder Matrix on Composite Propellant Ballistic Properties, AFRPL Contract F04611-80-C-0002.

[18] Stacer, H. L., LaRue, J. C., and Miller, R. R., Approximate Analysis of Instantaneous Burn Rate Behavior, 19th JANNAF Combustion Meeting, 1982.

[19] Becker, R.J., Research Physicist, Personal Communication Concerning A Diode Array Servocontroller for Propellant Strand Experiments, University of Dayton Research Institute, Dayton, OH

[20] Brooks, W.T., Workshop Report: Burn Rate Determination Methodology, 18th JANNAF Combustion Meeting, Jet Propulsion laboratory, Pasadena California, October 1981.

[21] Boggs, T.L., Crump. J.E., Kraetle, K.J., and Zurn, D.E., "Cinemicrophotography and Scanning Electron Microscopy as Used to Study Solid Propellants," Experimental Diagnostics in Combustion of Solid Propellants, Progress in Astronautics and Aeronautics, Vol. 63, American Institute of Aeronautics and Astronautics, 1978.

[22] Goetz, F., and Mann, D.M., "Design and use of a Servo-Controlled High Pressure Window Bomb in Spectroscopic Studies of Solid Propellant Combustion," 17th JANNAF Combustion Meeting, CPIA Publication 162, October, 1967, pp 417-435.

[23] Crawford, B.L., Huggett, C., Daniels, F. and Wilfong, R.E., "Direct Determination of Burning Rates of Propellant Powders," Analytical Chemistry, Vol. 19, No. 9, September, 1947.

[24] Anderson, J.B., An Investigation of the Effect of Acceleration on the Burning Rate of Composite Propellants, PhD Thesis, United States Naval Postgraduate School, No. NPS-57RV 8121A, December, 1968.

[25] Hamke, R. Personal Communication Regarding Thermocouples with Solid Propellant Strands, Purdue University School of Aeronautics & Astronautics, April,1986.

[26] Osborn, J.R., Combustion of Solid Propellants, Class Notes-A&AE 539, School of Aeronautics and Astronautics, Purdue University, W. Lafayette, In, 47907. May 1986.

[27] Dickenson, L.A. and Reichenbach, R.E., "A Study of the Burning Rate of Polyurethane Propellants in Rocket Motors," 8th Symposium (International) on Combustion, 1962.

[28] Blum, E.H. and Wilhelm, R.H., "Approach to Random Packed Beds," AIchE–Industrial Chemical Engineering Symposium Series, No. 4, London Institute of Chemical Engineers, pp.4:21-4:27, 1965.

[29] Becker, R., Personal Communication regarding the Use of Laser Beams in Combustion Measurements, University of Dayton Research Institute, Dayton, OH, March, 1980.

[30] Osborn, J.R., et al, "Continuous Measurement of Solid Propellant Burning Rate," The Review of Scientific Instruments, Vol. 37, No. 1, June 1966.

[31] Strum, E.J. and Reichenbach, R.E., A Study of the Burning Rate of Composite Solid Propellants in Acceleration Fields, NPS Report No, NPS-57RV8121A, U.S. Naval Postgraduate School, December 1968.

[32] Benedict, R., Personal Communication Concerning Pressure Threshold Measurement, Air Force Rocket Propulsion Laboratory, Edwards AFB, CA, July, 1986.

[33] Cole, R.B., Burning Rates of Solid Composite Propellants at Pressures up to 20,000 psig, Report N0. S-80, Rohm and Haas, Huntsville, Alabama, Sept.15, 1966.

[34] Koury, J.L., Solid Strand Burn Rate Technique for Predicting Fullscale Motor Performance, Air Force Rocket Propulsion Laboratory, AFRPL-TR-73-49, Edwards AFB, CA, October, 1973.

[35] Saber, A.J., Johnston, M.D., Caveny, L.H., Summerfield, M., and Koury, J.L., "Acoustic Emissions from Burning Propellant Strands," 11th JANNAF Combustion Meeting, CPIA Publication No. 261, Vol. I, Laurel, MD, Dec. 1975, pp 389-402.

[36] Strahle, W.C., Craig, J.I., and Palfery, J.G., "Audible and Ultrasonic Acoustic Emissions from Composite Solid Propellants," 12th JANNAF Combustion Meeting, CPIA Publication No. 273, Vol. II, Laurel, MD, Dec. 1975 pp 389-402.

[37] Caveny, L.H., Saber, A.J., and Summer- field, M., "Propellant Burning Rate Uniformity Identified by Ultrasonic Acoustic Emission," Journal of Spacecraft and Rockets, Vol.14, No. 7, July, 1977, pp 433-437.

[38] Varney, A.M., An Experimental Investigation of Burning Rate Mechanisms in Ammonium Perchlorate Composite Solid Propellants, PhD Thesis, Georga Institute of Technology, 226 p., May 1970

[39] Becker, R.J. and Laird, J.L., Optical Considerations in Obtaining a Statistical Data Base on Propellant Deflagration, 22nd JANNAF Combustion Meeting, Pasadena, CA, October 1985.

[40] Shelukin, G. G., Bulkadov, V. P., and Belov, V.P., "Experimental Investigation of Combustion Processes in Heterogeneous Condensed Media," Fizika Goreniya i Vztyva , Vol. 5, No. 1, pp42-51, 1969.

[41] Miller, R.R., and Stacer, H.L., Effects of Curative Type on Incremental Burning Behavior and Ballistics of HTPB Reduced Smoke Propellants, 19th JANNAF Combustion Meeting, 1982.

[42] Boggs, T. L., Personal Communication Concerning Combustion Bomb Design and Operation, Naval Weapons Center, China Lake, Ca, 11 October, 1985.

[43] Frederick, R.A. and Osborn, J.R., Effect of Acceleration on Propellant Combustion, AFRPL - TR-84-073 Final Report, Air Force Rocket Propulsion Laboratory, Air Force Space Technology Center, Space Division, Air Force Systems Command, Edwards AFB, CA 93523-5000, October, 1984.

[44] Rekers, R. G. and Vilars, D.S., "Flame Zone Spectroscopy of Solid Propellants," Review of Scientific Instruments, Vol 25, No.5, May 1954.

[45] Osborn, J.R., Buric, R.J., and Panella, R.F., "Continuous Measurement of Solid Propellant Burning Rate," The Review of Scientific Instruments, Vol. 37, No. 1, January, 1966 pp 86-92.

[46] Derr, R. L. and Osborn, J. R., "A Technique for Controlling the Position of a Burning Solid-Propellant Sample in a Combustion Bomb," Journal of Spacecraft and Rockets, Vol. 6, No. 10, October 1969, pp.1120-1124.

[47] Lilley, J. S., The Design and Operationof a Servo–Controlled Solid Propellant Window Bomb, Masters Thesis, Purdue University, School of Aeronautics and Astronautics, December, 1981.

[48] Renie, J.P., Lilley, J.S., Frederick, R.A., and Osborn, J.R., Aluminum Particle Combustion in Composite Solid AIAA/SAE/ASME 18th Joint Propulsion Conference, Cleveland, OH, June, 1982.

[49] Goetz, F. , A High Pressure Combustion Measurements of the Combustion Products, Final Report, AFRPL-TR-80-79, Air Force Rocket Propulsion Laboratory, Edwards AFB, CA, December, 1981.

[50] Caveny, L. H., Collins, K. L. and Cheng, S. W., "Direct Measurements of Acoustic Admittance Using Laser Doppler Velocimetery", AIAA Journal, Vol 19, No. 7, July 1981.

[51] Volpi, A.V. and De Luigi, Unsteady Burning of Solid Propellants, Second Informal Semi-Annual Progress Report, AFOSR-81-01431, Professor Currado Casi, PI, Instituto di Macchine-CNPM, Politecnico di Milano, 32 Piazza Lenardo da Vinci, 20133 Milano, Italy, December, 1981.

[52] Burick, R.J., Erosive Burning of Solid Rocket Propellants, PhD Thesis, Purdue University School of Mechanical Engineering, W. Lafayette, In 47907, June 1967. Vol. 37, No. 1, June 1966.

[53] Strand, L. D., Schultz, A. L., and Reedy, W. W., "Microwave Doppler Shift Technique for Determining Solid Propellant Transient Regression Rates," Journal of Spacecraft and Rockets, Vol. III, No. 2, Feb 1974, pp. 75-83.

[54] O'Brien, W. , Microwave Combustion Measurements, 10th JANNAF Combustion Meeting Naval Postgraduate School, Monterey, CA, October 1983.

[55] Johnston, A. D., Andrepont, W. C., and Vogt, G. L., Combustion Response Measurements, AFRPL-TR-76-72, Air Force Rocket Propulsion Laboratory, Edwards AFB, CA, October, 1976.

[56] Battles, J. , Personal Communication Concerning Microwave Technique, Naval Weapons Center, China Lake, Ca, 10 October, 1985.

[57] Park, C.P., Extinguishment of Composite Propellant at Low Pressures, AF-AFOSR 69-1656, University of Utah, Department of Chemical Engineering, December 1973.

[58] Illukin, V.S., et al, "Role of Heterogeneity of Composite Propellants in the Mechanism of Pulsating Burning," Fizika Gorenya i Vzryva, Vol. 11, No. 3, pp 498-501, May-June, 1975.

[59] Fagan, A.M. and Goldstein, J.B., "Evaluation of Solid Propellant Ballistic Properties by Constant Volume Burning," Combustion and Flame, Vol. 10, pp 23-28, March 1966.

[60] Osborn, J.R., "Evaluation of Solid Propellant Ballistic Properties," Combustion and Flame, Vol.20, pp 193-198, 1973.

[61] Frederick, R. A. and Matson, J. C., Technique for Local Instantaneous Burning Rate Measurement, AIAA-84-1424, AIAA/SAE/ASME 20th Joint Propulsion Conference, Cinn., Ohio, 1984.

[62] Laird, J.L., The Development of Polymeric Coatings for Solid Propellants, Masters Thesis, University of Dayton, Dayton, OH, December, 1986.

[63] Edwards, T., Weaver, D.P., and Campbell, D.H., "Laser Induced Fluorescence in High Pressure Solid Propellant Flames," Applied Optics, Vol. 26, No., 1 Sept, 1987.

[64] Frederick, R.A.,Jr, and Matson, J.C., Technique for Local Instantaneous Burning Rate Measurement, AIAA/SAE/ASME 20th Joint Propulsion Conference, AIAA-84-1474, Cincinnati, OH, June 11-13,1984.

[65] TOTALP Computer Program, Version 1.0 (6-1-85), Developed from TOTAL written by S.J. Larime, USAF, in partial fulfillment of his Master's Thesis at AFIT/ENG, Wright Patterson AFB, OH, March, 1978.

[66] Miller, R.R., Self–Extinguishment Propellant Development , AFRPL-TR-82-096, Air Force Rocket Propulsion Laboratory, Edwards AFB, CA December, 1982.

[67] Matson, J.C., Combustion Response Measurements of Solid Propellant by a Microwave Technique , Master's Thesis, Purdue University, School of Aeronautics and Astronautics, May, 1984.

[68] Schmidt, W.G., Lovine, R.L., and Poynter, R.G., Zirconium/Aluminun Combustion , AFRPL-TR-81-19, Final Report, Air Force Rocket Propulsion Laboratory, Edwards AFB, CA, April, 1981.

[69] King, M.K., Model for Steady–State Combustion of Unimodal Composite Propellants , AIAA-78-216, AIAA 16th Aerospace Sciences Meeting, Jan. 1978.

[70] Miller, R.R., et al, Self Extinguishment Propellant Development , Final Report, AFRPL-TR-84-026, Air Force Rocket Propulsion Laboratory, Edwards AFB, CA, April, 1984.

[71] Foster, R.L., Condon, J.A., and Miller, R.R., Low Exponent Technology, AFRPL-TR-81-95, Hercules Incorporated, Allegahny Ballistics Labortaory, Cumberland, Md, 1982.

[72] Wengan, X., Boxuan, L., and Kexiu, W., "Mechanism of Steady-State Burning of Composite Propellants Including Those with Negative Pressure Exponents," Acta Astronautica, Vol. 15, No. 2, pp 83-96, 1987.

APPENDICES

Appendix A: Transfer Function Estimations

The transfer function for each electronic component was estimated from experimentally determined Bode plots. The detector, scanner, acousto-optic deflector, lock-in amplifier, and controller were all tested. This appendix presents a brief description of the technique, each experiment, and the results. Example data are shown for each device plotted along with the estimated transfer function.

Technique

The data required for the Bode plots are the amplitude ratio and the phase lag as a function of frequency. Harmonic inputs of known amplitude and frequency were input into each device while measuring the output response.

The amplitude ratio and phase were determined from measurements of the resulting Lissajous figure. Figure A1 shows an example Lissajous figure with the x-axis representing the input signal; the y-axis representing the output signal.

The two distances shown in Figure A1: the output amplitude, ΔV_{out}; and the intercept voltage ΔV_y; are used to determine the amplitude ratio.

$$AR = 20 \log (\Delta V_{out}/\Delta V_o) \tag{A1}$$

and the phase angle

$$\Phi_I = -\sin^{-1} (\Delta V_y/\Delta V_{out}) \tag{A2}$$

$$\Phi_{II} = \sin^{-1} (\Delta V_y/\Delta V_{out}) - 180^o \tag{A3}$$

where

AR is the amplitude ratio,

ΔV_o is the output amplitude at low frequency

Φ_I is the phase lag if the major axis is in 1st quad. and

Φ_{II} is the phase lag if the major axis is in 2nd quad.

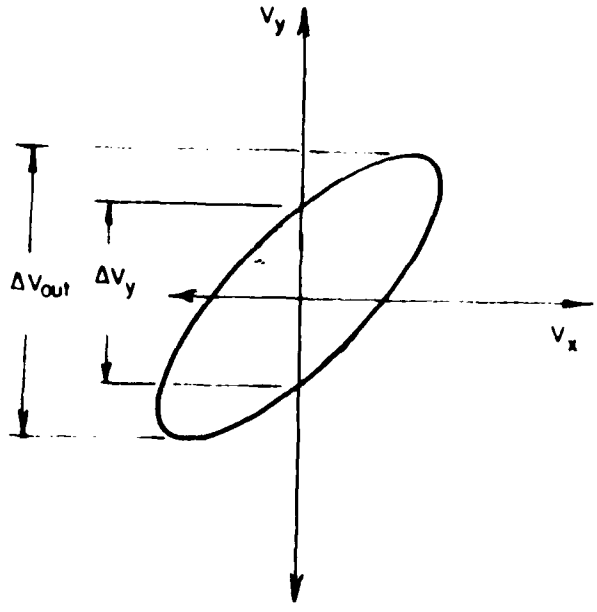

Figure A1. Lissajous Figure

The voltages ΔV_y, ΔV_{out}, and ΔV_o were determined using either an oscilloscope or digitized data.

The amplitude ratio and phase angle are then plotted as a function of frequency. Transfer functions are estimated from the characteristics of the curves using first and second order systems or combinations of the two.

Detector Response

The experiment to test the detector frequency response is shown in Figure A2. The detector is is tested in the configuration it is actually used by focusing a diffusely reflected laser beam spot through a pinhole. An acousto-optic crystal driven by an A-O amplifier controls the position of the beam spot on the target surface. The input to the experiment is the A-O amplifier input voltage which is controlled by a signal generator. The output to the experiment is the amplified detector voltage. Because of the geometry, the frequency of the output wave is twice the frequency of the input wave.

Figure A3 shows the results of the amplitude ratio measurements. The amplitude ratio suggests a first-order response with a corner frequency at 1000 hz. On this basis, the general form of the transfer function is

$$\bar{D}(s) = \frac{D(s)}{K_{PDL}} = \frac{1/\tau_{PD}}{s + 1/\tau_{PD}} \tag{A4}$$

A corner frequency of 1000 hz makes

$$\tau_D = \frac{1}{2\pi(1000)} = \frac{1}{6280} \tag{A5}$$

so that the transfer function for the detector is

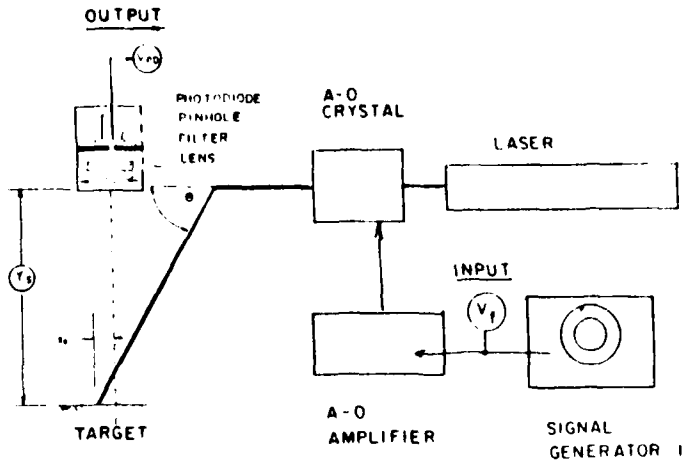

Figure A2. Detector Frequency Response Experiment

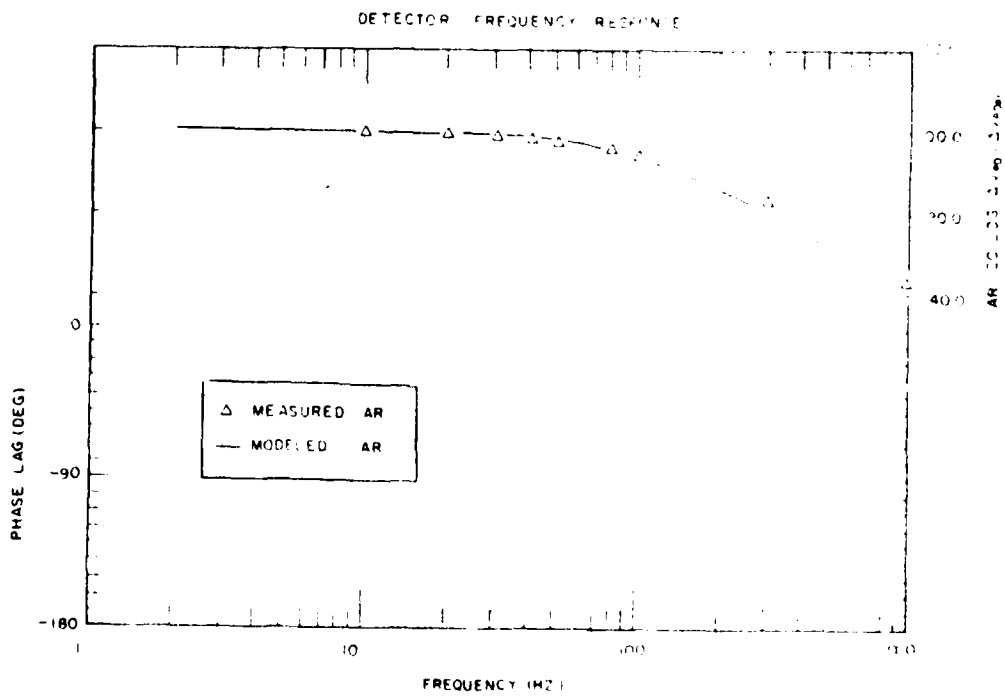

Figure A3. Detector Frequency Response

$$\bar{D}(s) = \frac{6280}{s + 6280} \qquad \text{(A6)}$$

Figure A3 also shows the curve computed with this transfer function plotted with the measured data. The corner frequency was estimated low to be conservative because the corner frequency was found to decrease with decreasing average light levels.

Scanner Response

Two scanners (galvonometers) were tested to obtain estimates for their transfer functions: a G108 and a G102 model. Figure A4 shows the experiment for determining the response of the scanner. A 2mW He-Ne laser beam is reflected off the scanner mirror and onto a position sensitive detector (PSD) chip (Hammatsu S1544). A signal generator drives the scanner amplifier causing the mirror to turn. The resulting movement of the laser spot is measured by the PSD whos output amplifier produces a voltage proportional to the lateral position of the beam centroid.

The scanner amplifier has adjustable "damping" that is set by a trim pot. This damping lowers the resonance amplitude at the natural frequency of the scanner. Figure A5 shows the experimental results of the minimum and maximum damping on the scanner response for the G108 scanner.

An intermediate damping was chosen for use with the system. An example of this frequency response is shown in Figure A6. This case is calibrated by adjusting the phase lag to -30° at 200 hz.

From the frequency response data, the general form of the transfer function for the scanner was estimated as a first and second-order system in series

SCANNER FREQUENCY RESPONSE EXPERIMENT

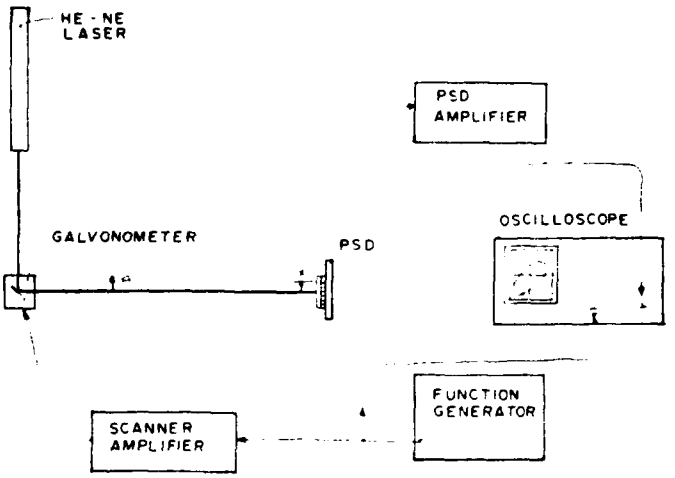

Figure A4. Scanner Response Experiment

$$S(s) = \frac{\phi}{V_c} = \frac{K_s(1/\tau_b)(\omega_n^2)}{(s+\frac{1}{\tau_b})(s^2+2\zeta\omega_n s+\omega_n^2)} \qquad (A7)$$

Changing the damping mainly changes the time constant of the first-order system, τ_b, while the other parameter remain fixed.

From Figure A6, the transfer function for the G102 scanner at intermediate damping is estimated as

$$\bar{S}_{102} = \frac{S}{K_s} = \frac{(1900)(12{,}315)^2}{(s+1900)(s^2+739s+12{,}315^2)} \qquad (A8)$$

The G102 scanner has a higher natural frequency but a lower angular range than the G108. The angular range of the G102 is 2°p-p while the G108 is 8°p-p.

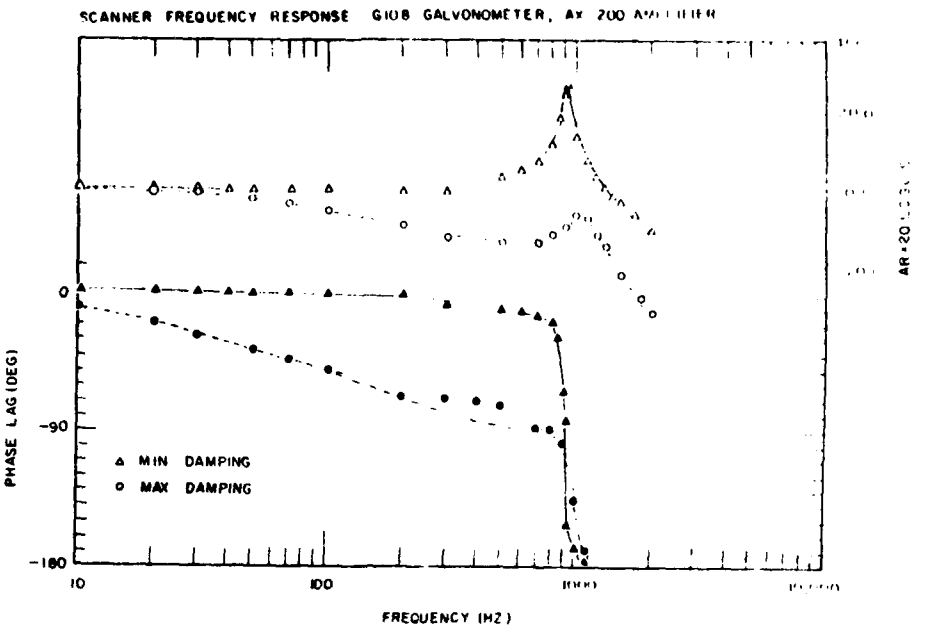

Figure A5. G108 Scanner Response - Min. and Max. Damping

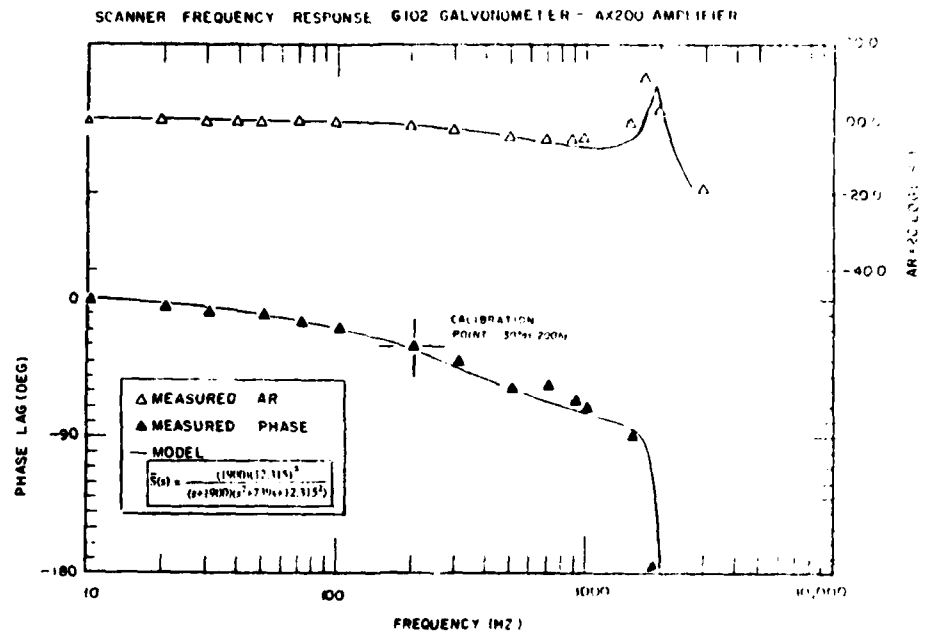

Figure A6. G102 Scanner Response - Intermediate Damping

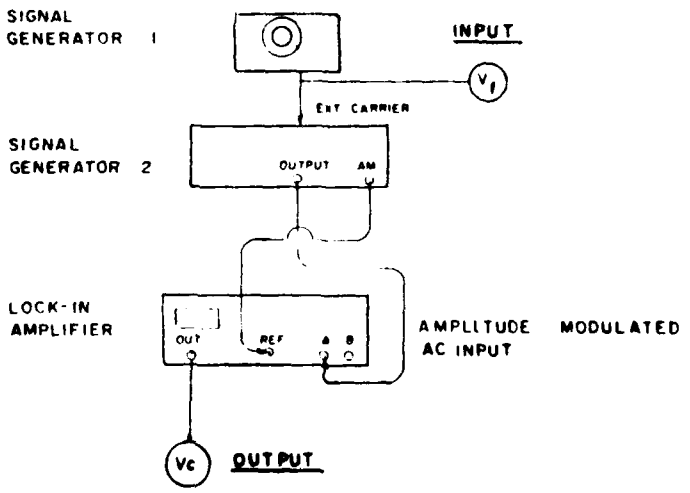

Figure A7. Lock-in Amplifier Frequency Response Experiment

Lock–in Amplifier Response

To experimentally determine the frequency response of the lock-in amplifier, an amplitude modulated signal must be applied to the AC input while monitoring the output voltage. Figure A7 shows the experiment for measuring the frequency response of the lock-in amplifier. Signal Generator 1 modulates the amplitude of a sinusoidal output wave produced by Signal Generator 2. The lock-in mixer circuit is synchronized to the carrier frequency by connecting the trigger circuit of Signal Generator 2 to the reference channel of the lock-in. An adjustable phase delay in the lock-in is set so that the phase angle between the reference channel and the input is zero for synchronous detection. For purposes of the determining the transfer function, the system input is the output voltage of Function Generator 1. The system output is the output of the lock-in amplifier.

Figure A8 shows the experimental amplitude ratio results for several values of lock-in amplifier time constant. From these results, it appears that the amplifier can be

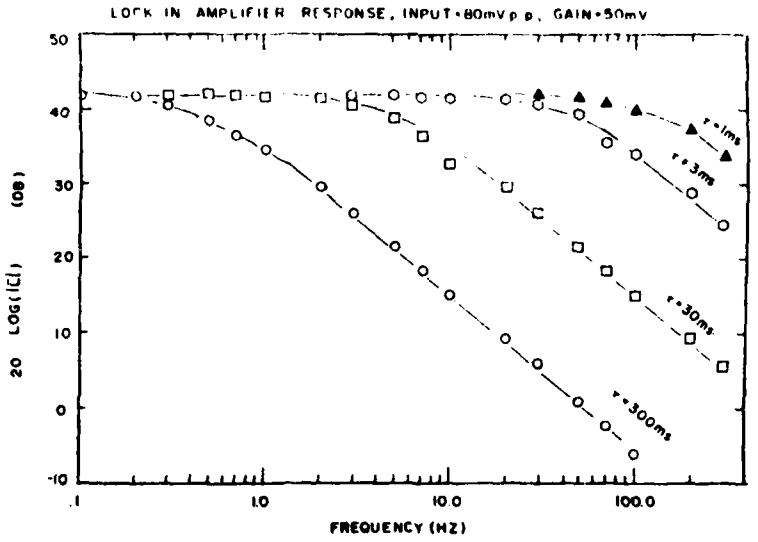

Figure A8. Lock-in Amplifier Frequency Response

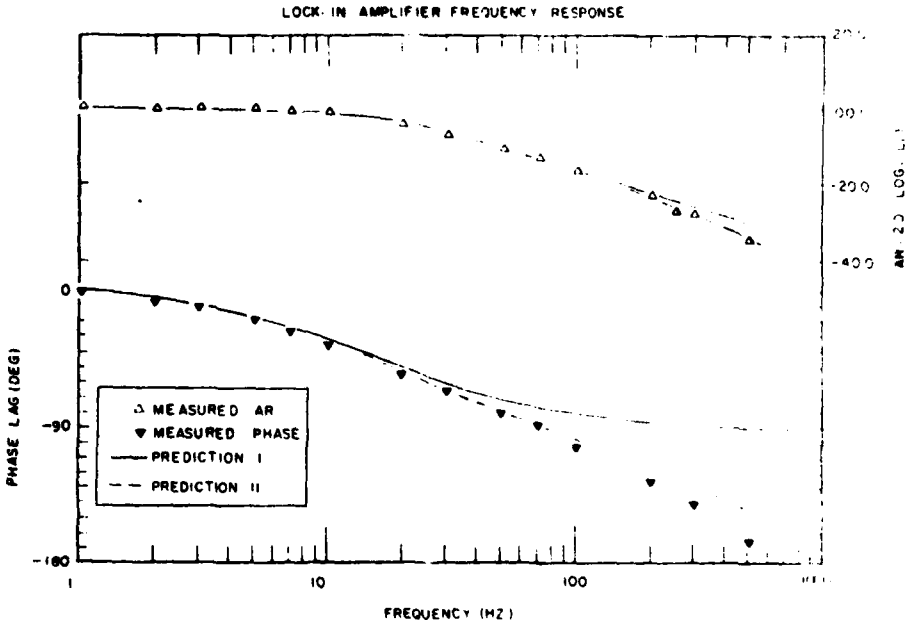

Figure A9. Lock-in Amplifier Frequency Response

modeled as a first-order system because the experimental corner frequencies closely correspond to those predicted using the panel value of the time constant

$$f_c = \frac{1}{2\pi\tau_{PLA1}} \tag{A9}$$

making the transfer function

$$\bar{L}(s) = \frac{100}{s + 100} \tag{A10}$$

for a time constant of $\tau_{PLA1} = 0.010$ sec.

Figure A9 shows the predicted curves frequency response (Prediction 1) and the measurements for $\tau = 0.010$ sec. Although the amplitude ratio matches well, additional phase lags start at 20 hz. This suggests an additional pole in the amplifier with a time constant, $\tau_{PLA2} = 0.004$ sec. This makes the transfer function for the lock-in amplifier

$$\bar{L}(s) = \frac{(100)(2500)}{(s + 100)(s + 2500)} \tag{A11}$$

and the predicted response for this estimation is shown in Figure A9 as "Prediction 2". It is not known exactly what produces the second time constant.

Controller Response

The controller was designed to have the transfer function

$$C(s) = \frac{K_c}{s}\,[s + 100] \tag{A12}$$

The electronics were designed and calibrated to match this condition.

Appendix B: Laser Position Detector Configurations

This appendix documents specific details of the electronics, hardware, and optics of the System-I and System-II configurations.

System–I

Details of the equipment are listed in Table B1. Settings used for System-I are listed in Table B 1. This system used a galvonometer scanner to point the beam. Figure B1 shows a wiring schematic of the system. Standard BNC connectors were used to connect the various instruments.

System–II

Details of the System-II configuration are listed in Table B2 and Figure B2.

Table B1

Equipment List

LASER

Aerotech Model LSR-2R

He-Ne (Red), 2 mW

S/N 112-09446-31

Power Supply: PS2

S/N 413-16034

SCANNER

General Scanning Model G108

S/N 143060

7x7 mm mirror

Amplifier: AX-200

Gain: Minimum

S/N 770852

LOCK-IN AMPLIFIER

Princton Applied Reseach Model 5207

Option 92 97

S/N BK 6807

Offset: 0 Expand

Polarity off

Modes: Reserve High Stab

f-band:Broadband

Time Const 10 msec

Reference f-ext

Phase 185.1 deg

Sensitivity: 50mV

Select off

Run/Clear inactive

DETECTOR ASSEMBLY

Lens: Wollensak, 2in, f/2

Filter: out

Pinhole 400 micron

Detector:United detector Technology PIN

Amplifier JFET OP-AMP 353

SIGNAL GENERATOR

Exact Function Generator Model 519 AM/FM

Frequency 4000 Hz

Carrier: Sin

Amplitude: 7.2V p-p

ACOUSTO-OPTIC DEFLECTOR

Intra-Action Model ADM-70

S/N 1117

VCO Deflector Driver Model DE-70M

S/N 2161

Carrier Freq 4.3

Carrier Level 10

CONTROLLER

$K_i = 10$

$K_b = 1 - 10$; $K_p = 10$

SURFACE

Beam Focused with 252mm lens

on a white surface

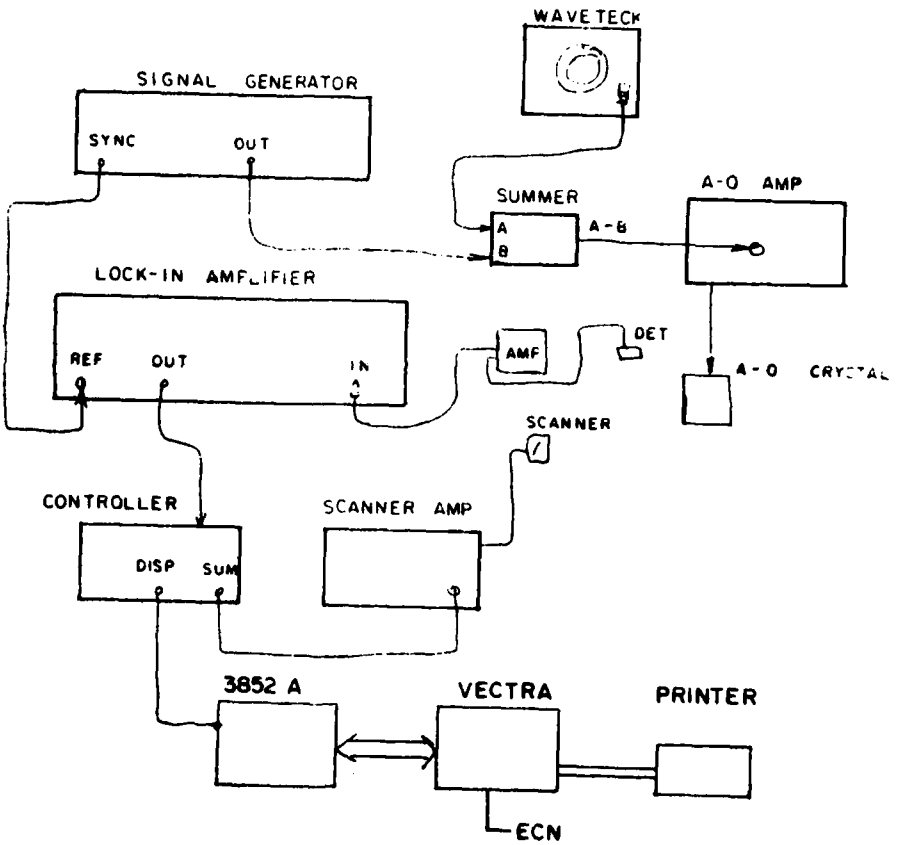

Figure B1. System-I Diagram

Table B2

System-II Details

TARGET
White/no filter

LOCK-IN AMPLIFIER
Offset: 10x
Modes:High Stab; Broad Band
Ref: f ext.; 4000hz; from syc. out of exact
Phase: 273.5deg.
Time Constant: 10 msec
Sens: 20mv

A/O DRIVER
Carrier: 6
Center Freq: 5.95
Inpit: from summer box

LASER LENS
252mm

OTHER PARTS
same as Configuration-I

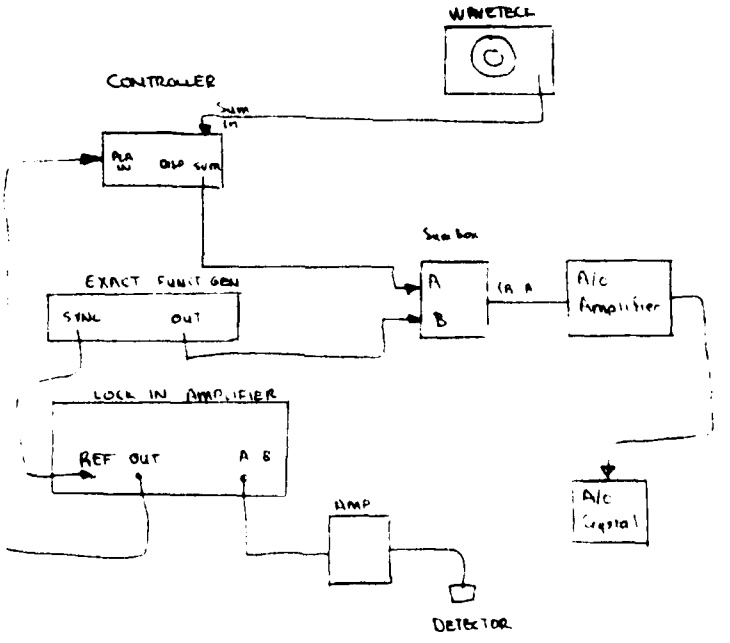

Figure B2. System-II Diagram

Appendix C: Combustion Vessel Drawings

This appendix gives a brief description of the high-pressure combustion bomb. Figures are provided to show the basic dimensions of the vessel.

The vessel was modified from a design provided by the Naval Weapons Center [42] and described in [21]. Their original design included two windows in the bomb body for photography and lighting.

The design was modified by adding three additional windows in the bomb as shown in Figure C1 and Figure C2. Figure C1 shows a section of the bomb body illustrating the relative position of the windows. Figure C2 shows the windows added to allow the Laser Position Detector to operate with this combustion bomb. Both widows are similar in design to the original windows in the bomb body providing interchangability of parts. The sleeve for the smaller window was machined on a lathe then welded into place.

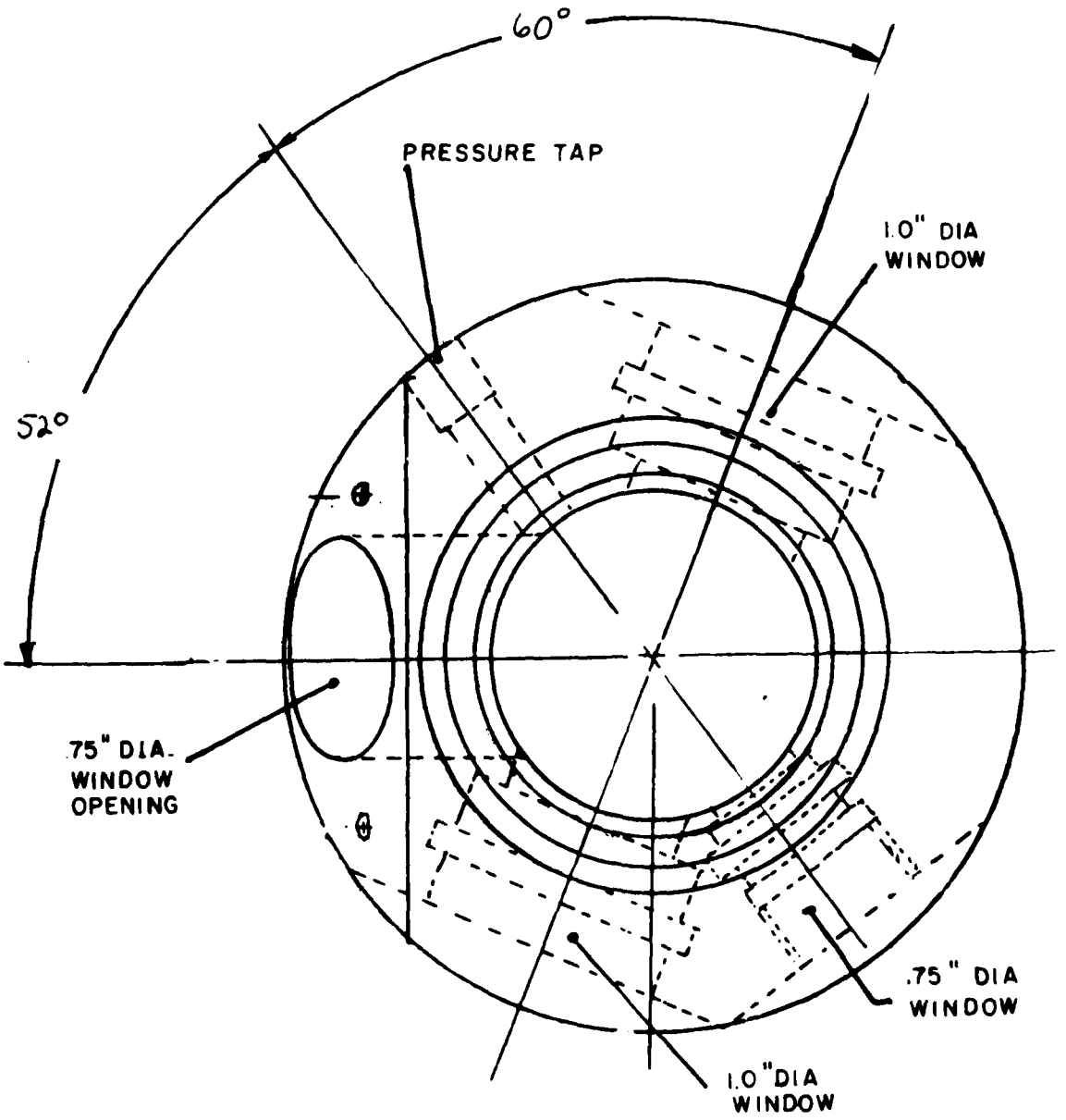

Figure C1 Position of Windows in Bomb Body

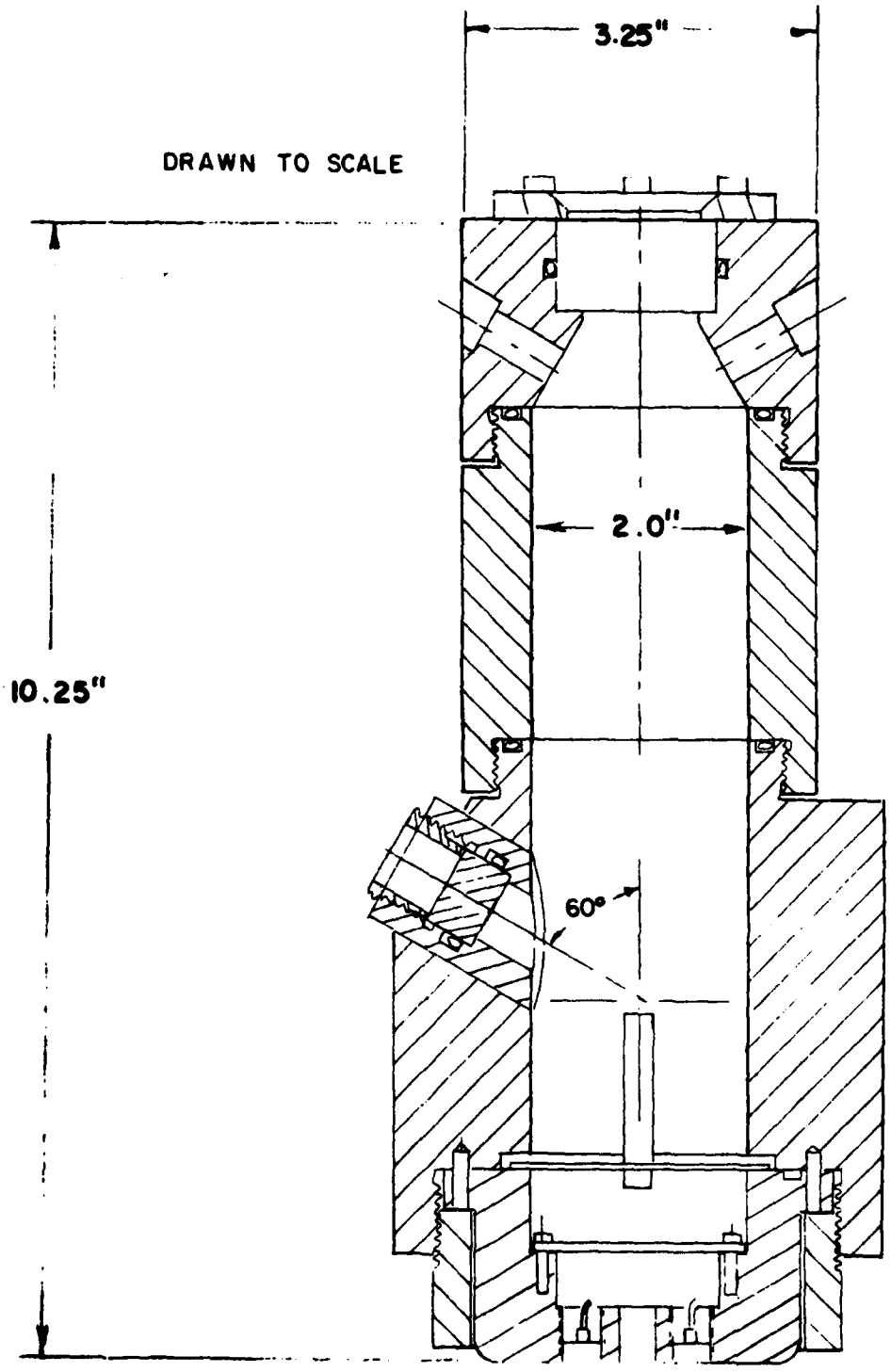

Figure C2 Cross-Section of Bomb

Appendix D: Pressure System Description

The schematic for the pressure system is shown in Figure D1. Gaseous Nitrogen is supplied by bottles connected to a manifold in the test cell. The pressure to the combustion bomb is regulated with a hand loader located in the control room. The mass flow rate of the gas through the system is controlled with a replaceable orifice located downstream of the combustion bomb.

Two solenoid valves are included for operation and safety. Valve SV-1 isolated the bomb from the pressure source and goes to a normally closed position in the event of a power failure. Valve SV-2 opens to bypass the orifice for fast depressurization of the bomb and gaes to its normally open position in the event or a power failure.

The bottle pressure is monitor in the cell with gage G1 and in the control room with gage G2. The bomb pressure is monitored in the control room with gage G4 and in the cell (for safety only-operation is always remote) with gage G5. Relief valve RV-1 protects gage G4 and RV-2 protects the bomb.

The system is operated by installing an orifice appropriate for the experiment, then adjusting the pressure with the hand loader using gage G4 to monitor the bomb pressure.

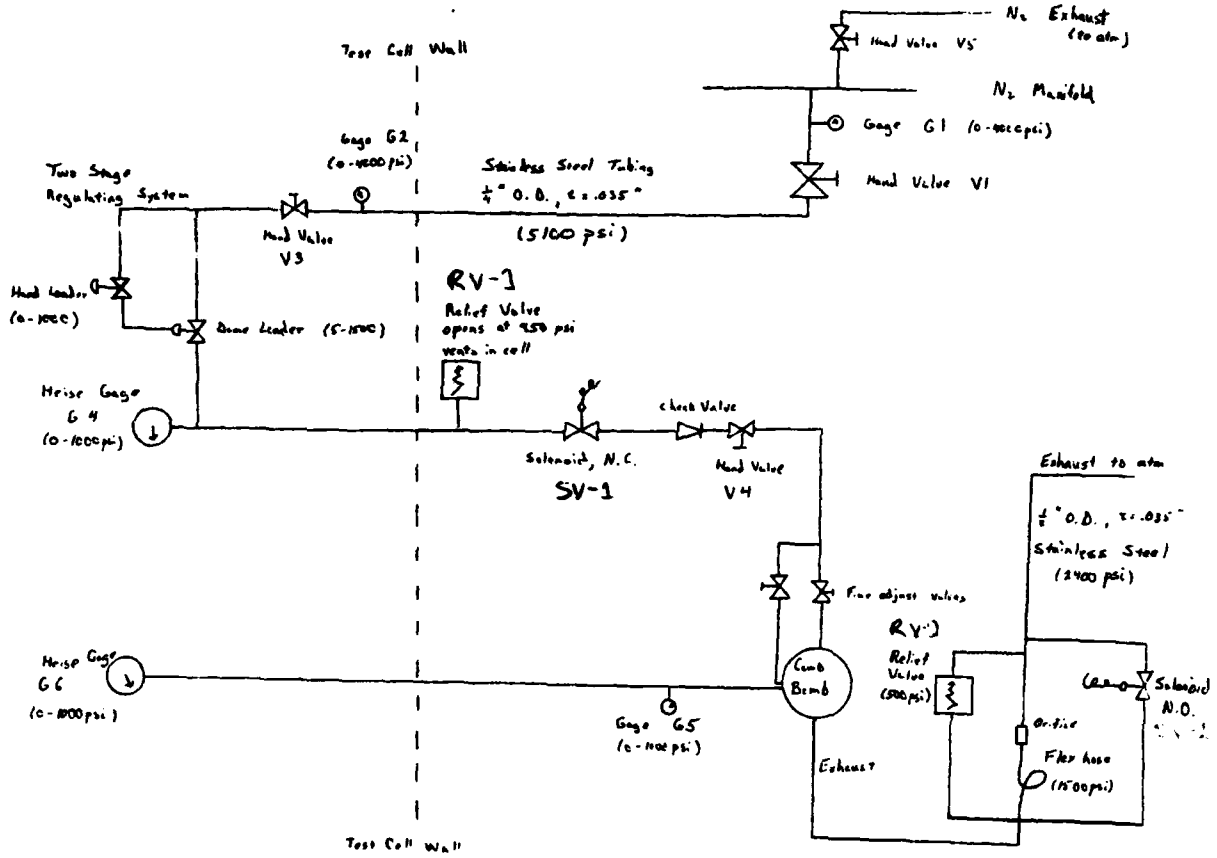

Figure D1 Pressure System Schematic

Appendix E: Propellant Formulation Equations and Tables

Bimodal Analogue Propellants

GIVEN:

Bimodal crystals of same density in a rubber binder

FIND:

Mass fraction of oxidizer in each mode as a function of pocket o/f ratio and coarse particle volume fraction

DEFINITIONS:

- α - mass fraction
- V_c - volume of coarse particles
- V_T - Total Volume
- OF_p - Oxidizer-to-fuel-Ratio of Pocket Propellant = α_f/α_b
- p - density
- m - mass

BASIC EQUATION:

MASS CONTINUITY

$$\alpha_c + \alpha_F + \alpha_b = 1 \tag{1}$$

$$\alpha_T = \alpha_c + \alpha_F \tag{2}$$

VOLUME CONTINUITY

$$\frac{V_c}{V_T} = \frac{m_c/\rho_{ox}}{m_c/\rho_{ox} + m_f/\rho_{ox} + m_b/\rho_b} \tag{3}$$

Normalizing equation (3) by m_f/ρ_{ox} gives an equation for the volume fraction

$$\frac{V_e}{V_T} = \frac{\alpha_c}{\alpha_T + (1-\alpha_T)\frac{\rho_{ox}}{\rho_b}} \tag{4}$$

The relation of the coarse fraction to the pocket of O/F is needed. The basic relation for the pocket propellant is:

$$\frac{\alpha_f}{\alpha_b} = OF_p = \frac{\alpha_T - \alpha_c}{1-\alpha_T} \tag{5}$$

Solving for α_c

$$\alpha_c = \alpha_T - OF_p\,(1-\alpha_T) \tag{6}$$

Substituting (6) into (4) and solving for α_T

$$\alpha_T = \frac{OF_p + \frac{V_c}{V_T}\left[\frac{\rho_{ox}}{\rho_b}\right]}{\left[1+OF_p + \frac{V_e}{V_T}\left[\frac{\rho_{ox}}{\rho_b}-1\right]\right]} \tag{7}$$

and from mass continuity

$$\alpha_F = OF_p(1-\alpha_T) \tag{8}$$

Combining equations (7) and (8) yields the desired relation of

Sample Calculation – ME 44

DATA

$$\rho_{ox} = 1.950\ g/cn^3$$

$$\rho_b = 0.920\ g/cn^3$$

REQUIREMENTS

$$OF_p = 3.0$$

$$V_c/V_T = .3050$$

Using Equation 7:

$$\alpha_T = \frac{3.0 + .3050\,(2.12)}{1 + 3.0 + .3050\,(2.12-1)}$$

$$\alpha_T = 0.84$$

Using equation 8

$$\alpha_F = 3.0\,(1-.84) = .48$$

using equation 2.

$$\alpha_c = \alpha_T - \alpha_F = .84 - .48 = .40$$

Bimodal Propellant with Salt.

GIVEN:

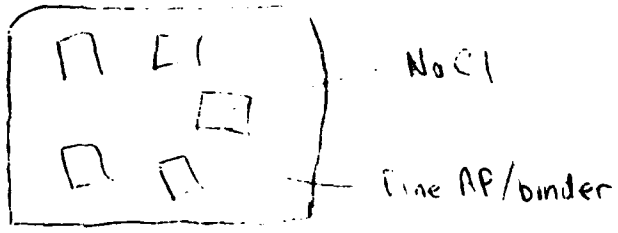

FIND:

Relation of α_c, α_F as a function of Volume Fraction of coarse material and oxidizer/fuel ratio of the pocket propellant:

$$\alpha_c = f(V_c/V_T, OF_p)$$

$$\alpha_f = f(\alpha_c, OF_p)$$

SOLUTION:

DEFINITIONS:

$$m_i = \qquad V_i = m_i/\rho_i$$

V_i = volume

$$\alpha_i = m_i/MT \qquad OF_p = m_f/m_b = \alpha_f/\alpha_b \tag{9}$$

BASIC EQUATIONS:

MASS CONTINUITY

$$m_c + m_f + m_b = m_T$$

$$\frac{m_c}{m_T} + \frac{m_f}{m_T} + \frac{m_b}{m_T} = 1$$

$$\alpha_c + \alpha_f + \alpha_b = 1 \qquad (10)$$

VOLUME CONTINUITY

$$V_T = V_b + V_f + V_c = \frac{m_b}{\rho_b} + \frac{m_f}{\rho_t} + \frac{m_c}{\rho_c}$$

$$\frac{V_c}{V_T} = \frac{m_c/pc}{\frac{m_b}{\rho_b} + \frac{m_f}{\rho_f} + \frac{m_c}{P_c}} = \frac{\alpha_c}{\alpha_b\left[\frac{\rho_c}{\rho_b}\right] + d_f\left[\frac{\rho_c}{\rho_f}\right] t\alpha_c} \qquad (11)$$

Rearranging (11)

$$\alpha_c = \frac{\frac{V_c}{V_T}\left[\alpha_b\left[\frac{\rho_c}{\rho_b}\right]\left[\frac{\rho_c}{\rho_f}\right]\right]}{\left[1 - \frac{V_c}{V_T}\right]} \qquad (11a)$$

Combining (1) and (2)

$$\alpha_b = \frac{1-\alpha_c}{(1 + OF)} \qquad (9a)$$

$$\alpha_f = \frac{1 - \alpha_c}{(1 + 1/OF)} \qquad (10a)$$

Substituting (9) and (10) into (11a)

$$\alpha_c = \frac{\frac{V_c}{V_T}\left[\left(\frac{1-\alpha_c}{1+OF_p}\right)\frac{\rho_c}{\rho_f}\right]}{\left[1-\frac{V_s}{V_T}\right]} \tag{12}$$

Rearranging, solve for α_c

$$\alpha_c = \frac{\frac{V_c}{V_T}\left[\frac{\rho_c}{\rho_b}\left(\frac{1}{1+OF_p}\right)+\frac{\rho_c}{\rho_f}\left(\frac{1}{1+1/OF_p}\right)\right]}{\left[1+\frac{V_c}{V_t}\left[\frac{\rho_c}{\rho_b}\left(\frac{1}{1+OF_p}\right)+\frac{\rho_c}{\rho_f}\left(\frac{1}{1+1/OF_p}\right)-1\right]\right]} \tag{13}$$

and

$$\alpha_f = \frac{1-\alpha_c}{1+1/OF_p} \tag{14}$$

Sample Calculation – ME 43

DATA

$$\rho_b = 0.920 g/cm^3 \quad HTPB$$

$$\rho_f = 1.950 g/cm^3 \quad AP$$

$$\rho_e = 2.165 g/cm^3 \quad NaCl$$

REQUIREMENTS

$$OF_p = 3.0$$

$$V_c/V_T = 0.3050 \quad \text{(Volume Fraction of NaCl)}$$

CALCULATION

$$\alpha_e = \frac{.3050\left[\frac{2.165}{.920}\left[\frac{1}{1+3.0}\right] + \frac{2.165}{1.950}\left[\frac{1}{1+1/3.0}\right]\right]}{\left[1+.3050\left[\frac{2.165}{.920}\left[\frac{1}{1+3.0}\right] + \frac{2.165}{1.950}\left[\frac{1}{1+1/3.0}\right] - 1\right]\right]}$$

$$\alpha_c = 0.384 \quad \text{(NaCl)}$$

$$\alpha_f = \frac{1-0.384}{1+1/3.0} = 0.462 \quad \text{(AP)}$$

$$\alpha_b = 1 - \alpha_c - \alpha_f = 1 - .384 - .462 = .154$$

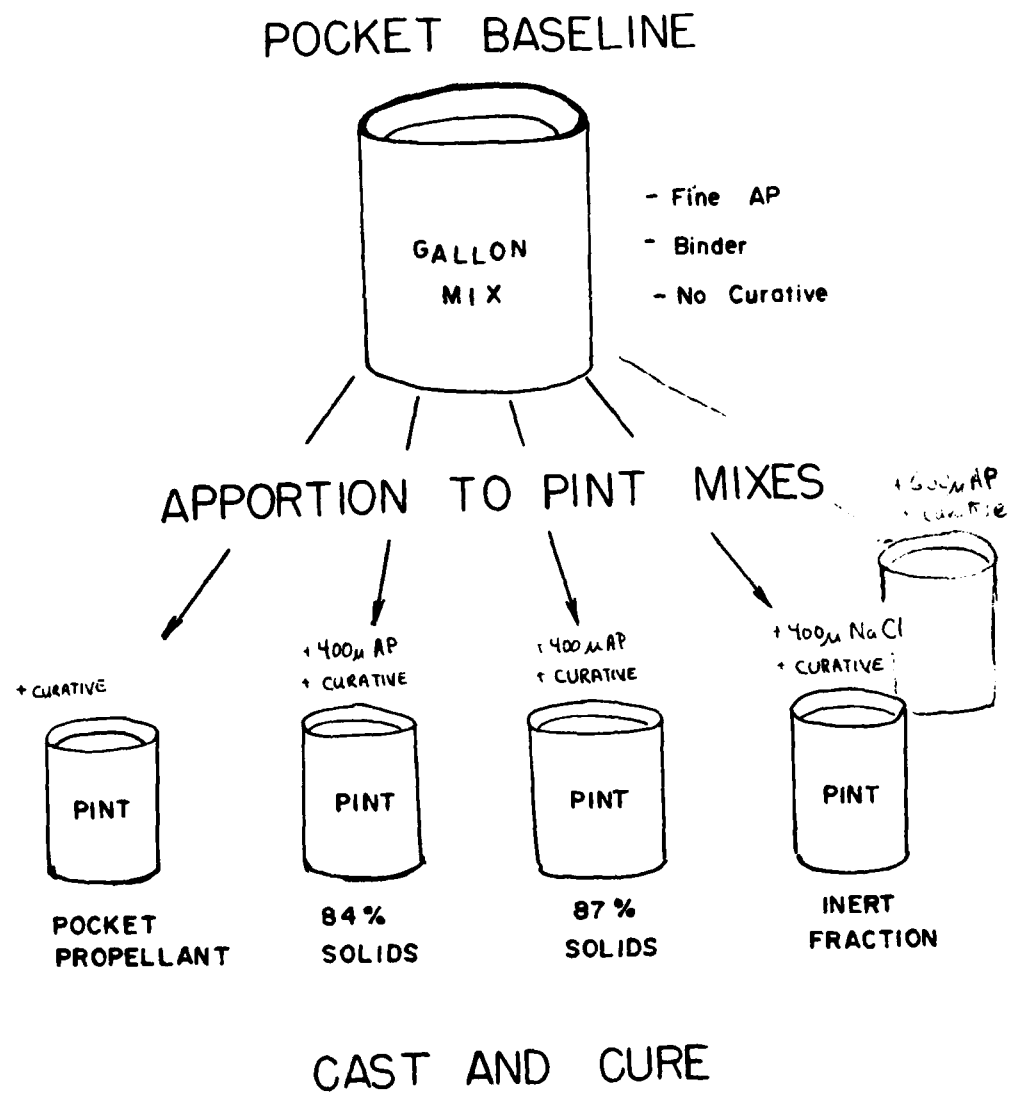

Figure E1 Mixing Procedure

Table E1
Mix Procedure

SOLID PROPELLANT PROCESSING SHEET

BATCH SIZE 4000 gr | DATE 20 May 85
MIXER 1 gal
BATCH NO 5110

I WEIGH OUT

MATERIAL	AMOUNT		WEIGHT	NOTES
	1162 %	G		102105
	464.7 GR	T		
		N		
	116.0 %	G		23047
	200.0 GR	T		
		N		
	2.0 %	G		10032-11A
	100.0 GR	T		
		N		
	230 %	G		60-518
	230.0 GR	T		
		N		
	%	G		
	GR	T		
		N		
	231 %	G		
	92.4 GR	T		
		N		
	116 %	G		
	4 GR	T		
		N		
	2.316 %	G		
	4 GR	T		
		N		
	%	G		
	GR	T		
		N		
	%	G		
	GR	T		
		N		

II MIX SCHEDULE

PROCESSING STEP	MIX TIME RPM OR SPEED	MIX TIME MIN	TEMP(°F) PROPELLANT	TEMP(°F) JACKET	INSTRUCTIONS
1 Add 12.5% IBDH, Mix, Agitate	1	(5)	no vac	140°F	(Blend AP)
2 +10% AP		(10)			
3 +25% AP		(10)			
4 +12.5% AP		(10)			
5 +15.5% AP		(10)			
6 Vac Mix		(60)	vac		(Scrape down)
7 Add IPDP	↓	(2/5)	no vac/vac	↓	
8 Cast					
9					
10					
11					
12					

A. Add ingredients directly to mixer
B. Mix without vacuum for one minute following solid addition
C. Mix under vacuum
VACUUM Lowest _____ mmHg
10 min. loss _____ mmHg

SOLVENT Dec
COMMENTS Class 1.3

III PHYSICAL PROPERTIES

A. VISCOSITY	1	2	3	4	5	6	AVERAGE
Spindle	E04						
Temperature (°F)	140°						
Reading	10.5						
Viscosity							

B. SHORE HARDNESS	1	2	3	4	5	6	AVERAGE
Initial							
Fifteen Seconds							

IV CURE 12 days

A. Use RAM-225 mold release as required.
B. Measure end-of-mix viscosity
C. Determine shore hardness on cooled cured sample.
D. Burn _____ inhibited strands as at _____

IN ___ OUT ___ TEMP
TOTAL TIME _____ MOLD
12 gal system

AFRPL FORM FEB 76 16

Table E2
Mix Charts - IPDI

Destinator	O/F_{pock}	Coarse Mat'l	Fine Mat'l	α_T	V_{cap}/V_T	α_c	α_F
ME-30	4,000	--	12μAP	.8000	0.0000	0.0000	0.8000
ME-31	4.000	--	12μAP	.8000	0.0000	0.0000	0.8000
ME-32	4.000	400μAP*	12μAP	.8400	.01690	0.200	0.6400
ME-33	4.000	400μAP	12μAP	.8700	0.305	0.3500	0.5200
ME-34	4.000	400μNaCl	12μAP	.8748	0.305	0.3740	0.5008
ME-35	4.000	600μAP	12μAP	.8700	0.305	0.3500	0.5200
ME-40	3.000	--	12μAP	.7500	0.0000	.0000	.7500
ME-41	3.000	--	12μAP	.7500	.0000	.0000	7500
ME-42	3.000	400μAP	12μAP	.8400	.3050	.3600	.4800
ME-43	3.000	400μNaCl	12μAP	.8461	.3050	.3845	.4616
ME-44	3.000	600μAP	12μAP	.8400	.3050	.3600	.4800
ME-45	3.000	400μAP	12μAP	.8700	.419	.4800	.3900
ME-50	2.000	--	12μAP	.6667	0.0000	.0000	.6667
ME-51	2.000	--	12μAP	.6667	.0000	.0000	.6667
ME-52	2.000	400μAP	12μAP	.7920	.3050	.3760	.4160
ME-53	2.000	400μNaCl	12μAP	.8004	.3050	.4012	.3992
ME-54	2.000	400μAP	12μAP	.8400	.4410	.5200	.3200
ME-55	2.000	400μAP	12μAP	.8700	.53247	.6100	.2600

Table E3
Mix Charts - DDI

Destinator	O/F_{pock}	Coarse Mat'l	Fine Mat'l	α_T	V_{cap}/V_T	α_c	α_F
ME-60	4.00	--	12μAP	.8000	0.0000	0.0000	0.8000
ME-61	4.00	--	12μAP	.8000	0.0000	0.0000	0.8000
ME-62	4.00	400μAP*	12μAP	.8400	0.1690	0.2000	0.6400
ME-63	4.00	400μAP	12μAP	.8700	0.305	0.3500	0.5200
ME-64	4.00	400μNaCa	12μAP	.8748	0.305	0.3740	0.5008
ME-65	4.00	600μAP	12μAP	.8700	.3050	0.3500	0.5200
ME-70	3.00	--	12μAP	.7500	0.0000	.0000	.7500
ME-71	3.00	--	12μAP	.7500	0.0000	.0000	.7500
ME-72	3.00	400μAP	12μAP	.8400	.3050	.3600	.4800
ME-73	3.00	400μNaCl	12μAP	.8461	.3050	.3845	.4616
ME-74	3.00	600μAP	12μAP	.8400	.3050	.3600	.4800
ME-75	3.00	400μAP	12μAP	.8700	.4190	.4800	.3900
ME-80	2.00	--	12μAP	.6667	0.0000	0.0000	.6667
ME-81	2.00	--	12μAP	.6667	0.0000	0.0000	.6667
ME-82	2.00	400μAP	12μAP	.7920	.3050	.3760	.4160
ME-83	2.00	400μNaCl	12μAP	.8004	.3050	.4012	.3992
ME-84	2.00	400μAP	12μAP	.8400	.441	.5200	.3200
ME-85	2.00	400μAP	12μAP	.870		.6100	.260

Appendix F: Propellant Ingredient Properties

Table F1
Ingredient Thermodynamic Properties

INGREDIENT	COMPOSITION	HEAT OF FORMATION
R-45M	$C_{7.332}H_{10.982}O_{0.058}$	-2.970 kcal/mole
IPDI	$C_{12}H_{18}O_2N_2$	-91.360
DDI	$C_{38}H_{66}O_2N_2$	-206.300
DOA	$C_{22}H_{42}O_4$	-312.80
Ag White	$C_{7.2124}H_{5.548}N_{.5548}$	28.43
HX-752	$C_{14}H_{16}N_2O_2$	-128.500
AP	NH_4ClO_4	-70.690

Table F2
Binder Ingredient Functions

ABBREVIATION	NAME	FUNCTION
R-45M	Hodroxyl-terminated Polybutadiene (HTPB)	Fuel
IPDI	Isophorone Diisocynate	Curative
DDI	Dimeracid Diisocynate	Curative
DOA	Dioctyladipate	Plasticzer
Agerite White™	Agerite White	Anti-Oxidant
HX-752	Substituted Diaziridene	Bonding Agent

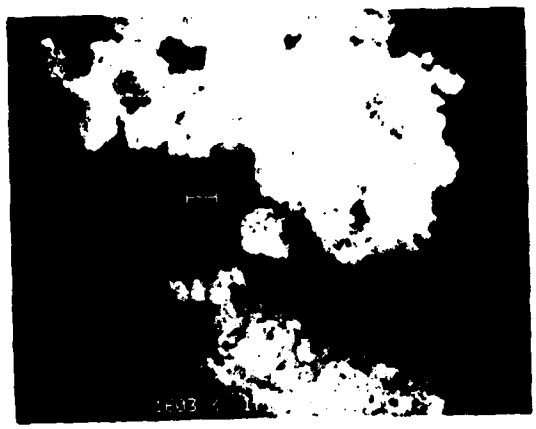

(a) 1.8μ, LOT 6-60-518-1520, AP

(b) 25μ, LOT 10092-11A, AP

(c) 400μ, LOT 73047, AP

Figure F1 SEM

(a) 16μ, LOT 310, AP

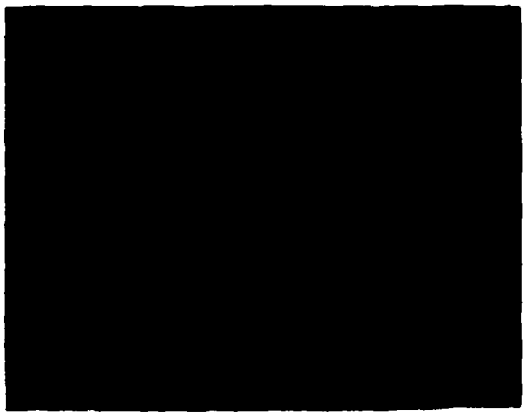

(b) 16μ, LOT 310, AP

Figure F2 SEM's

(a) 400μ sieved, LOT 73047

(b) 400μ sieved, NaC1, Morton

(c) 600μ, LOT 600-1-74, AP

Figure F3 SEM's of AP

Appendix G: Acoustic Emission Data-Monomodal and Bimodal Formulations

This appendix presents the burning rate data for the individual acoustic emission experiments. The results are tabulated according to the original mix numbers with each table showing the burning rate, strand number, and pressure for one propellant. Figure G-1 shows a diagram of how the samples were cut, labeled and tested. Table G-1 shows a cross-reference index between the designators used in this report and the mix numbers used to inde the data.

Tables G-2 to G-31 present the detailed burning rate results. These experiments were performed at the AFAL in the fall of 1986.

Table G 1
Propellant Designator Index

Text Designator	Mix Number		Text Designator	Mix Number
A-I	ME-31		A-II	ME-61
B-I	ME-41		B-II	ME-71
C-I	ME-51		C-II	ME-81
D-I	ME-32		D-II	ME-62
E-I	ME-42		E-II	ME-72
E-I-400S	ME-43		E-II-400S	ME-73
EI-600-A	ME-44		E-II-600A	ME-74
F-I	ME-54		F-II	ME-84
G-I	ME-33		G-II	ME-63
G-I-400S	ME-34		G-II-400S	ME-64
G-I-600A	ME-35		G-II-600A	ME-65
H-I	ME-45		H-II	ME-75
J-I	ME-55		J-II	ME-85
K-I	ME-52		K-II	ME-82
K-I-400S	ME-53		K-II-400S	ME-83
L-I	ME-6		L-II	ME-10
M-I	ME-7		M-II	ME-11
N-I	ME-5		N-II	ME-12
O-I	ME-8		O-II	ME-13
P-I	ME-9		P-II	ME-14

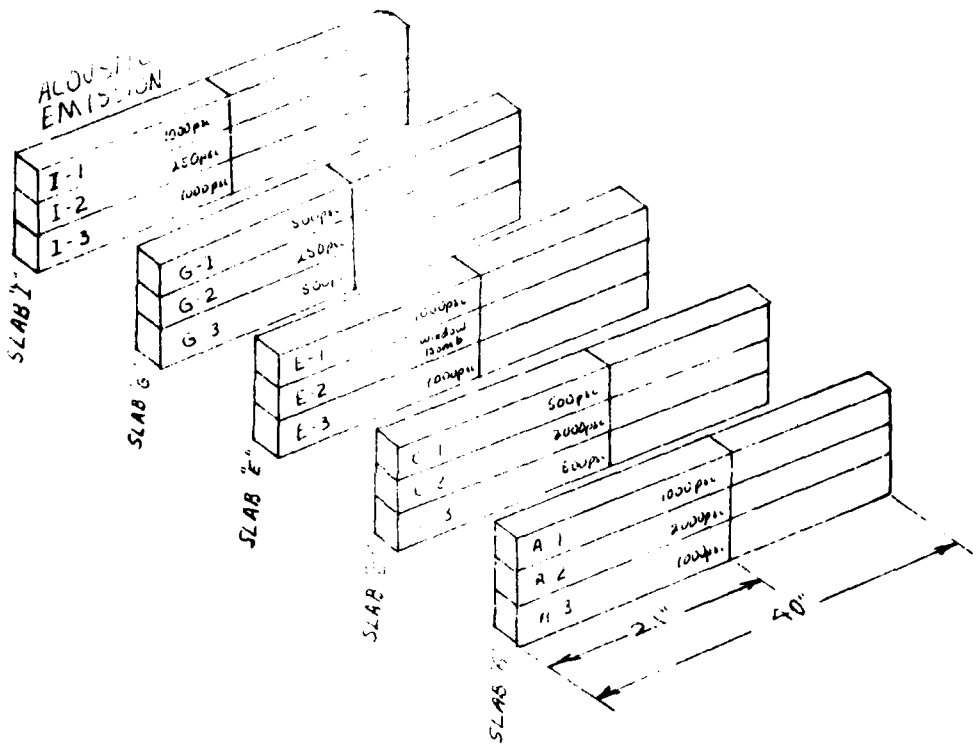

Figure G 1. Strand Testing Index

Table G 2
Burning Rate Results
Me-31 (A-I)

Press	Strand	Rate (in/sec)	Residue (in)	t_b (sec)	$\bar{r}$ (in/sec)	σ
125	A-2	x	x			
125	C-2	x	x			
250	G-2	.187	none		.189	
250	I-2	.189	none			
500	C-1	.247	none			
500	C-3	.249	none		.248	.001
500	G-1	.249	none			
500	G-3	.248	none			
1000	A-1	.361	none			
1000	A-3	.371	none			
1000	E-1	.356	none		.361	.006
1000	E-3	.361	none			
1000	I-1	.329	none			
1000	I-3	.359	none			
2000	A-2	.529	none		.535	
2000	C-2	.541	none			

Table G 3
Burning Rate Results
ME-32 (D-I)

Press	Strand	Rate (in/sec)	Residue (in)	t_b (sec)	$\bar{r}$ (in/sec)	σ
125	A-2	x			x	
125	C-2	x				
250	G-2	.188	none		.188	
250	I-2	.189	none			
500	C-1	.258	none			
500	C-3	.268	none			.006
500	G-1	.264	none			
500	G-3	.254	none			
1000	A-1	.380	none			
1000	A-3	.390	none			
1000	E-1	.374	none		.38	.009
1000	E-3	.391	none			
1000	I-1	.399	none			
1000	I-3	.385	none			
2000	A-2	.590	none			
2000	C-2	.571	none			

Table G 4
Burning Rate Results
ME-33 (G-I)

Press	Strand	Rate (in/sec)	Residue (in)	t_b (sec)	$\bar{r}$ (in/sec)	σ
125	A-2	x	none		x	
125	C-2	x				
250	G-2	.196			.201	
250	I-2	.205				
500	C-1	.285			.279	.005
500	C-3	.275				
500	G-1	.281				
500	G-3	.276				
1000	A-1	.456			.443	.021
1000	A-3	.439				
1000	E-1	.444				
1000	E-3	.404				
1000	I-1	.454				
1000	I-3	.460				
2000	A-2	.653			.641	
2000	C-2	.630				

Table G 5
Burning Rate Results
ME-34 (G-I-400S)

Press	Strand	Rate (in/sec)	Residue (in)	t_b (sec)	$\bar{r}$ (in/sec)	σ
125	A-2	x			x	
125	C-2	x				
250	G-2	.207			.207	
250	I-2	.207				
500	C-1	.309			.315	.008
500	C-3	.306				
500	G-1	.321				
500	G-3	.322				
1000	A-1	.537			.529	.030
1000	A-3	.491				
1000	E-1	.522				
1000	E-3	.478				
1000	I-1	.537				
1000	I-3	.554				
2000	A-2	.789			.783	
2000	C-2	.777				

Table G 6
Burning Rate Results
ME-35 (G-I-600A)

Press	Strand	Rate (in/sec)	Residue (in)	t_b (sec)	$\bar{r}$ (in/sec)	$\bar{\sigma}$
125	A-2	x			x	
125	C-2	x				
250	G-2	.260				
250	I-2	.199				
500	C-1	.318				
500	C-3	.281				
500	G-1	.284				
500	G-3	.283				
1000	A-1	.675*				
1000	A-3	.478				
1000	E-1	.425				
1000	E-3	.448				
1000	I-1	.508				
1000	I-3	.475				
2000	A-2	.727				
2000	C-2	.685				

*Omit, no ignition on first try

Table G-7
Burning Rate Results
ME-41 (B-I)

Press	Strand	Rate (in/sec)	Residue (in)	t_b (sec)	$\bar{r}$ (in/sec)	$\bar{\sigma}$
125	A-2	x	x			
125	C-2	x	x		x	
250	G-2	.152				
250	I-2	.151				
500	C-1	.190				
500	C-3	.174				
500	G-1	.189				
500	G-3	.190				
1000	A-1	.256				
1000	A-3	.243				
1000	E-1	.230				
1000	E-3	.241				
1000	I-1	.247				
1000	I-3	.244				
2000	A-2	.350				
2000	C-2	.351				

Table G 8
Burning Rate Results
ME-42 (E-I)

Press	Strand	Rate (in/sec)	Residue (in)	t_b (sec)	$\bar{r}$ (in/sec)	σ
125	A-2	x	x		x	x
125	C-2	x	x			
250	G-2	.164			.163	
250	I-2	.162				
500	C-1	.232			.232	.012
500	C-3	.228				
500	G-1	.222				
500	G-3	.225				
1000	A-1	.323			.322	.012
1000	A-3	.321				
1000	E-1	.326				
1000	E-3	.301				
1000	I-1	.319				
1000	I-3	.339				
2000	A-2	.462			.463	
2000	C-2	.465				

Table G 9
Burning Rate Results
ME-43 (E-I-400S)

Press	Strand	Rate (in/sec)	Residue (in)	t_b (sec)	$\bar{r}$ (in/sec)	σ
125	A-2	x	x		x	x
125	C-2	x	x			
250	G-2	.148			.150	
250	I-2	.151				
500	C-1	.232			.225	.006
500	C-3	.219				
500	G-1	.223				
500	G-3	.226				
1000	A-1	.386			.379	.005
1000	A-3	.374				
1000	E-1	.383				
1000	E-3	.373				
1000	I-1	.377				
1000	I-3	.383				
2000	A-2	.601			.596	
2000	C-2	.591				

Table G 10
Burning Rate Results
ME-44 (E-I-600A)

Press	Strand	Rate (in/sec)	Residue (in)	t_b (sec)	$\bar{r}$ (in/sec)	σ
125	A-2	x	x		x	x
125	C-2	x	x			
250	G-2	.170			.171	
250	I-2	.172				
500	C-1	.260				
500	C-3	.233			.241	.013
500	G-1	.239				
500	G-3	.231				
1000	A-1	.354				
1000	A-3	.342				
1000	E-1	.344			.348	.008
1000	E-3	.344				
1000	I-1	.363				
1000	I-3	.346				
2000	A-2	.456			.449	
2000	C-2	.443				

Table G 11
Burning Rate Results
ME-45 (H-I)

Press	Strand	Rate (in/sec)	Residue (in)	t_b (sec)	$\bar{r}$ (in/sec)	σ
125	A-2	x	x		x	x
125	C-2	x	x			
250	G-2	.170			.171	
250	I-2	.173				
500	C-1	.250				
500	C-3	.233			.241	.013
500	G-1	.249				
500	G-3	.229				
1000	A-1	.359				
1000	A-3	.359				
1000	E-1	.363			.348	.008
1000	E-3	.346				
1000	I-1	.357				
1000	I-3	.365				
2000	A-2	.509			.485	
2000	C-2	.485				

Table G-12
Burning Rate Results
ME-51 (C-I)

Press	Strand	Rate (in/sec)	Residue (in)	t_b (sec)	$\bar{r}$ (in/sec)	σ
125	A-2		1.823			
125	C-2		1.965			
250	G-2	.080	--		.078	
250	I-2	.077	--			
500	C-1		1.922			
500	C-3		1.642			
500	G-1		1.920			
500	G-3		1.978			
1000	A-1		1.975			
1000	A-3		1.940			
1000	E-1		1.864			
1000	E-3		1.954			
1000	I-1		1.875			
1000	I-3		1.930			
2000	A-2	x	x		x	x
2000	C-2	x	x			

Table G 13
Burning Rate Results
ME-52 (K-I)

Press	Strand	Rate (in/sec)	Residue (in)	t_b (sec)	$\bar{r}$ (in/sec)	σ
125	A-2	.080			.081	
125	C-2	.082				
250	G-2	.122			.121	
250	I-2	.120				
500	C-1	.192				
500	C-3	.167			.180	.016
500	G-1	.195				
500	G-3	.164				
1000	A-1	.254				
1000	A-3	.228				
1000	E-1	.278			.249	.022
1000	E-3	.232				
1000	I-1	.273				
1000	I-3	.231				
2000	A-2	x	x		x	x
2000	C-2	x	x			

Table G 14
Burning Rate Results
ME-53 (K-I-400S)

Press	Strand	Rate (in/sec)	Residue (in)	t_b (sec)	$\bar{r}$ (in/sec)	σ
125	A-2	0.000	2.1		0.000	
125	C-2	0.000	2.1			
250	G-2	.062	none		.060	
250	I-2	.058	none			
500	C-1	.095	none		.097	005
500	C-3	.101	none			
500	G-1	.101	none			
500	G-3	.092	none			
1000	A-1	.153	none		175	
1000	A-3	.176	none			
1000	E-1	.187	none			
1000	E-3	.176	none			
1000	I-1	.182	none			
1000	I-3	.173	none			
2000	A-2	x	x			
2000	C-2	x	x			

Table G 15
Burning Rate Results
ME-54 (F-I)

Press	Strand	Rate (in/sec)	Residue (in)	t_b (sec)	$\bar{r}$ (in/sec)	σ
125	A-2	.089	none		093	
125	C-2	.098	none			
250	G-2	.151	none		144	
250	I-2	.137	none			
500	C-1	.216	none		206	008
500	C-3	.206	none			
500	G-1	.202	none			
500	G-3	.198	none			
1000	A-1	.285	none		278	008
1000	A-3	.273	none			
1000	E-1	.279	none			
1000	E-3	.268	none			
1000	I-1	.281	none			
1000	I-3	.281	none			
2000	A-2	x	x			
2000	C-2	x	x			

Table G 16
Burning Rate Results
ME-55 (J-I)

Press	Strand	Rate (in/sec)	Residue (in)	t_b (sec)	$\bar{r}$ (in/sec)	σ
125	A-2	.095	none		.094	
125	C-2	.092	none			
250	G-2	.144	none		.14	
250	I-2	.143	none			
500	C-1	.231	none		.227	.005
500	C-3	.222	none			
500	G-1	.225	none			
500	G-3	.231	none			
1000	A-1	.332	none		.311	.014
1000	A-3	.308	none			
1000	E-1	.313	none			
1000	E-3	.783	none			
1000	I-1	.304	none			
1000	I-3	.296	none			
2000	A-2	x	x			
2000	C-2	x	x			

Table G 17
Burning Rate Results
ME-61 (A-II)

Press	Strand	Rate (in/sec)	Residue (in)	t_b (sec)	$\bar{r}$ (in/sec)	σ
125	A-2	.122	none		.121	
125	C-2	.120	none			
250	G-2	.159	none		.16	
250	I-2	.169	none			
500	C-1	(.23)*	1.88	5.2	(.15)*	(.05)*
500	C-3	(.132)*	1.723	2.12		
500	G-1	(.208)*	1.900	.48		
500	G-3	(.100)*	1.822	1.77		
1000	A-1	(.41)*	1.935	.16	(.6)*	(.5)*
1000	A-3	(.25)*	1.665	1.38		
1000	E-1	(.39)*	1.910	.23		
1000	E-3	(.5)*	1.912	.16		
1000	I-1	(1.6)*	1.935	.03		
1000	I-3	(.2)*	1.820	.77		
2000	A-2	x	x		x	x
2000	C-2	x	x			

*based upon portion that burned

Table G-18
Burning Rate Results
ME-62 (D-II)

Press	Strand	Rate (in/sec)	Residue (in)	t_b (sec)	$\bar{r}$ (in/sec)	σ
125	A-2	.127	none		.128	
125	C-2	.128	none			
250	G-2	.163	none		.164	
250	I-2	.164	none			
500	C-1	.178	none		.190	.011
500	C-3	.204	none			
500	G-1	.193	none			
500	G-3	.186	none			
1000	A-1	.264	none		.259	
1000	A-3	.264	none			
1000	E-1	.249	none			
1000	E-3	.249	none			
1000	I-1	.251	none			
1000	I-3	.276	none			
2000	A-2	x	x			
2000	C-2	x	x			

Table G-19
Burning Rate Results
ME-63 (G-II)

Press	Strand	Rate (in/sec)	Residue (in)	t_b (sec)	$\bar{r}$ (in/sec)	σ
125	A-2	.134			.135	
125	C-2	.136				
250	G-2	.181			.177	
250	I-2	.173				
500	C-1	.215				
500	C-3	.203			.208	
500	G-1	.210				
500	G-3	.204				
1000	A-1	-	burned			
1000	A-3	.290				
1000	E-1	.334			.302	
1000	E-3	.302				
1000	I-1	.291				
1000	I-3	.292				
2000	A-2	x	x			
2000	C-2	x	x			

Table G 20
Burning Rate Results
ME-64 (G-II-400S)

Press	Strand	Rate (in/sec)	Residue (in)	t_b (sec)	$\bar{r}$ (in/sec)	σ
125	A-2	.092			.095	
125	C-2	.098				
250	G-2	.143			.165	
250	I-2	.186				
500	C-1	.116			.121	
500	C-3	.131				
500	G-1	.120				
500	G-3	.119				
1000	A-1	.191			.195	.036
1000	A-3	.185				
1000	E-1	.179				
1000	E-3	.267				
1000	I-1	.173				
1000	I-3	.174				
2000	A-2	x	x			
2000	C-2	x	x			

Table G-21
Burning Rate Results
ME-65 (G-II-600A)

Press	Strand	Rate (in/sec)	Residue (in)	t_b (sec)	$\bar{r}$ (in/sec)	σ
125	A-2	.138			.134	
125	C-2	.130				
250	G-2	.175			.180	
250	I-2	.185				
500	C-1	.219			.218	.005
500	C-3	.211				
500	G-1	.223				
500	G-3	.221				
1000	A-1	.336			.323	.009
1000	A-3	.327				
1000	E-1	.313				
1000	E-3	.325				
1000	I-1	.314				
1000	I-3	.323				
2000	A-2	x	x			
2000	C-2	x	x			

Table G 22
Burning Rate Results
ME-71 (B-II)

Press	Strand	Rate (in/sec)	Residue (in)	t_b (sec)	$\bar{r}$ (in/sec)	σ
125	A-2	(.32)*	1.29	2.16	(.16)*	
125	C-2	(.13)*	1.55	.33		
250	G-2	(.10)*	1.94	.83	(.10)*	
250	I-2	(.10)*	1.90	.96		
500	C-1	(.10)*	1.90	.95	(.11)*	
500	C-3	(.14)*	1.87	1.06		
500	G-1	(.11)*	1.88	.87		
500	G-3	(.10)*	1.915	.83		
1000	A-1	(.20)*	1.905	.47	(.18)*	
1000	A-3	(.25)*	1.90	.41		
1000	E-1	(.26)*	1.91	.35		
1000	E-3	(.20)*	1.895	.50		
1000	I-1	(.15)*	1.94	.41		
1000	I-3	(.15)*	1.93	.48		
2000	A-2	x	x			
2000	C-2	x	x			

*based upon portion that burned

Table G-23
Burning Rate Results
ME-72 (E-II)

Press	Strand	Rate (in/sec)	Residue (in)	t_b (sec)	$\bar{r}$ (in/sec)	σ
125	A-2	.109	none		.103	
125	C-2	.098	none			
250	G-2	.134	none		.133	
250	I-2	.132	none			
500	C-1	(.12)*	1.82	1.45	(.14)*	
500	C-3	(.14)*	1.79	2.09		
500	G-1	(.10)*	1.935	.70		
500	G-3	(.15)*	1.855	.92		
1000	A-1	.189	none		.204	.008
1000	A-3	.206	none			
1000	E-1	.189	none			
1000	E-3	(.18)*	1.82	1.00		
1000	I-1	.198	none			
1000	I-3	(.30)*	1.165	2.79		
2000	A-2	x	x			
2000	C-2	x	x			

*based upon portion that burned

Table G 24
Burning Rate Results
ME-73 (E-II-400S)

Press	Strand	Rate (in/sec)	Residue (in)	t_b (sec)	$\bar{r}$ (in/sec)	σ
125	A-2	.053			.049	
125	C-2	.046				
250	G-2	.061			.061	
250	I-2	.060				
500	C-1	.065			.066	
500	C-3	(.07)*	1.16	.12		
500	G-1	.069				
500	G-3	.065				
1000	A-1	.105			.102	.009
1000	A-3	.084				
1000	E-1	.106				
1000	E-3	.104				
1000	I-1	.111				
1000	I-3	.104				
2000	A-2	x	x			
2000	C-2	x	x			

*based upon portion that burned

Table G 25
Burning Rate Results
ME-74 (E-II-600A)

Press	Strand	Rate (in/sec)	Residue (in)	t_b (sec)	$\bar{r}$ (in/sec)	σ
125	A-2	.163			.134	
125	C-2	.105				
250	G-2	.134			.132	
250	I-2	.130				
500	C-1	.165			.163	.009
500	C-3	.166				
500	G-1	.158				
500	G-3	(.14)*	1.66	2.45		
1000	A-1	.248			.234	.009
1000	A-3	.238				
1000	E-1	.230				
1000	E-3	.236				
1000	I-1	.220				
1000	I-3	.233				
2000	A-2	x	x			
2000	C-2	x	x			

*based upon portion that burned

Table G 26
Burning Rate Results
ME-75 (H-II)

Press	Strand	Rate (in/sec)	Residue (in)	t_b (sec)	$\bar{r}$ (in/sec)	σ
125	A-2	.144	none		.130	
125	C-2	.116	none			
250	G-2	.155	none		.151	
250	I-2	.148	none			
500	C-1	.191	none		.188	
500	C-3	.181	none			
500	G-1	.186	none			
500	G-3	.193	none			
1000	A-1	.236	none		.251	
1000	A-3	.255	none			
1000	E-1	.250	none			
1000	E-3	.247	none			
1000	I-1	.245	none			
1000	I-3	.274	none			
2000	A-2	x	x			
2000	C-2	x	x			

Table G 27
Burning Rate Results
ME-81 (C-II)

Press	Strand	Rate (in/sec)	Residue (in)	t_b (sec)	$\bar{r}$ (in/sec)	σ
125	A-2	(.26)*	1.835	.626	(.14)*	
125	C-2	(.02)*	1.985	.841		
250	G-2	(.05)*	1.945	1.134	(.05)*	
250	I-2	(.06)*	1.923	1.132		
500	C-1	(.05)	1.215	16.83	(.04)*	
500	C-3	(.05)*	1.785	3.82		
500	G-1	(.05)*	1.460	11.75		
500	G-3	(.08)	2.100	86		
1000	A-1	(.06)*	1.570	7.82	(.03)*	
1000	A-3	(.03)*	1.940	2.07		
1000	E-1	(.04)*	1.940	1.57		
1000	E-3	(.03)*	1.950	1.99		
1000	I-1	(.01)*	1.955	1.07		
1000	I-3	(.01)*	1.99	90		
2000	A-2	x	x			
2000	C-2	x	x			

*based upon portion that burned

Table G 28
Burning Rate Results
ME-82 (K-II)

Press	Strand	Rate (in/sec)	Residue (in)	t_b (sec)	$\bar{r}$ (in/sec)	σ
125	A-2	.076	none		.075	
125	C-2	.074	none			
250	G-2	.099	none		.099	
250	I-2	.099	none			
500	C-1	(.16)*	1.835	1.04	(.12)*	.03
500	C-3	(.10)*	1.690	3.17		
500	G-1	(.10)*	1.390	6.48		
500	G-3	(.13)*	1.900	.77		
1000	A-1	.011	none		(.16)*	.02
1000	A-3	(.15)*	1.255	5.14		
1000	E-1	(.13)*	1.750	1.84		
1000	E-3	(.15)*	1.865	0.88		
1000	I-1	(.18)*	1.830	.095		
1000	I-3	(.18)*	1.835	0.94		
2000	A-2	x	x			
2000	C-2	x	x			

*based upon portion that burned

Table G 29
Burning Rate Results
ME-83 (K-II-400S)

Press	Strand	Rate (in/sec)	Residue (in)	t_b (sec)	$\bar{r}$ (in/sec)	σ
125	A-2	(.00)*	2.1	1.14	(.00)*	
125	C-2	(.00)*	2.1	1.53		
250	G-2	(.00)*	2.1	1.64	(.00)*	
250	I-2	(.00)*	2.1	.26		
500	C-1	.045			.045	
500	C-3	(.00)*	2.1	.79		
500	G-1	(.04)*	.5	35.82		
500	G-3	(.00)*	2.1	.85		
1000	A-1	.077			.072	
1000	A-3	(.00)*	2.1	.76		
1000	E-1	(.04)*	1.86	3.49		
1000	E-3	(.04)*	1.55	10.49		
1000	I-1	.067				
1000	I-3	(.00)*	2.1	1.42		
2000	A-2	x	x			
2000	C-2	x	x			

Table G-30
Burning Rate Results
ME-84 (F-II)

Press	Strand	Rate (in/sec)	Residue (in)	t_b (sec)	$\bar{r}$ (in/sec)	σ
125	A-2	.092	none		.092	
125	C-2	.092	none			
250	G-2	.119	none		.120	
250	I-2	.121	none			
500	C-1	.161	none		.155	
500	C-3	.152	none			
500	G-1	.152	none			
500	G-3	.154	none			
1000	A-1	.209	none		.209 (.004)	
1000	A-3	.211	none			
1000	E-1	.205	none			
1000	E-3	.215	none			
1000	I-1	.206	none			
1000	I-3	.206	none			
2000	A-2	x	x			
2000	C-2	x	x			

Table G 31
Burning Rate Results
ME-85 (J-II)

Press	Strand	Rate (in/sec)	Residue (in)	t_b (sec)	$\bar{r}$ (in/sec)	σ
125	A-2	.111	none		.108	
125	C-2	.106	none			
250	G-2	.132	none		.136	
250	I-2	.141	none			
500	C-1	.190	none		.193	.033
500	C-3	.184				
500	G-1	.209	none			
500	G-3	.180	none			
1000	A-1	.270	none		.263	
1000	A-3	.270	none			
1000	E-1	.263	none			
1000	E-3	.244	none			
1000	I-1	.257	none			
1000	I-3	.261	none			
2000	A-2	x	x			
2000	C-2	x	x			

Appendix H: Acoustic Emission Data: Trimodal Propellants

The average burning rate as a function of pressure and location in the casting was determined using the combustion bomb with acoustic emission. The 1/2 gallon cartons were cut into strands and slabs according to the diagram shown in Figure H1. Eleven strands were cut from three planes in both the top and bottom half of the carton. Strands from the top half were cut in the vertical direction, while those in the bottom half were cut in the horizontal direction.

Half of the strands from sections B, G, and L were burned at 1000 psi and the remaining strands were burned according to the following (also illustrated in Figure H1):

Table H1
Strand Testing Schedule

Section	Pressure (psi)	Strand No.
T-B	2000	1,3,5,8,10
	1000	2,4,7,9,11
B-B	2000	1,3,5,8,10
	1000	2,4,7,9,11
T-G	500	1,3,5,8,10
	1000	2,4,7,9,11
B-G	500	1,3,5,8,10
	1000	2,4,7,9,11
T-L	250	1,3,5,8,10
	1000	2,4,7,9,11
B-L	250	1,3,5,8,10
	1000	2,4,7,9,11

The strands were burned in a nitrogen filled combustion bomb. The burning time is determined using an acoustic emission sensor.

The data are tabulated according to the original mix number. Table H2 lists a cross-reference guide between the propellant designators used in this report and the original mix numbers. Each table lists the individual strand burning rates and combined statistics. Averages and standard deviations were computed for each slab, the top half of the carton, the bottom half of the carton, and the total carton for the strands tested at 1000 psi. Averages and standard deviations for 250,500 and 2000 psi were computed for each slab, and all strands at a given pressure. These results are tabulated in Tables H2 to H12.

Table H2
Propellant Designator Index

Text Designator	Mix Number		Text Designator	Mix Number
L-I	ME-6		L-II	ME-10
M-I	ME-7		M-II	ME-11
N-I	ME-5		N-II	ME-12
O-I	ME-8		O-II	ME-13
P-I	ME-9		P-II	ME-14

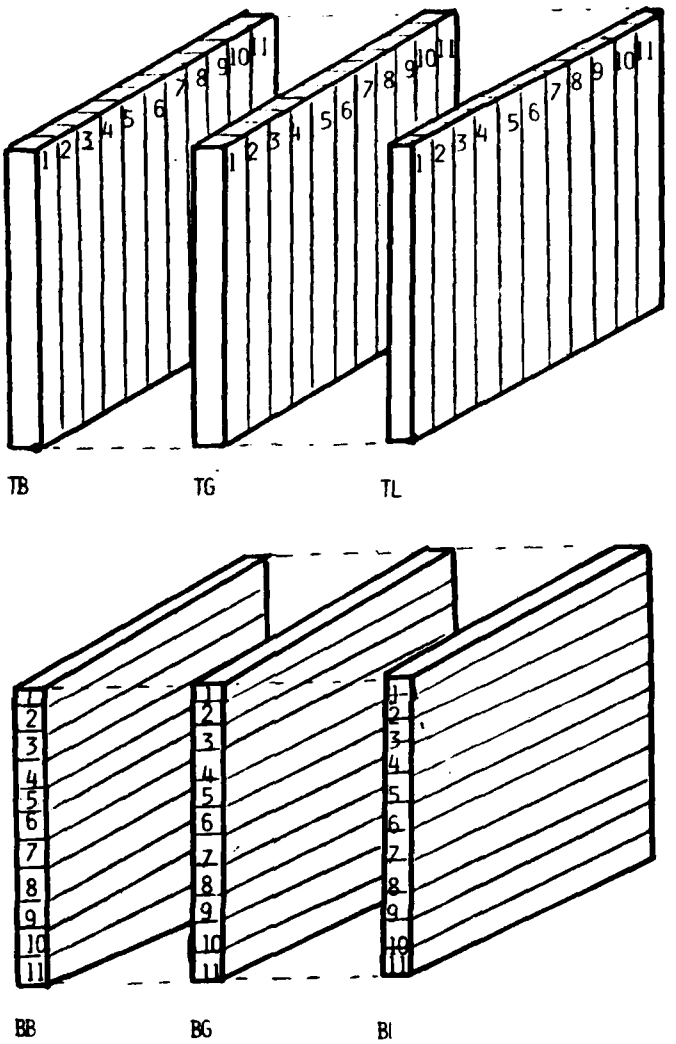

Figure H1. Gallon-Casting Strand Diagram

Table H3
Burning Rate Results
ME-5 (N-I)

STRAND NO.	BURNING RATE 1000 psi (in/sec)					
	TB	BB	TG	BG	TL	BL
2	.381	.388	.398	.398	.427	.431
4	.387	.392	.398	.423	.410	.420
7	.385	.400	.422	.413	.409	.431
9	.411	.402	.407	.414	.415	.416
11	.389	.402	.415	.428	.419	.432
STATISTICS						
$\bar{r}_1$	.391	.397	.408	.415	.416	.423
σ_1	.012	.007	.010	.012	.007	.009
$\bar{r}_2$	.394		.412		.421	
σ_2	.394		.412		.421	
$\bar{r}_3$	.410					
σ_3	.016					

$\bar{r}_T$	.405
σ_T	.014
$\bar{r}_B$	.415
σ_B	.017

STRAND NO	250 psi		500 psi		2000 psi	
	TB	BB	TG	BG	TL	BL
1	.163	.176	.254	.261	.791	.833
3	.167	.177	.248	.260	.826	.840
5	.170	.181	.242	.265	.935	.949
8	.173	.175	.252	.272	.929	.952
10	.171	.172	.257	.253	.896	.870
STATISTICS						
$\bar{r}_1$	.169	.177	.251	.266	.856	.875
σ_1	.004	.003	.006	.006	.069	.049
$\bar{r}_2$	.173		.258		.866	
σ_2	.005		.010		.055	

Table H4
Burning Rate Results
ME-6 (L-I)

STRAND NO.	BURNING RATE 1000 psi (in/sec)					
	TB	BB	TG	B6	TL	BL
2	.487	.550	.485	.539	.566	.483
4	.515	.570	.469	.540	.563	.515
7	.513	.619	.467	.524	.555	.541
9	.535	.593	.500	.535	.584	.531
11	.529	.601	.526	*	.564	.512
STATISTICS						
$\bar{r}_1$	.516	.587	.490	.531	.566	.522
σ_1	.019	.027	.024	.007	.011	.023
$\bar{r}_2$	.551		.510		.544	
σ_2	.043		.029		.029	
$\bar{r}_3$	.536					
σ_3	.038					

$\bar{r}_T$	.536
σ_T	.038
$\bar{r}_B$	.549
σ_B	.036

STRAND NO	250 psi		500 psi		2 000 psi	
	TB	BB	TG	BG	TL	BL
1	.192	.213s	.418	.343	1.099	1 023
3	.199	.202	.322	.329	1.111	1 240
5	.185	.205	.315	.343	1.121	1 245
8	.201	.213	.320	.340	1 176	1.299
10	.210	.210	.328	.336	1 186	*
STATISTICS						
$\bar{r}_1$	.197	.209	.317	.338	1 139	1 253
σ_1	.010	.005	.057	.006	039	.031
$\bar{r}_2$	.203		.312		1.190	
σ_2	.009		.080		.069	

Table H5
Burning Rate Results
ME-7 (M-I)

STRAND NO.	BURNING RATE 1000 psi (in/sec)					
	TB	BB	TG	BG	TL	BL
2	.508	.419	.533	.435	.532	.478
4	.467	.437	.431	.431	.467	.476
7	.496	.418	.420	.432	.506	.476
9	.496	.418	.419	.437	.472	.489
11	.497	.457	.456	.414	.496	.471
STATISTICS						
$\bar{r}_1$	.493	.412	.458	.437	.491	.478
σ_1	.015	.014	.011	.005	.027	.007
$\bar{r}_2$	.467		.447		.486	
σ_2	.030		.032		.020	
$\bar{r}_3$	.467					
σ_3	.031					

$\bar{r}_T$	.482
σ_T	.033
$\bar{r}_B$	.452
σ_B	.021

STRAND NO	250 psi		500 psi		2000 psi	
	TB	BB	TG	BG	TL	BL
1	.184	.194	.433	.313	.935	1.104
3	.184	.191	.317	.301	.913	.971
5	.184	.193	.290	.352	.962	1.042
8	.184	.192	.302	.291	1.014	1.017
10	.186	.192	.303	.348	.963	1.049
STATISTICS						
$\bar{r}_1$	.184	.192	.329	.313	.954	1.011
σ_1	.001	.001	.059	.030	.031	.025
$\bar{r}_2$	.188		.326		.967	
σ_2	.004		.048		.033	

Table H6
Burning Rate Results
ME-8 (O-I)

STRAND NO.	BURNING RATE 1000 psi (in/sec)					
	TB	BB	TG	BG	TL	BL
2	.387	.376	.382	.369	.392	.426
4	.395	.400	.382	.362	.398	.401
7	.388	.383	.374	.365	.396	.399
9	.393	.394	.397	.368	.401	.402
11	.407	.381	.398	.373	.402	.401
STATISTICS						
$\bar{r}_1$	.394	.388	.387	.368	.398	.406
σ_1	.008	.009	.011	.004	.004	.011
$\bar{r}_2$	.391		.377		.402	
σ_2	.009		.013		.009	
$\bar{r}_3$	.390					
σ_3	.014					

$\bar{r}_T$	.390
σ_T	.009
$\bar{r}_B$	.398
σ_B	.018

STRAND NO	250 psi		500 psi		2000 psi	
	TB	BB	TG	BG	TL	BL
1	.164	.182	.243	.251	.557	.652
3	.166	.177	.250	.245	.599	.637
5	.182	.178	.238	.247	.628	.601
8	.173	.195	.235	.252	.616	.651
10	.180	.176	.241	.251	.612	.651
STATISTICS						
$\bar{r}_1$	.173	.182	.241	.249	.602	.656
σ_1	.008	.008	.006	.003	.028	.020
$\bar{r}_2$	.177		.245		.629	
σ_2	.009		.003		.037	

Table H7
Burning Rate Results
ME-9 (P-I)

STRAND NO.	BURNING RATE 1000 psi (in/sec)					
	TB	BB	TG	BG	TL	BL
2	.352	.339	.349	.346	.345	.334
4	.350	.339	.346	.347	.348	.336
7	.350	.346	.343	.355	.346	.341
9	.353	.341	.352	.350	.348	.341
11	.358	.348	.352	.357	.353	.348
STATISTICS						
$\bar{r}_1$	.353	.342	.348	.351	.348	.340
σ_1	.004	.004	.005	.005	.003	.006
$\bar{r}_2$	.348		.350		.344	
σ_2	.007		.004		.006	
$\bar{r}_3$	.347					
σ_3	.006					

$\bar{r}_T$	.350
σ_T	.004
$\bar{r}_B$	.345
σ_B	.007

STRAND NO.	250 psi		500 psi		2000 psi	
	TB	BB	TG	BG	TL	BL
1	156	149	234	224	350	337
3	157	153	230	225	324	311
5	155	153	225	230	[illegible]	[illegible]
8	157	155	227	228	[illegible]	[illegible]
10	157	[illegible]	231	[illegible]	[illegible]	[illegible]
STATISTICS						
$\bar{r}_1$	156	151	230	226	337	[illegible]
σ_1	.001	[illegible]	.004	[illegible]	[illegible]	[illegible]
$\bar{r}_2$	153		229		[illegible]	
σ_2	[illegible]		[illegible]		[illegible]	

Table H8
Burning Rate Resuls
ME-10 (L-II)

STRAND NO.	BURNING RATE 1000 psi (in/sec)					
	TB	BB	TG	B6	TL	BL
2	.290	.287	.275	*	.303	.304
4	.288	.311	.283	.286	.328	.297
7	.308	.304	.281	.280	.292	.305
9	.298	.304	.287	.266	.288	.318
11	.317	.303	.288	.304	.297	.294
STATISTICS						
$\bar{r}_1$	300	.302	.283	.284	.302	.304
σ_1	.012	.009	.005	.016	.016	.009
$\bar{r}_2$	.301		.283		.303	
σ_2	.010		.010		.012	
$\bar{r}_3$	.296					
σ_3	.014					

$\bar{r}_T$	.295
σ_T	.014
$\bar{r}_B$	.297
σ_B	.014

STRAND NO	250 psi		500 psi		2000 psi	
	TB	BB	TG	BG	TL	BL
1	.230	.255	.221	.226	.404	*
3	.239	.252	.217	.231	.452	.414
5	.247	.251	.231	.217	.452	.416
8	.245	.257	.217	.238	.474	.450
10	.237	.260	.237	.226	464	458
STATISTICS						
$\bar{r}_1$	.240	.255	.225	.228	449	442
σ_1	.007	.004	.009	.008	.027	.019
$\bar{r}_2$	.247		.226		.446	
σ_2	010		008		023	

Table H9
Burning Rate Results
ME-11 (M-II)

STRAND NO.	BURNING RATE 1000 psi (in/sec)					
	TB	BB	TG	BG	TL	BI
2	272	267	275	278	330	261
4	283	*	276	272	294	268
7	282	282	302	270	284	280
9	279	274	278	271	282	286
11	288	273	*	282	*	287
STATISTICS						
$\bar{r}_1$	281	274	283	275	298	276
σ_1	006	006	013	005	022	012
$\bar{r}_2$	278		278		286	
σ_2	007		010		019	
$\bar{r}_3$	281					
σ_3	013					

$\bar{r}_1$	248
σ_1	039
$\bar{r}_2$	275
σ_2	005

STRAND NO	250 psi		500 psi		2000 psi	
	TB	BB	TG	BG	TL	BI
1	238	258	220	202	405	407
3	239	241	212	208	426	405
5	231	249	217	*	457	436
8	240	246	215	210	472	449
10	242	300	229	213	472	457
STATISTICS						
$\bar{r}_1$	238	279	217	207	444	423
σ_1	005	024	005	004	027	019
$\bar{r}_2$	248		213		437	
σ_2	019		009		029	

Table H10
Burning Rate Results
ME-12 (N-II)

STRAND NO.	BURNING RATE 1000 psi (in/sec)					
	TB	BB	TG	B6	TL	BL
2	.280	.305	*	.311	.320	.298
4	.273	.287	.276	.308	.288	.296
7	.277	.292	.312	.292	.297	.292
9	.284	.287	.312	.289	.300	.293
11	.285	.306	.281	.355	.368	.269
STATISTICS						
$\bar{r}_1$	.280	.296	.295	.317	.315	.295
σ_1	.005	.009	.020	.030	.032	.003
$\bar{r}_2$	.288		.307		.305	
σ_2	.011		.027		.021	
$\bar{r}_3$	.300					
σ_3	.022					

$\bar{r}_T$	.277
σ_T	.031
$\bar{r}_B$	.303
σ_B	.020

STRAND NO	250 psi		500 psi		2000 psi	
	TB	BB	TG	BG	TL	BL
1	.183	.175	.208	.202	.382	.393
3.	.184	.181	.203	.204	.371	.382
5	.197	.184	.225	.202	.375	.418
8	.181	.181	.208	.203	.402	.376
10	.203	.184	.217	.208	.394	.428
STATISTICS						
$\bar{r}_1$	.190	.181	.212	.204	.385	.410
σ_1	.010	.004	.009	.003	.013	.052
$\bar{r}_2$	.185		.208		.402	
σ_2	.008		.007		.040	

Table H11
Burning Rate Results
ME-13 (O-II)

STRAND NO.	BURNING RATE 1000 psi (in/sec)					
	TB	BB	TG	BG	TL	BL
2	*	.296	.282	.294	.290	.267
4	.276	.286	.283	.282	.365	.281
7	.278	.285	.278	.287	.316	.279
9	.309	.283	.286	.281	.308	.280
11	.281	.282	.279	.287	.280	.290
STATISTICS						
$\bar{r}_1$	.286	.286	.282	.286	.312	.285
σ_1	.015	.006	.003	.005	.033	.008
$\bar{r}_2$	/286		.284		.299	
σ_2	.010		.005		026	
$\bar{r}_3$	.290					
σ_3	.018					

$\bar{r}_T$	.274
σ_T	.031
$\bar{r}_B$	.330
σ_B	050

STRAND NO	250 psi		500 psi		2 000 psi	
	TB	BB	TG	BG	TL	BL
1	154	160	.202	194	317	.000
3	155	166	215	195	.326	299
5	156	173	.198	000	.349	327
8	162	164	197	205	331	350
10	151	166	207	199	337	322
STATI-TICS						
$\bar{r}_1$	158	166	204	198	332	327
σ_1	004	005	007	005	011	021
$\bar{r}_2$	162		201		328	
σ_2	009		007		015	

Table H12
Burning Rate Results
ME-14 (P-II)

STRAND NO.	BURNING RATE 1000 psi (in/sec)					
	TB	BB	TG	B6	TL	BL
2	.273	.274	.276	.285	.286	.283
4	.267	.274	.290	.280	.297	.280
7	.267	.284	.277	.299	.275	.284
9	.273	.278	.280	.300	.276	.311
11	.285	.283	.276	.283	.278	.289
STATISTICS						
$\bar{r}_1$	.273	.279	.280	.289	.282	.290
σ_1	.007	.005	.006	.010	.009	.012
$\bar{r}_2$	.276		.285		.286	
σ_2	.006		.009		.011	
$\bar{r}_3$	.282					
σ_3	.010					

$\bar{r}_T$	.279
σ_T	.008
$\bar{r}_B$	.306
σ_B	.024

STRAND NO	250 psi		500 psi		2000 psi	
	TB	BB	TG	BG	TL	BL
1	.141	.155	.198	.200	.333	.313
3	.149	.163	.198	.224	.302	.319
5	.153	.160	.197	.207	.355	.000
8	.163	.183	.198	.201	.426	.312
10	.151	.155	.200	.219	.33	.319
STATISTICS						
$\bar{r}_1$	.151	.163	.198	.210	.349	.316
σ_1	.008	.012	.001	.011	.017	.004
$\bar{r}_2$	.157		.204		.334	
σ_2	.011		.010		.038	

GLOSSARY

accuracy	the difference between the measured value and the actual value
bandwidth	the frequency range (of the input) over which the system will respond satisfactorily
damping ratio	an indication the amplitude of the output to the amplitude of the input for harmonic inputs at the natural frequency
DDI	dimeracid diisocynate (curative)
DOA	dioctyladipate (plasticizer)
gain crossover frequency	the frequency at which the open-loop amplitude ratio is unity (0 db)
gain margin	amount of additional gain above the nominal that may be present in the system before the system becomes marginally stable.
HTPB	hydroxyterminated polybutadiene (polymer fuel)
IPDI	isophorone diisocynate (curative)
NCO/OH	isocynate to hydroxyl ratio
phase crossover freq	frequency at which the phase lag is -180 deg
phase margin	the number of degrees the phase is greater than -180 deg at the gain crossover frequency
pocket propellant	propellant composition that would exist if coarse particles were removed from a bimodal propellant
resolution	the smallest change that can be measured
rise time	the time required for the response from a unit-step function to rise from 10% to 90% of its final value
steady-state error	measure of the system accuracy when a specific input is applied